université PARIS-SACLAY

Fractional quantum Hall states in graphene systems

États de Hall quantique fractionnaire des systèmes de graphène

Thèse de doctorat de l'université Paris-Saclay

École doctorale n° 564, Physique en Île-de-France (PIF)
Spécialité de doctorat: Physique
Graduate School : Physique, Référent : Faculté des Sciences d'Orsay

Thèse préparée dans l'unité de recherche **IPhT (Université Paris-Saclay, CNRS, CEA)**, sous la direction de **M. Thierry JOLICOEUR**, Directeur de recherche

Thèse soutenue à Paris-Saclay, le 28 juin 2023, par

Ngoc Duc LE

Composition du jury

Membres du jury avec voix délibérative

M. Sylvain CAPPONI Professeur des Universités, Université de Toulouse	Président
Mme. Karyn LE HUR Directrice de Recherche, Institut Polytechnique de Paris	Rapporteur & Examinatrice
M. Thierry MARTIN Professeur des Universités, Université de Marseille	Rapporteur & Examinateur
M. Grégoire MISGUICH Directeur de Recherche, Institut de Physique Théorique de Saclay	Examinateur

THESE DE DOCTORAT

NNT : 2023UPASP059

université PARIS-SACLAY

ÉCOLE DOCTORALE
Physique en Île-de-France (PIF)

Titre: États de Hall quantique fractionnaires des systèmes de graphène
Mots clés: effet Hall fractionnaire, graphène, cristal de Wigner

Résumé: Le graphène est un matériel bidimensionel. Outre le degré de liberté du spin, les électrons de basse énergie dans le graphène possèdent un nouveau degré de liberté: la vallée, qui joue le rôle du pseudospin, si bien que les électrons dans graphène sont quatre fois dégénérés. Par conséquent, le graphène est un nouveau système physique pour étudier l'effect Hall quantique multicomposante. Dans cette thèse, nous étudions les états de Hall quantique fractionnaires dans deux systèmes de graphène: le graphène monocouche et le graphène bicouche dans l'empilement du Bernal.

Dans le graphène monocouche, nous étudions l'ordre du spin et de la vallée causé par la brisure de la symmétrie SU(4) due aux anisotropies à courte portée dépendantes de la vallée. Nous avons fait des diagonalisations exactes sur les états de Hall quantique de facteur de remplissage n/3 et comparé les résultats avec ceux d'une méthode variationnelle. Les diagrammes de phase des états à deux composantes (1,1/3), (2/3,2/3) et (1,2/3) ont la même allure que celui du cas de la neutralité des charges. La phase ferromagnétique des états (1,1/3) et (1,2/3), dont les spins sont polarisés, présentent une symétrie SU(2) de vallée, tandis que le Hamiltonien ne possède pas cette symétrie. En particulier, le diagramme de phase de l'état à trois composantes (1,1/3,1/3) n'est pas décrit par la méthode variationnelle: il contient une phase singulet de spin et non-polarisée de vallée, qui n'est pas prédite variationnellement.

Le spectre des niveaux de Landau du graphène bicouche est unique parce que les deux niveaux de Landau N=0 et N=1 sont approximativement dégénérés. Son niveau de Landau central est huit fois dégénéré. On peut contrôler l'état du graphène bicouche en modifiant le champs électrique perpendiculaire à la bicouche. Sous la présence de l'effet de Zeeman et du biais intercouche, les huit sous-niveaux du niveau de Landau central sont séparés. Cela permet d'observer de nouveaux phénomènes lors du croisement entre les niveaux d'énergies d'une seule particule.

Dans la seconde partie de cette thèse, nous étudions la compétition entre l'état de Hall quantique de fraction $\nu = 1/3$ et le solide d'électron au croisement de niveaux avec index orbital N=0 et N=1, en supposant que les électrons aient le même spin et la même vallée. Dans ce cas, la coïncidence entre les deux niveaux de Landau rappelle le cas d'un mélange extrême entre les niveaux de Landau et entraîne la formation du cristal de Wigner. La transition de phase entre l'état de Laughlin et le cristal d'électron est continue ou faiblement de premier ordre. La possibilité de créer un cristal de Wigner en variant le biais intercouche dans le graphène bicouche promet une plateforme simple et pratique pour étudier cet état de la matière.

université PARIS-SACLAY | ÉCOLE DOCTORALE Physique en Île-de-France (PIF)

Title: Fractional quantum Hall states in graphene systems
Keywords: fractional quantum Hall effect, graphene, Wigner crystal

Abstract: Graphene is a member of the family of two-dimensional materials. Apart from the familiar spin degree of freedom, low-energy electrons in graphene have an additional degree of freedom: the valley, which plays the role of a pseudospin, implying that electrons in graphene have a fourfold degeneracy. Therefore, graphene is a new platform for studying the multicomponent quantum Hall effect. In this thesis, we study the fractional quantum Hall states in two graphene systems: the monolayer graphene and the Bernal-stacked bilayer graphene.

In monolayer graphene, we study the ordering of spin and valley caused by the breaking of the SU(4) symmetry due to short-range valley-dependent anisotropies. We performed exact diagonalization studies on quantum Hall states of filling factors n/3 (n=1,2,4,5) and compared the results with those of a variational method. The phase diagrams of the two-component states (1, 1/3), (2/3, 2/3), and (1, 2/3) have the same shape as the one of the charge neutrality case. The spin-polarized ferromagnetic phase of the states (1,1/3) and (1,2/3) exhibits an emergent SU(2) valley symmetry, while the Hamiltonian does not have this symmetry. Significantly, the phase diagram of the three-component state (1,1/3,1/3) cannot be captured by the variational method: it has a spin-singlet and valley unpolarized phase that is not predicted variationally.

The Landau level spectrum of Bernal-stacked bilayer graphene is unique because the two Landau levels N=0 and N=1 are nearly degenerate. It gives rise to the orbital degree of freedom, leading to an almost eightfold degenerate central Landau level. Interestingly, one can control the state of Bernal bilayer graphene by tuning the electric field across its two layers. Under the presence of the interlayer bias and the Zeeman energy, the eight degenerate sublevels of the central Landau level are split, promising the observation of interesting physics at the crossing between the single-particle energy levels.

In the second part of this thesis, we study the competition between the fractional quantum Hall liquid of filling fraction 1/3 and the electron solid at the crossing between the two orbitals, supposing that the spin and valley degrees of freedom are frozen. In this situation, the coincidence between the two Landau levels is reminiscent of the case of extreme Landau level mixing, giving rise to the formation of the Wigner crystal. The phase transition between the Laughlin state and the electron crystal is continuous or weakly first-order. The possibility of electrically-induced Wigner crystal in Bernal bilayer graphene promises a simple and practical platform to study this phase of matter.

Acknowledgments

First of all, I want to express my deepest acknowledgments to my doctoral advisor, Dr. Thierry Jolicoeur, for his kind guidance, patience, and explanations during these three years at the Institut de Physique Théorique IPhT. At the beginning of the Ph.D., I knew almost nothing about the quantum Hall effect. Under his supervision, my knowledge of the quantum Hall effect and computational physics has improved. I am lucky to have the opportunity to work with him. His code is a standard of the exact diagonalization method for quantum Hall systems and high-performance computing. He also has a broad vision of condensed matter physics and exceptional ideas for interpreting numerical results.

Second, I am grateful to Lien T. Le for the lecture notes and exercises she shared when she studied at the Abdus Salam International Center for Theoretical Physics (ICTP) and the University of Chicago. I could not have enough knowledge and skills to solve physics problems without studying with her. She went with me during the first and the second years of my Ph.D., sharing the same passion and encouraging me.

I want to thank my tutor Dr. Grégoire Misguich for his kind support and advice during my Ph.D and Prof. Philippe Lecheminant for accepting to be a member of my Comité de suivi de thèse. I am also grateful for the kind support from the Administration and IT teams of IPhT, especially Laure Sauboy, Laurent Sengmanivanh, Emmanuelle de Laborderie, Camille Flouret, and Maxime Leroy. I would also thank Prof. Marietta Manolessou for relaxing discussions during coffee time.

I want to thank Dr. Huy-Viet Nguyen for his technical advice to perform parallel computing, Dr. Dung Xuan Nguyen and Prof. Dam Thank Son, Prof. Jainendra Jain and Dr. Ajit Balram, Dr. Benjamin Wieder and Dr. Hai Son Nguyen for valuable discussions. Thanks to Dr. Preden Roulleau and the other members of the Graphene Meeting for the exciting discussions.

I want to thank Prof. Christophe Mora and Dr. Leonardo Mazza for their interesting Topology in Condensed Matter course. I want to thank Dr. François Gélis for his excellent courses in Quantum Field Theory and Ms. Picot for her kind support during the registration. I also thank Prof. Christophe Kopper, Dr. Cédric Lorcé, and Prof. Adel Bilal for giving courses when Dr. Gélis was unavailable. I want to thank Prof. Leticia Cugliandolo, Dr. Marco Tarzia, Prof. Silke Bierman, and Dr. Paul Indranil for their Statistical Physics and Condensed Matter Theory courses. I also thank Prof. Antoine Georges for his exciting lectures on the Hubbard model and Dr. Karyn Le Hur for her enlightening lectures on Geometry and Topology.

I want to thank Prof. Sylvain Capponi, Dr. Karyn Le Hur, Prof. Thierry Martin, and Dr. Grégoire Misguich for accepting to become members of my jury. The enlightening discussions with them during and after the defense gave me insights into quantum geometry, bilayer graphene, edge states, and excitations.

I also thank my colleagues at IPhT: Linnéa, Daniela, Louis, Émile, Pablo, Rémy, Adel, Peng, Shaun, Nejc, Soumangsu, Bin, Benjamin, Marc, Pavel, Sigtryggur, Dimitris, Nathalie, Souffiane, Corentin, Pierre, Tomas, Du, Persia and many others; and my Vietnamese friends: Khánh Linh, Tú, Thái, Tùng, Tuấn Anh for enjoying the lunchtime together. There are too many names to list you all without taking the risk of forgetting someone, so I mention here the names of the ones with whom I had lunch the most frequently, supposing that I am also sending my gratitude to the people I do not mention here.

Last but not least, I would like to thank my parents, who are in Vietnam but always take care of me. When I graduated from high school, they worried that becoming a scientist would be difficult and opposed my choice to study fundamental science. Nevertheless, they always provide me with solid support, care, and love to pursue this challenging career as a researcher.

Abbreviations

AF	Antiferromagnetic
AR	Aspect ratio
BLG	Bernal-stacked bilayer graphene
CAF	Canted antiferromagnetic
CDW	Charge density wave
CF	Composite fermion
CNP	Charge-neutrality point
DOS	Density of States
F	Ferromagnetic
FQHE	Fractional quantum Hall effect
hBN	Hexagonal boron nitride
IQHE	Integer quantum Hall effect
KD	Kékulé Distortion
LL	Landau level
LLL	Lowest Landau level
MLWF	Maximally Localized Wannier Function
QHE	Quantum Hall effect
STM	Scanning tunneling microscopy
STS	Scanning tunneling spectroscopy
ZLL	Zero-energy Landau level

Contents

Chapter1 - Introduction

The quantum Hall effect is one of the most striking discoveries of physics in the 20^{th} century. In 1980, nearly one century after the discovery of the classical Hall effect, von Klitzing, Dorda, and Pepper discovered its integral version [1]. Tsui, Stormer, and Gossard observed the fractional quantum Hall effect two years later [2]. Since then, the quantum Hall effect has opened perspectives to study the topological phases of matter and exotic states of matter. The study of the integer quantum Hall effect is the precursor to the expanding field of topological insulators [3–6]. The research on the fractional quantum Hall effect gives rise to important concepts of composite fermion [7, 8] and topological order [9, 10]. The fractionally quantized Hall effect is also an ideal platform for studying electron interaction. Studying excited states of the fractional quantum Hall liquid leads to the concepts of fractional charge [11–13]. The fractional quantum Hall effect also plays a key role in studying fractional statistics and anyon [14–17]. After its discovery in conventional semiconductors, experiments observed the quantum Hall effect in other materials like graphene [18–21], bilayer graphene [22–25], and transition metal dichalcogenides [26]. Forty years after its discovery, the research on the quantum Hall effect is still an active subfield of condensed matter physics.

Graphene [27, 28] remained a hypothetical material during the 20^{th} century until Geim and Novoselov successfully isolated it in 2005 [29]. The discovery of graphene is a breakthrough and triggers the research on two-dimensional materials. In physics, the study of graphene opens many insights, like Dirac fermion and electron quantum optics. The quantum Hall effect in graphene is remarkable due to its relativistic Landau levels [18, 30]. Moreover, graphene is a richer platform to study the multicomponent quantum Hall effect because electrons in this material have the valley degree of freedom apart from their intrinsic spin degree of freedom. The presence of one more degree of freedom makes each Landau level in graphene fourfold degenerate, so the multicomponent quantum Hall effect in graphene is described by the SU(4) symmetry.

In graphene, the interaction between electrons in different valleys induces anisotropies, which break the SU(4) symmetry of the Coulomb interaction. As a consequence, the case of charge neutrality has a rich phase diagram, including ferromagnetic (F), canted antiferromagnetic (CAF), Kékulé distortion (KD), charge-density wave (CDW) [31], and especially an SO(5) symmetry that connects the CAF and the KD phases [32]. During the last decade, the problem of anisotropies-induced symmetry-breaking phases in graphene has made significant progress in theory and experiments. In 2014, Sodemann and MacDonald started studying the problem of valley anisotropies in graphene under the fractional quantum Hall effect [33]. Nevertheless, there remain open questions about the phase diagram of graphene in both the integer and fractional quantum Hall regimes, and experimental works have not been able to confirm the theoretical results completely.

Bernal-stacked bilayer graphene consists of two monolayers stacked together with a dimer site bonding perpendicular to the graphene plane. Similarly to its monolayer partner, bilayer graphene also provides exciting physics. For example, researchers have observed exciton condensate in double bilayer graphene [34]. Especially one can easily control the state of bilayer graphene by varying the electric field perpendicular to the sample. Interestingly, bilayer graphene has an exceptional eightfold quasi-degenerate

zero-energy Landau level due to the degeneracy of the Landau levels N=0 and N=1. That means the zero-energy Landau level in bilayer graphene has one more degree of freedom in companion with the well-known spin and valley degrees of freedom. This is the so-called orbital degree of freedom. By tuning the layer polarization electric field, the eight levels with different spin, valley, and orbital orders cross each other. New exotic phases of matter are predicted at the crossing between the levels, such as the helical phase [35] and a transition between the Moore-Read state and the composite fermion liquid [36].

In this thesis, we study the multicomponent quantum Hall effect in monolayer and bilayer graphene. First, we investigate the broken-symmetry ground states of monolayer graphene for quantum Hall states having filling factors $n/3$ $(n = 1, 2, 4, 5)$. Second, we study the competition between the Laughlin state and the electron crystal (Wigner crystal) at the crossing of the two orbitals in the zero-energy Landau level of bilayer graphene. For this purpose, we will employ the exact diagonalization numerical method and the analytical variational method.

The structure of this Ph.D. thesis is as follows:

The present **Chapter 1** Introduction gives an overview of the motivations and the objectives of this work.

Chapter 2 provides a review of the quantum Hall effect. The chapter starts with a brief presentation of the classical Hall effect. Then, I will show the main ideas of the integer quantum Hall effect. Next, I will present the fractional quantum Hall effect. The chapter is restricted to the quantum Hall effect in semiconductors.

The **chapters 3, 4, and 5** contain the results of the first project of my Ph.D.: *the ordering of spin and valley in monolayer graphene under the quantum Hall effects with filling factors* $n/3$ $(n = 1, 2, 4, 5)$.

Chapter 3 starts with a review of monolayer graphene, its lattice and band structures, its particular relativistic Landau level quantization, the concept of quantum Hall ferromagnetism, and a summary of the experimental situation. Then, we will discuss the Hamiltonian of a two-dimensional electron system under a magnetic field. This Hamiltonian contains the following contributions: the Coulomb interaction, the Zeeman energy, the substrate-induced sublattice-splitting energy, and the short-range valley-dependent interaction. We will focus on the short-range valley-dependent energy, which breaks the SU(4) symmetry of the Coulomb interaction and gives a variety of symmetry-breaking phases. The phases of monolayer graphene under the *integer* quantum Hall effect of filling factor $\nu = 0$ will be described in detail. Although this chapter does not contain new results, it provides the concepts indispensable to understanding the discussions in chapters 4 and 5.

In **chapter 4** we develop a variational method to establish the phase diagram of monolayer graphene under the *fractional* quantum Hall regime. We propose the trial wavefunctions, which are SU(4) eigenstates of the Coulomb interaction. By assuming that the valley-dependent interaction is not strong enough to break the electron correlation of those wavefunctions, we will search for the spin and valley ordering that minimizes the energy of each trial wavefunction. These spin and valley orders define the characteristics of the corresponding phases. The chapter ends with the phase diagrams calculated by using the variational method for the two component-state of flavor composition $(1, \nu)(0 < \nu < 1)$ and the three component-state $(1, \nu, \nu)$ $(0 < \nu < 1)$.

In **chapter 5** we discuss the spin and valley ordering of all quantum Hall states of filling factors $n/3(n = 1, 2, 4, 5)$. For the filling factors $\tilde{\nu} = 4/3$ and $\tilde{\nu} = 5/3$, we verify the prediction of the variational method by comparing its results with the ones of exact diagonalizations. Exact diagonalization studies find evidence of a symmetry-breaking order that is not captured by the variational method. Then, we discuss the spin transition between states having different numbers of components. We end the chapter by summarizing the project.

The **chapters 6, 7 and 8** cover the second project of my Ph.D.: *the competition between the Laughlin state and the Wigner crystal in Bernal-stacked bilayer graphene*.

Chapter 6 gives an introduction to Bernal-stacked bilayer graphene. We begin with its lattice and electronic structures and derive its unique eightfold degenerate zero-energy Landau level. We present the concept of the *orbital degree of freedom* in detail, showing the single-electron wavefunctions and the single-electron energy diagram. That leads to the definition of the weight γ and the orbital splitting energy Δ_{10}, which plays the role of the pseudo-Zeeman energy for the orbital degree of freedom. These two parameters play an important role in our model, serving as parameters of the phase diagram of bilayer graphene.

Chapter 7 briefly reviews the exotic phase of the Wigner crystal and the competition between the Wigner crystal and the fractional quantum Hall liquid in conventional semiconductors. The chapter points out the key role of Landau level mixing to the formation of this phase of matter.

Chapter 8 presents the main result of this project: the phase diagram of bilayer graphene in the vicinity of the crossing between the orbitals N=0 and N=1 for electrons having the same valley and same spin. The coincidence of the two Landau levels is *reminiscent of* an extreme Landau level mixing, which favors the localization of electrons and leads to the formation of the Wigner crystal. Here the Wigner crystal competes with the Laughlin state of filling factor $\nu = 1/3$.

Chapter 9 Conclusion summarizes the results of this thesis and gives the conclusion, perspectives, and future directions.

Chapter2 - The physics of the Quantum Hall effect

2.1 . The classical Hall effect

In 1879, Edwin H. Hall placed a gold leaf under a magnetic field and turned on an electromotive force to make an electric current traversing the gold leaf. He observed a transverse electromotive force perpendicular to the initial one [37]. Nowadays, the appearance of a transverse electromotive force perpendicular to the electric current under a magnetic field is called the (classical) ***Hall effect***. Fig.2.1 illustrates the Hall setup. A voltage V is applied between the two ends of the sample, leading to a current I. Then, a magnetic field $\mathbf{B}$ perpendicular to the sample is turned on. The voltage V_H is the so-called *Hall voltage*.

We can understand the physics of the classical Hall effect by simply using classical electromagnetism. Here we follow the line of reasoning in Ref.[38]. Electrons moving under a magnetic field are subjected to the Lorentz force. According to Newton's second law, we write their equation of motion as follows:

$$m\frac{d\mathbf{v}}{dt} = -\frac{e}{c}\mathbf{v}\times\mathbf{B} \tag{2.1}$$

Here, m is the electron mass. For an electron moving in two dimensions, $\mathbf{v} = (v_x, v_y, 0)$. The magnetic field perpendicular to the two-dimensional electron gas has the formula $\mathbf{B} = (0, 0, B)$. The equation (2.1) becomes:

$$\begin{aligned}\frac{dv_x}{dt} &= -\frac{eB}{mc}v_y \\ \frac{dv_y}{dt} &= \frac{eB}{mc}v_x\end{aligned} \tag{2.2}$$

By taking a further derivative, we see that v_x and v_y are solutions for the second-order differential equations:

$$\begin{aligned}\frac{d^2v_x}{dt^2} + \omega_c^2 v_x &= 0 \\ \frac{d^2v_y}{dt^2} + \omega_c^2 v_y &= 0\end{aligned} \tag{2.3}$$

The quantity $\omega_c = eB/mc$ is called the ***cyclotron frequency***. By solving this system of differential equations, we see that electrons move in circular orbits with frequency ω_c. In the Hall experiment, there are two other contributions to the total force acting on each electron: the electric force $-e\mathbf{E}$ and the friction force $-m\mathbf{v}/\tau$ due to impurities, which causes the resistance. Here, τ is the *scattering time*. According to Drude's model, the equation of motion of each electron reads:

$$m\frac{d\mathbf{v}}{dt} = -e\mathbf{E} - \frac{e}{c}\mathbf{v}\times\mathbf{B} - \frac{m}{\tau}\mathbf{v} \tag{2.4}$$

In the steady state, $d\mathbf{v}/dt = 0$ and this equation is written in the matrix form as:

$$\begin{pmatrix} 1 & \omega_c\tau \\ -\omega_c\tau & 1 \end{pmatrix}\begin{pmatrix} v_x \\ v_y \end{pmatrix} = -\frac{e\tau}{m}\begin{pmatrix} E_x \\ E_y \end{pmatrix} \tag{2.5}$$

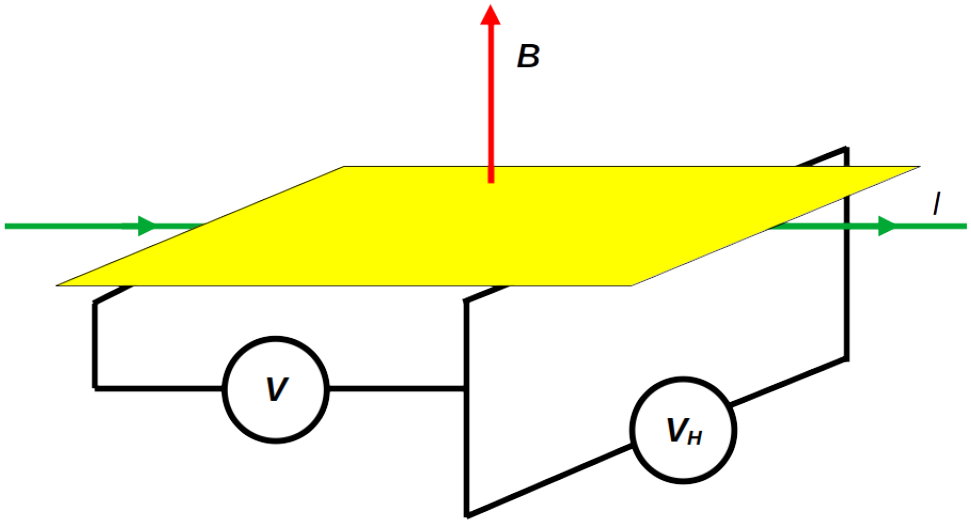

Figure 2.1: Schematic of the Hall experiment.

The formula of the current density is $\mathbf{j} = -ne\mathbf{v}$ with n the (two-dimensional) electron density. The Ohm's law reads:

$$\mathbf{j} = \sigma \mathbf{E} \tag{2.6}$$

We define $\sigma_{DC} = ne^2\tau/m$ as the conductivity without magnetic field. The tensor σ is the ***conductivity tensor*** and has the formula:

$$\sigma = \frac{\sigma_{DC}}{1+\omega_c^2\tau^2}\begin{pmatrix} 1 & \omega_c\tau \\ -\omega_c\tau & 1 \end{pmatrix} \tag{2.7}$$

The conductivity tensor has non-zero off-diagonal entries σ_{xy}. This off-diagonal conductivity is responsible for the transverse electromotive force in the Hall experiment. The resistivity tensor, which is the inverse of the conductivity tensor, has the formula:

$$\rho = \frac{1}{\sigma_{DC}}\begin{pmatrix} 1 & \omega_c\tau \\ -\omega_c & 1 \end{pmatrix} \tag{2.8}$$

The value of the transverse resistivity is:

$$\rho_{xy} = \frac{\omega_c\tau}{\sigma_{DC}} = \frac{B}{ne} \tag{2.9}$$

The transverse resistivity is a linear function of the applied magnetic field. By contrast, the longitudinal resistivity is constant:

$$\rho_{xx} = \frac{1}{\sigma_{DC}} = \frac{m}{ne^2\tau} \tag{2.10}$$

We assume that the current flows in the x direction $\mathbf{j} = j_x\hat{\mathbf{x}}$ [1]. We set L_x and L_y as the sample size in the x and y directions, respectively. In the experiments, one measures

[1] In the following subsections, we consider an electric current flowing in the y direction instead.

the transverse resistance instead of the resistivity. Let R_H be the transverse resistance, or *Hall resistance*. The value of the Hall resistance equals to:

$$R_H = \frac{V_H}{I} = \frac{E_y L_y}{j_x L_y} = \frac{E_y}{j_x} = \rho_{xy} \tag{2.11}$$

To summarize, in a conductor under magnetic field, the charge carriers are deflected by the Lorentz force. They accumulate on the edges of the sample, resulting in the transverse voltage V_H. The classical Hall effect has many applications [39]. On the one hand, the Hall effect is the principle of magnetic sensors. Hall effect sensors are usually made of semiconductors. They convert the magnetic field into electrical signals. Knowing the material properties and the device geometry, the Hall voltage V_H gives information about the direction and strength of the magnetic field $\mathbf{B}$. On the other hand, the Hall effect allows us to characterize the materials. One can fabricate a Hall device made of the material of interest with a specific geometry. Then one can control the applied magnetic field and longitudinal voltage and measure the Hall voltage. The latter gives information about the material: the sign (positive/negative) and the density of the charge carriers. The applications of Hall effect devices have become significant since the beginning of the semiconductor technology.

2.2 . The integer quantum Hall effect

2.2.1 . The discovery of the integer quantum Hall effect

In 1980, von Klitzing, Dorda, and Pepper published a paper on their discovery of the integer quantum Hall effect [1]. They placed a degenerate electron gas in the inversion layer of a MOSFET under a magnetic field of 18T at a temperature of 1.5K; the source-drain current is $1\,\mu\mathrm{A}$. By varying the gate voltage V_g, they observed the plateaus in the graph of the Hall voltage V_H. The values of the Hall resistance at the plateaus are $R_H \approx 25\,812.807\,\Omega/n = h/(e^2 n)(2 \leq n \leq 8)$. It corresponds to the quantization of the Hall conductivity:

$$\sigma_{xy} = n\frac{e^2}{h}(n \in \mathbb{N}) \tag{2.12}$$

The corresponding values of the longitudinal resistivity ρ_{xx} and the longitudinal conductivity σ_{xx} get minima. The value of V_H is independent of the sample geometry and the direction of the magnetic field if $\sigma_{xx} = 0$. Their results are shown in Fig.2.2.

Surprisingly, at a high magnetic field, the Hall resistivity ρ_{xy} is not a linear function of the magnetic field B as shown in (2.9), but is quantized. Nowadays, the value $R_K = h/e^2 = 25\,812.807\,\Omega$ is called the *von Klitzing constant*. In 1985, von Klitzing was awarded the Nobel Prize in Physics.

After the discovery of the integer quantum Hall effect, physicists rapidly understood the physics behind this striking phenomenon. In their pioneering paper [1], von Klitzing et al. explained the phenomenon using the quantization of the electron kinetic energy into discrete Landau levels. The presence of disorder explains the existence of the plateaus. Laughlin explained the quantized Hall effect using his pumping argument and his idea of spectral flow [40]. The Landauer approach [41] provides a complete explanation of the Hall conductance quantization and the edge states in the picture of electron transport without backscattering [42–45]. Although the Laughlin's argument is more abstract

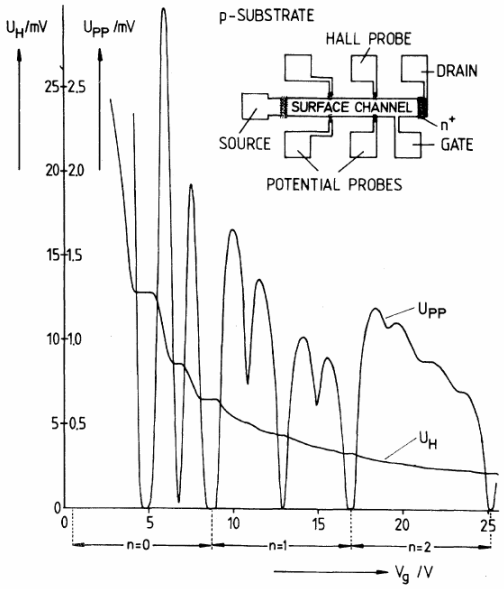

Figure 2.2: The recordings of the Hall voltage and longitudinal voltage by von Klitzing et al. [1]. In their notations, U_H is the Hall voltage, while U_{PP} is the longitudinal voltage, and V_g is the gate voltage. The inset is the schematic of the Hall bar device. The figure is taken from Ref.[1]. Reprinted figure with permission from K. v. Klitzing, G. Dorda, and M. Pepper, Phys. Rev. Lett., 45, 494 (1980). Copyright (2023) by the American Physical Society.

while the Landauer-Büttiker approach is more concrete and closer to experiments, they are closely related. A deeper explanation revealing the topological origin of the Hall quantization was developed by Thouless, Kohmoto, Nightingale, and den Nijs (TKNN) using the Kubo formalism [46]. The TKNN argument identifies the integer n in (2.12) as the *Chern number*. For this reason, two-dimensional electron systems under the integer quantum Hall effect is the first known topological insulator.

The following subsections review the basic knowledge of the integer quantum Hall effect. First, we solve the problem of two-dimensional electrons under magnetic field. Next, we prove the quantization of the Hall conductance. Then, we discuss the role of disorder in the formation of the plateaus. Finally, we will show the general points about edge states.

2.2.2 . Two-dimensional electrons under magnetic field: Landau level quantization

One explains the physics of the integer quantum Hall effect using the single-electron picture [47]. We consider two-dimensional electrons moving in the $x-y$ plane, under the magnetic field $\mathbf{B} = B\hat{\mathbf{z}}$. In this subsection, we use the Landau gauge $\mathbf{A} = (0, Bx, 0)$. The Hamiltonian of one electron under this magnetic field is given by:

$$\begin{aligned} H =& \frac{1}{2m}\Pi^2 = \frac{1}{2m}\left(-i\hbar\nabla + \frac{e}{c}\mathbf{A}(\mathbf{r})\right)^2 \\ =& \frac{1}{2m}\left[-\hbar^2\frac{\partial^2}{\partial x^2} + \left(-i\hbar\frac{\partial}{\partial y} + \frac{eB}{c}x\right)^2\right] \end{aligned} \tag{2.13}$$

We solve the corresponding Schrödinger equation by separating the variables. An ansatz for the single-particle eigenfunction is:

$$\phi(x,y) = e^{-ik_y y}\chi(x) \tag{2.14}$$

The function $\chi(x)$ satisfies the following ordinary differential equation:

$$-\frac{\hbar^2}{2m}\frac{d^2\chi(x)}{dx^2} + \frac{1}{2}m\omega_c^2\left(x - \frac{\hbar k_y}{m\omega_c}\right)^2\chi(x) = E\chi(x) \tag{2.15}$$

The cyclotron frequency $\omega_c = eB/mc$ is the same as the one we defined in section 2.1. We define the ***magnetic length*** $l = (\hbar c/eB)^{1/2}$. By defining $X = \hbar k_y/m\omega_c = k_y l^2$, the Schrödinger equation becomes the equation for one-dimensional harmonic oscillator along the x-direction and centered at X:

$$\left[-\frac{\hbar^2}{2m}\frac{d^2}{dx^2} + \frac{1}{2}m\omega_c^2(x-X)^2\right]\chi(x) = E\chi(x) \tag{2.16}$$

Therefore, the energy of one particle is quantized into discrete levels:

$$E_N = \hbar\omega_c\left(N + \frac{1}{2}\right)(N \in \mathbb{N}) \tag{2.17}$$

Those levels are called ***Landau levels*** [47]. They are labeled by the quantum number N. The one-particle wavefunction is given by:

$$\phi_{N,k_y}(x,y) = e^{-ik_y y}e^{-\frac{(x-k_y l^2)^2}{2l^2}}H_N\left(\frac{x-k_y l^2}{l}\right) \tag{2.18}$$

Here, H_N is the N$^{\text{th}}$ Hermite polynomial. The periodic boundary condition on the y-direction leads to the quantization of the momentum k_y into $k_y = 2\pi n_y/L_y$ $(n_y \in \mathbb{Z})$. The condition $0 \leq X < L_x$ implies that:

$$0 \leq n_y < \frac{L_x L_y}{2\pi l^2} = \frac{L_x L_y B}{\phi_0} \tag{2.19}$$

We define the ***magnetic flux quantum*** $\phi_0 = hc/e$. The condition (2.19) shows that the number of allowed values of n_y (corresponding k_y) equals to the number N_ϕ of magnetic flux quanta passing through the sample. Indeed, $N_\phi = L_x L_y B/\phi_0$.

To sum up, in this subsection, we have shown that the kinetic energy of two-dimensional electrons under magnetic field is quantized into Landau levels. The degeneracy of each Landau level equals to the number of magnetic flux quanta passing through the sample. In the next subsection, we prove the Hall conductance quantization.

2.2.3 . Quantization of the Hall conductance

In real samples, there is an external electric field due to the Hall voltage V_H. Real samples have edges at which there exist confinement potentials. We continue considering a system which is translationally invariant along the y-direction and confined in the x-direction. According to the treatment in subsection 2.2.2, electrons propagate along the y-direction and are subjected to the Hall voltage across the x-direction. Therefore,

we sum up the contributions from these potentials into the potential energy $V(x)$, which is y-independent. We modify the Hamiltonian (2.13) by adding a potential energy $V(x)$ into it:

$$H = \frac{1}{2m}\left(\mathbf{p} + \frac{e}{c}\mathbf{A}\right)^2 + V(x) \tag{2.20}$$

The Hamiltonian (2.20) commutes with the momentum $\hat{p}_y$, so k_y is still a good quantum number to label the eigenstates. The eigenstate with quantum number k_y is localized at position $x = y(k_y)$. We consider a full Landau level, which contains the electrons such that $k_- < k_y < k_+$. The total electric current contributed by electrons in one Landau level equals:

$$\begin{aligned} I_y =& -e\int_{k_-}^{k_+}\frac{dk_y}{2\pi}\langle v_y\rangle = -e\int_{p_-}^{p_+}\frac{dp_y}{2\pi\hbar}\frac{1}{m}\langle p_y + \frac{e}{c}A_y\rangle \\ =& -e\int_{p_-}^{p_+}\frac{dp_y}{2\pi\hbar}\left\langle\frac{\partial H}{\partial p_y}\right\rangle = -e\int_{p_-}^{p_+}\frac{dp_y}{2\pi\hbar}\frac{dE}{dp_y} = -\frac{e}{h}\int_{-}^{+} dE \end{aligned} \tag{2.21}$$

The energy E contains the kinetic and the potential energy. The integral is equal to:

$$I_y = -\frac{e}{h}(\mu_+ - \mu_-) \tag{2.22}$$

Here $\mu_\pm$ are the chemical potentials at the Fermi level at the edges. Their difference is exactly proportional to the Hall voltage:

$$\mu_+ - \mu_- = -eV_H \tag{2.23}$$

Therefore, we get:

$$I_y = \frac{e^2}{h}V_H \tag{2.24}$$

The Hall conductance of one fully occupied Landau level is:

$$\sigma_{xy} = \frac{I_y}{V_H} = \frac{e^2}{h} \tag{2.25}$$

For a system with n fully occupied Landau levels ($n \in \mathbb{N}$), the Hall conductance equals:

$$\sigma_{xy} = n\frac{e^2}{h} \tag{2.26}$$

The Hall resistance is given by:

$$\rho_{xy} = \frac{h}{ne^2} \tag{2.27}$$

We define the ***filling factor*** ν as the number of Landau levels occupied by electrons. For the integer quantum Hall effect, $\nu = n$ integer. In the fractional quantum Hall effect, ν takes rational values (see section 2.3). In general, we write the Hall conductance and the Hall resistance as follows:

$$\begin{aligned} \sigma_{xy} =& \nu\frac{e^2}{h} \\ \rho_{xy} =& \frac{h}{\nu e^2} \end{aligned} \tag{2.28}$$

To summarize, we have proved the quantization of the Hall conductance. One obtain the same result by using the Laughlin's argument or the Kubo formalism [40, 46]. To explain the existence of the plateaus, we need to consider the effect of disorder.

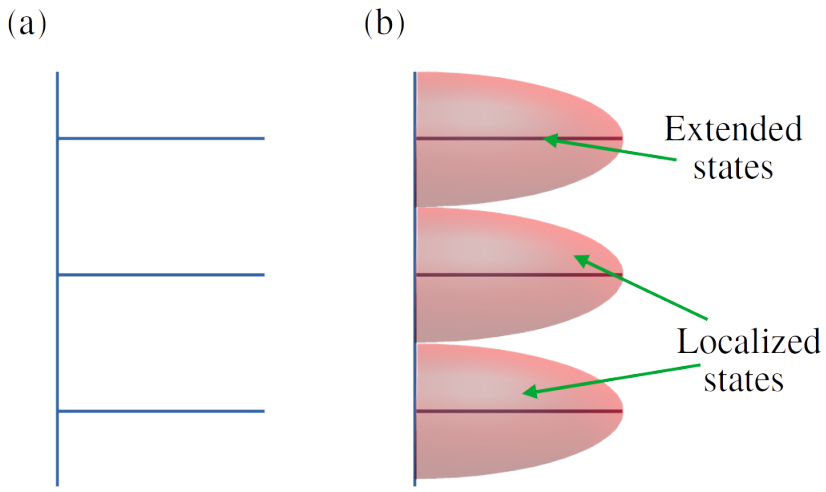

Figure 2.3: (a) Equally spaced Landau levels in disorder-free samples. (b) Broadened Landau levels are centered at the extended states, while the localized states have energy lying in the gap between Landau levels.

2.2.4 . Effect of disorder

In the previous subsections, we explained the quantization of the Hall conductance by using the picture of Landau levels. Landau level quantization explains why the plateaus appear at the observed values of the Hall conductance/resistance. However, this picture is insufficient to explain why there are plateaus there.

Real samples are not perfectly clean but have impurities. Those impurities induce disorder in the system, causing the potential landscape $V(\mathbf{r})$, with potential "hills" or "valleys". In the semiclassical picture, one can imagine that the electrons follow closed trajectories around each hill or valley. Those states are localized and do not contribute to the electric current. However, states corresponding to $V = 0$ are not trapped around the potential hills or valleys. They have energy equal to the Landau level energies and contribute to the transport.

Consequently, the Landau levels broaden into bands. Those Landau bands are centered at the quantized values of the Landau levels. The states at the center of the Landau bands are extended states. The localized states have energy lying inside the energy gap. Such a spectrum is illustrated by Fig.2.3. The energy gap disappears. However, because the localized states do not contribute to the transport, we call the gap the "mobility gap".

Now we fill the states up to the Fermi energy. At the beginning, electrons fill the localized states trapped at the valleys. The picture resembles when one fills the valley with water to form lakes. When one electron fills the energy level of the extended state, this state is delocalized and contributes to the transport. In the "water pouring" picture, this situation is like an ocean surrounding the islands (hills). This is the so-called percolation transition. After that, the incoming electrons will fill the hills.

In a perfect system without disorder, additional electrons do contribute to the electric current and plateaus do not appear. In systems containing weak disorder, electrons

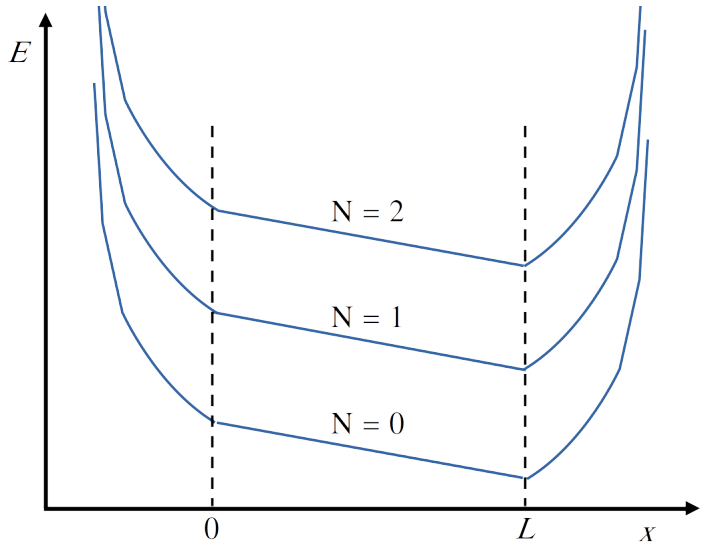

Figure 2.4: Spectrum of the Landau levels along the transverse direction. The Landau levels are bent at the edge. Due to the presence of the Hall voltage V_H, the Landau levels are tilted.

occupying localized states do not contribute to the transport. As a result, the Hall conductance remains unchanged with increasing filling factor. This explains the formation of the plateaus. We note that the quantum Hall effect requires weak disorder. Strong disorder can mix the states across the gap, or even modify the eigenstates. In this case, one no longer observes the quantum Hall effect.

2.2.5 . Edge states

Due to the confinement potential at the edges, the Landau levels are not homogenously flat across the whole sample. They are bent at the edges (Fig.2.4). Consequently, the edge states have non-zero group velocity $v_g = \frac{1}{\hbar}\frac{dE}{dk_y}$. Those electrons propagate along the edges from one end to the other end of the sample and travel in opposite directions along opposite edges. The edges do not have an energy gap like the bulk and behave like a metal whereas the bulk is an insulator.

In this section, we discussed the physics of the integer quantum Hall effect. We showed that the energy of the two-dimensional electrons under magnetic field is quantized into discrete Landau levels. In systems with fully occupied Landau levels, the Hall conductance is quantized. Weak disorders lead to the formation of the localized states, and broaden the Landau levels, resulting in plateaus at integer filling factors. Although the bulk of the integer quantum Hall system is insulating, its edges conduct electricity like a metal. Electrons in opposite edges move along opposite directions. The next section is a review of the fractional quantum Hall effect.

2.3 . The fractional quantum Hall effect

2.3.1 . The discovery of the fractional quantum Hall effect

After discovering the integer quantum Hall effect, physicists searched for the electron solid, *i.e.*, the Wigner crystal [48]. They believed the electron liquid would condense into a crystalline phase at a high magnetic field. They increased the magnetic field to place all the electrons into the lowest Landau level. Their objective was to create a system where the electron kinetic energy is quenched, which favors electron crystallization. Surprisingly, they observed a plateau, which corresponds to a quantum Hall effect with filling factor $\nu = 1/3$. The fractional quantum Hall effect was discovered by Tsui, Stormer, and Gossard in 1982, two years after the discovery of its integer version [2].

After the discovery by Tsui, Stormer, and Gossard, physicists observed various fractional quantum Hall effects with odd denominators [49–55]. Fractional quantum Hall states with even denominators have not been observed in the lowest Landau level. However, the fraction 5/2 was observed in the second Landau level [53, 56]. The fractional quantum Hall effect needs weak disorder, and requires very clean samples with high mobility.

Immediately after the discovery of the fractional quantum Hall effect, physicists tried to explain the mystery of this phenomenon. In 1983, Laughlin proposed a wavefunction for the filling fraction $1/m$ (m odd) [11]. This wavefunction is nowadays named the Laughlin wavefunction. He also predicted that the excitations of the quantum Hall liquid - the quasielectrons and quasiholes - are fractionally charged. Another explanation of the fractional quantum Hall effect is the hierarchy scenario, which can explain all observed odd-denominator fractions [57, 58].

The most successful approach to explain the fractional quantum Hall effect is the composite fermion theory by Jain [7, 8]. In this picture, the fractional quantum Hall effect is approximately equivalent to the integer quantum Hall effect of composite fermions-the bound state of one electron with an even number of magnetic flux quanta. The composite fermion theory also succeeds in explaining why there is no incompressible state for filling fraction 1/2. For the fraction 5/2, many non-abelian wavefunctions were proposed to explain this incompressible state [59, 60].

The following subsections review the basic knowledge of the fractional quantum Hall effect. We begin with the Hamiltonian of interacting electron systems. After that, we move on to the Laughlin wavefunction. Next, we present the key points of the composite fermion theory. Then, we discuss the fractional quantum Hall effect with spin, whose results are used in this thesis to discuss the more general multicomponent quantum Hall effects in monolayer and bilayer graphene. The content of this section is restricted to the fractional quantum Hall effect in semiconductors as a preparation for the analysis of the multicomponent quantum Hall effects in graphene and bilayer graphene.

2.3.2 . Hamiltonian of two-dimensional electron systems under magnetic field

To explore the fractional quantum Hall effect, we need to consider the electron-electron Coulomb interaction. The Hamiltonian of a system containing N_e electrons under a magnetic field $\mathbf{B}$ is:

$$\mathcal{H} = \sum_{i=1}^{N_e} \frac{1}{2m} \left(\mathbf{p}_i + \frac{e}{c} \mathbf{A}(\mathbf{r}_i) \right)^2 + \sum_{i<j} \frac{e^2}{\varepsilon |\mathbf{r}_i - \mathbf{r}_j|} - g\mu_B B \sum_{i=1}^{N_e} \sigma_i \tag{2.29}$$

Here, m is the electron (effective) mass, $\mu_B = e\hbar/2m = 9.27 \times 10^{-24}\mathrm{J/T}$ is the Bohr magneton. ε is the dielectric constant of the material. The g-factor of electron is

dependent on the materials. σ_i is the electron spin, which can be either +1/2 or -1/2.

The first term in (2.29) is the familiar electron kinetic energy, which is quantized into Landau levels as shown in subsection 2.2.2. For fractional quantum Hall effects in the lowest Landau level, this contribution equals a constant for all electrons, and we say the kinetic energy is quenched. The third term is the Zeeman energy, which splits the energy of the spin-up and spin-down electrons. The second term is the electron-electron interaction, which plays a major role in the physics of the fractional quantum Hall effect.

For filling factors $0 < \nu < 1$ and when the spin degree of freedom of electrons is frozen, the kinetic energy is quenched, and the Zeeman energy becomes a constant. In this case, we only have to consider the electron-electron interaction, and the Hamiltonian is reduced to:

$$\mathcal{H} = \mathcal{P}_{LLL} \sum_{i<j} \frac{e^2}{\varepsilon |\mathbf{r}_i - \mathbf{r}_j|} \mathcal{P}_{LLL} \tag{2.30}$$

Here, $\mathcal{P}_{LLL}$ is the lowest Landau level projection operator. For filling factors $\nu > 1$, the completely occupied Landau levels are considered inert, and we only need to take into account electrons in partially occupied Landau levels. In higher Landau levels, the interaction term should be modified to be an effective interaction.

2.3.3 . Laughlin wavefunction

In 1983, Laughlin proposed the following wavefunction to explain the fractional quantum Hall effects with filling factors $\nu = 1/m$ (m odd) [11]:

$$\Psi_{1/m} = \prod_{i<j} (z_i - z_j)^m \exp\left(-\frac{1}{4} \sum_i |z_i|^2 \right) \tag{2.31}$$

Here he adopted the symmetric gauge $\mathbf{A} = \frac{B}{2}(-y, x, 0)$. The two-dimensional coordinate (x, y) of a particle is written in complex form $z = x - iy$. By using this wavefunction, he predicted that the quasihole and quasielectron excitations are fractionally charged, with charge $\pm e/m$. Exact diagonalization calculations agreed with the Laughlin wavefunction for $\nu = 1/3$ and $\nu = 1/5$ [61, 62]. Nowadays, we call the fractional quantum Hall effect states with filling factor $\nu = 1/m$ the *Laughlin states*.

2.3.4 . Composite fermion theory

Jain made a brilliant idea linking the two versions of the quantum Hall effect: he introduced a new type of quasiparticle-the composite fermion [7, 8]. The composite fermion is the bound state between an electron and an even number of magnetic flux quanta. We denote a composite fermion formed by binding $2p$ magnetic flux quanta to one electron as ^{2p}CF. For this reason, composite fermions do not feel the total magnetic field $\mathbf{B}$ with N_ϕ magnetic flux quanta. Instead, they are subjected to an effective magnetic field $\mathbf{B}^*$ and an effective number of magnetic flux quanta N_ϕ^*. They are related by the relations:

$$\begin{aligned} N_\phi &= N_\phi^* + 2pN_e \\ B &= B^* + 2p\rho\phi_0 \end{aligned} \tag{2.32}$$

We remark that N_ϕ^* can be negative and the effective magnetic field $\mathbf{B}^*$ can have opposite direction to the original magnetic field $\mathbf{B}$. The picture of strongly interacting

electrons under strong magnetic field can be approximated as the picture of weakly interacting composite fermions under the effective magnetic field. The fractional quantum Hall effect with N_e electrons and N_ϕ magnetic flux quanta is approximatively equivalent to the integer quantum Hall effect with N_e ^{2p}CF occupying n Landau levels. The filling factor $\nu = N_e/N_\phi$ equals:

$$\nu = \frac{n}{2pn \pm 1} \tag{2.33}$$

provided that $N_e = n|N_\phi^*|$. The sign "plus" is taken for positive effective flux, while the sign "minus" is taken for negative effective flux. To distinguish the composite fermion Landau levels from the electron Landau levels, people often call the former Λ-levels. The many-electron wavefunction $\Psi_{\frac{n}{2pn\pm1}}$ is related to the wavefunction $\Phi_{\pm n}$ of N_e particles occupying n Landau levels as follows:

$$\Psi_{\frac{n}{2pn\pm1}} = \mathcal{P}_{LLL}\Phi_{\pm n}\prod_{j<k}(z_j - z_k)^{2p} \tag{2.34}$$

Usually, $\Phi_{\pm n}$ is a Slater determinant of single-particle wavefunctions. With $n = 1$ and the "plus" sign, the wavefunction $\Psi_{\frac{1}{2p+1}}$ for $\nu = 1/(2p+1)$ is exactly the Laughlin wavefunction (2.31) with $m = 2p+1$. One can derive the Laughlin wavefunction from the composite fermion theory.

For $\nu = N_e/N_\phi = 1/2$, (2.32) implies that $p = 1$ and $N_\phi^* = 0$. The fraction $\nu = 1/2$ corresponds to a system of free ^{2}CFs without effective magnetic field. There is no quantum Hall effect for such a system. This state is called the *composite fermion Fermi sea*. The composite fermion theory successfully explains why there are no plateaus for filling fraction $\nu = 1/2$.

2.3.5 . Quantum Hall effect with spin

In the Hamiltonian (2.29), there is a contribution from the Zeeman energy, which is spin-dependent. Under a large magnetic field, the spin degree of freedom is frozen: the spins of all electrons are polarized in the same direction. Usually, the Zeeman energy is some multiple of tens times weaker than the cyclotron energy and the Coulomb energy. For example, in GaAs, the g-factor is $g \approx -0.4$ [8], the electron effective mass is $m_e \approx 0.063m_0$ (m_0 is the electron bare mass) [63], the dielectric constant is $\varepsilon_{\text{GaAs}} = 12.35\varepsilon_0$ [64]. The ratio between the Coulomb energy and the Zeeman energy is about:

$$\frac{e^2/(\varepsilon l)}{|g|\mu_B B} \approx 305/\sqrt{B[\text{T}]} \tag{2.35}$$

If the magnetic field is $B = 15\,\text{T}$, the Coulomb energy is about 79 times larger than the Zeeman energy. If the Zeeman energy is weak, electrons can reverse their spins to gain more interaction energy and form a spin-unpolarized configuration, which is more stable than the polarized configuration. Let $N_\uparrow$, and $N_\downarrow$ are the numbers of electrons having spin-up or spin-down, respectively; their sum equals the total number of electrons:

$$N_e = N_\uparrow + N_\downarrow \tag{2.36}$$

The total filling factor equals the sum of the filling factors of electrons having each kind of spin:

$$\nu = \nu_\uparrow + \nu_\downarrow \tag{2.37}$$

In the composite fermion picture, we can have a situation where electrons with spin-up occupying $n_\uparrow$ Λ levels and electrons with spin-down occupying $n_\downarrow$ Λ levels. In general, $n_\uparrow$ and $n_\downarrow$ can be different, but they should satisfy:

$$\nu = \frac{n_\uparrow + n_\downarrow}{2p(n_\uparrow + n_\downarrow) \pm 1} \tag{2.38}$$

For a determined value of ν and p, we can have more than one combination $(n_\uparrow, n_\downarrow)$ satisfying this relation. From $N_{\uparrow/\downarrow} = \nu_{\uparrow/\downarrow} N_\phi = n_{\uparrow/\downarrow} |N_\phi^*|$, we get $\nu_{\uparrow/\downarrow} = n_{\uparrow/\downarrow} |N_\phi^*| / N_\phi$. The first equality in (2.32) implies that:

$$\frac{|N_\phi^*|}{N_\phi} = \frac{1}{2p(n_\uparrow + n_\downarrow) \pm 1} \tag{2.39}$$

Therefore, the filling factor of each component equals:

$$\nu_{\uparrow/\downarrow} = \frac{n_{\uparrow/\downarrow}}{2p(n_\uparrow + n_\downarrow) \pm 1} \tag{2.40}$$

We particularly focus on the state of filling factor $\nu = 2/3$. At this filling factor, there is competition between the fully polarized and the singlet states. Both cases can be viewed as ^{2}CF under a negative effective magnetic field. In the former case, all electrons have the same spin. They are bound to magnetic flux quanta and occupy two composite fermion Λ levels. Under a finite Zeeman field, the spin is polarized along the direction of the magnetic field $\mathbf{B}$ to minimize the Zeeman energy. The total spin is $S_{tot}^z = +N_e/2$. In the limit of zero Zeeman field (that means the Zeeman effect is very weak), the total Hamiltonian equals the Coulomb interaction and has the SU(2) symmetry. The ground state is therefore a fully SU(2) degenerate spin multiplet. In the case of the singlet state, all ^{2}CF occupy the lowest Λ level. Half of the composite fermions have spin-up and the other half have spin-down, so that the total spin of the system vanishes $S_{tot}^z = 0$. Numerical calculations showed that in the limit of vanishing Zeeman field, the singlet state is more stable than the fully polarized state. The former is the ground state, while the latter is the excited state [65]. When the Zeeman energy becomes strong enough, the fully polarized state is the ground state, and the singlet state becomes the excited state. Transport measurements observed the transition between spin-unpolarized state and spin-polarized state of filling factors $\nu = 8/5$ and $\nu = 4/3$ (corresponding to filling factors $\nu = 2/5$ and $\nu = 2/3$ of holes) when increasing the total magnetic field B_T while keeping the normal component $B_\perp$ unchanged [66].

The spinful electron system is the simplest example of multicomponent quantum Hall effects. In some materials like graphene, the valley degree of freedom plays the role of pseudospin, and the electrons occupy more than two components. Multicomponent quantum Hall effects in monolayer and bilayer graphene are the subject of this thesis. In the next chapter, we start the discussion of the quantum Hall effect in monolayer graphene, and the spin and valley ordering in this material at charge-neutrality $\nu = 0$.

Chapter3 - Spin and valley ordering of monolayer graphene at charge neutrality

3.1 . Introduction to the chapter

In the last chapter, we presented the fundamental knowledge of the quantum Hall liquid. Now, we begin the first project of this thesis: *Spin and valley ordering of fractional quantum Hall states in monolayer graphene*. The results of the project are published in Ref. [67]. The content of this work is presented in three chapters: the present chapter 3, chapter 4, and chapter 5.

Monolayer graphene was isolated in 2005 [29] and rapidly became an attractive research topic for both theory and experiments. The quantum Hall effect in graphene was detected almost immediately after the isolation of the material [18, 19]. Unlike many semiconductors, the graphene Landau levels are fourfold degenerate due to the valley degree of freedom, which is twofold degenerate and behaves as a pseudospin.

The multicomponent quantum Hall effect in graphene has become an intensive research topic in the last two decades. The appearance of intermediate plateaus at filling factors $\nu = 0, \pm 1$ [68, 69] is explained in the framework of the quantum Hall ferromagnetism [70]. Those plateaus result from the electron-electron interaction, which breaks the SU(4) symmetry of the Coulomb interaction and gives rise to a variety of spin and valley orders [31, 71, 72]. During the last decade, experiments on this topic have made much progress [73, 74], especially the visualization of those symmetry-breaking orders by scanning tunneling microscopy [75–77]. However, most research focuses on the filling factor $\nu = 0$ at the Charge neutrality point (CNP).

In this work, we study the spin and valley ordering of the quantum Hall states of filling factors $\nu = n/3 (n = 1, 2, 4, 5)$ in monolayer graphene. In the present chapter, we begin by recalling the graphene band structure and defining the valley degree of freedom. Then, we present the relativistic Landau level quantization in this material. We will focus on the physics of the central Landau level, which has zero energy and is half-filled at charge neutrality. We show the Hamiltonian of the two-dimensional electron gas projected to the central Landau level and discuss the symmetry-breaking due to short-range valley interaction. We present a variational method to calculate the phase diagram at charge neutrality. After that, we will describe in detail the four symmetry-breaking phases of the case $\nu = 0$. Although this chapter does not contain any new results, it is crucial to discuss the case $\nu = 0$ in detail to prepare the discussions of the cases of fractional quantum Hall states in chapters 4 and 5.

3.2 . Graphene

3.2.1 . Crystal structure

The two-dimensional crystalline structure of graphene is shown in Fig.3.1. Graphene has a honeycomb lattice of carbon atoms with two sublattices, A (red) and B (blue). A primitive cell of graphene contains two atoms: one belongs to the A-sublattice and the other belongs to the B-sublattice. Each sublattice is a hexagonal lattice with primitive

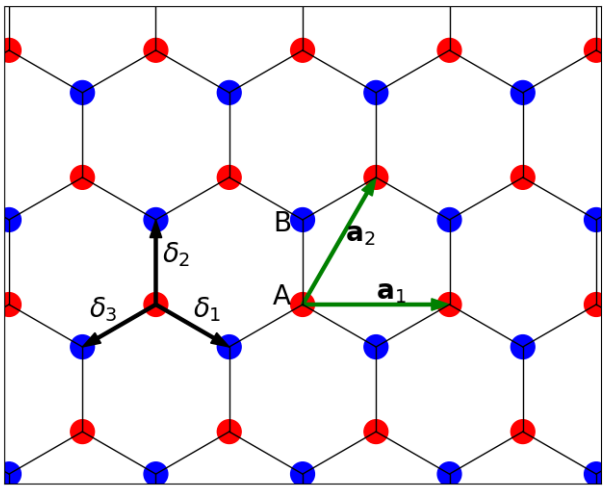

Figure 3.1: Crystal structure of monolayer graphene. The red atoms belong to the A-sublattice, and the blue atoms belong to the B-sublattice. The vectors $\mathbf{a}_1$ and $\mathbf{a}_2$ are primitive vectors of the two-dimensional lattice. The vectors $\boldsymbol{\delta}_1$, $\boldsymbol{\delta}_2$ and $\boldsymbol{\delta}_3$ represent the relative positions of B-atoms with respect to A-atoms, that means the relative positions between nearest-neighbors.

vectors:

$$\begin{aligned} \mathbf{a}_1 =& (a, 0) \\ \mathbf{a}_2 =& \left(\frac{a}{2}, \frac{\sqrt{3}a}{2}\right) \end{aligned} \tag{3.1}$$

The lattice parameter $a = 2.46$Å. The distance between neighboring carbon atoms is 1.42Å. The relative position from each atom A to the three nearest atoms B is given by the vectors:

$$\begin{aligned} \boldsymbol{\delta}_1 &= \left(0, \frac{a}{\sqrt{3}}\right) \\ \boldsymbol{\delta}_2 &= \left(\frac{a}{2}, -\frac{a}{2\sqrt{3}}\right) \\ \boldsymbol{\delta}_3 &= \left(-\frac{a}{2}, -\frac{a}{2\sqrt{3}}\right) \end{aligned} \tag{3.2}$$

The first Brillouin zone of the graphene honeycomb lattice in the reciprocal space is a hexagon (see Fig.3.2). Its six corners are classified into two classes, such that the points belonging to the same class are related to each other by a rotation of angle $2\pi/3$. To sum up, there are two inequivalent points K$\left(\frac{4\pi}{3a}, 0\right)$ and K'$\left(-\frac{4\pi}{3a}, 0\right)$. They are

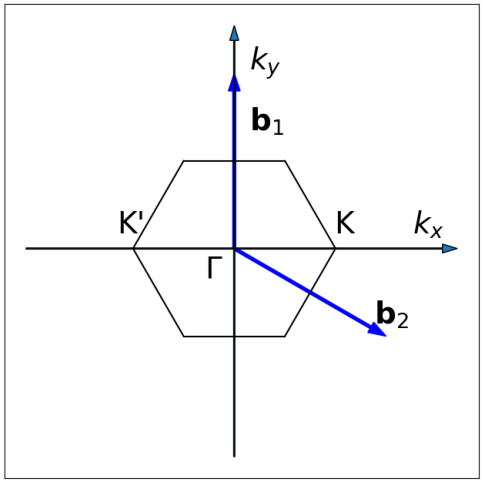

Figure 3.2: The first Brillouin zone of graphene is a hexagon. The vectors $\mathbf{b}_1$ and $\mathbf{b}_2$ are primitive vectors of the graphene reciprocal lattice. The points $\mathbf{K}$ and $\mathbf{K}'$ are the Dirac points.

the so-called ***Dirac points***. The primitive vectors of the graphene reciprocal lattice are:

$$\begin{aligned} \mathbf{b}_1 &= \left(\frac{2\pi}{a}, -\frac{2\pi}{\sqrt{3}a}\right) \\ \mathbf{b}_2 &= \left(0, \frac{4\pi}{\sqrt{3}a}\right) \end{aligned} \tag{3.3}$$

3.2.2 . Electronic structure of graphene

In this subsection, we present the band structure of graphene by doing the tight-binding model to the nearest-neighbors. One can find pedagogical reviews of the graphene electronic structure by Castro Neto, Goerbig [28, 30] or in the paper by Jung and MacDonald [78].

Each carbon atom has four outermost electrons. They occupy the $2s$ orbital and the $2p$ orbitals. The three orbitals $2s$, $2p_x$, $2p_y$ hybridize, become three sp^2 orbitals and form the σ bonds between the carbon atoms. The remaining $2p_z$ orbital is unhybridized and perpendicular to the graphene plane. The remaining electron in this orbital participates in the formation of the π bond, resulting in a conjugated π bond system delocalized over the whole graphene sample. Therefore, only the π electrons are responsible for the electronic properties of graphene at low energy. The other electrons occupy energy levels far from the Fermi level and are not involved in the low-energy processes. In a π bond approximation, we only consider those π electrons, and each atom has one available electronic orbital. Because each primitive cell contains two carbon atoms (A-site and B-site), we consider that there are two orbitals in one unit cell.

Let $\mathbf{R}_{iA/B}$ be the position of the A(B)-atom in the primitive cell i. The Bloch wavefunction of wavevector $\mathbf{k}$ is a linear combination of the Maximally Localized Wannier

Functions (MLWF) [78]:

$$\Phi_{\mathbf{k},A/B}(\mathbf{r}) = \frac{1}{\sqrt{N}} \sum_{i=1}^{N} e^{i\mathbf{k}\cdot\mathbf{R}_{iA/B}} \phi_{A/B}(\mathbf{r} - \mathbf{R}_{iA/B}) \tag{3.4}$$

We write this wavefunction in the bra-ket notation:

$$|\Phi_{\mathbf{k},A/B}\rangle = \frac{1}{\sqrt{N}} \sum_{i=1}^{N} e^{i\mathbf{k}\cdot\mathbf{R}_{iA/B}} |\phi_{A/B}(\mathbf{R}_{iA/B})\rangle \tag{3.5}$$

The MLWFs are orthonormal, implying that $|\Phi_{\mathbf{k},A/B}\rangle$ form an orthonormal basis. The wavefunction of wavevector $\mathbf{k}$ is expressed in the basis of the wavefunctions in the A-site and B-site as:

$$|\Psi_{\mathbf{k}}\rangle = a_{\mathbf{k}}|\Phi_{\mathbf{k}A}\rangle + b_{\mathbf{k}}|\Phi_{\mathbf{k}B}\rangle \tag{3.6}$$

The Schrödinger equation reads:

$$H(\mathbf{k})|\Psi_{\mathbf{k}}\rangle = E_{\mathbf{k}}|\Psi_{\mathbf{k}}\rangle \tag{3.7}$$

Because the wavefunctions $|\Phi_{\mathbf{k}A/B}\rangle$ form an orthonormal set, we express the Schrödinger equation in the matrix form as:

$$\begin{pmatrix} H_{AA} & H_{AB} \\ H_{BA} & H_{BB} \end{pmatrix} \begin{pmatrix} a_{\mathbf{k}} \\ b_{\mathbf{k}} \end{pmatrix} = E_{\mathbf{k}} \begin{pmatrix} a_{\mathbf{k}} \\ b_{\mathbf{k}} \end{pmatrix} \tag{3.8}$$

The matrix elements H_{AA} and H_{BB} are just the energy of the electron at the sites A and B: $H_{AA} = \varepsilon_A$ and $H_{BB} = \varepsilon_B$. The matrix element H_{AB} is given by:

$$H_{AB} = \langle \Phi_{\mathbf{k}A}|H(\mathbf{k})|\Phi_{\mathbf{k}B}\rangle = -\gamma_0 f(\mathbf{k}) \tag{3.9}$$

Here γ_0 is the hopping integral between nearest neighbors (that means i and j are nearest-neighbor primitive cells):

$$\gamma_0 = -\langle \phi_A(\mathbf{R}_{iA})|H|\phi_B(\mathbf{R}_{jB})\rangle \tag{3.10}$$

The value of γ_0 is $\gamma_0 \approx 2.992$ eV [78]. $f(\mathbf{k})$ is the structure factor, given by:

$$f(\mathbf{k}) = \sum_{j=1}^{3} e^{i\mathbf{k}\cdot\delta_j} = e^{ik_y a/\sqrt{3}} + 2e^{-ik_y a/2\sqrt{3}} \cos\frac{k_x a}{2} \tag{3.11}$$

The Hamiltonian in the matrix form is:

$$H(\mathbf{k}) = \begin{pmatrix} \epsilon_A & -\gamma_0 f(\mathbf{k}) \\ -\gamma_0 f(\mathbf{k})^* & \epsilon_B \end{pmatrix} \tag{3.12}$$

In normal conditions, the energies of electron at site-A and site-B are equal. Therefore, we can set $\epsilon_A = \epsilon_B = 0$. The energy eigenvalues are given by:

$$E_{\pm}(\mathbf{k}) = \pm\gamma_0|f(\mathbf{k})| = \pm\gamma_0\sqrt{1 + 4\cos\frac{k_x a}{2}\cos\frac{k_y a\sqrt{3}}{2} + 4\cos^2\frac{k_x a}{2}} \tag{3.13}$$

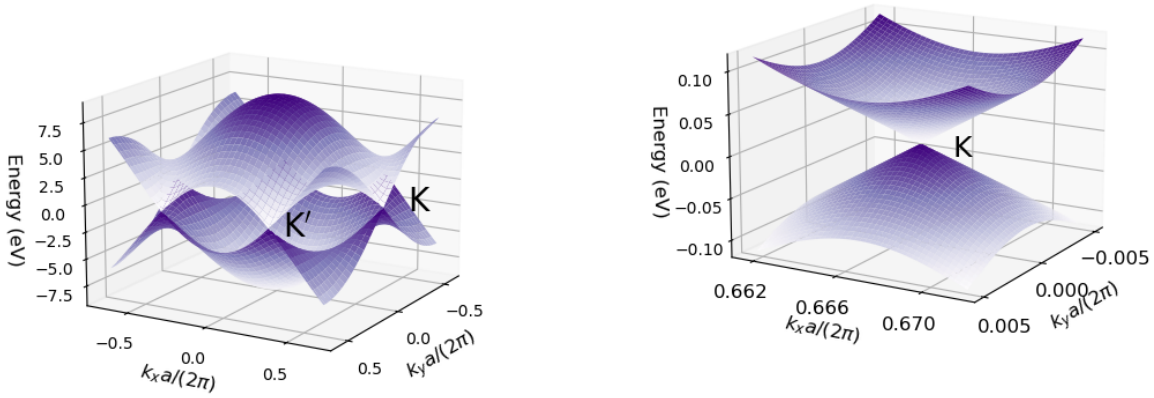

(a) (b)

Figure 3.3: (a) The graphene band structure. Here we set $\gamma_0 = 2.992\,\mathrm{eV}$. The conduction band and valence band touch at the points K and K'. (b) A zoom in the vicinity in the K-point, showing that the band structure is a cone with linear dispersion (Dirac cone).

Fig.3.3a shows the band structure of graphene. The valence band and the conduction band touch each other at the Dirac points K and K'. We denote the Dirac points K_ξ with $\xi = +$ for K and $\xi = -$ for K'. Hence $\mathbf{K}_\xi = \left(\xi\frac{4\pi}{3a}, 0\right)$.

The physics of graphene in the vicinity of the Dirac points attracts a particular interest. Here, the band structure has a linear cone-like shape so that we call these bands the ***Dirac cones*** (see Fig. 3.3b). Consequently, electrons have zero effective mass and behave like relativistic massless particles. Indeed, we introduce the momentum $\mathbf{p} = \hbar(\mathbf{k} - \mathbf{K}_\xi)$ in the vicinity of the Dirac points, so that $\mathbf{k} = \mathbf{K}_\xi + \mathbf{q}$ where $\mathbf{q} = \mathbf{p}/\hbar$. In the limit $qa \ll 1$, we approximate the structure factor to first order in $|q|$ as follows:

$$f(\mathbf{k}) = -\frac{\sqrt{3}}{2}a(\xi q_x - iq_y) + o(|q|) \tag{3.14}$$

Hence, the Hamiltonian has the Dirac form up to first order in $|q|$:

$$H_\xi(\mathbf{q}) = \xi\hbar v_F(\sigma_x q_x + \xi\sigma_y q_y) \tag{3.15}$$

with $v_F = \sqrt{3}a\gamma_0/(2\hbar) \approx 9.68 \times 10^5 \mathrm{m/s}$ the ***Fermi velocity***. The matrices σ_x and σ_y are the Pauli matrices:

$$\sigma_x = \begin{pmatrix} 0 & 1 \\ 1 & 0 \end{pmatrix}, \sigma_y = \begin{pmatrix} 0 & -i \\ i & 0 \end{pmatrix} \tag{3.16}$$

The energy eigenvalues are linear functions of $|q|$:

$$E_\pm(\mathbf{q}) = \pm\hbar v_F|q| \tag{3.17}$$

It proves that in the vicinity of the Dirac points, electrons behave as massless relativistic fermions. We denote λ the band index: $\lambda = +$ for the conduction band and

$\lambda = -$ for the valence band. For a spinful system, because each of the two atoms in the primitive cell contributes one electron, the two electrons fill the valence band up to the Fermi energy $E_F = 0$. At charge neutrality, the Fermi level lies at the intersection between the two bands. The Fermi surface reduces to the set of Dirac points. Graphene is a semimetal.

3.2.3 . Valley pseudospin

In the last subsection, we proved that the graphene Hamiltonian has two different forms in the vicinity of the points K_+ and K_-. At those points, the minimum of the conduction band touches the maximum of the valence band. We call those two points the two *valleys*. Low-energy excitations (electrons and holes) have energy and momentum in the vicinity of the two Dirac points. We introduce the ***valley pseudospin***. The valley pseudospin behaves like the intrinsic spin. It takes the value $\xi = +1$ in the vicinity of K and the value $\xi = -1$ in the vicinity of K'. For this reason, we also use the Pauli matrices to describe the valley pseudospin. To distinguish the valley Pauli matrices from the spin Pauli matrices, we denote them τ instead of σ:

$$\tau_x = \begin{pmatrix} 0 & 1 \\ 1 & 0 \end{pmatrix}, \tau_y = \begin{pmatrix} 0 & -i \\ i & 0 \end{pmatrix}, \tau_z = \begin{pmatrix} 1 & 0 \\ 0 & -1 \end{pmatrix} \tag{3.18}$$

We define the angle $\varphi_{\mathbf{q}} (0 \leq \varphi_{\mathbf{q}} < 2\pi)$ such that $q_x + iq_y = |q| e^{i\varphi_{\mathbf{q}}}$. The eigenstates for the eigenvalues $E_\lambda(\mathbf{q}) = \lambda \hbar v_F |q|$ ($\lambda = +1$ for conduction band and $\lambda = -1$ for valence band) are given by the following spinors in the basis of the sublattice wavefunctions A and B $(\psi_{K_\xi A}, \psi_{K_\xi B})^T$:

- In the valley K ($\xi = +1$):

$$\psi_{K+} = \frac{1}{\sqrt{2}} \begin{pmatrix} 1 \\ e^{i\varphi_{\mathbf{q}}} \end{pmatrix}, \psi_{K-} = \frac{1}{\sqrt{2}} \begin{pmatrix} 1 \\ -e^{i\varphi_{\mathbf{q}}} \end{pmatrix} \tag{3.19}$$

- In the valley K' ($\xi = -1$):

$$\psi_{K'+} = \frac{1}{\sqrt{2}} \begin{pmatrix} 1 \\ -e^{-i\varphi_{\mathbf{q}}} \end{pmatrix}, \psi_{K'-} = \frac{1}{\sqrt{2}} \begin{pmatrix} 1 \\ e^{-i\varphi_{\mathbf{q}}} \end{pmatrix} \tag{3.20}$$

Instead of writing the spinor in the valley K' in the form $(\psi_{K'A}, \psi_{K'B})^T$, we write it in the form $(\psi_{K'B}, \psi_{K'A})^T$. In this representation, the matrix σ_x remains unchanged while we must replace the matrix σ_y by its opposite $-\sigma_y$. In the basis $(\psi_{K'B}, \psi_{K'A})^T$, the Dirac Hamiltonian of the valley K' has the same form as the one of the valley K:

$$H_{\xi=-1}(\mathbf{q}) = -\hbar v_F (\sigma_x q_x + \sigma_y q_y) \tag{3.21}$$

We introduce the four-spinor representation:

$$\psi_{\mathbf{q}} = \begin{pmatrix} \psi_{KA} & \psi_{KB} & \psi_{K'B} & \psi_{K'A} \end{pmatrix}^T \tag{3.22}$$

In this representation, we write the effective Hamiltonian as follows:

$$H(\mathbf{q}) = \hbar v_F \tau^z \otimes \boldsymbol{\sigma} \cdot \mathbf{q} \tag{3.23}$$

with

$$\tau^z \otimes \boldsymbol{\sigma} = \begin{pmatrix} \boldsymbol{\sigma} & 0 \\ 0 & -\boldsymbol{\sigma} \end{pmatrix} \tag{3.24}$$

and $\boldsymbol{\sigma} = (\sigma_x, \sigma_y)$.

Overall, electrons in graphene have a new degree of freedom - the valley, which plays the role of a pseudospin. In general, the valley degree of freedom not only exists in graphene, but also in semiconductors (Si [79, 80], AlAs [81, 82]), bismuth [83], and transition-metal dichalcogenides [84, 85]. The idea of using the valley degree of freedom to process, transmit and store information paves the way to a new information technology - the valleytronics [86]. In the next subsection, we will discuss the Landau level quantization in graphene.

3.3 . Quantum Hall effect in graphene

3.3.1 . Relativistic Landau levels

In the previous subsection, we derived the low-energy effective Hamiltonian of graphene in the valley ξ as:

$$H_\xi = \xi \hbar v_F (\sigma_x q_x + \sigma_y q_y) \tag{3.25}$$

Here the Hamiltonian is written in the basis (ψ_{KA}, ψ_{KB}) in the valley K while it is written in the basis $(\psi_{K'B}, \psi_{K'A})$ in the valley K'. Under magnetic field, we modify the momentum by using the Peierls substitution:

$$\mathbf{q} \to \boldsymbol{\Pi} = \mathbf{q} + \frac{e}{c}\mathbf{A}(\mathbf{r}) \tag{3.26}$$

The Hamiltonian is written as follows:

$$H_\xi = \xi \hbar v_F (\sigma_x \Pi_x + \sigma_y \Pi_y) \tag{3.27}$$

The operators Π_x and Π_y satisfy the algebra:

$$[\Pi_x, \Pi_y] = -i\frac{\hbar^2}{l^2} \tag{3.28}$$

This commutation relation allows us to define the ladder operators:

$$\begin{aligned} a &= \frac{l}{\sqrt{2}}(\Pi_x - i\Pi_y) \\ a^\dagger &= \frac{l}{\sqrt{2}}(\Pi_x + i\Pi_y) \end{aligned} \tag{3.29}$$

These ladder operators satisfy the commutation relation:

$$[a, a^\dagger] = 1 \tag{3.30}$$

The Hamiltonian is written in terms of these ladder operators as follows:

$$H_\xi = \xi\hbar\frac{\sqrt{2}v_F}{l}\begin{pmatrix} 0 & a \\ a^\dagger & 0 \end{pmatrix} \tag{3.31}$$

Because the electron effective mass equals zero, we cannot define the cyclotron frequency as $\omega_c = eB/mc$ as in the case of the quantum Hall effect in conventional semiconductors. Instead, in this case, the cyclotron frequency is defined as:

$$\omega_c = \frac{\sqrt{2}v_F}{l} \tag{3.32}$$

so that the Hamiltonian becomes:

$$H_\xi = \xi\hbar\omega_c \begin{pmatrix} 0 & a \\ a^\dagger & 0 \end{pmatrix} \tag{3.33}$$

We search for the energy eigenvalues and the corresponding eigenstates of this Hamiltonian. We write the eigenstates under the form of the spinor $\psi = (u, v)^T$. The Schrödinger equation reads:

$$H_\xi\psi = E\psi \tag{3.34}$$

This implies that:

$$\begin{aligned} \xi\hbar\omega_c a v &= Eu \\ \xi\hbar\omega_c a^\dagger u &= Ev \end{aligned} \tag{3.35}$$

Consequently, we obtain the equation:

$$a^\dagger a v = \left(\frac{E}{\hbar\omega_c}\right)^2 v \tag{3.36}$$

This equation is solved when v takes the form of the single-harmonic oscillator wavefunction $v = \phi_N (N \in \mathbb{N})$ and the corresponding energy eigenvalues are:

$$E_{\pm,N} = \pm\hbar\omega_c\sqrt{N} = \pm\frac{\hbar v_F}{l}\sqrt{2N} \tag{3.37}$$

Therefore, the energy spectrum is not the same as the one in the case of the quantum Hall effect in semiconductors. Instead of being a linear function of the magnetic field B, the energy of the Landau levels is proportional to $B^{1/2}$, as shown in Fig. 3.4. For each value of $N (N \geq 1)$ there are two Landau levels: one with positive energy (conduction band) and one with negative energy (valence band). Especially, there is only one Landau level with index $N = 0$. This Landau level has energy $E_0 = 0$ and is usually called the ***central Landau level*** or the ***zero-energy Landau level (ZLL)*** instead of the *Lowest Landau level (LLL)*.

Electrons in graphene have two twofold degrees of freedom: the (intrinsic) spin and the valley pseudospin. Under weak Zeeman effect, each Landau level is approximately fourfold degenerate and is divided into four sublevels (components). The electrons belonging to each sublevel have the same state in the tensor product spin-valley Hilbert space. With its fourfold degenerate Landau levels, the quantum Hall effect in graphene is a more complicated example of multicomponent quantum Hall effects, compared to the case of the quantum Hall effect with spin (see subsection 2.3.5).

At charge neutrality, almost all Landau levels ($N \geq 1$) are completely filled by either electrons or holes, except the central Landau level $(N = 0)$, which is half-filled. This is the origin of the unusual half-integer Landau level spectrum of graphene, as we will

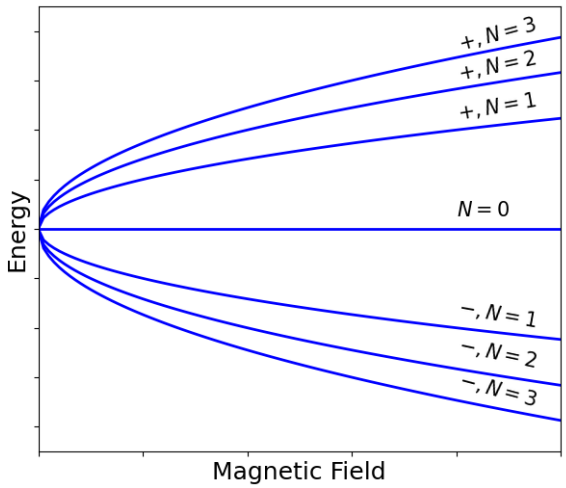

Figure 3.4: Relativistic Landau level spectrum.

discuss in subsection 3.3.2. When the degeneracy of the components (sublevels) is broken, the valley can be a superposition of the valleys K and K', and the spin can be canted away from the direction of the magnetic field $\mathbf{B}$. We will discuss these situations in section 3.7.

For the Landau levels $N \geq 1$, valley ξ, band index λ ($\lambda = +$ for conduction band and $\lambda = -$ for valence band) the eigenstate is given by the spinor:

$$\psi_{\lambda,\xi,N\geq 1} = \frac{1}{\sqrt{2}} \begin{pmatrix} \phi_{N-1} \\ \lambda\xi\phi_N \end{pmatrix} \tag{3.38}$$

In the central Landau level (ZLL), the eigenstate is given by the following spinor (for both valleys):

$$\psi_0 = \begin{pmatrix} 0 \\ \phi_0 \end{pmatrix} \tag{3.39}$$

Consequently, the central Landau level wavefunction is localized in the B-sublattice for valley K and is localized in the A-sublattice for valley K'. In higher Landau levels, the eigenstate wavefunction is a linear combination of harmonic oscillator wavefunctions localized in different sublattices.

3.3.2 . Experimental observations

In 2004, Novoselov, Geim *et al.* isolated few layer graphene by using mechanical exfoliation [87]. In one of the few-layer graphene samples, they observed a plateau-like feature in the graph of the transverse resistivity ρ_{xy} as a function of the magnetic field B, but it was not fully developed. In 2005, they successfully isolated monolayer graphene by using mechanical cleavage [29]. This is the first example of two-dimensional materials.

In 2005, the groups of Novoselov-Geim at the University of Manchester [18] and Philip Kim at Columbia University [19] finally observed the integer quantum Hall effect in graphene [18, 19]. The experiments confirmed the fourfold degeneracy of graphene Landau levels, which is due to the doubly degenerate spin and doubly degenerate valley. Especially,

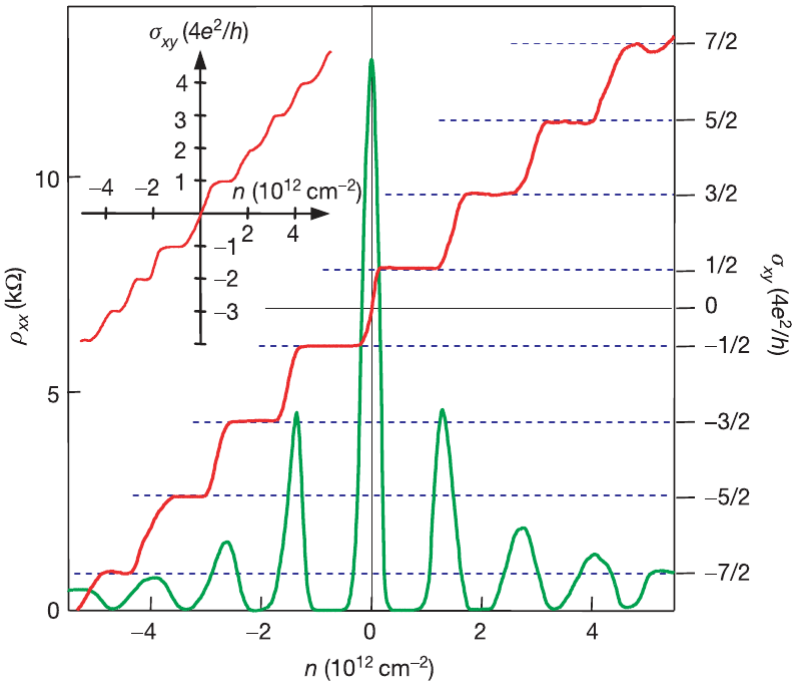

Figure 3.5: Integer quantum Hall effect in graphene (figure taken from Ref. [18]). *Reproduced with permission from Springer Nature.*

the plateaus appear for transverse conductivity $\sigma_{xy} = (4e^2/h)(N + 1/2)(N \in \mathbb{Z})$ instead of at the expected values $\sigma_{xy} = (4e^2/h)N$ like in the case of conventional semiconductors.

This half-integer quantum Hall effect is a consequence of the relativistic Landau level quantization. As shown in Fig. 3.6, each Landau level, except the central Landau level $(N = 0)$, has two versions: one for electrons $(\lambda = +)$ and one for holes $(\lambda = -)$. Consequently, at charge neutrality graphene, the Fermi level is not located inside the energy gap between two adjacent Landau levels. By contrast, it is inside the central Landau level $(N = 0)$ so that the central Landau level is half-filled. Therefore, the $N = 0$ Landau level is completely empty at filling factor $\nu = -2$ and is completely filled at filling factor $\nu = 2$. The integer quantum Hall effect in graphene occurs at filling factors $\nu = \pm(4N + 2)(N \in \mathbb{N})$. One can find detailed proofs of this unusual Hall conductivity in Refs. [88, 89].

The plateaus corresponding to filling factors $\nu = \pm 1$ were discovered in 2006 and 2007 [68, 69]. The corresponding samples were graphene on SiO_2/Si substrates. Those discoveries show that the central Landau level splits into four sublevels as the Fermi level sweeps this Landau level. Plateaus at filling factors $\nu = \pm 4$ also developed in the samples of Zhang *et al.* [68]. These integer quantum Hall effects were suggested to result from the electron-electron interaction, which lifts the spin and valley degeneracy [90]. The quantum Hall plateaus were also observed at room temperature with filling factors $\nu = \pm 2$ [91]. This discovery promises potential applications of the quantum Hall effect in daily life.

It took longer time to observe the fractional quantum Hall effect in graphene after the discovery of its integer version, compared to the time separating the two discoveries of the quantum Hall effects in conventional semiconductors. The fractions $\nu = \pm 1/3$ were

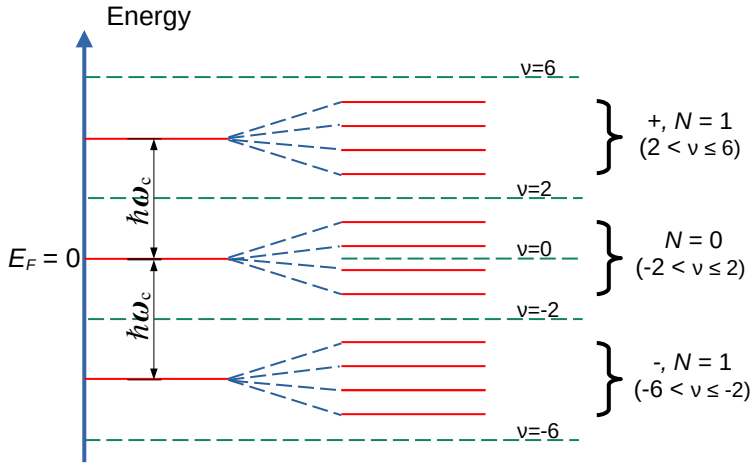

Figure 3.6: Graphene Landau levels. Here we represent the Landau levels $N = 0, \pm 1$. They are equally spaced by the energy $\hbar\omega_c = \hbar v_F \sqrt{2}/l$. Each Landau level is fourfold degenerate. Their energy levels are split under the Zeeman effect and the substrate-induced sublattice splitting energy. At charge neutrality ($E_F = 0$), the central Landau level ($N = 0$) is half-filled ($\nu = 0$). The other Landau levels are either completely filled or completely empty.

observed in 2009 in suspended graphene [20, 21]. Later, an experiment on suspended graphene also reported the fraction $\nu = 1/3$ together with the broken symmetry integer quantum Hall states [92]. Other fractions with denominators 5, 7 and 9 were also found in suspended graphene by doing measurement with a single-electron transistor (SET) [93, 94].

The use of hexagonal boron nitride (hBN) substrate permits to fabricate clean and high-quality devices [95]. The lattice parameters of hBN are close to the one of graphene. hBN also has atomically smooth surface, which is free of dangling bonds. This reduces the surface roughness, intrinsic doping, chemical reactivity, while increases the carrier mobility. It allows to observe a variety of fractional quantum Hall states not only in the central Landau level, but also in higher Landau levels [96]. Even denominator fractional quantum Hall states were observed at filling fractions $\nu = \pm 1/2$ in the central Landau level [97], and in higher Landau levels [98].

3.4 . Hamiltonian of two-dimensional electrons in graphene Central Landau Level

We focus on the central Landau level ($N = 0$) and neglect the mixing between different Landau levels. Because the kinetic energy of electrons in this Landau level is quenched, the physics of this Landau level is governed by the interaction between electrons and between electrons with the external fields. The total Hamiltonian is given by:

$$\mathcal{H} = \mathcal{H}_C + \mathcal{H}_V + \mathcal{H}_Z + \mathcal{H}_{AB} \tag{3.40}$$

Coulomb electron-electron interaction

$\mathcal{H}_C$ is the Coulomb electron-electron interaction. Because the wavefunction in the central Landau level is the Lowest Landau level wavefunction in both valleys, the expression of $\mathcal{H}_C$ includes the Lowest Landau Level projection:

$$\mathcal{H}_C = \mathcal{P}_{LLL} \sum_{i<j} \frac{e^2}{\varepsilon |\mathbf{r}_i - \mathbf{r}_j|} \mathcal{P}_{LLL} \tag{3.41}$$

Here ε is the graphene dielectric constant, which is of the order of 5 times the vacuum permittivity $\varepsilon_0 = 8.86 \times 10^{-12}\ \mathrm{F/m}$ [71]. The Coulomb interaction is approximately spin and valley (sublattice) independent. Therefore, it has the SU(4) symmetry: it is invariant under any rotation inside the spin-valley Hilbert space. The typical scale of the Coulomb energy for a magnetic field B of 1T is $e^2/\varepsilon l \approx 7\,\mathrm{meV}$ [99].

We consider the single-electron wavefunction, which is a product state between an orbital (spatial) wavefunction with quantum number m and a spinor $|\alpha\rangle$:

$$\psi_{m\alpha}(\mathbf{r}) = \phi_m(\mathbf{r})|\alpha\rangle \tag{3.42}$$

The orbital part $\phi_m(\mathbf{r})$ is a wavefunction in the Lowest Landau Level. The quantum number m can be either the linear momentum (torus geometry) or angular momentum (spherical geometry). The vector $|\alpha\rangle$ is a ket vector in the spin-valley Hilbert space. In the second quantization language, we write this wavefunction under the form:

$$|\psi_{m\alpha}\rangle = c^\dagger_{m\alpha}|0\rangle \tag{3.43}$$

Let M be the number of orbital wavefunctions. $M = N_\phi$ in the torus geometry and $M = 2|Q| + 1 = N_\phi + 1$ in the spherical geometry. The set of $4M$ wavefunctions $\psi_{m\alpha}(\mathbf{r})$ forms a basis for the central Landau level wavefunctions. In this basis, the expression of the Coulomb interaction is:

$$\mathcal{H}_C = \frac{1}{2} \sum_{\substack{p_1 p_2 p_3 p_4 \\ \chi\chi'}} V_{p_1 p_2 p_3 p_4} c^\dagger_{p_1\chi} c^\dagger_{p_2\chi'} c_{p_3\chi'} c_{p_4\chi} \tag{3.44}$$

In this expression, χ and χ' run over the four orthonormal spinors describing the four components. The matrix elements $V_{p_1 p_2 p_3 p_4}$ is evaluated as follows:

$$V_{p_1 p_2 p_3 p_4} = \int d^2\mathbf{r} d^2\mathbf{r}' \phi^*_{p_1}(\mathbf{r}) \phi^*_{p_2}(\mathbf{r}') \frac{e^2}{\varepsilon |\mathbf{r} - \mathbf{r}'|} \phi_{p_3}(\mathbf{r}') \phi_{p_4}(\mathbf{r}) \tag{3.45}$$

The SU(4) symmetry mixing spin and valley is, however, broken by the terms $\mathcal{H}_V$, $\mathcal{H}_Z$ and $\mathcal{H}_{AB}$. These contributions are called anisotropies.

Zeeman energy

$\mathcal{H}_Z$ is the Hamiltonian of the Zeeman energy. It splits the energies of spin-up and spin-down electrons and breaks the $\mathrm{SU(2)_s}$ symmetry of the spin Hilbert space. Its formula is as follows:

$$\mathcal{H}_Z = -g\mu_B B \sum_{i=1}^{N_e} S^z_i \tag{3.46}$$

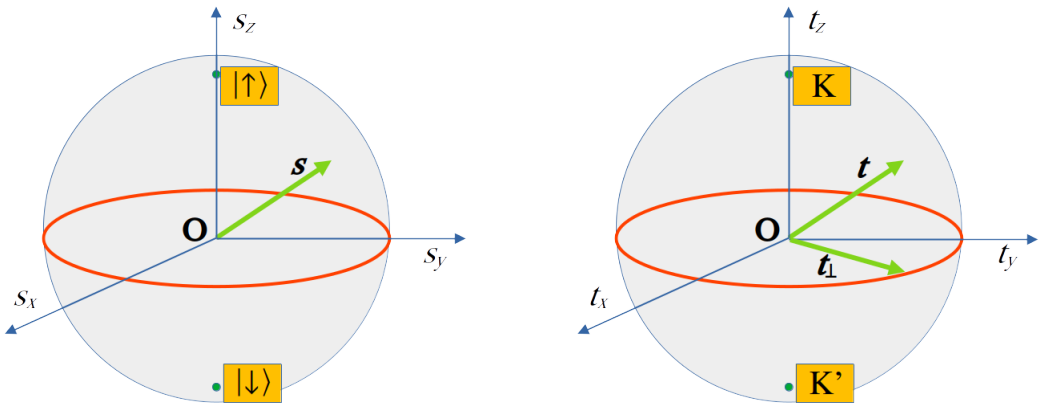

(a) (b)

Figure 3.7: (a) Bloch sphere for spin: the North/South poles represent spin-up/spin-down. (b) Bloch sphere for valley: the North/South poles represent valley K/valley K'.

as shown in (2.29). B is the total magnetic field, the z-direction of the spin is along the direction of the magnetic field $\mathbf{B}$, and S_i^z takes the values $\pm 1/2$. In graphene, the Landé g-factor $g = 2$. The typical scale of the Zeeman energy in graphene is around $0.115\,\mathrm{meV}$ under a magnetic field $B = 1\,\mathrm{T}$ [99], which is around 60 times smaller than the Coulomb energy. We represent the spin of the state in the spin Bloch sphere by using the unit vector $\mathbf{s}$ (Fig. 3.7a). The vector $\mathbf{s} = \hat{\mathbf{z}}$ corresponds to spin-up $\uparrow$, and the vector $\mathbf{s} = -\hat{\mathbf{z}}$ corresponds to spin-down $\downarrow$.

The expression of the Zeeman energy in the second quantization language is:

$$\mathcal{H}_Z = -h \sum_{\chi\chi'} \sum_{m} \langle \chi | \sigma^z | \chi' \rangle c^\dagger_{m\chi} c_{m\chi'} \tag{3.47}$$

The matrices σ^x,σ^y,σ^z are the Pauli matrices working in the spin Hilbert space, and $h = g\mu_B B/2$.

Substrate-induced sublattice splitting

$\mathcal{H}_{AB}$ is the Hamiltonian of the substrate-induced sublattice splitting energy. It splits the energies between the electrons residing in sublattices A and B. Because it plays a similar role as the Zeeman energy for the spin, this contribution is also called *valley Zeeman field*. In the central Landau level, electrons located in opposite valleys in the momentum space are localized in opposite sublattices. Therefore, $\mathcal{H}_{AB}$ separates the energy of the two valleys and breaks the $\mathrm{SU(2)_v}$ symmetry of the valley Hilbert space. Its formula is:

$$\mathcal{H}_{AB} = \Delta_{AB} \sum_{i=1}^{N_e} T_i^z \tag{3.48}$$

In the case of the hBN substrate, the value of Δ_{AB} is typically of the order $4\,\mathrm{meV}$ for $B = 1\,\mathrm{T}$ and is field-independent [97, 99]. T_i^z takes values $T_i^z = +1/2$ for valley K and $T_i^z = -1/2$ for valley K'. Similarly to all twofold degenerate degrees of freedom like the spin, the valley has its Bloch sphere (Fig. 3.7b). The sublattice splitting energy is strong

compared to the Zeeman field but is still weak compared to the Coulomb energy. We remark that the t_z-direction of the valley is not identical to the s_z-direction of spin and is neither the spatial z-direction perpendicular to the two-dimensional electron system. In the valley Bloch sphere, the North pole describes valley K, and the South pole represents valley K'. All states lying on the surface of the Bloch sphere are superpositions of valleys K and K'. In particular, the states lying on the equator have an equal probability of being in valley K as in valley K'. We represent the valley of the state by using the unit vector $\mathbf{t}$ in the valley Bloch sphere. The symbol $\mathbf{t}_\perp$ illustrates the valleys pointing along the equator. For valleys K/K', we still write K/K' instead of $\mathbf{t} = \pm\hat{\mathbf{z}}$.

In the second quantization language, the expression of the substrate-induced sublattice splitting energy is:

$$\mathcal{H}_{AB} = \Delta_{AB} \sum_{\chi\chi'} \sum_{m} \langle \chi | \tau^z | \chi' \rangle c^\dagger_{m\chi} c_{m\chi'} \tag{3.49}$$

The matrix τ^x, τ^y, τ^z are the Pauli matrices working in the valley Hilbert space. Here we merge the 1/2 factor of T^z into Δ_{AB} for convenience.

Short-range valley-dependent interaction

The last contribution $\mathcal{H}_V$ is the short-range valley-dependent interaction. $\mathcal{H}_V$ is a two-body interaction similar to $\mathcal{H}_C$. Its formula was proposed in Refs. [71, 100]:

$$\mathcal{H}_V = \sum_{i<j} [g_\perp(\tau_i^x \tau_j^x + \tau_i^y \tau_j^y) + g_z \tau_i^z \tau_j^z] \delta^{(2)}(\mathbf{r}_i - \mathbf{r}_j) \tag{3.50}$$

where $\tau_i^a (a = x, y, z)$ are the Pauli matrices operating in the valley Hilbert space. The delta Dirac means that $\mathcal{H}_V$ is a short-range point-contact interaction. Actually, physicists have yet to be able to control the coupling constants $g_\perp$ and g_z in the experiments. We consider the case where the anisotropy energy is weak compared to the Coulomb energy and does not destroy the Coulomb correlations of a given trial wavefunction. It separates the energies of the many-body quantum states having different total spin quantum number $S_{z,total}$ and total valley quantum number $T_{z,total}$. Depending on the values of $g_\perp$ and g_z, the ground state has different quantum numbers $S_{z,total}, S_{total}, T_{z,total}, T_{total}$. Therefore, we can establish a phase diagram in the $(g_\perp, g_z)$-plane (Fig. 3.8). We parameterize $g_\perp$ and g_z with a parameter $\theta (0 \leq \theta < 2\pi)$:

$$\begin{aligned} g_\perp &= g \cos\theta \\ g_z &= g \sin\theta \end{aligned} \tag{3.51}$$

In other words, $\mathcal{H}_V$ breaks the SU(4) symmetry of the Coulomb interaction $\mathcal{H}_C$. At a point $(g_\perp, g_z) \neq (0, 0)$, the SU(4) symmetry is reduced down to $\mathrm{SU}(2)_s \times \mathrm{U}(1)_v$. The valley quantum number T_z is conserved, whereas the Hamiltonian $\mathcal{H}_V$ is spin-rotationnally invariant. However, for particular values of $(g_\perp, g_z)$, the Hamiltonian $\mathcal{H}_V$ still has the following higher symmetries [32]:

1. On the line $g_\perp = 0$, $\mathcal{H}_V$ has the symmetry $\mathrm{SU}(2)_s^K \times \mathrm{SU}(2)_s^{K'} \times \mathrm{U}(1)_v$. The system is not only invariant under global spin rotations, but it is invariant under separate spin rotations in different valleys. The generators of this symmetry group are: $S^a = \frac{1}{2}\sum_i \sigma_i^a$, $N^a = \frac{1}{2}\sum_i \tau_i^z \sigma_i^a$ $(a = x, y, z)$ and $T^z = \frac{1}{2}\sum_i \tau_i^z$.

2. On the line $g_\perp = g_z$, $\mathcal{H}_V$ has the symmetry $\mathrm{SU}(2)_s \times \mathrm{SU}(2)_v$. The conservation of the valley T_z is replaced by a full rotational symmetry in the valley space. The generators of this symmetry group are: S^a and $T^a = \frac{1}{2}\sum_i \tau_i^a$.

3. On the line $g_\perp = -g_z$, $\mathcal{H}_V$ has the symmetry SO(5). The generators of this symmetry group are: S^a, T^z, $\Pi_a^x = \frac{1}{2}\sum_i \tau_i^x \sigma_i^a$, $\Pi_a^y = \frac{1}{2}\sum_i \tau_i^y \sigma_i^a$. The five remaining SU(4) generators form a five-dimensional order parameter $(T^{x,y}, N^{x,y,z})$ which characterizes the phases.

The expression of the short-range valley-dependent interaction energy is:

$$\mathcal{H}_V = \frac{1}{2} \sum_{\substack{\mu\mu'\nu'\nu \\ p_1p_2p_3p_4}} \mathcal{A}^{\mu\mu'\nu'\nu}_{p_1p_2p_3p_4} c^\dagger_{p_1\mu} c^\dagger_{p_2\mu'} c_{p_3\nu'} c_{p_4\nu} \tag{3.52}$$

In this expression, the value of $\mathcal{A}^{\mu\mu'\nu'\nu}_{p_1p_2p_3p_4}$ is expressed as follows:

$$\begin{aligned} \mathcal{A}^{\mu\mu'\nu'\nu}_{p_1p_2p_3p_4} =& \int d^2\mathbf{r}_i d^2\mathbf{r}_j \psi^\dagger_{p_1\mu}(\mathbf{r}_i)\psi^\dagger_{p_2\mu'}(\mathbf{r}_j)[g_\perp(\tau_i^x\tau_j^x + \tau_i^x\tau_j^y) + g_z\tau_i^z\tau_j^z]\times \\ & \times \delta^{(2)}(\mathbf{r}_i - \mathbf{r}_j)\psi_{p_3\nu'}(\mathbf{r}_j)\psi_{p_4\nu}(\mathbf{r}_i) \\ =& [g_\perp(\tau^x_{\mu\nu}\tau^x_{\mu'\nu'} + \tau^y_{\mu\nu}\tau^y_{\mu'\nu'}) + g_z\tau^z_{\mu\nu}\tau^z_{\mu'\nu'}]D_{p_1p_2p_3p_4} \end{aligned} \tag{3.53}$$

The value $D_{p_1p_2p_3p_4}$ is the integral:

$$D_{p_1p_2p_3p_4} = \int d^2\mathbf{r} \phi^*_{p_1}(\mathbf{r})\phi^*_{p_2}(\mathbf{r})\phi_{p_3}(\mathbf{r})\phi_{p_4}(\mathbf{r}) \tag{3.54}$$

We can write the expression of $\mathcal{H}_V$ in a more elegant form by defining the field operator:

$$\begin{aligned} \hat{\psi}_\mu(\mathbf{r}) =& \sum_p \phi_p(\mathbf{r}) c_{p\mu} \\ \hat{\psi}^\dagger_\mu(\mathbf{r}) =& \sum_p \phi^*_p(\mathbf{r}) c^\dagger_{p\mu} \end{aligned} \tag{3.55}$$

By introducing $g_x = g_y = g_\perp$, we have:

$$\begin{aligned} \mathcal{H}_V =& \frac{1}{2} \sum_{\substack{\mu\mu'\nu'\nu \\ p_1p_2p_3p_4}} \left(\sum_{a=x,y,z} g_a \tau^a_{\mu\nu}\tau^a_{\mu'\nu'} \right) D_{p_1p_2p_3p_4} c^\dagger_{p_1\mu} c^\dagger_{p_2\mu'} c_{p_3\nu'} c_{p_4\nu} \\ =& \frac{1}{2} \sum_{\mu\mu'\nu'\nu} \int d^2\mathbf{r}_i d^2\mathbf{r}_j \hat{\psi}^\dagger_\mu(\mathbf{r}_i)\hat{\psi}^\dagger_{\mu'}(\mathbf{r}_j) \left[\sum_a g_a \tau_i^a \tau_j^a \right] \delta^{(2)}(\mathbf{r}_i - \mathbf{r}_j)\hat{\psi}_{\nu'}(\mathbf{r}_j)\hat{\psi}_\nu(\mathbf{r}_i) \\ =& \frac{1}{2} \sum_{\mu\mu'\nu'\nu} \left[\sum_a g_a \tau^a_{\mu\nu}\tau^a_{\mu'\nu'} \right] \int d^2\mathbf{r} \hat{\psi}^\dagger_\mu(\mathbf{r})\hat{\psi}^\dagger_{\mu'}(\mathbf{r})\hat{\psi}_{\nu'}(\mathbf{r})\hat{\psi}_\nu(\mathbf{r}) \end{aligned} \tag{3.56}$$

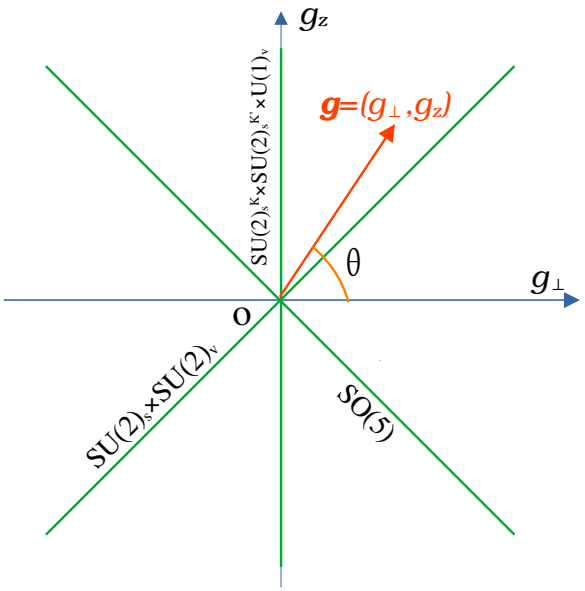

Figure 3.8: The $(g_\perp, g_z)$ plane of coupling constants. The high symmetry lines $g_\perp = 0$, $g_\perp = g_z$ and $g_\perp = -g_z$ are green.

3.5 . Quantum Hall ferromagnetism

3.5.1 . The one-component state

We begin by considering the case of one Landau level with spinful electrons and neglect all Landau level mixing. The spinor $|\alpha\rangle$ in the single-electron wavefunction (3.42) can be either spin-up $|\uparrow\rangle$ or spin-down $|\downarrow\rangle$. The Coulomb interaction $\mathcal{H}_C = \sum_{i<j} \frac{e^2}{\varepsilon|\mathbf{r}_i - \mathbf{r}_j|}$ (projected to this Landau level) has the SU(2) symmetry: it is invariant under any spin rotation. This SU(2) symmetry doubles the degeneracy of the Landau level.

In the state with filling factor $\nu = 1$, this Landau level is half filled. Similar to a ferromagnet, the ground state wavefunction should have an antisymmetric orbital part with a symmetric spin part in order to minimize the Coulomb energy of the many-electron system. The situation is similar to the one in a ferromagnet so we call this situation ***quantum Hall ferromagnetism***. This ferromagnetic multiplet maximizes the total spin S^z and has the wavefunction with a Slater determinant orbital part:

$$|\Psi_{\nu=1}\rangle = \prod_{i<j}(z_i - z_j)|++\cdots+\rangle \tag{3.57}$$

In the second quantization language, its wavefunction is given by:

$$|\Psi_{\nu=1}\rangle = c^\dagger_{1\alpha}c^\dagger_{2\alpha}\cdots c^\dagger_{N_\phi\alpha}|0\rangle \tag{3.58}$$

with some spin state $|\alpha\rangle$.

The wavefunction $|\Psi_{\nu=1}\rangle$ is an exact eigenstate of the Coulomb interaction (with no Landau level mixing). We prove this statement by directly applying $\mathcal{H}_C$ into $|\Psi_{\nu=1}\rangle$:

$$\mathcal{H}_C|\Psi_{\nu=1}\rangle = E_1|\Psi_{\nu=1}\rangle = \sum_{i<j}(V_{ijji} - V_{ijij})|\Psi_{\nu=1}\rangle \tag{3.59}$$

The previous equality shows that $|\Psi_{\nu=1}\rangle$ is an exact eigenstate of $\mathcal{H}_C$. The eigenvalue energy has two contributions corresponding to the direct and exchange energies. The direct energy is cancelled by the electron-background and background-background interaction energies (in the thermodynamic limit). Hence, the energy eigenvalue of the state $|\Psi_{\nu=1}\rangle$ has only one contribution from the exchange energy and equals[1]:

$$E_1 = -\sqrt{\frac{\pi}{8}}\frac{e^2}{\varepsilon l} \tag{3.60}$$

This reasoning can be generalized to the case of a SU(N) quantum Hall ferromagnet. In this case, $|\alpha\rangle$ is a N-component vector. The quantum Hall effect in graphene is therefore a kind of SU(4) quantum Hall ferromagnetism [70]. Quantum Hall ferromagnetism explains the existence of the quantum Hall states in graphene at filling factors $\nu = 0, \pm 1$.

3.5.2 . The two-component state

We move on to the two-component state $\nu = 0$ in the graphene central Landau level:

$$|\Psi_{\nu=0}\rangle = c^\dagger_{1\alpha}c^\dagger_{2\alpha}\cdots c^\dagger_{N_\phi\alpha}c^\dagger_{1\beta}c^\dagger_{2\beta}\cdots c^\dagger_{N_\phi\beta}|0\rangle \tag{3.61}$$

where $|\alpha\rangle$ and $|\beta\rangle$ are two vectors in the four-dimensional spin-valley Hilbert space. We neglect all Landau level mixing. In the case of the SU(4) quantum Hall ferromagnetism in graphene, the $|\Psi_{\nu=0}\rangle$ state is an eigenstate of the SU(4)-symmetric Coulomb Hamiltonian $\mathcal{H}_C$:

$$\mathcal{H}_C|\Psi_{\nu=0}\rangle = \left[2\sum_{i<j}(V_{ijji} - V_{ijij}) + \sum_{ij}V_{ijji}\right]|\Psi_{\nu=0}\rangle \tag{3.62}$$

In the cases of filling factors $\nu = \pm 1$, the spin and the valley can be simultaneously polarized, for example, if all the electrons (holes) have spin-up and occupy the valley K. By contrast, for the two-component state $|\Psi_{\nu=0}\rangle$, if the two components $|\alpha\rangle$ and $|\beta\rangle$ have the same spin, they should have different valleys, due to the exclusion principle. Similarly, if $|\alpha\rangle$ and $|\beta\rangle$ have the same valley, they should have different spins. The spin and the valley cannot be simultaneously polarized.

In the presence of anisotropies $\mathcal{H}_V + \mathcal{H}_Z + \mathcal{H}_{AB}$, anisotropies break the SU(4) symmetry of the Coulomb interaction $\mathcal{H}_C$. The two-component state $|\Psi_{\nu=0}\rangle$ is no longer an exact eigenstate of the total Hamiltonian $\mathcal{H}$. The total energy depends on the components $|\alpha\rangle$ and $|\beta\rangle$. The ground state is the one that minimizes the total anisotropy energy $\mathcal{H}_V + \mathcal{H}_Z + \mathcal{H}_{AB}$. One use the two-component state $|\Psi_{\nu=0}\rangle$ as a trial wavefunction to determine the symmetry-broken orders.

[1] See Ref. [101], subsections 1.3.2 and 1.5.3. We obtain the value of E_1 in (3.60) by directly applying the formula (10.78) of Ref. [101] with $\nu = 1$ and the Laguerre polynomial $L^1_0(x) = 1$.

The competition between $\mathcal{H}_Z$, $\mathcal{H}_{AB}$ and $\mathcal{H}_V$ determines the ground state of the system. The Zeeman effect encoded in $\mathcal{H}_Z$ favors the spin-polarized states. On the contrary, the substrate-induced sublattice splitting energy $\mathcal{H}_{AB}$ polarizes the valley to either K or K'. The short-range valley-dependent interaction $\mathcal{H}_V$ has two contributions: the XY-like contribution (with coupling constant $g_\perp$) and the Ising-like contribution (with coupling constant g_z). The XY-like contribution prefers the polarization of the valley along the equator of the Bloch sphere, described by the vector $\mathbf{t}_\perp$ (see Fig. 3.7b). The Ising-like contribution, however, prefers a valley polarized to either the K or K' states. The competition between the XY-like and Ising-like contributions determines the valley of the ground state. Consequently, it affects the electron density distribution in the two sublattices.

3.6 . Variational method for the Charge neutrality case $\nu = 0$

As previously discussed, we are working in a regime where the Zeeman energy, sublattice splitting energy and short-range valley-dependent energy are weak compared to the Coulomb interaction. Therefore, the eigenstate of the total Hamiltonian can be well approximated by the eigenstate $|\Psi_{\nu=0}\rangle$ of the SU(4) Coulomb interaction. The symmetry-breaking terms $\mathcal{H}_V$, $\mathcal{H}_Z$ and $\mathcal{H}_{AB}$ select the components $|\alpha\rangle$ and $|\beta\rangle$ so that the flavors of the most stable phase minimize the total anisotropy energy. We solve for the problem by using the variational method. First of all, we have:

$$\langle\Psi_{\nu=0}|c^\dagger_{m\chi}c_{m\chi'}|\Psi_{\nu=0}\rangle = \begin{cases} 1 & \text{if } \chi=\chi'=\alpha \text{ or } \chi=\chi'=\beta \\ 0 & \text{otherwise} \end{cases} \tag{3.63}$$

By using this relation, the Zeeman energy per flux quantum equals:

$$E_Z = \frac{\langle\Psi_{\nu=0}|\mathcal{H}_Z|\Psi_{\nu=0}\rangle}{N_\phi} = -h(\langle\alpha|\sigma^z|\alpha\rangle + \langle\beta|\sigma^z|\beta\rangle) = -h\mathsf{Tr}(P_i\sigma^z) \tag{3.64}$$

where P_i is the projection operator on the occupied components:

$$P_i = |\alpha\rangle\langle\alpha| + |\beta\rangle\langle\beta| \tag{3.65}$$

Similarly, the substrate-induced sublattice splitting energy per flux quantum equals:

$$E_{AB} = \Delta_{AB}\mathsf{Tr}(P_i\tau^z) \tag{3.66}$$

The expectation value of the product of four creation and annihilation operators equals (see Ref. [101]):

$$\langle\Psi_{\nu=0}|c^\dagger_{p_1\mu}c^\dagger_{p_2\mu'}c_{p_3\nu'}c_{p_4\nu}|\Psi_{\nu=0}\rangle = \delta_{p_1p_4}\delta_{\mu\nu}\delta_{p_2p_3}\delta_{\mu'\nu'} - \delta_{p_1p_3}\delta_{\mu\nu'}\delta_{p_2p_4}\delta_{\mu'\nu} \tag{3.67}$$

The formula of the valley-dependent interaction energy per flux quantum:

$$\begin{aligned} E_V =& \frac{\langle\Psi_{\nu=0}|\mathcal{H}_V|\Psi_{\nu=0}\rangle}{N_\phi} = \frac{1}{2}\sum_{\substack{\mu,\nu=\alpha,\beta \\ p_1p_2}} \left(\mathcal{A}^{\mu\nu\nu\mu}_{p_1p_2p_2p_1} - \mathcal{A}^{\mu\nu\mu\nu}_{p_1p_2p_1p_2}\right) \\ =& \frac{1}{2}\sum_{\mu,\nu=\alpha,\beta}\sum_{a=x,y,z} g_a(\tau^a_{\mu\mu}\tau^a_{\nu\nu} - \tau^a_{\mu\nu}\tau^a_{\nu\mu})\left(\frac{1}{N_\phi}\sum_{p_1p_2} D_{p_1p_2p_2p_1}\right) \end{aligned} \tag{3.68}$$

We evaluate the quantity

$$D = \sum_{p_1 p_2} D_{p_1 p_2 p_2 p_1} = \int d^2\mathbf{r} \left(\sum_{p_1} |\phi_{p_1}(\mathbf{r})|^2 \right) \left(\sum_{p_2} |\phi_{p_2}(\mathbf{r})|^2 \right) \tag{3.69}$$

by recalling that the (normalized) basis wavefunctions $\phi_p(\mathbf{r})(0 \leq p < N_\phi - 1)$ have the following formula:

$$\phi_p(\mathbf{r}) = \left(\frac{1}{L_y \sqrt{\pi} l} \right)^{1/2} e^{-ip\frac{2\pi}{L_y}y} e^{-\frac{(x - p\frac{2\pi}{L_y}l^2)^2}{2l^2}} \tag{3.70}$$

For all $p' \in \{0, 1, 2, \ldots, N_\phi - 1\}$, the following integral equals:

$$\begin{aligned} &\int_0^{L_x} dx \int_0^{L_y} dy \sum_{p=0}^{N_\phi - 1} |\phi_p(x,y)|^2 |\phi_{p'}(x,y)|^2 \\ =& \left(\frac{1}{L_y \sqrt{\pi} l} \right)^2 \int_0^{L_y} dy \sum_{p=0}^{N_\phi - 1} \int_0^{L_x} dx \exp\left[-\frac{\left(x - p\frac{2\pi}{L_y} l^2 \right)^2}{l^2} - \frac{\left(x - p'\frac{2\pi}{L_y} l^2 \right)^2}{l^2} \right] \end{aligned} \tag{3.71}$$

The integral over dy gives the size L_y of the sample in the y-direction. In the thermodynamic limit, we can approximate the integral over dx as an integral from $-\infty$ to $+\infty$. Its value is given by the following formula:

$$l\sqrt{\frac{\pi}{2}} \exp\left[-\frac{1}{2} \left((p - p') \frac{2\pi l}{L_y} \right)^2 \right] \tag{3.72}$$

This implies that for all $p' \in \{0, 1, 2, \ldots, N_\phi - 1\}$, we have:

$$\begin{aligned} &\int_0^{L_x} dx \int_0^{L_y} dy \sum_{p=0}^{N_\phi - 1} |\phi_p(x,y)|^2 |\phi_{p'}(x,y)|^2 \\ =& \left(\frac{1}{L_y \sqrt{\pi} l} \right)^2 L_y l \sqrt{\frac{\pi}{2}} \sum_{p=0}^{N_\phi - 1} \exp\left[-\frac{1}{2} \left((p - p') \frac{2\pi l}{L_y} \right)^2 \right] \end{aligned} \tag{3.73}$$

For a macroscopically large value of N_ϕ, we can approximate the sum over p by an integral of the variable $u = (p - p')\dfrac{2\pi l}{L_y}$ over the whole real axis[2]. Hence, for all $p' \in \{0, 1, 2, \ldots, N_\phi - 1\}$:

$$\begin{aligned} &\int_0^{L_x} dx \int_0^{L_y} dy \sum_{p=0}^{N_\phi - 1} |\phi_p(x,y)|^2 |\phi_{p'}(x,y)|^2 \\ =& \left(\frac{1}{L_y \sqrt{\pi} l} \right)^2 L_y l \sqrt{\frac{\pi}{2}} \frac{L_y}{2\pi l} \int_{-\infty}^{+\infty} du e^{-\frac{u^2}{2}} du \\ =& \frac{1}{2\pi l^2} \end{aligned} \tag{3.74}$$

[2]One can argue that the approximation of the integral $\int dx$ and the sum $\sum_p$ is not relevant for x approaches $x = 0$ and $x = L_x$ as well as when $p' = 0$ or $p' = N_\phi$. However, in the thermodynamic limit, $L_x \gg l$ and N_ϕ is macroscopically large, we can neglect those discrepancies at the edges.

The value of the integral is the same for all p'. The integral D is therefore a sum of N_ϕ terms having the same value, so it equals:

$$D = \frac{N_\phi}{2\pi l^2} \tag{3.75}$$

It allows us to simplify the formula of the short-range valley-dependent interaction by defining the parameters $V_\perp$ and V_z:

$$\begin{aligned} V_\perp =& \frac{g_\perp}{2\pi l^2} \\ V_z =& \frac{g_z}{2\pi l^2} \end{aligned} \tag{3.76}$$

The short-range valley-dependent interaction energy per flux quantum equals:

$$E_V = \sum_{a=x,y,z} V_a[\mathsf{Tr}(P_\alpha \tau^a)\mathsf{Tr}(P_\beta \tau^a) - \mathsf{Tr}(P_\alpha \tau^a P_\beta \tau^a)] \tag{3.77}$$

Here $P_\alpha = |\alpha\rangle\langle\alpha|$ and $P_\beta = |\beta\rangle\langle\beta|$. The symmetry-broken phases are determined by minimizing the anisotropy energy, which is the sum of E_Z, E_{AB} and E_V. The total anisotropy energy per flux quantum equals:

$$\boxed{\begin{aligned} E_A =& E_V + E_Z + E_{AB} \\ =& \sum_{a=x,y,z} V_a \left[\mathsf{Tr}(P_\alpha \tau^a)\mathsf{Tr}(P_\beta \tau^a) - \mathsf{Tr}(P_\alpha \tau^a P_\beta \tau^a)\right] \\ & - h\mathsf{Tr}(P_i \sigma^z) + \Delta_{AB}\mathsf{Tr}(P_i \tau^z) \end{aligned}} \tag{3.78}$$

Instead of working on the $(g_\perp, g_z)$-plane, we will work on the $(V_\perp, V_z)$-plane. In the absence of the Zeeman effect, the broken-symmetry phases depend on the parameters $V_\perp$ and V_z. In the presence of the Zeeman effect, the phases depend on the ratio between $V_\perp/h$ and V_z/h.

3.7 . Phase diagram at Charge neutrality $\nu = 0$

In this section, we establish the phase diagrams of charge neutrality graphene by using the variational method. For the two-component state $|\Psi_{\nu=0}\rangle$, we will select the fully occupied components $|\alpha\rangle$ and $|\beta\rangle$ from a set of four orthonormal basis wavefunctions $\{|\chi_1\rangle, |\chi_2\rangle, |\chi_3\rangle, |\chi_4\rangle\}$ of the spin-valley Hilbert space. We restrict our analysis to the states which have no spin-valley entanglement. That means, we will consider spinors $|\chi_i\rangle (1 \leq i \leq 4)$ of the form $|\mathbf{t}, \mathbf{s}\rangle = |\mathbf{t}\rangle \otimes |\mathbf{s}\rangle$. Here $\mathbf{t}$ and $\mathbf{s}$ are the unit vectors representing the valley and the spin in the corresponding Bloch sphere. The sets of four orthonormal basis wavefunctions $\{|\chi_1\rangle, |\chi_2\rangle, |\chi_3\rangle, |\chi_4\rangle\}$ fall into two classes:

1. ***Valley-ordered states:*** The set of four spinors is partitioned into two subsets having opposite spins $\mathbf{s}$ and $-\mathbf{s}$. The two spinors in each subset (having the same spin) reside in opposite valleys. The valley polarization vectors $\mathbf{t}_1$ and $\mathbf{t}_2$ (corresponding to spins $\mathbf{s}$ and $-\mathbf{s}$, respectively) are independent of each other.

$$\begin{aligned} |\chi_1\rangle =& |\mathbf{t}_1, \mathbf{s}\rangle \quad & |\chi_2\rangle =& |-\mathbf{t}_1, \mathbf{s}\rangle \\ |\chi_3\rangle =& |\mathbf{t}_2, -\mathbf{s}\rangle & |\chi_4\rangle =& |-\mathbf{t}_2, -\mathbf{s}\rangle \end{aligned} \tag{3.79}$$

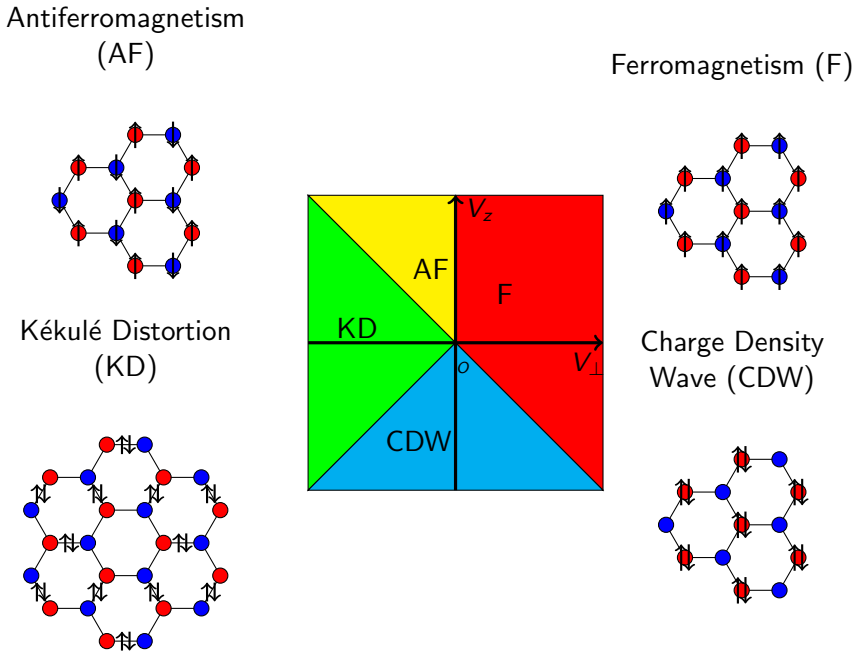

Figure 3.9: Phase diagram of graphene at charge neutrality point ($\nu = 0$) when $h = 0$ and $\Delta_{AB} = 0$. The symmetry-breaking orders are: ferromagnetism (F), antiferromagnetism (AF), Kékulé distortion (KD), and Charge density wave (CDW).

2. ***Spin-ordered states:*** The set of four spinors is partitioned into two subsets having opposite valleys $\mathbf{t}$ and $-\mathbf{t}$. The two spinors in each subset (residing in the same valley) have opposite spins. The spin polarization vectors $\mathbf{s}_1$ and $\mathbf{s}_2$ (corresponding to valleys $\mathbf{t}$ and $-\mathbf{t}$, respectively) are independent of each other.

$$\begin{aligned} |\chi_1\rangle &= |\mathbf{t}, \mathbf{s}_1\rangle & |\chi_2\rangle &= |\mathbf{t}, -\mathbf{s}_1\rangle \\ |\chi_3\rangle &= |-\mathbf{t}, \mathbf{s}_2\rangle & |\chi_4\rangle &= |-\mathbf{t}, -\mathbf{s}_2\rangle \end{aligned} \tag{3.80}$$

Not loosing the generality, we select the first fully occupied component $|\alpha\rangle = |\chi_1\rangle$. We have two possibilities to select the spinor for the second component $|\beta\rangle$: either $|\beta\rangle = |\chi_2\rangle$ or $|\beta\rangle = |\chi_3\rangle$. If $|\beta\rangle = |\chi_4\rangle$, by defining $\mathbf{t}'_2 = -\mathbf{t}_2$, we have $|\chi_4\rangle = |\mathbf{t}'_2, -\mathbf{s}\rangle$. It is in fact the same thing as if $|\beta\rangle = |\chi_3\rangle$. For each class of states, we have to consider two cases.

The plan of the section is as follows: First, we examine the case where $h = \Delta_{AB} = 0$ and search for the minimum of E_V. And then, we add the Zeeman energy E_Z into the total anisotropy energy.

3.7.1 . Phase diagram with no Zeeman and no valley-splitting energy

We begin by the case where $h = 0$ and $\Delta_{AB} = 0$. The total anisotropy energy is given by:

$$E_A = E_V = \sum_{a=x,y,z} V_a[\mathrm{Tr}(P_\alpha \tau^a)\mathrm{Tr}(P_\beta \tau^a) - \mathrm{Tr}(P_\alpha \tau^a P_\beta \tau^a)] \tag{3.81}$$

For the *valley-ordered states*, we have two cases:

- $|\alpha\rangle = |\chi_1\rangle$, $|\beta\rangle = |\chi_2\rangle$: We have the phase 1 with spinor composition $\{|\mathbf{t}, \mathbf{s}\rangle, |-\mathbf{t}, \mathbf{s}\rangle\}$. Phase 1 is stable on the whole $(V_\perp, V_z)$ plane and has as energy:

$$E_1 = -(2V_\perp + V_z) \tag{3.82}$$

- $|\alpha\rangle = |\chi_1\rangle$, $|\beta\rangle = |\chi_3\rangle$: We have phase 2 with spinor composition $\{|\mathbf{t}_1, \mathbf{s}\rangle, |\mathbf{t}_2, -\mathbf{s}\rangle\}$. Phase 2 is stable on the whole $(V_\perp, V_z)$ plane and has as energy:

$$E_2 = V_\perp(t_{1x}t_{2x} + t_{1y}t_{2y}) + V_z t_{1z}t_{2z} \tag{3.83}$$

The *spin-ordered states* involves two cases:

- $|\alpha\rangle = |\chi_1\rangle$, $|\beta\rangle = |\chi_2\rangle$: We have phase 3 with spinor composition $\{|\mathbf{t}, \mathbf{s}\rangle, |\mathbf{t}, -\mathbf{s}\rangle\}$. Phase 3 is stable on the whole $(V_\perp, V_z)$ plane and has as energy:

$$E_3 = V_\perp + (V_z - V_\perp)t_z^2 \tag{3.84}$$

- $|\alpha\rangle = |\chi_1\rangle$, $|\beta\rangle = |\chi_3\rangle$: We have the fourth formula of the energy with spinor composition $\{|\mathbf{t}, \mathbf{s}_1\rangle, |-\mathbf{t}, \mathbf{s}_2\rangle\}$. The energy of this phase is:

$$E_4 = -\left[V_\perp + \frac{1}{2}(1 + \mathbf{s}_1 \cdot \mathbf{s}_2)(V_\perp + V_z)\right] + \frac{1}{2}(1 - \mathbf{s}_1 \cdot \mathbf{s}_2)(V_\perp - V_z)t_z^2 \tag{3.85}$$

The phase diagram is shown in Fig.3.9. This phase diagram contains four phases:

1. The first phase is the **Ferromagnetic (F)** phase. The two occupied components are $|\mathbf{t}, \mathbf{s}\rangle$ and $|-\mathbf{t}, \mathbf{s}\rangle$. The energy of the ferromagnetic phase is given by:

$$E = -(2V_\perp + V_z) \tag{3.86}$$

   The two completely occupied components have the same spin but opposite valleys. Electrons locate in both sublattices. Electrons residing in opposite sublattices have the same spin. Because all electrons residing in all the lattice sites have the same spin, the phase is called Ferromagnetic.

2. The second phase is the **Antiferromagnetic (AF)** phase. The two fully occupied components are $|K, \mathbf{s}\rangle$ and $|K', -\mathbf{s}\rangle$. The energy of the antiferromagnetic phase is given by:

$$E = -V_z \tag{3.87}$$

   The two completely occupied components have opposite spins and opposite valleys. Electrons reside equally in the two sublattices. Electrons locating in the two sublattices have opposite spins. The situation is similar to an antiferromagnet.

3. The third phase is the **Kékulé Distortion (KD)** phase. The two fully occupied components are $|\mathbf{t}_\perp, \mathbf{s}\rangle$ and $|\mathbf{t}_\perp, -\mathbf{s}\rangle$. The energy of the Kékulé Distortion phase is given by:

$$E = V_\perp \tag{3.88}$$

Phase	Occupied components	Energy
F	$\{\|\mathbf{t},\mathbf{s}\rangle, \|-\mathbf{t},\mathbf{s}\rangle\}$	$-(2V_\perp + V_z)$
AF	$\{\|K,\mathbf{s}\rangle, \|K',-\mathbf{s}\rangle\}$	$-V_z$
KD	$\{\|\mathbf{t}_\perp,\mathbf{s}\rangle, \|\mathbf{t}_\perp,-\mathbf{s}\rangle\}$	$V_\perp$
CDW	$\{\|K,\mathbf{s}\rangle, \|K,-\mathbf{s}\rangle\}$	V_z

Table 3.1: Phases of graphene at charge neutrality $\nu = 0$, $h = \Delta_{AB} = 0$.

The valley part of the single-electron wavefunction is $\mathbf{t}_\perp$. That means each electron has an equal probability of occupying the two sublattices (valleys). The spin is, however, singlet. In this phase, the electron density distribution forms a periodic pattern, with a lattice parameter $\sqrt{3}$ times greater than the graphene lattice parameter. This allows to detect this phase by using Scanning Tunneling Microscopy (STM).

4. The last phase is **Charge Density Wave (CDW)**. The two fully occupied components are $|K,\mathbf{s}\rangle$ and $|K,-\mathbf{s}\rangle$. The energy of the Charge Density Wave phase is given by:

$$E = V_z \tag{3.89}$$

In this phase, the valley is polarized, whereas the spin is singlet. All the electrons are localized in the same sublattice.

All the phase transitions across phase boundaries are first order. We have reproduced the phase diagram that Kharitonov established by using the mean-field theory [31]. The results are summarized in Table. 3.1.

3.7.2 . Phase diagram with Zeeman energy

The total anisotropy energy in the presence of the Zeeman effect ($h \neq 0$) is:

$$\begin{aligned} E_A =& E_V + E_Z \\ =& \sum_{a=x,y,z} V_a[\mathsf{Tr}(P_\alpha\tau^a)\mathsf{Tr}(P_\beta\tau^a) - \mathsf{Tr}(P_\alpha\tau^a P_\beta\tau^a)] - h\mathsf{Tr}((P_\alpha + P_\beta)\sigma^z) \end{aligned} \tag{3.90}$$

For the *valley-ordered phases*, we consider two cases:

- $|\alpha\rangle = |\chi_1\rangle$, $|\beta\rangle = |\chi_2\rangle$. We have phase 1 with flavor composition $\{|\mathbf{t},\uparrow\rangle, |-\mathbf{t},\uparrow\rangle\}$. The energy of phase 1 is given by:

$$E_1 = -(2V_\perp + V_z) - 2h \tag{3.91}$$

- $|\alpha\rangle = |\chi_1\rangle$, $|\beta\rangle = |\chi_3\rangle$. We have phase 2 with flavor composition $\{|\mathbf{t}_1,\mathbf{s}\rangle, |\mathbf{t}_2,-\mathbf{s}\rangle\}$. The energy of this phase is given by:

$$E_2 = V_\perp(t_{1x}t_{2x} + t_{1y}t_{2y}) + V_z t_{1z}t_{2z} \tag{3.92}$$

For the *spin-ordered phases*, we consider two cases:

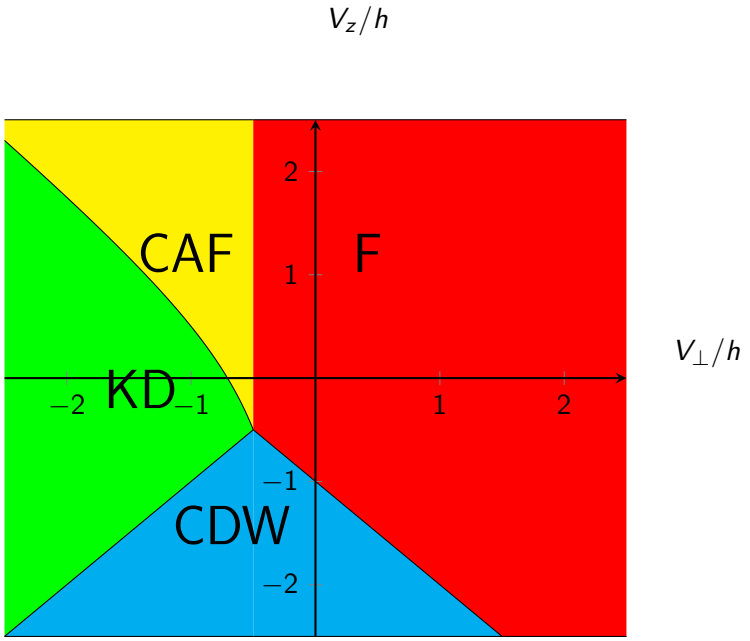

Figure 3.10: The phase diagram at charge neutrality $\nu = 0$ with Zeeman effect. The phase boundaries are shifted. There are also four phases: ferromagnetic (F), canted antiferromagnetic (CAF), Kékulé distortion (KD), and charge density wave (CDW). The colinear antiferromagnetic (AF) phase is replaced by the canted antiferromagnetic (CAF) phase.

- $|\alpha\rangle = |\chi_1\rangle$, $|\beta\rangle = |\chi_2\rangle$. The flavor composition of the phase is $\{|\mathbf{t}, \mathbf{s}\rangle, |\mathbf{t}, -\mathbf{s}\rangle\}$. The energy of the phase is given by:

$$E_3 = V_\perp + (V_z - V_\perp)t_z^2 \tag{3.93}$$

- $|\alpha\rangle = |\chi_1\rangle$, $|\beta\rangle = |\chi_3\rangle$. The flavor composition of the phase is $\{|\mathbf{t}, \mathbf{s}_1\rangle, |-\mathbf{t}, \mathbf{s}_2\rangle\}$. The energy of the phase is given by:

$$\begin{aligned} E_4 = &- \left[V_\perp + \frac{1}{2}(1 + \mathbf{s}_1 \cdot \mathbf{s}_2)(V_\perp + V_z)\right] + \frac{1}{2}(1 - \mathbf{s}_1 \cdot \mathbf{s}_2)(V_\perp - V_z)t_z^2 \\ &- h(s_{1z} + s_{2z}) \end{aligned} \tag{3.94}$$

The phase diagram at charge neutrality consists of 4 phases and is shown in Fig. 3.10 and summarized in Table. 3.2:

1. The Zeeman effect shifts the phase boundaries. The lines separating the phases meet at the point $(V_\perp, V_z) = \left(-\frac{h}{2}, -\frac{h}{2}\right)$ instead of the point $(V_\perp, V_z) = (0, 0)$.

2. The first phase is the **Ferromagnetic (F)** phase. The flavor content of the ferromagnetic phase is $\{|\mathbf{t}, \uparrow\rangle, |-\mathbf{t}, \uparrow\rangle\}$. The energy of the phase is given by:

$$E = -(2V_\perp + V_z) - 2h \tag{3.95}$$

   Because of the Zeeman effect, the spin of electrons in both sublattices are polarized to spin-up, and is no longer an arbitrary vector $\mathbf{s}$ as in the case where $h = 0$.

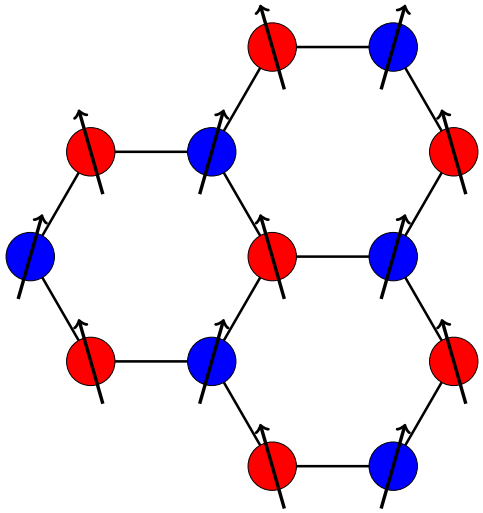

Figure 3.11: Spin polarization of electrons residing in different sublattices in the phase CAF. The spin are canted away from the spin-up direction.

3. The **Antiferromagnetic (AF)** phase is replaced by the **Canted Antiferromagnetic (CAF)** phase. The flavour content is $\{|K, \mathbf{s}_1\rangle, |K', \mathbf{s}_2\rangle\}$. The energy of the phase is given by:

$$E = -V_z + \frac{h^2}{2V_\perp} \tag{3.96}$$

The two sublattices A and B have different spin polarizations (Fig. 3.11). The vectors $\mathbf{s}_1$ (sublattice B) and $\mathbf{s}_2$ (sublattice A) are no longer spin-up and spin-down. They are canted away from the spin-up direction. Their projections on the direction of the magnetic field are equal $s_{1z} = s_{2z}$, while the projections on the plane perpendicular to the magnetic field are antiparallel. The component along the direction of the magnetic field is:

$$s_{1z} = s_{2z} = -\frac{h}{2V_\perp} \tag{3.97}$$

The unit vectors representing spin $\mathbf{s}_1$ and $\mathbf{s}_2$ in the Bloch sphere are shown in Fig. 3.12.

4. The transition between the Ferromagnetic phase and the Canted Antiferromagnetic phase is not first order, but continuous, contrary to the case where $h = 0$. The spin in both sublattices is spin-up at the boundary of the two phases. As the absolute value of $V_\perp$ increases, they are canted away from the initial direction. The value of $s_{1z} = s_{2z}$ decreases down to 0 with increasing $|V_\perp|$ (Fig. 3.13). For large values of $|V_\perp|$ the phase tends to the (Colinear) AF phase (in the case $h = 0$). In this Colinear AF phase, the spin polarizations in both sublattices are perpendicular to the magnetic field $\mathbf{B}$ but are antiparallel.

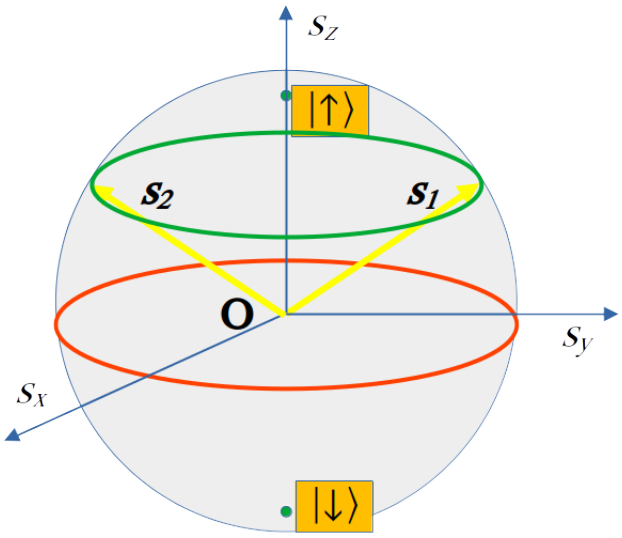

Figure 3.12: The vectors $\mathbf{s}_1$ and $\mathbf{s}_2$ representing the spin polarization in the two sublattices in the Bloch sphere (CAF phase). They have the same projection in the s_z direction, but opposite projections in the (s_x, s_y) plane.

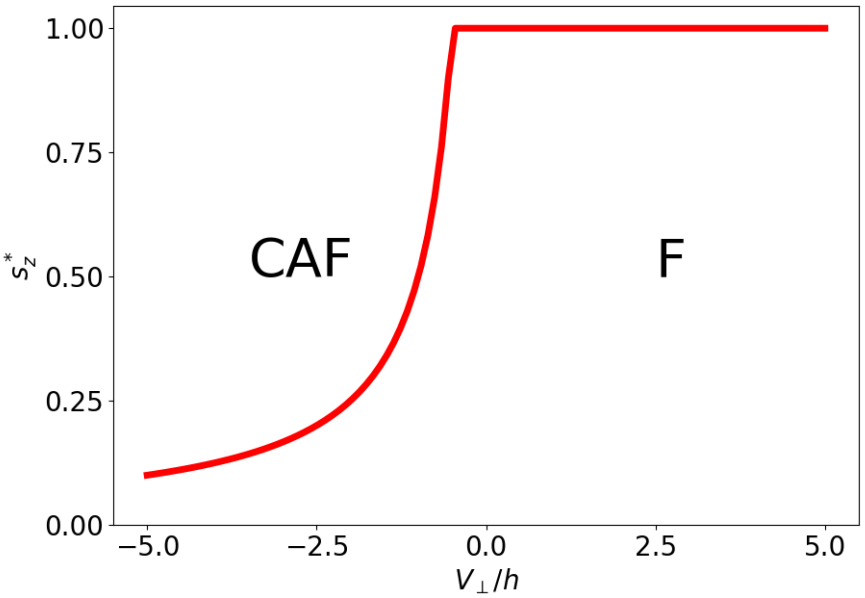

Figure 3.13: The value of the projection s_z^* of the canted spin on the s_z direction (Phase CAF).

Phase	Occupied components	Energy
F	$\{\|\mathbf{t},\uparrow\rangle, \|-\mathbf{t},\uparrow\rangle\}$	$-(2V_\perp + V_z) - 2h$
CAF	$\{\|K,\mathbf{s}_1\rangle, \|K',\mathbf{s}_2\rangle\}$	$-V_z + \frac{h^2}{2V_\perp}$
KD	$\{\|\mathbf{t}_\perp,\mathbf{s}\rangle, \|\mathbf{t}_\perp,-\mathbf{s}\rangle\}$	$V_\perp$
CDW	$\{\|K,\mathbf{s}\rangle, \|K,-\mathbf{s}\rangle\}$	V_z

Table 3.2: Phases of graphene at charge neutrality $\nu = 0$, $h \neq 0$, $\Delta_{AB} = 0$.

5. The third phase is **Kékulé Distortion (KD)**. Its flavor composition is $\{|\mathbf{t}_\perp,\mathbf{s}\rangle, |\mathbf{t}_\perp,-\mathbf{s}\rangle\}$. The energy of the phase is given by:

$$E = V_\perp \tag{3.98}$$

   The phase retains the characteristics it has in the case where $h = 0$.

6. The boundary between the CAF phase and the KD phase is no longer a straight line as the boundary between the AF phase and the KD phase when $h = 0$. It is a hyperbola starting from the point $(V_\perp, V_z) = \left(-\frac{h}{2}, -\frac{h}{2}\right)$ and approaches the SO(5) symmetry line $V_\perp + V_z = 0$ for large values of $|V_\perp|$. Its equation is:

$$V_z = -V_\perp + \frac{h^2}{2V_\perp} \tag{3.99}$$

7. The last phase is the **Charge Density Wave (CDW)** phase. Its flavor composition is $\{|K,\mathbf{s}\rangle, |K,-\mathbf{s}\rangle\}$. The energy of the CDW phase is given by:

$$E = V_z \tag{3.100}$$

   Similarly to the KD phase, the CDW phase retains the characteristics it has in the case where $h = 0$.

8. The boundary between the KD phase and the CDW phase keeps its position, but it starts from the point $(V_\perp, V_z) = \left(-\frac{h}{2}, -\frac{h}{2}\right)$ instead of the point $V_\perp = V_z = 0$.

9. The phase transitions CAF-KD, KD-CDW, and CDW-F are first order. Only the phase transition F-CAF is second order.

3.8 . Experimental observations

In 2012, Young et al. performed tilted field experiment on graphene on hBN substrate [73]. This early experiment showed that the ground state at $\nu = 0$ is spin-unpolarized (AF, CAF, KD, or CDW phases), rather than the spin-polarized F phase. Nevertheless, they suggested that the spin-polarized F phase could still exist under high tilt angle under (total) magnetic field $B_T < 45$T. In 2014, they measured the edge state conductance and observed the transition between the gapped edge states of the CAF phase and the gapless edge states of the quantum spin Hall phase, which is identified as to be the spin-polarized F phase (Fig. 3.14) [74]. As expected, the F phase appeared only under

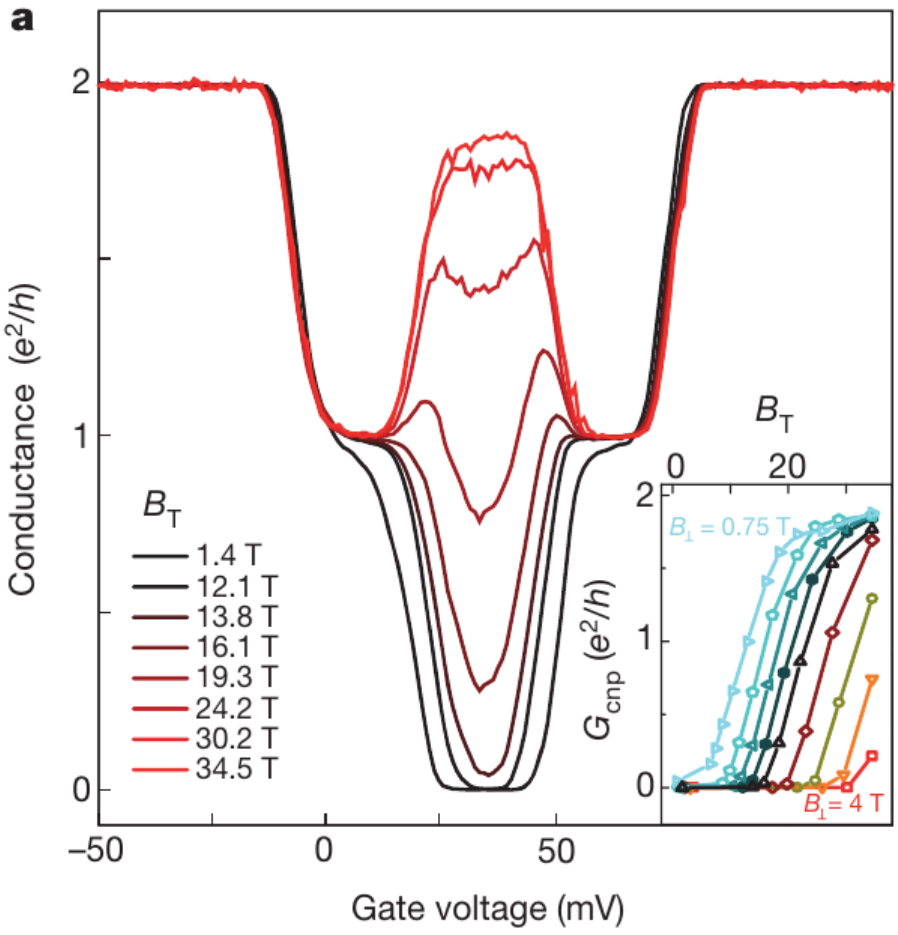

Figure 3.14: The phase transition from the CAF phase to the F phase in monolayer graphene at $\nu = 0$ observed in the tilted field experiment. The main figure shows the results with fixed perpendicular magnetic field $B_\perp$ =1.4 T and varying total magnetic field strength from B_T = 1.4 T to B_T =34.5 T. As the total magnetic field B_T increases, the Hall conductance increases from 0 to $1.8e^2/h$. This corresponds to a continuous phase transition from the insulating CAF phase to the conducting quantum spin Hall state, which is identified as the F phase. The inset shows the conductance at CNP with respect to B_T for different values of $B_\perp$ = 0.75, 1.0, 1.4, 1.6, 2.0, 3.0 and 4.0 T. The figure is taken from Ref. [74]. *Reproduced with permission from Springer Nature.*

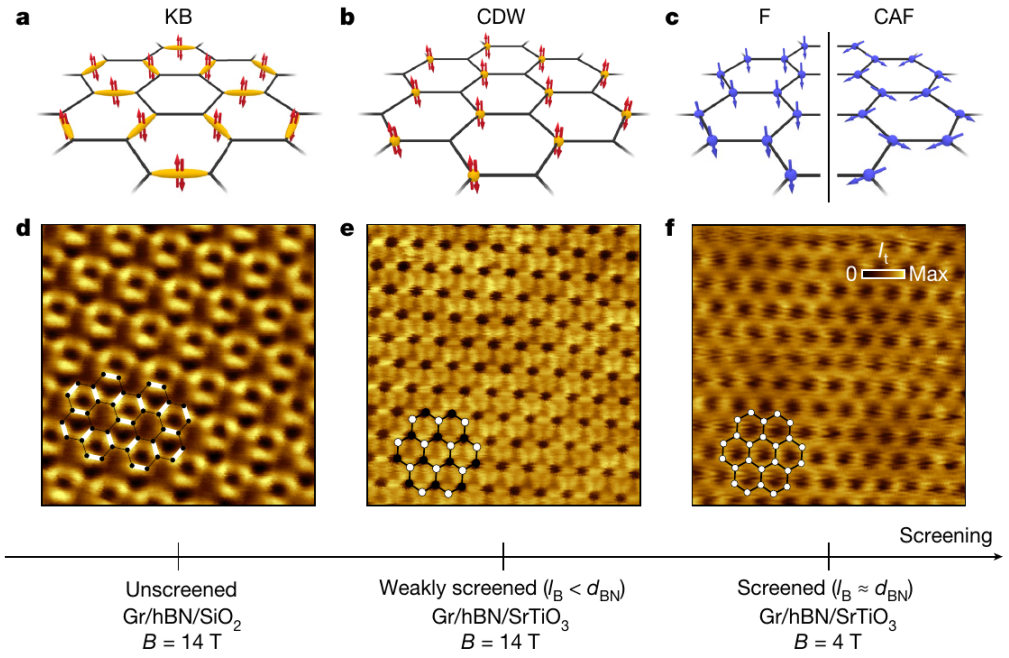

Figure 3.15: The Scanning tuneling spectroscopy images of the phases Kékulé distortion (d), Charge density wave (e), and Ferromagnetic/Canted antiferromagnetic (f). Each image includes the corresponding lattice drawing of the phase. The arrow below the figures d, e, f indicates the strength of the substrate screening. The figures a, b, c show the spin distribution of the four phases, predicted by the theory. The figure is taken from Ref. [77]. *Reproduced with permission from Springer Nature.*

extremely tilted magnetic field. When the tilting angle decreases, the quantum spin Hall state (F phase) continuously transits to CAF and becomes finally AF phase (when $\mathbf{B}$ is perpendicular to the graphene plane).

Since the end of the 2010s decade, scanning tuneling spectroscopy (STS) gives a clearer picture of the symmetry-broken phases in graphene. This type of experiments is advantageous because it visualizes the atomic scale distribution of electron density. Therefore, these experiments allow to determine the sublattice, *i.e.* valley, that electrons occupy in the ZLL. One can easily distinguish the valley-polarized CDW phase from the valley-unpolarized phases (F/AF-CAF) and the KD phase in the STS images. Although, this technique does not permit to distinguish between the valley-unpolarized phases: F, AF, and CAF.

In 2019, by using the STS technique, Li et al. observed an electron density pattern whose unit cell area is three time larger than the one of graphene [75]. This characteristic confirmed the existence of the KD phase. The KD phase was also observed in the recent experiment by Liu et al. [76]. This work was done in 2021 and published in 2022. Simultaneously, Coissard et al. successfully observed not only the KD phase, but also the CDW phase and a valley-unpolarized phase, which is either the F phase or the AF-CAF phase (Fig. 3.15) [77]. Hence, all the phases in the diagram of Kharitonov [31] are experimentally confirmed. However, the work by Coissard et al. observed the coexistence of the KD phase with a new phase that they call K-CDW. The new K-CDW phase has a lattice parameter $\sqrt{3}$ times larger than the graphene lattice parameter, whereas the familiar CDW phase has the same lattice parameter as the graphene honeycomb lattice.

This new discovery requires new theoretical works beyond the present theory to explain this new phase.

3.9 . Summary of the chapter

This chapter reviews the phase diagram of the quantum Hall effect in graphene at charge neutrality $\nu = 0$. The phase diagram contains four phases: (1) the spin-polarized and valley unpolarized Ferromagnetic (F) phase; (2) the spin and valley singlet Antiferromagnetic (AF) phase, which becomes canted (CAF) under a strong Zeeman field; (3) the Kékulé distortion (KD) phase, which is spin-singlet and has a valley polarized along the equator of the Bloch sphere; and (4) the Charge density wave (CDW) phase, which is spin-singlet and valley-polarized. All phase transitions are first-order, except the phase transition between the CAF and the F phases under a nonvanishing Zeeman field. We also review an analytical variational method, which serves as deriving this phase diagram. In the next chapter, we will develop the variational method for the fractional quantum Hall effect and calculate the phase diagram of some two- and three-component fractional quantum Hall states.

Chapter4 - Spin and valley ordering of monolayer graphene in some fractional quantum Hall states: Variational method

4.1 . Introduction to the chapter

In the last chapter, we introduced the phase diagram of monolayer graphene at the charge neutrality point, that means under the quantum Hall regime of filling factor $\nu = 0$. In this chapter, we move on to the phase diagrams of filling factors $n/3(n = 1, 2, 4, 5)$. Ref. [33] proposed an extension of the Hartree-Fock theory to solve the problem in the case of the fractional quantum Hall effect. Here we propose a set of variational wavefunctions for two- and three-component states and systematically derive the formula of the short-range valley interaction of those variational wavefunctions. We found that in the general case, the short-range valley interaction energy contains contributions that do not appear in the formula of Ref. [33]. Then, we establish the phase diagrams of the cases $(1, \nu)$ $(0 < \nu < 1)$ and $(1, \nu, \nu)$ $(0 < \nu < 1)$ [1] by using this variational method. The prediction of this variational method will be checked by the numerical exact diagonalizations in Chapter 5.

4.2 . Experiments on fractional quantum Hall effect in graphene

We begin our discussions with the experiments which motivate our research. After the discovery of the fractional quantum Hall effect in graphene [20, 21], the 2010 decade witnessed the observations of various fractional quantum Hall states. The use of hBN substrate allows us to fabricate high-quality samples and permits to observe various states with filling factor of denominator 3 in both the central Landau level and the second Landau level [96] (see Fig. 4.1). The Jain sequence with denominator up to 9 was also observed near $\nu = 1/2$ for $0 < \nu < 1$ [93]. In the work of Feldman et al. [93], only even numerator fractions were observed for $1 < \nu < 2$. The lack of odd numerators shows that composite fermions in those states have degeneracy 2. They proposed one possible explanation: the spin degree of freedom is lifted by the Zeeman energy, while the valley degree of freedom remains intact. At odd-numerator filling factors, the large valley skyrmions form at a minimal energy cost, so there is no incompressible states at odd-denominator filling factors. That means the $SU(2)_s$ symmetry is broken while the $SU(2)_v$ symmetry is preserved. Fractional quantum Hall states were observed in not only the ZLL, but also for Landau levels $N = 1$ and $N = 2$ [102]. Especially, the filling fractions $\nu = \pm 1/4$ and $\nu = \pm 1/2$ were observed in a narrow range of magnetic field B by Zibrov et al. in 2018 [97].

The inverse compressibility [94] and penetration field capacitance [97] measurements revealed transitions between quantum Hall states with different spin and valley polarizations. Fig. 4.2 shows the experiment by Feldman et al. [94]. The figure shows that when one keeps the same filling factor and varies the magnetic field, the incompressible

[1] The meaning of the symbols $(1, \nu)$ and $(1, \nu, \nu)$ will be explained in section 4.3.

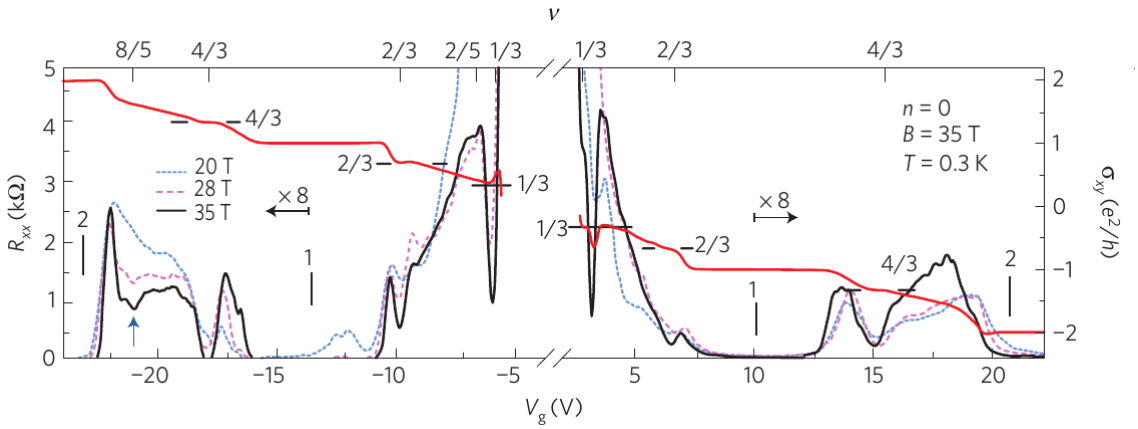

Figure 4.1: Incompressible states detected in the experiments by Dean et al. [96]. Figure taken from Ref. [96]. *Reproduced with permission from Springer Nature.*

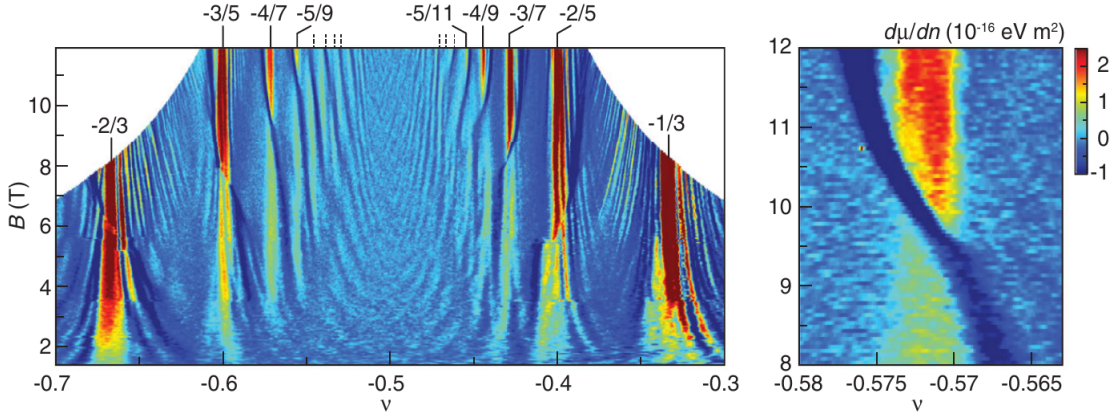

Figure 4.2: Inverse compressibility diagram measured by Feldman et al. [94] in the filling factor range $-0.7 < \nu < -0.3$ (left) and $-0.58 < \nu < -0.56$ (right). They observed that the incompressible peaks were interrupted in narrow range of magnetic field B. The right figure shows the peak discontinuity for filling factor $\nu = -4/7$ at $B = 10$T. Reprinted figure with permission from Benjamin E. Feldman, Andrei J. Levin, Benjamin Krauss, Dmitry A. Abanin, Bertrand I. Halperin, Jurgen H. Smet, and Amir Yacoby, Phys. Rev. Lett., 111, 076802 (2013) [94]. Copyright (2023) by the American Physical Society.

state disappears in a narrow range of the magnetic field, resulting in discontinuities in the incompressible peaks. One recalls that in the case of the two-component quantum Hall effect, strengthening the magnetic field results in a spin transition from the singlet state to the polarized state. Therefore, those interruptions in the incompressible peaks can be associated to the transitions between the different symmetry-broken orders with different spin and valley quantum numbers.

All these discoveries motivate the study of the broken-symmetry phases of the fractional quantum Hall effect in graphene in this chapter. Similar to the case of charge neutrality $\nu = 0$, in the case of the fractional quantum Hall effect, spin and valley anisotropies break the SU(4) symmetry of the Coulomb interaction, resulting in different phases with different spin and valley ordering. We focus on the quantum Hall states of filling factors $n/3(n = 1, 2, 4, 5)$ and discuss the competition between the symmetry-breaking orders. We will finally examine the transition between states having the same total filling factor

but with different flavor occupation numbers - that means the transition exhibited by the incompressible peak interruptions in Refs. [94] and [97]. This content will be presented in the present chapter and the chapter 5.

4.3 . SU(4) representations

In this section, we discuss the way of using the irreducible representations of the SU(4) group to characterize the eigenstates of the electron system in graphene. There are six independent SU(2) subgroups of the group SU(4), three among them are convenient to describe the eigenstates of an arbitrary SU(4)-symmetric Hamiltonian: the pure spin subgroups generated by $S^\alpha = \sigma^\alpha \otimes 1 (\alpha = x, y, z)$, the pure pseudospin subgroups generated by $T^\alpha = 1 \otimes \tau^\alpha$, and the subgroups generated by the operators $N^\alpha = \sigma^\alpha \otimes \tau^z$ inspired by the Néel antiferromagnetic order. Because all SU(4)-symmetric Hamiltonians commute with T^z, S^z and N^z, the quantum numbers (T^z, S^z, N^z) are good quantum numbers to characterize the eigenstates of such Hamiltonians.

The energy levels of those SU(4)-symmetric Hamiltonians form irreducible representations. Each of these irreducible representations has a one-to-one correspondence to one Young tableau [103]. The Young tableaux characterizing the SU(4) energy levels consist three rows: the first row contains L_1 boxes, the second row contains L_2 boxes, and the third row contains L_3 boxes with $L_1 \geq L_2 \geq L_3$. We define the integers $p_1 = L_1 - L_2, p_2 = L_2 - L_3, p_3 = L_3$. The dimension of such irreducible representation is given by:

$$\mathcal{D}(p_1, p_2, p_3) = \frac{1}{12}(p_1+1)(p_2+1)(p_3+1)(p_1+p_2+2)(p_2+p_3+2)(p_1+p_2+p_3+3) \quad (4.1)$$

One can identify each irreducible representation by its highest weight. We recall the case of the SU(2) group describing the spin. If one finds an energy eigenvalue belonging to a sector of quantum number $S^z = M$, one cannot conclude that the total spin is M. One needs to search for this energy eigenvalue in the sectors $S^z = M + 1$, $S^z = M + 2$ and so on, up to the value of S^z where the energy level disappears. This value is the highest weight and gives us the *total spin*. We generalize this reasoning for the SU(4) case. For a value of the highest weight $(T^z, S^z, N^z) = (m_1, m_2, m_3)$ the corresponding SU(4) irreducible representation is characterized by integers $p_1 = m_2 - m_3$, $p_2 = m_1 - m_2$ and $p_3 = m_2 + m_3$. Then we deduce the corresponding values L_1, L_2, L_3 of the length of the rows of its Young tableau.

The Coulomb Hamiltonian $\mathcal{H}_C$ has the SU(4) symmetry. It preserves the number n_i of the electrons occupying the component i having definite spin and valley. Therefore, we impose the set of occupation numbers (n_1, n_2, n_3, n_4) and perform exact diagonalizations. The energy eigenstates have definite quantum numbers (T^z, S^z, N^z) and form irreducible representations. One can find the highest weights and establish the Young tableaux of those irreducible representations by using the procedure described in the previous paragraph.

The state of occupation numbers (n_1, n_2, n_3, n_4) can also be characterized by the set of filling factors $(\nu_1, \nu_2, \nu_3, \nu_4)$ ($\nu_i = n_i/N_e, 1 \leq i \leq 4$). The total filling factor of the state is $\tilde{\nu} = \nu_1 + \nu_2 + \nu_3 + \nu_4$. For example, for total filling factor $\tilde{\nu} = 5/3$, the symbol $(1, 2/3, 0, 0)$ denotes an SU(4) eigenstate with one fully-filled component and the second component has filling factor $\nu_2 = 2/3$, while the symbol $(1, 1/3, 1/3, 0)$ denotes

an SU(4) eigenstate with one fully filled component and two components of filling factors $\nu_2 = \nu_3 = 1/3$. The other components are completely empty. To avoid double counting of the states, we denote the filling factors in decreasing order $1 \geq \nu_1 \geq \nu_2 \geq \nu_3 \geq \nu_4 \geq 0$. And then, to simplify the notation, we write explicitely only the filling factors of non-empty components. For instance, we write the flavor composition of the state as $(1, 2/3)$ instead of $(1, 2/3, 0, 0)$.

In the presence of anisotropies (encoded in $\mathcal{H}_V$, $\mathcal{H}_Z$, $\mathcal{H}_{AB}$), anisotropies perturbatively lift the energy eigenvalues of the eigenstates belonging to one irreducible representation. This is valid as long as the anisotropies are small compared to the Coulomb energy scale. This point of view is supported by current experiments. All the symmetry considerations are valid in all geometries, including the spherical and the torus geometry. Because the ground state is uniform in space, in the spherical geometry it has quantum number $L = 0$ while in the torus geometry, its magnetic many-body translations have zero many-body momentum $K_x = K_y = 0$. In this work, we consider the effect of the short-range valley-dependent anisotropies $\mathcal{H}_V$. This Hamiltonian admits the conservation of the quantum numbers T^z, S^z and the total spin quantum number S. For practical reasons, in chapter 5 we will perform exact diagonalizations on sectors with definite (T^z, S^z) quantum numbers, that means we implement only the conservation of T^z and S^z.

4.4 . Model wavefunctions

Now, we discuss the trial wavefunctions describing the four-component fractional quantum Hall effects with spin and valley degrees of freedom in graphene. The SU(4)-symmetric Coulomb interaction Hamiltonian is written in the second quantization language as follows:

$$\mathcal{H}_C = \frac{1}{2} \sum_{\substack{p_1 p_2 p_3 p_4 \\ \mu\nu}} V_{p_1 p_2 p_3 p_4} c^\dagger_{p_1 \mu} c^\dagger_{p_2 \nu} c_{p_3 \nu} c_{p_4 \mu} \tag{4.2}$$

where the indices μ, ν run over the four flavors.

We remark that any SU(2) eigenstate is also a SU(4) eigenstate, only the degeneracy changes. Indeed, we consider a SU(2) Coulomb eigenstate $|\Psi_{\alpha\beta}\rangle = \hat{\psi}^\dagger_{\alpha\beta}|0\rangle$ occupying two components $|\alpha\rangle$ and $|\beta\rangle$. The ket vectors $|\alpha\rangle$ and $|\beta\rangle$ form an orthonormal basis of the Hilbert space of the spin degree of freedom, for example $|\alpha\rangle = |\uparrow\rangle$ (spin-up) and $|\beta\rangle = |\downarrow\rangle$(spin-down). Let $\mathcal{H}'_C$ be the SU(2)-symmetric Coulomb interaction Hamiltonian, the formula of $\mathcal{H}'_C$ is also given by Eq. (4.2), but the indices μ and ν run on the set of two elements $\{\alpha, \beta\}$. Because $\hat{\psi}^\dagger_{\alpha\beta}|0\rangle$ is an eigenstate of $\mathcal{H}'_C$, let $E_{\alpha\beta}$ be its energy eigenvalue, we have:

$$\mathcal{H}'_C \hat{\psi}^\dagger_{\alpha\beta}|0\rangle = E_{\alpha\beta} \hat{\psi}^\dagger_{\alpha\beta}|0\rangle \tag{4.3}$$

We do an extension from the two-dimensional Hilbert space of the spin degree of freedom to the four-dimensional Hilbert space that is the tensor product between the latter and the Hilbert space of the valley degree of freedom. We assume that the spins $|\alpha\rangle$ and $|\beta\rangle$ lie in the valley K, and still denote the generalized spinors in the four-dimensional Hilbert space as $|\alpha\rangle$ and $|\beta\rangle$ (here $|\alpha\rangle = |K\rangle_v \otimes |\alpha\rangle_s$ and $|\beta\rangle = |K\rangle_v \otimes |\beta\rangle_s$, the symbols

s and v means spin and valley, respectively)[2]. The Gram-Schmidt process allows us to choose two ket-vectors $|\gamma\rangle$ and $|\delta\rangle$ to form an orthonormal basis $\{|\alpha\rangle, |\beta\rangle, |\gamma\rangle, |\delta\rangle\}$ of the 4-dimensional spin-valley Hilbert space.

Now, we apply the SU(4)-symmetric Hamiltonian $\mathcal{H}_C$ on $\hat{\psi}^\dagger_{\alpha\beta}|0\rangle$. In this case, the indices μ and ν run over the set of four indices $\{\alpha, \beta, \gamma, \delta\}$. All the terms containing $c^\dagger_{p_1\mu}c^\dagger_{p_2\nu}c_{p_3\nu}c_{p_4\mu}$ vanish unless $(\mu, \nu) \in \{(\alpha,\alpha), (\alpha,\beta), (\beta,\alpha), (\beta,\beta)\}$. Consequently, we have:

$$\mathcal{H}_C\hat{\psi}^\dagger_{\alpha\beta}|0\rangle = \mathcal{H}'_C\hat{\psi}^\dagger_{\alpha\beta}|0\rangle = E_{\alpha\beta}\hat{\psi}^\dagger_{\alpha\beta}|0\rangle \tag{4.4}$$

That means the SU(2) eigenstate $\hat{\psi}^\dagger_{\alpha\beta}|0\rangle$ is also an eigenstate of the SU(4) Coulomb interaction. The degeneracy of the eigenstate changes because we have one more degree of freedom when changing from the SU(2) case to the SU(4) case.

In the SU(4) case, we assume that the two-component state $\hat{\psi}^\dagger_{\alpha\beta}|0\rangle$ has total filling factor $\nu_{\alpha\beta}$. By gluing this state to a completely filled shell of flavor $|\gamma\rangle$, we obtain a three-component state:

$$|\Psi_{\alpha\beta\gamma}\rangle = \left(\prod_{m=1}^{N_\phi} c^\dagger_{m\gamma}\right)\hat{\psi}^\dagger_{\alpha\beta}|0\rangle \tag{4.5}$$

which is an exact eigenstate of the Coulomb interaction Hamiltonian $\mathcal{H}_C$. Indeed, we denote $\mathcal{H}_{\mu\nu} = \frac{1}{2}\sum_{p_1p_2p_3p_4} V_{p_1p_2p_3p_4}c^\dagger_{p_1\mu}c^\dagger_{p_2\nu}c_{p_3\nu}c_{p_4\mu}$, so that $\mathcal{H}_C = \sum_{\mu\nu}\mathcal{H}_{\mu\nu}$. We apply $\mathcal{H}_C$ on $|\Psi_{\alpha\beta\gamma}\rangle$. The terms giving contribution to the eigenvalue energy E_C are those such that $(\mu,\nu) \in \{(\alpha,\alpha), (\alpha,\beta), (\alpha,\gamma), (\beta,\alpha), (\beta,\beta), (\beta,\gamma), (\gamma,\alpha), (\gamma,\beta), (\gamma,\gamma)\}$.

The sum of the contributions in which μ, ν run over α, β gives the eigenvalue energy $E_{\alpha\beta}$ of the two-component state $\hat{\psi}^\dagger_{\alpha\beta}|0\rangle$:

$$\sum_{\mu,\nu\in\{\alpha,\beta\}} \mathcal{H}_{\mu\nu}|\Psi_{\alpha\beta\gamma}\rangle = E_{\alpha\beta}|\Psi_{\alpha\beta\gamma}\rangle \tag{4.6}$$

The contribution in which $\mu = \nu = \gamma$ gives the energy of the completely filled shell $|\gamma\rangle$:

$$\mathcal{H}_{\gamma\gamma}|\Psi_{\alpha\beta\gamma}\rangle = \left(\mathcal{H}_{\gamma\gamma}\prod_{m=1}^{N_\phi} c^\dagger_{m\gamma}\right)\hat{\psi}^\dagger_{\alpha\beta}|0\rangle = E_1|\Psi_{\alpha\beta\gamma}\rangle \tag{4.7}$$

where $E_1 = -\sqrt{\pi/8}e^2/(\varepsilon l)$ as shown in (3.60). The remaining four contributions $(\alpha,\gamma), (\gamma,\alpha), (\beta,\gamma), (\gamma,\beta)$ contribute to the direct energy, so are cancelled by the background energy. We explicitely prove the case where $\mu = \alpha, \nu = \gamma$ as follows:

$$\mathcal{H}_{\alpha\gamma}|\Psi_{\alpha\beta\gamma}\rangle = \frac{1}{2}\sum_{p_1p_2p_3p_4} V_{p_1p_2p_3p_4}c^\dagger_{p_1\alpha}c^\dagger_{p_2\gamma}c_{p_3\gamma}c_{p_4\alpha}|\Psi_{\alpha\beta\gamma}\rangle \tag{4.8}$$

Because $c_{p_4\alpha}$ anticommutes with both $c^\dagger_{p_2\gamma}$ and $c_{p_3\gamma}$, we transform the previous equation into the form:

$$\mathcal{H}_{\alpha\gamma}|\Psi_{\alpha\beta\gamma}\rangle = \frac{1}{2}\sum_{p_1p_2p_3p_4} V_{p_1p_2p_3p_4}c^\dagger_{p_1\alpha}c_{p_4\alpha}c^\dagger_{p_2\gamma}c_{p_3\gamma}\left(\prod_{m=1}^{N_\phi} c^\dagger_{m\gamma}\right)\hat{\psi}^\dagger_{\alpha\beta}|0\rangle \tag{4.9}$$

[2]We can also associate the spin $|\alpha\rangle_s$ to valley K and spin $|\beta\rangle_s$ to valley K', or in general to any valley vector $|\mathbf{t}\rangle$.

The terms vanish unless $p_2 = p_3$ so that $c^\dagger_{p_2\gamma} c_{p_3\gamma}$ becomes the number operator, acting on the fully occupied shell, giving 1. Because the Coulomb interaction conserves the momentum: $p_1 + p_2 = p_3 + p_4$, leading to $p_1 = p_4$. It shows that the final results only contains terms of the form $V_{p_1p_2p_3p_4}|\Psi_{\alpha\beta\gamma}\rangle$ where $p_1 = p_4$ and $p_2 = p_3$. In other words, $|\Psi_{\alpha\beta\gamma}\rangle$ is also an eigenstate of $\mathcal{H}_{\alpha\gamma}$. The eigenvalue energy contains the terms of the form $V_{p_1p_2p_2p_1}$ and is therefore a part of the direct energy. We have similar results for the three remaining terms. Those contributions to the direct energy are cancelled by the neutralizing background. Overall, $|\Psi_{\alpha\beta\gamma}\rangle$ is an eigenstate of $\mathcal{H}_C$:

$$\mathcal{H}_C|\Psi_{\alpha\beta\gamma}\rangle = (E_1 + E_{\alpha\beta})|\Psi_{\alpha\beta\gamma}\rangle \tag{4.10}$$

The Coulomb energy of the state (4.5) is given by:

$$E_C = E_1 + E_{\alpha\beta} \tag{4.11}$$

If either α or β is an empty component, we have a state consisting of one full shell glued to one partially filled component:

$$|\Psi_{\alpha\gamma}\rangle = \left(\prod_{m=1}^{N_\phi} c^\dagger_{m\gamma}\right) \hat{\psi}^\dagger_\alpha|0\rangle \tag{4.12}$$

where E_α is the energy of the partially filled eigenstate $\psi^\dagger_\alpha|0\rangle$ of the Coulomb Hamiltonian $\mathcal{H}_C$ with filling factor $\nu_\alpha (0 < \nu_\alpha < 1)$. The Coulomb energy of this state is given by the formula:

$$E_C = E_1 + E_\alpha \tag{4.13}$$

This gluing argument also works when we glue a three partially filled component state $\hat{\psi}^\dagger_{\alpha\beta\gamma}|0\rangle$ to a completely filled shell $|\delta\rangle$. Similarly, from a two-component state $|\psi_{\alpha\beta}\rangle$ with total filling factor $0 < \tilde{\nu} < 1$, we can form a particle-hole transformation and obtain a two-component state with total filling factor $2 - \tilde{\nu}$. This transformed state has as energy:

$$E_{2-\tilde{\nu}} = E_{\alpha\beta} + 2(1 - \tilde{\nu})E_1 \tag{4.14}$$

SU(4) eigenstates having the same total filling factor but with different flavor partitions can be either the two-component states $|\psi_{\alpha\beta}\rangle$, $|\Psi_{\alpha\gamma}\rangle$, or the three-component state $|\Psi_{\alpha\beta\gamma}\rangle$. They belong to different irreducible representations. We call the states $|\psi_{\alpha\beta}\rangle$ and $|\psi_\alpha\rangle$ (which contain one or two partially filled components) the *parent states*. The formulae (4.11) and (4.13) allow us to find the ground state among a set of competing parent states having the same total filling factor. In the presence of anisotropies ($\mathcal{H}_V$, $\mathcal{H}_Z$ and $\mathcal{H}_{AB}$), the latter are small compared to the Coulomb interaction so that they do not destroy the electron correlation in the trial state (4.5). Therefore, we consider the contributions $\mathcal{H}_V$, $\mathcal{H}_Z$ and $\mathcal{H}_{AB}$ as small perturbations to the SU(4) Coulomb Hamiltonian $\mathcal{H}_C$ by assuming that the ground state wavefunction keeps the form of the trial wavefunctions (4.5) or (4.12). Anisotropies select the vectors $|\alpha\rangle$, $|\beta\rangle$ and $|\gamma\rangle$ so as to minimize the total anisotropy energy. Minimizing the total anisotropy energy allows us to determine the symmetry-broken phases issued from one parent state, as we did in Chapter 3.

4.5 . Variational method

4.5.1 . State $(1, \nu)$

Trial wavefunction

We examine the two-component state with one fully occupied component $|\alpha\rangle$ and one partially occupied component $|\beta\rangle$. The component $|\beta\rangle$ is occupied by N_1 electrons such that its filling factor is $\nu = N_1/N_\phi$. We choose the following trial wavefunction:

$$|\Psi\rangle = \sum_{\{m_i\}} F_{\{m_i\}} c^\dagger_{m_1\beta} \dots c^\dagger_{m_{N_1}\beta} c^\dagger_{1\alpha} \dots c^\dagger_{N_\phi\alpha} |0\rangle \tag{4.15}$$

The sum is over all possible subsets $\{m_i\} = \{m_1, m_2, \dots, m_{N_1}\}$ of $\{1, 2, \dots, N_\phi\}$, arranged in increasing order $1 \leq m_1 < m_2 < \dots < m_{N_1} \leq N_\phi$. The sum contains $C^{N_1}_{N_\phi} = \frac{N_\phi!}{N_1!(N_\phi - N_1)!}$ terms, and the state is normalized:

$$\sum_{\{m_i\}} |F_{\{m_i\}}|^2 = 1 \tag{4.16}$$

To simplify the notation, we denote the fully occupied component $|\alpha\rangle$ as:

$$|\Omega\rangle = c^\dagger_{1\alpha} \dots c^\dagger_{N_\phi\alpha} |0\rangle \tag{4.17}$$

so that

$$|\Psi\rangle = \sum_{\{m_i\}} F_{\{m_i\}} c^\dagger_{m_1\beta} \dots c^\dagger_{m_{N_1}\beta} |\Omega\rangle \tag{4.18}$$

Zeeman energy

The expectation value of the Zeeman energy per flux quantum is written as:

$$E_Z = \frac{\langle\Psi|\mathcal{H}_Z|\Psi\rangle}{N_\phi} = -\frac{h}{N_\phi} \sum_{\chi\chi'} \sum_m \langle\chi|\sigma^z|\chi'\rangle \langle\Psi|c^\dagger_{m\chi} c_{m\chi'}|\Psi\rangle \tag{4.19}$$

The expectation value $\langle\Psi|c^\dagger_{m\chi} c_{m\chi'}|\Psi\rangle$ is nonzero if either $\chi = \chi' = \alpha$ or $\chi = \chi' = \beta$ and vanishes otherwise. This implies that:

$$E_Z = -\frac{h}{N_\phi} \left(\langle\alpha|\sigma^z|\alpha\rangle \sum_m \langle\Psi|c^\dagger_{m\alpha} c_{m\alpha}|\Psi\rangle + \langle\beta|\sigma^z|\beta\rangle \sum_m \langle\Psi|c^\dagger_{m\beta} c_{m\beta}|\Psi\rangle \right) \tag{4.20}$$

Obviously, $\langle\Psi|c^\dagger_{m\alpha} c_{m\alpha}|\Psi\rangle = 1$ for all $m \in \{1, 2, \dots, N_\phi\}$, so:

$$\sum_m \langle\Psi|c^\dagger_{m\alpha} c_{m\alpha}|\Psi\rangle = N_\phi \tag{4.21}$$

Now, we evaluate the expectation value of component $|\beta\rangle$:

$$\begin{aligned} &\langle\Psi|c^\dagger_{m\beta} c_{m\beta}|\Psi\rangle \\ &= \sum_{\{m_i\}\{m'_i\}} F^*_{\{m_i\}} F_{\{m'_i\}} \langle\Omega|c_{m_{N_1}\beta} \dots c_{m_1\beta} c^\dagger_{m\beta} c_{m\beta} c^\dagger_{m'_1\beta} \dots c^\dagger_{m'_{N_1}\beta}|\Omega\rangle \end{aligned} \tag{4.22}$$

All terms where $\{m_i'\}$ does not contain m vanish. For terms where $m \in \{m_i'\}$, they vanish unless the two sets of orbital indices $\{m_i\} = \{m_i'\}$. For this reason, we have:

$$\langle\Psi|c_{m\beta}^{\dagger}c_{m\beta}|\Psi\rangle = \sum_{\{m_i\}:m\in\{m_i\}} |F_{\{m_i\}}|^2 \tag{4.23}$$

That means the sum contains only the weight coefficients corresponding to the occupation sets $\{m_i\}$ such that $m \in \{m_i\}$. When we sum over all values of m:

$$\sum_m \langle\Psi|c_{m\beta}^{\dagger}c_{m\beta}|\Psi\rangle = \sum_m \sum_{\{m_i\}:m\in\{m_i\}} |F_{\{m_i\}}|^2 \tag{4.24}$$

each term $|F_{\{m_i\}}|^2$ appears exactly N_1 times, for all sets $\{m_i\}$. Therefore, we arrive to the delicate identity:

$$\sum_m \langle\Psi|c_{m\beta}^{\dagger}c_{m\beta}|\Psi\rangle = N_1 \sum_{\{m_i\}} |F_{\{m_i\}}|^2 = N_1 \tag{4.25}$$

Overall, the Zeeman energy per flux quantum equals to:

$$\begin{aligned} E_Z =& -h\left(\langle\alpha|\sigma^z|\alpha\rangle + \nu\langle\beta|\sigma^z|\beta\rangle\right) \\ =& -h\left[\mathsf{Tr}(P_\alpha\sigma^z) + \nu\mathsf{Tr}(P_\beta\sigma^z)\right] \end{aligned} \tag{4.26}$$

Substrate-induced sublattice splitting energy

The reasoning for E_Z also holds for the other one-body Hamiltonians. In the case of the substrate-induced sublattice splitting energy, we get a similar formula:

$$\begin{aligned} E_{AB} =& \frac{\langle\Psi|\mathcal{H}_{AB}|\Psi\rangle}{N_\phi} = \frac{\Delta_{AB}}{N_\phi}\sum_{\chi\chi'}\sum_m \langle\chi|\tau^z|\chi\rangle\langle\Psi|c_{m\chi}^{\dagger}c_{m\chi'}|\Psi\rangle \\ =& \Delta_{AB}\left[\mathsf{Tr}(P_\alpha\tau^z) + \nu\mathsf{Tr}(P_\beta\tau^z)\right] \end{aligned} \tag{4.27}$$

Short-range valley-valley interaction energy

The last contribution to the total anisotropy energy is the short-range valley-valley interaction energy E_V. The expectation value of $\mathcal{H}_V$ is given by:

$$\langle\Psi|\mathcal{H}_V|\Psi\rangle = \frac{1}{2}\sum_{\mu\mu'\nu'\nu}\left(\sum_{a=x,y,z} g_a\tau_{\mu\nu}^a\tau_{\mu'\nu'}^a\right)G_{\mu\mu'\nu'\nu} \tag{4.28}$$

where

$$G_{\mu\mu'\nu'\nu} = \langle\Psi|\int d^2\mathbf{r}\hat{\psi}_\mu^{\dagger}(\mathbf{r})\hat{\psi}_{\mu'}^{\dagger}(\mathbf{r})\hat{\psi}_{\nu'}(\mathbf{r})\hat{\psi}_\nu(\mathbf{r})|\Psi\rangle \tag{4.29}$$

For the two-component state $|\Psi\rangle$, all the terms $G_{\mu\mu'\nu'\nu}$ vanish, except $G_{\alpha\beta\beta\alpha}$, $G_{\alpha\beta\alpha\beta}$, $G_{\beta\alpha\alpha\beta}$ and $G_{\beta\alpha\beta\alpha}$. Obviously, $G_{\alpha\beta\alpha\beta} = -G_{\alpha\beta\beta\alpha}$, $G_{\beta\alpha\beta\alpha} = -G_{\beta\alpha\alpha\beta}$ and $G_{\beta\alpha\alpha\beta} = G_{\alpha\beta\beta\alpha}$. To simplify the notation, we denote $G_{\alpha\beta} = G_{\alpha\beta\beta\alpha}$. Hence, the expectation value of $\mathcal{H}_V$ has a simpler formula:

$$\langle\Psi|\mathcal{H}_V|\Psi\rangle = \sum_{a=x,y,z} g_a(\tau_{\alpha\alpha}^a\tau_{\beta\beta}^a - \tau_{\alpha\beta}^a\tau_{\beta\alpha}^a)G_{\alpha\beta} \tag{4.30}$$

The value of $G_{\alpha\beta}$ is given by:

$$\begin{aligned} G_{\alpha\beta} &= \int d^2\mathbf{r} \langle \Psi | \hat{\psi}^\dagger_\alpha(\mathbf{r}) \hat{\psi}^\dagger_\beta(\mathbf{r}) \hat{\psi}_\beta(\mathbf{r}) \hat{\psi}_\alpha(\mathbf{r}) | \Psi \rangle \\ &= \sum_{p_1 p_2 p_3 p_4} \left(\int d^2\mathbf{r} \phi^*_{p_1}(\mathbf{r}) \phi^*_{p_2}(\mathbf{r}) \phi_{p_3}(\mathbf{r}) \phi_{p_4}(\mathbf{r}) \right) \langle \Psi | c^\dagger_{p_1\alpha} c^\dagger_{p_2\beta} c_{p_3\beta} c_{p_4\alpha} | \Psi \rangle \end{aligned} \tag{4.31}$$

We evaluate the expectation value:

$$\begin{aligned} &\langle \Psi | c^\dagger_{p_1\alpha} c^\dagger_{p_2\beta} c_{p_3\beta} c_{p_4\alpha} | \Psi \rangle \\ &= \sum_{\{m_i, m'_i\}} F^*_{\{m_i\}} F_{\{m'_i\}} \langle \Omega | c_{m_{N_1}\beta} \cdots c_{m_1\beta} (c^\dagger_{p_1\alpha} c^\dagger_{p_2\beta} c_{p_3\beta} c_{p_4\alpha}) c^\dagger_{m'_1\beta} \cdots c^\dagger_{m'_{N_1}\beta} | \Omega \rangle \end{aligned} \tag{4.32}$$

The non-vanishing expectation values have $p_1 = p_4$ and gives the occupation number of the state $|p_1\alpha\rangle$ in $|\Psi\rangle$, which is 1. Because the momentum is conserved, $p_1 + p_2 = p_3 + p_4$, so $p_2 = p_3$. Therefore, we have:

$$\begin{aligned} &\langle \Psi | c^\dagger_{p_1\alpha} c^\dagger_{p_2\beta} c_{p_3\beta} c_{p_4\alpha} | \Psi \rangle \\ =&\delta_{p_1 p_4} \delta_{p_2 p_3} \sum_{\{m_i, m'_i\}} F^*_{\{m_i\}} F_{\{m'_i\}} \langle \Omega | c_{m_{N_1}\beta} \cdots c_{m_1\beta} (c^\dagger_{p_2\beta} c_{p_2\beta}) c^\dagger_{m'_1\beta} \cdots c^\dagger_{m'_{N_1}\beta} | \Omega \rangle \end{aligned} \tag{4.33}$$

The expectation vanishes unless $p_3 = p_2$ belongs to the set $\{m'_i\}$ and the two sets $\{m_i\} = \{m'_i\}$. Hence, we have:

$$\langle \Psi | c^\dagger_{p_1\alpha} c^\dagger_{p_2\beta} c_{p_3\beta} c_{p_4\alpha} | \Psi \rangle = \delta_{p_1 p_4} \delta_{p_2 p_3} \sum_{\{m_i\} : p_2 \in \{m_i\}} |F_{\{m_i\}}|^2 \tag{4.34}$$

We have the expression of $G_{\alpha\beta}$:

$$\begin{aligned} G_{\alpha\beta} =& \sum_{p_1 p_2} \left(\int d^2\mathbf{r} |\phi_{p_1}(\mathbf{r})|^2 |\phi_{p_2}(\mathbf{r})|^2 \right) \sum_{\{m_i\} : p_2 \in \{m_i\}} |F_{\{m_i\}}|^2 \\ =& \sum_{p_2} \left[\int d^2\mathbf{r} \left(\sum_{p_1} |\phi_{p_1}(\mathbf{r})|^2 \right) |\phi_{p_2}(\mathbf{r})|^2 \right] \sum_{\{m_i\} : p_2 \in \{m_i\}} |F_{\{m_i\}}|^2 \end{aligned} \tag{4.35}$$

We recall that for all $p_2 \in \{0, 1, 2, \ldots, N_\phi - 1\}$ (see (3.74), Section 3.6):

$$\int d^2\mathbf{r} \left(\sum_{p_1} |\phi_{p_1}(\mathbf{r})|^2 \right) |\phi_{p_2}(\mathbf{r})|^2 = \frac{1}{2\pi l^2} \tag{4.36}$$

This implies that:

$$G_{\alpha\beta} = \frac{1}{2\pi l^2} \sum_{p_2} \sum_{\{m_i\} : p_2 \in \{m_i\}} |F_{\{m_i\}}|^2 = \frac{N_1}{2\pi l^2} \tag{4.37}$$

Again, by defining:

$$\begin{aligned} V_\perp =& \frac{g_\perp}{2\pi l^2} \\ V_z =& \frac{g_z}{2\pi l^2} \end{aligned} \tag{4.38}$$

The parameters $V_\perp$ and V_z are the same as the ones in the case of charge neutrality $\nu = 0$. The short-range valley-valley interaction energy per flux quantum equals:

$$E_V = \frac{\langle\Psi|\mathcal{H}_V|\Psi\rangle}{N_\phi} = \nu \sum_{a=x,y,z} V_a[\tau^a_{\alpha\alpha}\tau^a_{\beta\beta} - \tau^a_{\alpha\beta}\tau^a_{\beta\alpha}] \tag{4.39}$$

We define:

$$\mathcal{F}_{\alpha\beta} = \sum_{a=x,y,z} V_a[\mathsf{Tr}(P_\alpha\tau^a)\mathsf{Tr}(P_\beta\tau^a) - \mathsf{Tr}(P_\alpha\tau^a P_\beta\tau^a)] \tag{4.40}$$

and write E_V in a more compact form:

$$E_V = g_{\alpha\beta}(\mathbf{0})\mathcal{F}_{\alpha\beta} \tag{4.41}$$

where $g_{\alpha\beta}(\mathbf{R})$ is the pair-correlation function between the components $|\alpha\rangle$ and $|\beta\rangle$ in the state $|\Psi\rangle$, defined as:

$$g_{\alpha\beta}(\mathbf{R}) = \frac{L_x L_y}{N_\phi^2}\int d^2\mathbf{r}d^2\mathbf{r}'\langle\Psi|\hat{\psi}^\dagger_\alpha(\mathbf{r})\hat{\psi}^\dagger_\beta(\mathbf{r}')\delta^{(2)}(\mathbf{r}-\mathbf{r}'-\mathbf{R})\hat{\psi}_\beta(\mathbf{r}')\hat{\psi}_\alpha(\mathbf{r})|\Psi\rangle \tag{4.42}$$

It is easy to see that:

$$G_{\alpha\beta} = \frac{N_\phi^2}{L_x L_y}g_{\alpha\beta}(\mathbf{0}) = \frac{N_\phi}{2\pi l^2}g_{\alpha\beta}(\mathbf{0}) \tag{4.43}$$

Therefore, we arrive to the elegant property:

$$g_{\alpha\beta}(\mathbf{0}) = \nu \tag{4.44}$$

Total anisotropy energy

Overall, the expression of the total anisotropy energy of the two-component state $(1,\nu)$ is:

$$\boxed{\begin{aligned} E_A =& E_V + E_Z + E_{AB} \\ =& \nu \sum_{a=x,y,z} V_a[\mathsf{Tr}(P_\alpha\tau^a)\mathsf{Tr}(P_\beta\tau^a) - \mathsf{Tr}(P_\alpha\tau^a P_\beta\tau^a)] \\ & - h[\mathsf{Tr}(P_\alpha\sigma^z) + \nu\mathsf{Tr}(P_\beta\sigma^z)] \\ & + \Delta_{AB}[\mathsf{Tr}(P_\alpha\tau^z) + \nu\mathsf{Tr}(P_\beta\tau^z)] \end{aligned}} \tag{4.45}$$

4.5.2 . State $(1, \nu, \nu)$

For the state $(1,\nu,\nu)$, our trial wavefunction has three components $|\alpha\rangle, |\beta\rangle, |\gamma\rangle$. Each component $|\alpha\rangle$ and $|\beta\rangle$ is occupied by N_1 electrons with filling fraction $\nu = N_1/N_\phi$. Component $|\gamma\rangle$ is fully filled. We choose the following trial wavefunction:

$$|\Psi\rangle = \sum_{\{m_i,n_j\}} F_{\{m_i,n_j\}} c^\dagger_{m_1\alpha}\cdots c^\dagger_{m_{N_1}\alpha}c^\dagger_{n_1\beta}\cdots c^\dagger_{n_{N_1}\beta}c^\dagger_{1\gamma}\cdots c^\dagger_{N_\phi\gamma}|0\rangle \tag{4.46}$$

where

$$\sum_{\{m_i,n_j\}} |F_{\{m_i,n_j\}}|^2 = 1 \tag{4.47}$$

Similar to the case of the $(1,\nu)$ state, we find the expression of the Zeeman energy:

$$E_Z = -h[\mathsf{Tr}(P_\gamma s^z) + \nu\mathsf{Tr}(P_\alpha s^z) + \nu\mathsf{Tr}(P_\beta s^z)] \tag{4.48}$$

and the substrate-induced sublattice splitting energy:

$$E_{AB} = \Delta_{AB}[\mathsf{Tr}(P_\gamma \tau^z) + \nu\mathsf{Tr}(P_\alpha \tau^z) + \nu\mathsf{Tr}(P_\beta \tau^z)] \tag{4.49}$$

The short-range valley-dependent interaction is given by:

$$E_V = g_{\alpha\gamma}(0)\mathcal{F}_{\alpha\gamma} + g_{\beta\gamma}(0)\mathcal{F}_{\beta\gamma} + g_{\alpha\beta}(0)\mathcal{F}_{\alpha\beta} \tag{4.50}$$

Because the component $|\gamma\rangle$ is fully filled, we also have the following:

$$g_{\alpha\gamma}(0) = g_{\beta\gamma}(0) = \nu \tag{4.51}$$

If $\psi^\dagger_{\alpha\beta}$ is a singlet state of filling factor (ν,ν), the pair correlation function $g_{\alpha\beta}(0)$ between the two partially filled components is, however, small $g_{\alpha\beta}(0) \approx 10^{-3}$. Therefore, the total anisotropy energy of the case $(1,\nu,\nu)$ is approximated as follows:

$$\boxed{\begin{aligned} E_A =& E_V + E_Z + E_{AB} \\ =& \nu\mathcal{F}_{\alpha\gamma} + \nu\mathcal{F}_{\beta\gamma} \\ & - h[\mathsf{Tr}(P_\gamma \sigma^z) + \nu\mathsf{Tr}(P_\alpha \sigma^z) + \nu\mathsf{Tr}(P_\beta \sigma^z)] \\ & + \Delta_{AB}[\mathsf{Tr}(P_\gamma \tau^z) + \nu\mathsf{Tr}(P_\alpha \tau^z) + \nu\mathsf{Tr}(P_\beta \tau^z)] \end{aligned}} \tag{4.52}$$

4.6 . Phase diagrams: Variational method

In this section, we use the formulae derived in section 4.5 to establish the phase diagrams of the following cases: $(1,\nu)$ and $(1,\nu,\nu)$ $(0<\nu<1)$. We will compare these theoretical results with those of the numerical Exact Diagonalization method in sections 5.3 and 5.4. We will only consider the case where $h = \Delta_{AB} = 0$.

Before considering each of these three cases, we recall the two classes of orthonormal basis states of the four-dimensional spin-valley Hilbert space:

1. ***Valley-ordered states:***

$$\begin{aligned} |\chi_1\rangle =& |\mathbf{t}_1, \mathbf{s}\rangle \quad & |\chi_2\rangle =& |-\mathbf{t}_1, \mathbf{s}\rangle \\ |\chi_3\rangle =& |\mathbf{t}_2, -\mathbf{s}\rangle & |\chi_4\rangle =& |-\mathbf{t}_2, -\mathbf{s}\rangle \end{aligned} \tag{4.53}$$

2. ***Spin-ordered states:***

$$\begin{aligned} |\chi_1\rangle =& |\mathbf{t}, \mathbf{s}_1\rangle \quad & |\chi_2\rangle =& |\mathbf{t}, -\mathbf{s}_1\rangle \\ |\chi_3\rangle =& |-\mathbf{t}, \mathbf{s}_2\rangle & |\chi_4\rangle =& |-\mathbf{t}, -\mathbf{s}_2\rangle \end{aligned} \tag{4.54}$$

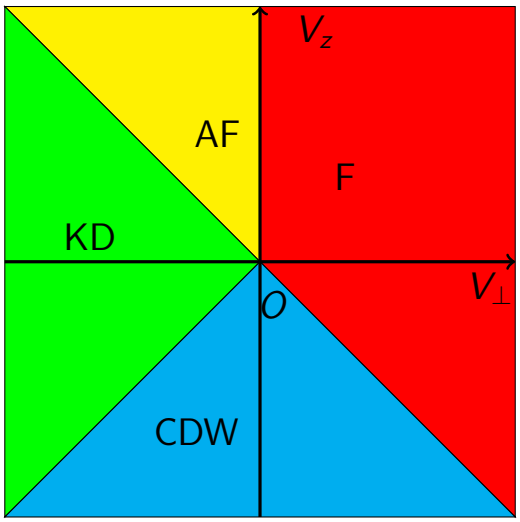

Figure 4.3: Phase diagram of the $(1, \nu)(0 < \nu < 1)$ state.

4.6.1 . State $(1, \nu)$

We consider the state with one fully occupied component $|\alpha\rangle$ and one partially occupied component $|\beta\rangle$. The filling factor of the component $|\beta\rangle$ is ν $(0 < \nu < 1)$. In the absence of the Zeeman effect and the substrate-induced sublattice splitting energy $(h = \Delta_{AB} = 0)$, the total anisotropy energy has the formula:

$$E_A = E_V = \nu \sum_{a=x,y,z} V_a[\mathrm{Tr}(P_\alpha \tau^a)\mathrm{Tr}(P_\beta \tau^a) - \mathrm{Tr}(P_\alpha \tau^a P_\beta \tau^a)] \tag{4.55}$$

For the valley-ordered phases, we consider two cases:

- $|\alpha\rangle = |\chi_1\rangle$ and $|\beta\rangle = |\chi_2\rangle$. The flavor composition of the phase is $\{|\mathbf{t}, \mathbf{s}\rangle, |-\mathbf{t}, \mathbf{s}\rangle\}$. In this notation, the first spinor characterizes the fully occupied component, while the second spinor characterizes the partially-occupied component. The energy of the phase is given by:
$$E_1 = -\nu(2V_\perp + V_z) \tag{4.56}$$
- $|\alpha\rangle = |\chi_1\rangle$ and $|\beta\rangle = |\chi_3\rangle$. The spinor composition of the phase is $\{|\mathbf{t}_1, \mathbf{s}\rangle, |\mathbf{t}_2, -\mathbf{s}\rangle\}$. The energy of the phase is given by:
$$E_2 = \nu[V_\perp(t_{1x}t_{2x} + t_{1y}t_{2y}) + V_z t_{1z}t_{2z}] \tag{4.57}$$

For the spin-ordered phases, we consider two cases:

- $|\alpha\rangle = |\chi_1\rangle$ and $|\beta\rangle = |\chi_2\rangle$. The spinor composition of the phase is $\{|\mathbf{t}, \mathbf{s}\rangle, |\mathbf{t}, -\mathbf{s}\rangle\}$. The energy of the phase is given by:
$$E_3 = \nu[V_\perp + (V_z - V_\perp)t_z^2] \tag{4.58}$$

- $|\alpha\rangle = |\chi_1\rangle$ and $|\beta\rangle = |\chi_3\rangle$. The spinor composition of the phase is $\{|\mathbf{t}, \mathbf{s}_1\rangle, |-\mathbf{t}, \mathbf{s}_2\rangle\}$. The energy of the phase is given by:

$$E_4 = -\nu \left[V_\perp + \frac{1}{2}(1 + \mathbf{s}_1 \cdot \mathbf{s}_2)(V_\perp + V_z) \right] + \frac{1}{2}\nu(1 - \mathbf{s}_1 \cdot \mathbf{s}_2)(V_\perp - V_z)t_z^2 \quad (4.59)$$

The phase diagram of the state $(1, \nu)$ has similar form as the case of Charge Neutrality Point (Fig. 4.3). It consists of 4 phases:

1. The **Ferromagnetic (F)** phase has flavor composition $\{|\mathbf{t}, \mathbf{s}\rangle, |-\mathbf{t}, \mathbf{s}\rangle\}$. The energy of the Ferromagnetic phase is given by:

$$E = -\nu(2V_\perp + V_z) \quad (4.60)$$

   In this phase, all electrons have the same spin polarization $\mathbf{s}$, regardless of the sublattice/valley they occupy. Because one component is completely occupied while the other is partially occupied, the total valley polarization is partially polarized, instead of being unpolarized as in the case of Charge Neutrality Point.

2. The **Antiferromagnetic (AF)** phase has flavor composition $\{|K, \mathbf{s}\rangle, |K', -\mathbf{s}\rangle\}$. The energy of the phase is given by:

$$E = -\nu V_z \quad (4.61)$$

   The two occupied components have opposite spins and opposite valleys. The electrons occupying different sublattices have opposite spin polarizations. Due to unequal occupations of the components, the total spin and total valley are partially polarized, not unpolarized.

3. The **Kékulé Distortion (KD)** phase has flavor composition $\{|\mathbf{t}_\perp, \mathbf{s}\rangle, |\mathbf{t}_\perp, -\mathbf{s}\rangle\}$. The energy of the phase is given by:

$$E = \nu V_\perp \quad (4.62)$$

   The flavor composition is similar to the Kékulé Distortion phase at Charge neutrality. The valley is polarized on the XY-plane, but the spin is partially polarized, due to unequal occupations of the components.

4. The **Charge Density Wave (CDW)** phase has flavor composition $\{|K, \mathbf{s}\rangle, |K, -\mathbf{s}\rangle\}$. The energy of the phase is given by:

$$E = \nu V_z \quad (4.63)$$

   All electrons occupy the same valley, so the same sublattice. Also, the spin is partially polarized, because the filling factors of the two components are not equal.

All the phase transitions are first order. We summarize the four phases in Table. 4.1. The total anisotropy energy has the same formula as in the case of charge neutrality, up to a factor ν. This explains why the phase diagram of $(1, \nu)$ has the same form as

Phase	Occupied components	Energy
F	$\{\|\mathbf{t},\mathbf{s}\rangle, \|-\mathbf{t},\mathbf{s}\rangle\}$	$-\nu(2V_\perp + V_z)$
AF	$\{\|K,\mathbf{s}\rangle, \|K',-\mathbf{s}\rangle\}$	$-\nu V_z$
KD	$\{\|\mathbf{t}_\perp,\mathbf{s}\rangle, \|\mathbf{t}_\perp,-\mathbf{s}\rangle\}$	$\nu V_\perp$
CDW	$\{\|K,\mathbf{s}\rangle, \|K,-\mathbf{s}\rangle\}$	νV_z

Table 4.1: Phases of the state $(1,\nu)(0<\nu<1)$.

the phase diagram of the Charge Neutrality Point case, and the corresponding energies equal the ones of the Charge Neutrality Point case multiplied by ν. Because the filling factors of the two components are not equal, the total spin and valley can be partially polarized instead of being singlet. This is the difference between the case $(1,\nu)$ compared to the case of Charge Neutrality Point. This result applies for two-component states like (1,1/3), (1,2/3), (1,1/5) and (1,2/5).

4.6.2 . State $(1,\nu,\nu)$

We consider the state with one fully occupied component $|\alpha\rangle$ glued to a singlet state (ν,ν) of total filling factor 2ν $(0<\nu<1/2)$ occupying two components $|\beta\rangle$ and $|\gamma\rangle$. As previously discussed in subsection 4.5.2, the term $g_{\beta\gamma}(0)\mathcal{F}_{\beta\gamma}$ is negligible. In the case where $h=\Delta_{AB}=0$, the total anisotropy energy equals:

$$\begin{aligned} E_A =& \nu\mathcal{F}_{\alpha\beta} + \nu\mathcal{F}_{\alpha\gamma} \\ =& \nu \sum_{a=x,y,z} V_a[\mathsf{Tr}(P_\alpha\tau^a)\mathsf{Tr}(P_\beta\tau^a) - \mathsf{Tr}(P_\alpha\tau^a P_\beta\tau^a)] \\ &+ \nu \sum_{a=x,y,z} V_a[\mathsf{Tr}(P_\alpha\tau^a)\mathsf{Tr}(P_\gamma\tau^a) - \mathsf{Tr}(P_\alpha\tau^a P_\gamma\tau^a)] \end{aligned} \tag{4.64}$$

For *valley-ordered phases*, we consider two cases:

- *Case 1:* $|\alpha\rangle = |\chi_1\rangle$, $|\beta\rangle = |\chi_2\rangle$,$|\gamma\rangle = |\chi_3\rangle$. The energy of the phase is given by:

$$E_1 = -\nu(2V_\perp + V_z) + \nu[V_\perp(t_{1x}t_{2x} + t_{1y}t_{2y}) + V_z t_{1z}t_{2z}] \tag{4.65}$$

- *Case 2:* $|\alpha\rangle = |\chi_1\rangle$, $|\beta\rangle = |\chi_3\rangle$, $|\gamma\rangle = |\chi_4\rangle$. The energy of the phase is given by:

$$E_2 = 0 \tag{4.66}$$

The remaining case $|\alpha\rangle = |\chi_1\rangle$, $|\beta\rangle = |\chi_2\rangle$, $|\gamma\rangle = |\chi_4\rangle$ becomes case 1 if we change the variable $\mathbf{t}_2' = -\mathbf{t}_2$. Hence, we do not consider this case.

For *spin-ordered phases*, we consider two cases:

- *Case 1:* $|\alpha\rangle = |\chi_1\rangle$, $|\beta\rangle = |\chi_2\rangle$, $|\gamma\rangle = |\chi_3\rangle$. The energy of the phase is given by:

$$E_3 = -\frac{1}{2}\nu(1+\mathbf{s}_1\cdot\mathbf{s}_2)[(V_\perp + V_z) + (V_\perp - V_z)t_z^2] \tag{4.67}$$

If $\mathbf{s}_1 = -\mathbf{s}_2$, this phase is a particular case of the case 2 of valley-ordered phases. Therefore, we only need to consider the case where $\mathbf{s}_1 \neq -\mathbf{s}_2$.

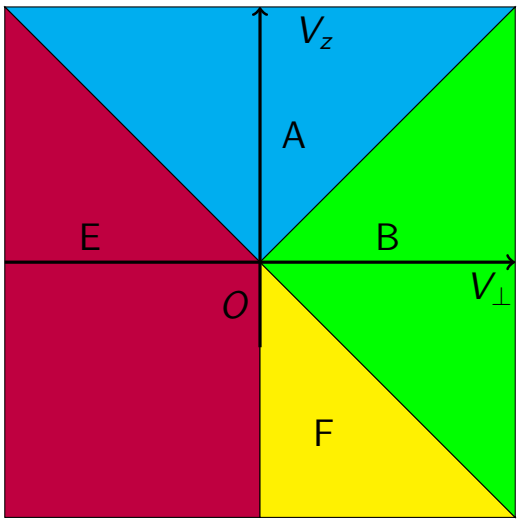

Figure 4.4: Phase diagram of the state $(1, \nu, \nu)$ $(0 < \nu < 1)$.

- *Case 2:* $|\alpha\rangle = |\chi_1\rangle$, $|\beta\rangle = |\chi_3\rangle$, $|\gamma\rangle = |\chi_4\rangle$. The energy of the phase is given by:

$$E_4 = -\nu(2V_\perp + V_z) - \nu[V_\perp + (V_z - V_\perp t_z^2)] \tag{4.68}$$

The phase diagram of the $(1, \nu, \nu)$ state is shown in Fig. 4.4. It contains 4 phases:

1. **Phase A** has spinor composition $\{|K, \mathbf{s}_1\rangle, |K', \mathbf{s}_2\rangle, |K', -\mathbf{s}_2\rangle\}$. In this notation, the first component is completely occupied, and the two remaining components forming the singlet state of total filling factor 2ν. Its energy is given by:

$$E = -2\nu(V_\perp + V_z) \tag{4.69}$$

   The two partially occupied components have the same valley and form a spin singlet. The two spin vectors $\mathbf{s}_1$ and $\mathbf{s}_2$ are independent of each other. The total valley of the three components is partially polarized.

2. **Phase B** has spinor composition $\{|\mathbf{t}_\perp, \mathbf{s}_1\rangle, |-\mathbf{t}_\perp, \mathbf{s}_2\rangle, |-\mathbf{t}_\perp, -\mathbf{s}_2\rangle\}$. Its energy is given by:

$$E = -\nu(3V_\perp + V_z) \tag{4.70}$$

   Similar to Phase A, the valley of the two partially occupied components is opposite to the valley of the completely occupied component. The former components also form a spin singlet. However, the valley polarization of Phase B is XY-like because in its region $|V_\perp| > |V_z|$. In contrast, the valley polarization of Phase A is Ising-like.

Phase	Spinor composition	Energy
A	$\{\|K,\mathbf{s}_1\rangle, \|K',\mathbf{s}_2\rangle, \|K',-\mathbf{s}_2\rangle\}$	$-2\nu(V_\perp+V_z)$
B	$\{\|\mathbf{t}_\perp,\mathbf{s}_1\rangle, \|-\mathbf{t}_\perp,\mathbf{s}_2\rangle, \|-\mathbf{t}_\perp,-\mathbf{s}_2\rangle\}$	$-\nu(3V_\perp+V_z)$
E	$\{\|\mathbf{t}_1,\mathbf{s}\rangle, \|\mathbf{t}_2,-\mathbf{s}\rangle, \|-\mathbf{t}_2,-\mathbf{s}\rangle\}$	0
F	$\{\|K,\mathbf{s}\rangle, \|K',\mathbf{s}\rangle, \|K,-\mathbf{s}\rangle\}$	$-2\nu V_\perp$

Table 4.2: Phases of the state $(1,\nu,\nu)$ $(0<\nu<1)$.

3. **Phase E** has spinor composition $\{|\mathbf{t}_1,\mathbf{s}\rangle, |\mathbf{t}_2,-\mathbf{s}\rangle, |-\mathbf{t}_2,-\mathbf{s}\rangle\}$. The energy of phase E is given by:
$$E=0 \tag{4.71}$$
Contrary to Phase A, the two partially occupied components of Phase B have the same spin, and form a valley singlet. The two vectors $\mathbf{t}_1$ and $\mathbf{t}_2$ are independent of each other. The total spin of the three components is partially polarized.

4. **Phase F** has spinor composition $\{|K,\mathbf{s}\rangle, |K',\mathbf{s}\rangle, |K,-\mathbf{s}\rangle\}$. The energy of Phase F is given by:
$$E=-2\nu V_\perp \tag{4.72}$$
Phase F has an Ising-like valley polarization, consistent with its domain where $|V_z|>|V_\perp|$. The two partially occupied components form a singlet for both spin and valley.

All the phase transitions are first order. The result is summarized in Table. 4.2.

4.7 . Summary of the chapter

In this chapter, we established the phase diagrams for the quantum Hall states of flavor compositions $(1,\nu)$ $(0<\nu<1)$ and $(1,\nu,\nu)$ $(0<\nu<1)$. We proposed a set of variational wavefunctions for the two-component and three-component states and calculated the short-range valley-dependent interaction energy of those trial wavefunctions. Then, we searched for the most stable phases by varying the polarization of the spin-valley isospins of the components and minimizing the anisotropy energy. The phase diagram of the state $(1,\nu)$ has the same shape as the one of the Charge Neutrality Point case. For the case $(1,\nu,\nu)$, the formula of the short-range valley-dependent interaction includes a term involving the correlation between electrons occupying the two partially-filled components. For the particular case where (ν,ν) is the singlet state of total filling factor $0<2\nu<2$ glued to a completely filled shell, this contribution is safely negligible, allowing us to establish a phase diagram having four phases as shown in Fig. 4.4. For other values of ν, this contribution can be significant and cannot be ignored. In the next chapter, we will consider the particular cases of the filling factors $\nu=4/3$ and $\nu=5/3$ and compare the results of the two methods.

Chapter5 - Spin and valley ordering of monolayer graphene in some fractional quantum Hall states: Exact diagonalizations

5.1 . Introduction to the chapter

In Chapter 4, we developed a variational method and analytically established the phase diagrams of the states $(1,\nu)(0<\nu<1)$ and $(1,\nu,\nu)(0<\nu<1)$. This chapter discusses the spin and valley ordering of the filling factors $\nu=-2+n/3(n=1,2,4,5)$. We begin by discussing the spin and valley ordering of the filling factors $\nu=-2+1/3$ and $\nu=-2+2/3$. And then, we will discuss the cases $\nu=-2+4/3$ and $\nu=-2+5/3$. In those cases, the total filling factor is greater than 1, meaning that more than one component are occupied. The short-range valley-dependent anisotropies play a crucial role in determining the spin and valley ordering of the ground states. For these two cases, we compare the results predicted by the variational method developed in Chapter 5 with the numerical results of exact diagonalizations. We will finally discuss the phase transitions between states having different flavor compositions. The chapter ends with the conclusion of the whole project. In this chapter, we use two different conventions to denote the total filling factor of the state: $\nu(-2<\nu<+2)$ means the filling factor with respect to the charge neutrality point, and $\tilde{\nu}=2+\nu$ means the total filling factor of the ZLL.

5.2 . The fractions $\tilde{\nu}<1$

5.2.1 . The fraction $\tilde{\nu}=1/3$

For filling factor $\tilde{\nu}=1/3(\nu=-2+1/3)$, the one-component state is an eigenstate of the SU(4) Coulomb interaction (in the limit of no Landau level mixing). It is a member of the irreducible representation with the highest weight $(N_e,0,0,0)$. That means all electrons have the same spin and valley. We can explicitely express this wavefunction as the product of the Laughlin state as spatial part by a symmetric spinor part:

$$\Psi_{1/3}(z_1,\ldots,z_{N_e})=\prod_{i<j}(z_i-z_j)^3|\alpha\alpha\ldots\alpha\rangle \tag{5.1}$$

where the ket state $|\alpha\rangle$ represents the single-electron state in the spin-valley Hilbert space.

The effect of anisotropies is as follows. The Zeeman energy $E_Z=\langle\mathcal{H}_Z\rangle$ orients the spin along the direction of the total magnetic field. The pseudo-Zeeman field selects the valley which minimizes the substrate-induced sublattice splitting energy $E_{AB}=\langle\mathcal{H}_{AB}\rangle$. In the absence of the pseudo-Zeeman field, the short-range valley-dependent interaction $\mathcal{H}_V$ does not affect the valley part of the state because it is a point contact interaction and vanishes for any antisymmetric spatial wavefunction. In other words, $\mathcal{H}_V$ is only nonzero when two electrons coincide in space, but in this situation, the wavefunction vanishes due to the Pauli exclusion principle. Therefore, the spinor $|\alpha\rangle=|\mathbf{t}\rangle_v\otimes|\uparrow\rangle_s$ with the valley vector $\mathbf{t}$ freely rotating on the Bloch sphere.

5.2.2 . The fraction $\tilde{\nu} = 2/3$

For filling factor $\tilde{\nu} = 2/3(\nu = -2 + 2/3)$, there are several known competing states. They differ in the number of components the electrons occupy. On the torus geometry, those states directly compete, whereas they have different shifts on the spherical geometry. We start by discussing the one-component and two-component states of filling factor $\tilde{\nu} = 2/3$ for electrons with spin degree of freedom.

The first state is the $\tilde{\nu} = 2/3$ polarized state in which all electrons have the same spin. It is the particle-hole symmetric of the Laughlin state with filling factor $\tilde{\nu} = 1/3$. Here we can use the composite fermion theory to establish the relation between the number of electrons N_e and the number of magnetic flux quanta N_ϕ. This state corresponds to a picture of ^{2}CF in negative flux where the ^{2}CFs occupy the lowest and the second Λ-levels. Let $N_\phi^* < 0$ be the number of effective magnetic flux quanta, on the spherical geometry, the total number of electrons (or ^{2}CF) equals $N_e = (|N_\phi^*| + 1) + (|N_\phi^*| + 3) = 4 - 2N_\phi^*$, so $N_\phi^* = 2 - \dfrac{N_e}{2}$. By substituting into the relation $N_\phi = N_\phi^* + 2p(N_e - 1)$ with $2p = 2$, we get $N_\phi = \dfrac{3}{2}N_e$. The spin of the electrons in this state is selected by the Zeeman effect. In the absence of the valley pseudoZeeman field, this state exhibits a SU(2) valley symmetry because the point-contact interaction $\mathcal{H}_V$ has no effect on this valley polarized state.

The second state is the SU(2) singlet state in which each of the two components has the filling factor 1/3. We can view this state in the composite fermion picture as one Λ level occupied by a singlet pair of ^{2}CF. Therefore, on the spherical geometry, $N_e = 2(|N_\phi^*| + 1) = 2(-N_\phi^* + 1)$, so $N_\phi^* = 1 - \dfrac{N_e}{2}$. This implies the relation between N_e and N_ϕ: $N_\phi = \dfrac{3}{2}N_e - 1$. That means the $\tilde{\nu} = 2/3$ singlet and polarized states have different shifts on the spherical geometry. Previous studies show that the SU(2) singlet state has lower energy than the polarized state [65]:

$$E_{(1/3,1/3)} < E_{(2/3,0)} \tag{5.2}$$

The previous reasoning is still valid when we generalize from the two-dimensional Hilbert space to the four-dimensional spin-valley Hilbert space. The singlet state of flavor composition $(1/3, 1/3, 0, 0)$ has lower Coulomb energy than the polarized state of flavor composition $(2/3, 0, 0, 0)$. Similarly to the Laughlin state $\tilde{\nu} = 1/3$, the one-component state $(2/3, 0, 0, 0)$ does not feel the point-contact interaction $\mathcal{H}_V$ and exhibits a SU(2) valley symmetry. By contrast, the two-component singlet state $(1/3, 1/3, 0, 0)$ has a nonvanishing probability for two electrons to be present at the same location in space. Consequently, its energy levels are split by anisotropies, giving rise to broken-symmetry phases. Similarly to the two-component state at charge neutrality $\nu = 0$, which has two components totally occupied by electrons, we can see this two-component singlet state as a two sub-Λ levels fully occupied by ^{2}CF under negative flux. The phase diagram of the state (1/3,1/3,0,0) is therefore similar to the phase diagram of the charge neutrality point case (section 3.7).

Apart from the previous two cases, there are the SU(3) and SU(4) singlet states with total filling factor $\tilde{\nu} = 2/3$ in which electrons equally occupy three and four components equally. They both have the shift $N_\phi = \dfrac{3}{2}N_e - 2$ and have lower Coulomb energy than

their one- and two-component counterparts [104]. These states cannot be described by the composite fermion picture. Unfortunately, one cannot establish their phase diagrams by using the variational method. The nature of the broken-symmetry phases of those states is still unknown.

5.3 . The fraction $\tilde{\nu} = 4/3$

For fraction $\tilde{\nu} = 4/3$, there are two candidate ground states, both of them are exact SU(4) eigenstates. The first one is the $(1, 1/3)$ state obtained by gluing the $\tilde{\nu} = 1/3$ polarized state to the $\tilde{\nu} = 1$ shell. We can obtain this state by considering a $\tilde{\nu} = 2/3$ polarized state and making the particle-hole transformation on both components. The second one is the $(2/3, 2/3)$ state. We obtain this state by applying particle-hole transformation on both components of a $\tilde{\nu} = 2/3$ SU(2) singlet. We refer to the $\tilde{\nu} = 2/3$ polarized state and SU(2) singlet state as the *seed states*.

Let $E_{\tilde{\nu}}$ be the energy per flux quantum of the seed state of filling fraction $\tilde{\nu}$ $(0 < \tilde{\nu} < 1)$, and $E_1 = -\sqrt{\pi/8}e^2/(\varepsilon l)$ the energy per flux quantum of the state having one completely occupied component. The energy of the two-component state obtained by taking particle-hole transformation on this seed state is given by (section 4.4):

$$E_{2-\tilde{\nu}} = E_{\tilde{\nu}} + (1 - \tilde{\nu})2E_1 \tag{5.3}$$

Let $E_{2/3}$ be the energy per flux quantum of the $\tilde{\nu} = 2/3$ polarized state, the energy of the two-component state $(1, 1/3)$ is given by:

$$E_{(1,1/3)} = E_{2-2/3} = E_{2/3} + \frac{2}{3}E_1 \tag{5.4}$$

Let $E_{(1/3,1/3)}$ be the energy per flux quantum of the $\tilde{\nu} = 2/3$ singlet state, the energy of the two-component state $(2/3, 2/3)$ is given by:

$$E_{(2/3,2/3)} = E_{2-(1/3,1/3)} = E_{(1/3,1/3)} + \frac{2}{3}E_1 \tag{5.5}$$

It is well known that the singlet $\tilde{\nu} = 2/3$ state has lower Coulomb energy than the polarized $\tilde{\nu} = 2/3$ state: $E_{(1/3,1/3)} < E_{2/3}$ in the thermodynamic limit [65]. This implies that the state $(2/3, 2/3)$ has lower Coulomb energy than the state $(1, 1/3)$ in the thermodynamic limit.

On the torus geometry, there is no shift, so these two states directly compete when we fix the number of electrons N_e and the number of flux quanta N_ϕ. The $(1, 1/3)$ state is the excited state, so it is computationally demanding to study it. Therefore, we numerically study the problem on the spherical geometry instead.

5.3.1 . The $(1, 1/3)$ state

Let N_1 and N_2 be the number of electrons in the fully occupied and in the partially occupied components, respectively. The total number of electrons is $N_e = N_1 + N_2$. In the spherical geometry, they are related to N_ϕ as follows:

$$\begin{aligned} N_\phi &= N_1 - 1 \\ N_\phi &= 3(N_2 - 1) \end{aligned} \tag{5.6}$$

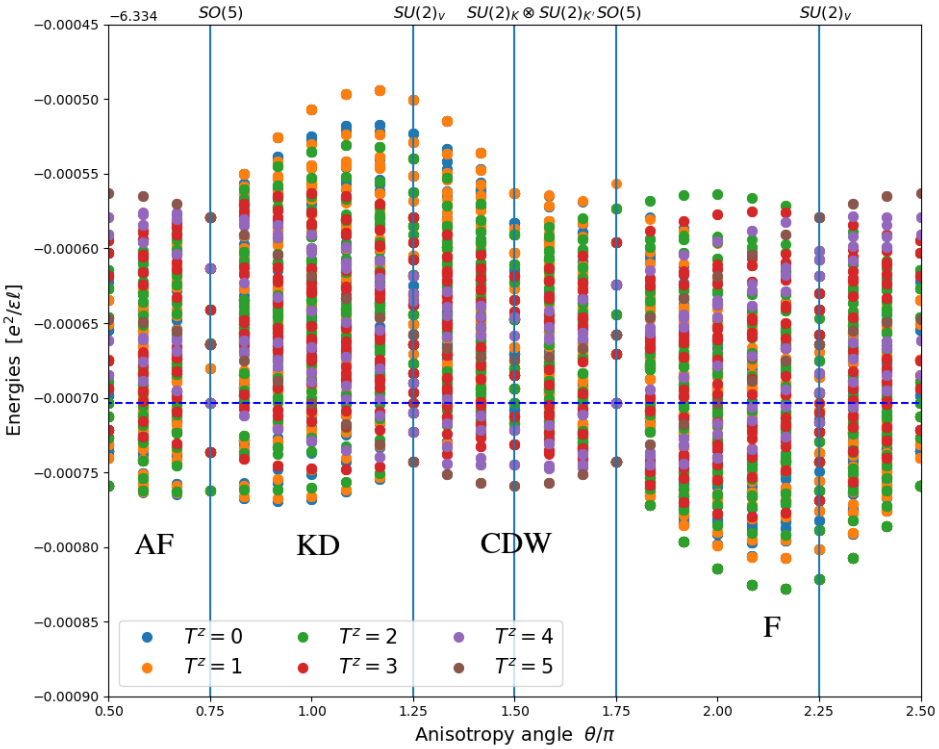

Figure 5.1: Energy levels of the $(1, 1/3)$ state on the sphere with $N_e = 10$, $N_\phi = 6$ as a function of anisotropy. The unperturbed parent state belongs to the SU(4) irreducible representation (7,3,0,0). In the SU(4) limit, this irreducible representation is the fourth excited state (fifth lowest-lying state). The energy of the SU(4) parent state is $E = -6.3347e^2/\varepsilon l$ (dashed blue horizontal line). The vertical lines mark the high symmetry lines of the anisotropy model we use.

This implies the relation between N_e and N_ϕ:

$$N_e = \frac{4}{3}N_\phi + 2 \tag{5.7}$$

We perform exact diagonalizations on the system with $N_e = 10$ and $N_\phi = 6$. The corresponding SU(4) irreducible representation is $(7, 3, 0, 0)$. In the SU(4) limit, the energy of the ground state of the system is $-6.33470e^2/(\varepsilon l)$ (Fig. 5.1). In the presence of anisotropies, the flavor occupation numbers are no longer good quantum numbers of the system. Instead, the valley and spin quantum numbers T^z, S, S^z are good quantum numbers of the many-electron wavefunction. A sector with well-defined S^z and T^z quantum numbers comprises different states belonging to different irreducible representations. The SU(4) irreducible representation (7,3,0,0) of the state (1,1/3) is the fourth excited state (fifth lowest-lying state) for $N_e = 10$, $N_\phi = 6$.

We show the energy levels of the $\tilde{\nu} = 4/3$ state with $N_e = 10$, $N_\phi = 6$ in Fig. 5.1. We have used a small value $g = 10^{-4}$ to avoid mixing between nearby irreducible reprensentations. Valley anisotropies split the energy levels having different quantum numbers. The flavor of the ground state changes with the anisotropy angle θ. The phase diagram (Fig. 5.2) consists of 4 phases with the same range of existence as in the case of $\nu = 0$. Nevertheless, they do not have the same quantum numbers as predicted by the variational method.

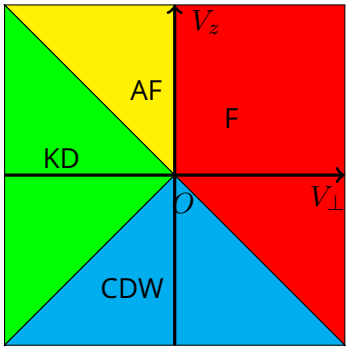

(a) Variational method

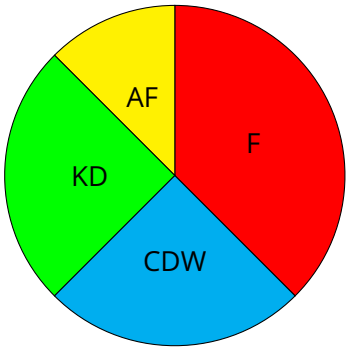

(b) Exact diagonalization

Figure 5.2: Phase diagrams of the state $(1, 1/3)$ calculated by using (a) the variational method and (b) the exact diagonalization method. The two phase diagrams have the same shape.

Phase	Variational method	Exact diagonalization
F	$\{\|\mathbf{t}, \mathbf{s}\rangle, \|-\mathbf{t}, \mathbf{s}\rangle\}$	$-2 \leq T^z \leq 2, S = 5$
AF	$\{\|K, \mathbf{s}\rangle, \|K', -\mathbf{s}\rangle\}$	$T^z = 0, S = 0$
KD	$\{\|\mathbf{t}_\perp, \mathbf{s}\rangle, \|\mathbf{t}_\perp, -\mathbf{s}\rangle\}$	$T^z = 0, S = 2$
CDW	$\{\|K, \mathbf{s}\rangle, \|K, -\mathbf{s}\rangle\}$	$T^z = 5, S = 2$

Table 5.1: The flavor composition (variational method) and quantum number (exact diagonalization) of the 4 phases of the $(1, 1/3)$ state.

1. The first phase with quantum numbers $-2 \leq T^z \leq +2, S = 5$ spans the region $-\pi/4 < \theta < +\pi/2$. It corresponds to the **Ferromagnetic (F)** phase calculated by using the variational method. According to the variational method, the spin is fully polarized, consistently to the maximum possible spin $S = 5$ done using exact diagonalizations. Because $N_1 = 7, N_2 = 3$, we can obtain the maximal valley polarization $T^z = 2$ if $\mathbf{t} = \mathbf{K}$, while the valley quantum number $T^z = 0$ corresponds to $\mathbf{t} = \mathbf{t}_\perp$.

   One remarks that the degeneracy of the states with $-2 \leq T^z \leq 2$ occurs although the Hamiltonian $\mathcal{H}_V$ does not have the SU(2) symmetry in the whole region, except when $\theta = \pi/4$. We explain this valley multiplet as follows: The particle-hole conjugate of the two-component $(1, 1/3)$ state is the $\tilde{\nu} = 2/3$ polarized state of holes. In this state, the holes occupy the same valley. Because holes obey the Pauli exclusion principle, the wavefunction vanishes when two holes coincide in space. Therefore, the point-contact interaction $\mathcal{H}_V$ has no effect on this valley polarized state. Consequently, anisotropies do not split states with different valley quantum numbers, resulting in a valley multiplet. We already showed this argument for the $\tilde{\nu} = 1/3$ state, and it still holds for all one-component states and their particle-hole symmetry images.

2. The second phase with quantum numbers $T^z = S = 0$ spans the region $+\pi/2 < \theta < +3\pi/4$. This phase is naturally **antiferromagnetic (AF)**. However, the variational method gives the quantum number $S = 2$ and $T^z = 2$. This phase is not captured by the variational method.

Phase	Variational method	Exact diagonalization
F	$\{\|\mathbf{t},\mathbf{s}\rangle, \|-\mathbf{t},\mathbf{s}\rangle\}$	$T^z=0, S=4$
AF	$\{\|K,\mathbf{s}\rangle, \|K',-\mathbf{s}\rangle\}$	$T^z=0, S^z=0$
KD	$\{\|\mathbf{t}_\perp,\mathbf{s}\rangle, \|\mathbf{t}_\perp,-\mathbf{s}\rangle\}$	$T^z=0, S^z=0$
CDW	$\{\|K,\mathbf{s}\rangle, \|K,-\mathbf{s}\rangle\}$	$T^z=4, S^z=0$

Table 5.2: The flavor composition (variational method) and quantum number (exact diagonalization) of the 4 phases of the $(2/3,2/3)$ state.

3. The third phase with quantum numbers $T^z=0, S=2$ spans the region $+3\pi/4 < \theta < +5\pi/4$. This phase is consistent with the flavor composition predicted by the variational method. We call this phase **Kékulé Distortion (KD)**.

4. The fourth phase with quantum numbers $T^z=5, S=2$ spans the region $+5\pi/4 < \theta < +7\pi/4$. The spin is correctly predicted by the variational method, while the maximal valley polarization means that all electrons reside in the same valley. This is the property of the **Charge Density Wave (CDW)** phase.

All the phase transitions are first-order. The total spin and valley polarizations led us to name the four phases F, AF, KD, and CDW. The phase diagram of the $(1,1/3)$ state has the same shape as that of the charge neutrality $\nu=0$ case (Fig. 5.2). We cannot describe the AF phase by using the trial wavefunction with spinors $|\alpha\rangle$ and $|\beta\rangle$ in the case of $\nu=0$.

5.3.2 . The $(2/3, 2/3)$ state

The relation between N_e and N_ϕ for the SU(2) singlet state $\tilde{\nu}=2/3$ is $N_\phi=\frac{3}{2}N_e-1$ with $N_1=N_2=\frac{N_e}{2}$ the occupation numbers of the two components. By making a particle-hole transformation $N_{1,2}\to N_\phi+1-N_{1,2}$, we obtain the $(2/3,2/3)$ state in which

$$N_\phi=\frac{3}{2}\left(2(N_\phi+1)-N_e\right)-1=3N_\phi-\frac{3}{2}N_e+2 \tag{5.8}$$

so that

$$N_\phi=\frac{3}{4}N_e-1 \tag{5.9}$$

The two-component state has the highest weight $(N_e/2,N_e/2,0,0)$. We perform exact diagonalizations on the sphere with $N_e=8, N_\phi=5$. The irreducible representations (4,4,0,0) is the ground state (lowest-lying state) for $N_e=8, N_\phi=5$ for each sector of defined quantum numbers (T_z,S_z) with energy $-5.20768e^2/(\varepsilon l)$ in the SU(4) limit (Fig. 5.3).

The energy level spectrum of the state is shown in Fig. 5.3. For each value of the anisotropy angle θ, the ground state quantum numbers are the same as those of the charge neutrality case $\nu=0$ (Table. 5.2). We also have 4 phases F, AF, KD, and CDW. The phase diagram is consistent with the results of the variational method. There is no ground-state level crossing at the AF/KD phase transition boundary. The results of the variational method and that of exact diagonalizations are consistent.

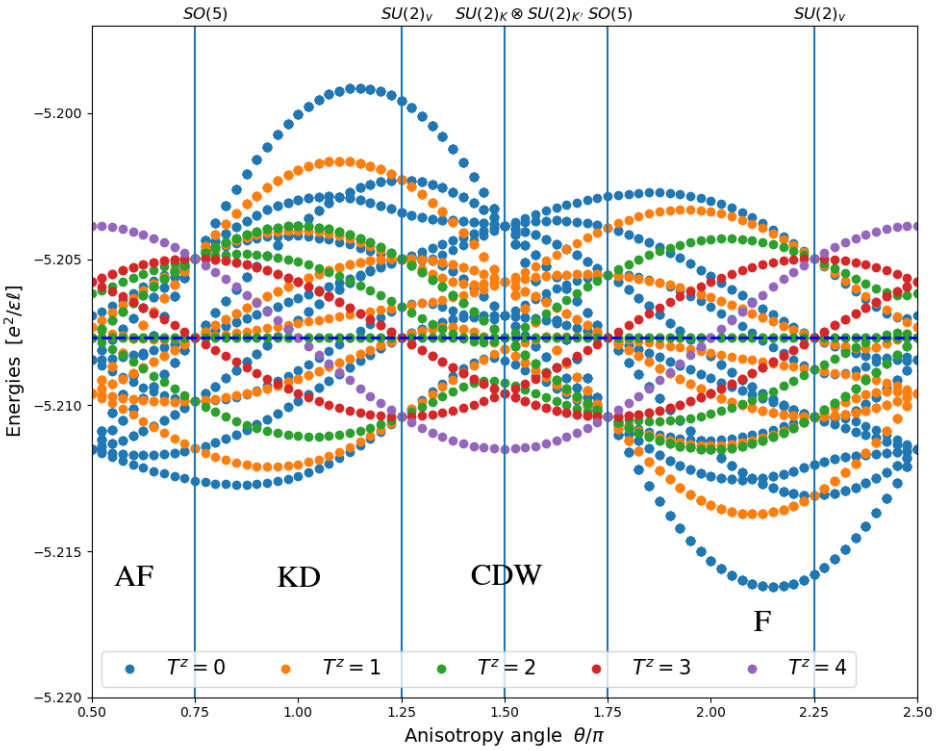

Figure 5.3: Energy levels of the $(2/3, 2/3)$ state on the sphere with $N_e = 8, N_\phi = 5$ as a function of anisotropy. The unperturbed parent state belongs to the SU(4) irreducible representation (4,4,0,0). In the SU(4) limit, this irreducible representation is the ground sate (lowest-lying state). The energy of the SU(4) parent state is $E = -5.20768e^2/\varepsilon l$ (dashed blue horizontal line). The vertical lines mark the high symmetry lines of the anisotropy model we use.

Phase	Variational method	Exact diagonalization
F	$\{\|\mathbf{t},\mathbf{s}\rangle, \|-\mathbf{t},\mathbf{s}\rangle\}$	$1/2 \leq T^z \leq 3/2, S = 11/2$
AF	$\{\|K,\mathbf{s}\rangle, \|K',-\mathbf{s}\rangle\}$	$T^z = 3/2, 1/2 \leq S^z \leq 3/2$
KD	$\{\|\mathbf{t}_\perp,\mathbf{s}\rangle, \|\mathbf{t}_\perp,-\mathbf{s}\rangle\}$	$T^z = 1/2, S^z = 3/2$
CDW	$\{\|K,\mathbf{s}\rangle, \|K,-\mathbf{s}\rangle\}$	$T^z = 11/2, 1/2 \leq S^z \leq 3/2$

Table 5.3: The flavor composition (variational method) and quantum number (exact diagonalization) of the 4 phases of the $(1, 2/3)$ state.

5.4 . The fraction $\tilde{\nu} = 5/3$

For fraction $\tilde{\nu} = 5/3$, there are two candidates for the ground state which are exact SU(4) eigenstates. The two-component state $(1, 2/3)$ is obtained by gluing the $\tilde{\nu} = 2/3$ polarized state to a fully filled $\tilde{\nu} = 1$ shell. The three-component state $(1, 1/3, 1/3)$ is obtained by gluing the $\tilde{\nu} = 2/3$ singlet state to a fully occupied component.

According to (4.11) and (4.13), the Coulomb energy per flux quantum of a multicomponent state formed by adding a seed state of filling factor $\tilde{\nu}$ to a fully occupied shell is given by:

$$E_{1+\tilde{\nu}} = E_{\tilde{\nu}} + E_1 \tag{5.10}$$

Therefore, the Coulomb energies of the two fraction $\tilde{\nu} = 5/3$ states are given by:

$$\begin{aligned} E_{(1,2/3)} =& E_{2/3} + E_1 \\ E_{(1,1/3,1/3)} =& E_{(1/3,1/3)} + E_1 \end{aligned} \tag{5.11}$$

Because $E_{(1/3,1/3)} < E_{2/3}$ [65], we have $E_{(1,1/3,1/3)} < E_{(1,2/3)}$. The three-component state $(1, 1/3, 1/3)$ has lower Coulomb energy than the two-component state $(1, 2/3)$.

5.4.1 . The two-component state $(1, 2/3)$

Let N_1 and N_2 be the numbers of electrons occupying the fully filled shell and the polarized $\tilde{\nu} = 2/3$ component of the state $(1, 2/3)$, respectively. The total number of electrons in the system is $N_e = N_1 + N_2$. We have $N_\phi = N_1 - 1$, $N_\phi = \frac{3}{2}N_2$. This implies that:

$$N_\phi = \frac{3}{5}(N_e - 1) \tag{5.12}$$

We perform exact diagonalization with $N_e = 11, N_\phi = 6$ on the sphere. In the SU(4) limit, the energy of the ground state of the irreducible representation (7,4,0,0) is $-7.02375e^2/(\varepsilon l)$. By taking into account the anisotropies, this state is the sixth excited state (seventh lowest-lying cluster) for $N_e = 7, N_\phi = 4$.

We show the energy level spectrum in Fig. 5.4 and the quantum numbers of the ground states in Table. 5.3. The phase diagram of the $(1, 2/3)$ state has 4 phases, similarly to the phase diagram of the $(1, 1/3)$ state:

1. The first phase spans on the range $-\pi/4 < \theta < +\pi/2$ and has quantum numbers $1/2 \leq T^z \leq 3/2, S = 11/2$. The fully spin polarization allows us to call it the **Ferromagnetic (F)** phase. Similarly to the case $(1, 1/3)$, there is an exact SU(2) valley degeneracy in the whole F phase. The spin and valley quantum numbers are consistent with the spinors obtained by using the variational method.

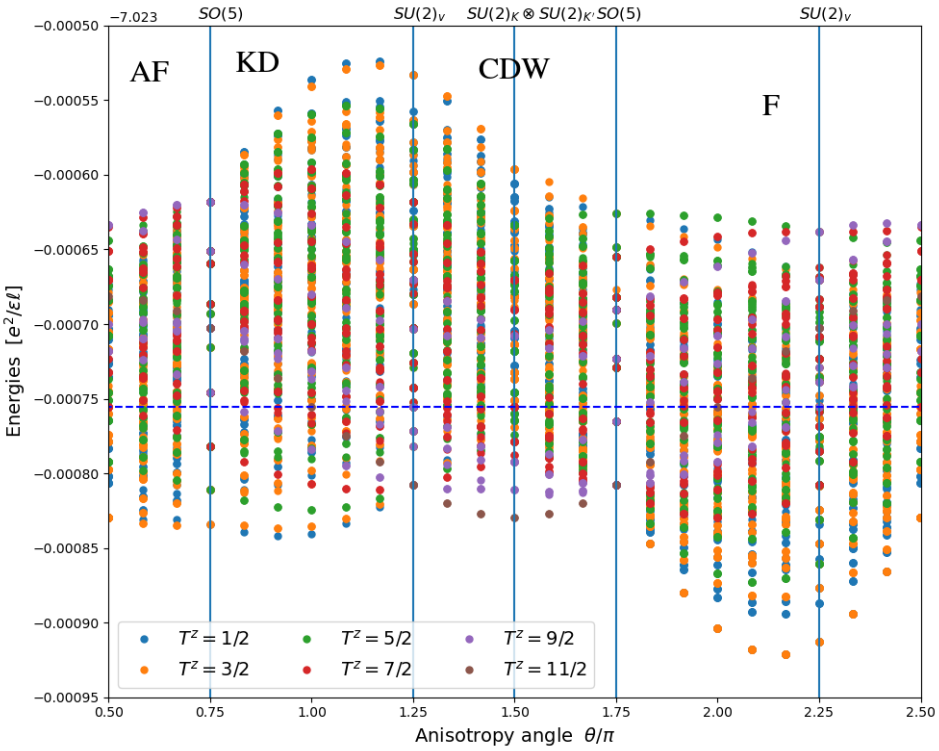

Figure 5.4: Energy levels of the $(1, 2/3)$ state on the sphere with $N_e = 11, N_\phi = 6$ as the function of the anisotropy. The unperturbed parent SU(4) irreducible representation is (7,4,0,0). In the SU(4) limit, this representation is the sixth excited state (seventh lowest-lying state). The energy of the SU(4) parent state is $E = -7.02375e^2/\varepsilon l$ (dashed blue horizontal line). The vertical lines mark the high symmetry lines of the model we use.

2. The second phase spans the range $+\pi/2 < \theta < +3\pi/4$ and has quantum numbers $T^z = 3/2, 1/2 \leq S^z \leq 3/2$. This phase has an **antiferromagnetic (AF)** behavior.

3. The third phase spans the region $+3\pi/4 < \theta < +5\pi/4$ and has quantum numbers $T^z = 1/2, S^z = 3/2$. The valley quantum number $T^z = 1/2$ is consistent to a XY-valley polarization $\mathbf{t} = \mathbf{t}_\perp$ in the context of the variational method (because the total number of electrons is odd, we do not have $T^z = 0$). However, the spin quantum number $S^z = 3/2$ corresponds to a spin polarization $\mathbf{s} =\uparrow$ or $\mathbf{s} =\downarrow$ instead of an arbitrary spin polarization $\mathbf{s}$ as predicted by the variational method. This phase is a **Kékulé Distortion (KD)** phase.

4. The fourth phase spans the region $+5\pi/4 < \theta < +7\pi/4$ and has as quantum number $T^z = 11/2, 1/2 \leq S^z \leq 3/2$. The fully valley polarization indicates that this is a **Charge density wave (CDW)** phase. This is consistent with the spinors obtained by using the variational method.

The phase diagram of the $(1, 2/3)$ state has the same shape when it is calculated by both methods. Due to the difference in quantum numbers between the AF and KD phases, there is a level-crossing phase transition at the SO(5) phase boundary.

5.4.2 . The three-component state $(1, 1/3, 1/3)$

In the three-component state $(1, 1/3, 1/3)$, we replace the $\tilde{\nu} = 2/3$ polarized state by the $\tilde{\nu} = 2/3$ singlet state. Let N_1 be the number of electrons in the fully filled component, $N_2 = N_3$ be the number of electrons in the two flavors of the singlet state. For the fully filled component, we have $N_\phi = N_1 - 1$. For the singlet state, we have:

$$N_\phi = \frac{3}{2}(N_2 + N_3) - 1 = 3N_2 - 1 \tag{5.13}$$

Because $N_e = N_1 + N_2 + N_3$, we obtain the relation between N_e and N_ϕ:

$$N_\phi = \frac{3}{5}N_e - 1 \tag{5.14}$$

We study the case $N_e = 10, N_\phi = 5$ on the sphere. In the SU(4) limit, the parent irreducible representation is (6,2,2,0) with energy $-6.60948e^2/(\varepsilon l)$. By taking into account anisotropies, the (6,2,2,0) irreducible representation is the lowest-lying energy irreducible representation for $N_e = 10, N_\phi = 5$. Its energy level spectrum is shown in Fig. 5.5.

There are differences between the phase diagrams calculated by using the variational method (Fig. 5.6a) and the exact diagonalization method (Fig. 5.6b). The former is obtained from the results of subsection 4.6.2 by substituting $\nu = 1/3$ and consists of 4 phases: A, B, F, and E. The later is obtained by extracting the quantum numbers of the ground states from exact diagonalization results and contains 5 phases: A, B, C, E_1 and E_2. The corresponding spinor composition and quantum numbers are shown in Table. 5.4.

1. **Phase A** spans the region $\pi/4 < \theta < 3\pi/4$. It can be described by the spinor composition $\{|K, \mathbf{s}_1\rangle, |K', \mathbf{s}_2\rangle, |K', -\mathbf{s}_2\rangle\}$ and the quantum numbers $T^z = 1, S = 3$. Phase A has Ising valley order.

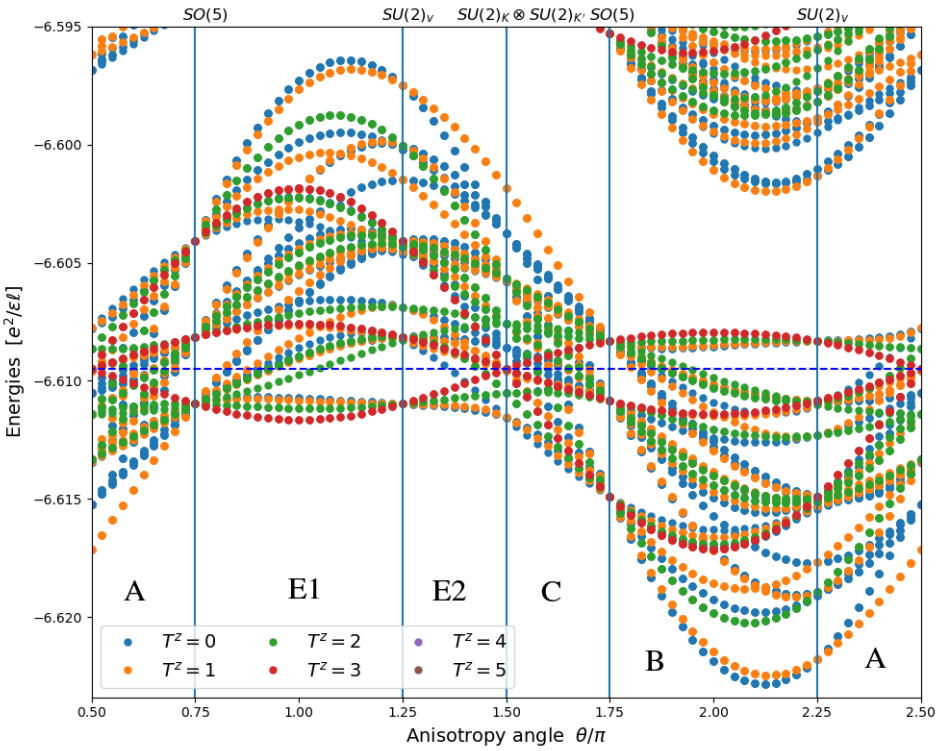

Figure 5.5: Energy levels of the filling factor $\nu = 5/3$ with $N_e = 10, N_\phi = 5$ as a function of the anisotropy angle θ. The unperturbed parent state belongs to the irreducible representation (6,2,2,0). This irreducible representation is the lowest-lying state for $N_e = 10, N_\phi = 5$. The energy of the SU(4) parent state is $E = -6.60948e^2/\varepsilon l$ (dashed blue horizontal line). The vertical lines mark the high symmetry lines of the model we use.

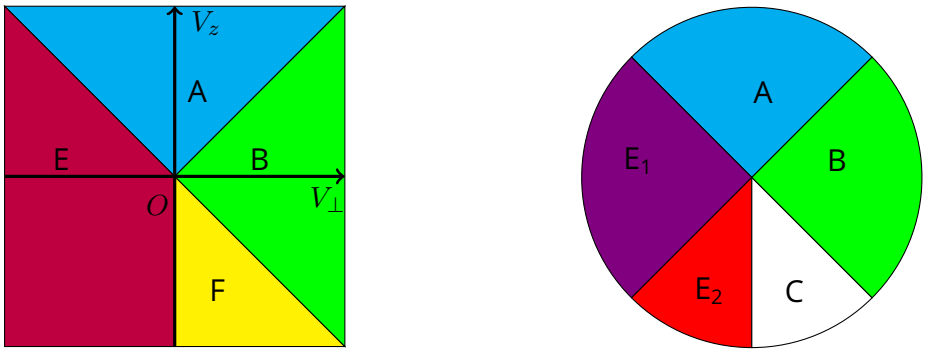

(a) Variational method

(b) Exact diagonalization

Figure 5.6: Phase diagrams of the $(1, 1/3, 1/3)$ state calculated by using (a) the variational method and (b) exact diagonalization.

Variational method		Exact diagonalization	
Phase	Spinor composition	Phase	Quantum numbers
A	$\{\|K,\mathbf{s}_1\rangle, \|K',\mathbf{s}_2\rangle, \|K',-\mathbf{s}_2\rangle\}$	A	$T^z=1, S=3$
B	$\{\|\mathbf{t}_\perp,\mathbf{s}_1\rangle, \|-\mathbf{t}_\perp,\mathbf{s}_2\rangle, \|-\mathbf{t}_\perp,-\mathbf{s}_2\rangle\}$	B	$T^z=0, S=3$
F	$\{\|K,\mathbf{s}\rangle, \|K',\mathbf{s}\rangle, \|K,-\mathbf{s}\rangle\}$	C	$T^z=0, S=0$
E	$\{\|\mathbf{t}_1,\mathbf{s}\rangle, \|\mathbf{t}_2,-\mathbf{s}\rangle, \|-\mathbf{t}_2,-\mathbf{s}\rangle\}$	E_1	$T^z=3, S=1$
		E_2	$T_z=0, S=1$

Table 5.4: Spinor composition (variational method) and quantum numbers (exact diagonalization) of the phases of the $(1,1/3,1/3)$ state.

2. **Phase B** spans the region $-\pi/4<\theta<+\pi/4$. It has the same spin polarization as phas A, but has a XY valley order instead. We can describe phase B by the spinor composition $\{|\mathbf{t}_\perp,\mathbf{s}_1\rangle, |-\mathbf{t}_\perp,\mathbf{s}_2\rangle, |-\mathbf{t}_\perp,-\mathbf{s}_2\rangle\}$ with the quantum numbers $T^z=0, S=3$.

3. The transition between Phase A and Phase B is first-order and associated to the change of the Ising valley order of Phase A to the XY valley order of Phase B.

4. In the region $3\pi/4<\theta<3\pi/2$, the variational method predicts a **phase E** with flavor composition $\{|\mathbf{t}_1,\mathbf{s}\rangle, |\mathbf{t}_2,-\mathbf{s}\rangle, |-\mathbf{t}_2,-\mathbf{s}\rangle\}$. Exact diagonalization finds two different phases E_1 and E_2, separated by the transition line $\theta=5\pi/4$. Both E_1 and E_2 have spin $S=1$, but they have different valley orders:

   (a) **Phase E_1** lies in range $3\pi/4<\theta<5\pi/4$ and has Ising valley order. Its spinor composition is $\{|K,\uparrow\rangle, |K,\downarrow\rangle, |K',\downarrow\rangle\}$, corresponding to $\mathbf{t}_1=\mathbf{t}_2=K$, $\mathbf{s}=\uparrow$.

   (b) **Phase E_2** lies in range $5\pi/4<\theta<7\pi/4$ and has XY valley order. Its spinor composition is $\{|\mathbf{t}_\perp,\uparrow\rangle, |\mathbf{t}_\perp,\downarrow\rangle, |-\mathbf{t}_\perp,\downarrow\rangle\}$, corresponding to $\mathbf{t}_1=\mathbf{t}_\perp, \mathbf{t}_2=\pm\mathbf{t}_\perp$.

   (c) The phase transition between E_1 and E_2 changes the valley order between Ising-like order and XY-like order. The variational approach does not distinguish between the Ising and XY valley orders and shows that the two phases are energetically degenerate.

5. In the region $3\pi/2<\theta<7\pi/4$, there is the fifth phase that we call **Phase C**. Phase C is spin singlet $S=0$ and valley unpolarized $T^z=0$. This phase is not predicted by the variational method according to which in this region there is a phase F with Ising valley order. Finding a wavefunction with the correct quantum number for phase C remains an open question.

To explore the nature of the phase C, we calculated the pair correlations between electrons with different flavors. Here we denote the ground state as $|\Psi_{GS}\rangle$ and calculated the pair correlation functions for the ground state at $\theta=3\pi/2+\pi/8$ (phase C). The formula of the pair-correlation function between one electron in flavor $|\alpha\rangle$ and one electron in flavor $|\beta\rangle$, separated by a distance r is given by:

$$g_{\alpha\beta}(r)=\langle\Psi_{GS}|\int d^2\mathbf{r}_1 d^2\mathbf{r}_2\hat{\psi}^\dagger_\alpha(\mathbf{r}_1)\hat{\psi}^\dagger_\beta(\mathbf{r}_2)\delta(\mathbf{r}_1-\mathbf{r}_2-\mathbf{r})\hat{\psi}_\beta(\mathbf{r}_2)\hat{\psi}_\alpha(\mathbf{r}_1)|\Psi_{GS}\rangle \quad (5.15)$$

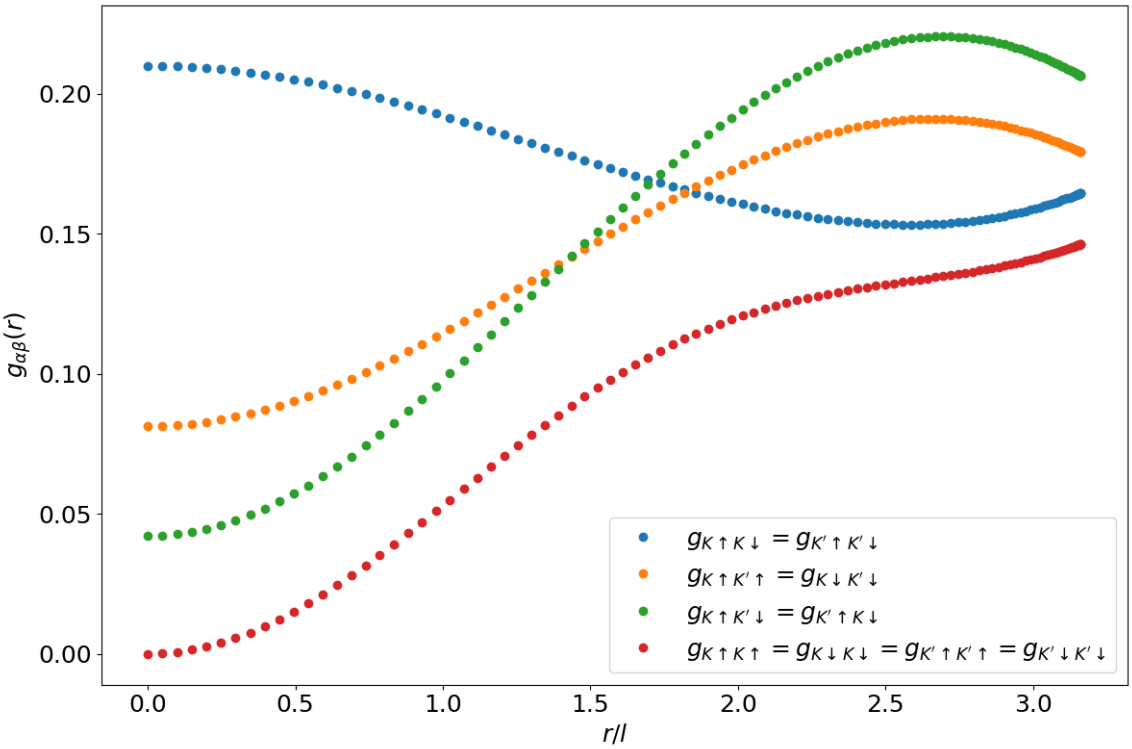

Figure 5.7: The pair correlation functions $g_{\alpha\beta}(r)$ calculated for phase C (anisotropy angle $\theta = 3\pi/2+\pi/8$). The results are calculated on the sphere for $N_e = 10$, $N_\phi = 5$.

In this formula, the coordinate on the sphere are $\mathbf{r}_{1,2} = R(\sin\theta_{1,2}\cos\phi_{1,2}, \sin\theta_{1,2}\sin\phi_{1,2}, \cos\theta_{1,2})$ where the radius of the sphere is related by the monopole strength by $R = \sqrt{|Q|}$ (see Appendix A). The chord distance is defined as $r = 2R\sin\dfrac{\theta}{2}$. In phase C, $S^z = 0$ and $T^z = 0$, so there are four independent combinations of spin and valley as shown in Fig. 5.7. At short distance, the leading correlation is $g_{K\uparrow K\downarrow}(0) = g_{K'\uparrow K'\downarrow}(0)$ and has a maximum value at $r = 0$. All the other three correlations have minimum at $r = 0$. This shows that the phase C forms spin singlet $S = 0$ pairs in each valley.

5.5 . Spin transitions

We consider the polarized and SU(2) singlet states of filling factor $\tilde{\nu} = 2/3$. In the absence of the Zeeman field, the singlet state has the lower Coulomb energy, so it is the ground state and the polarized state is the excited state. When the Zeeman energy gets stronger, the energy of the polarized state gets lower while the energy of the singlet state remains unchanged. At a critical magnetic field B_{crit}, the polarized state has lower energy than the singlet state and becomes the ground state. The crossing between the two levels happens when the Zeeman energy is strong enough to balance the difference ΔE in the Coulomb energy between the two states:

$$\Delta E = \epsilon_Z B_{crit} \tag{5.16}$$

The situation in graphene is more complicated. The energy per particle of the state i

is given by:

$$\varepsilon_i = E_{Ci} + a_i B + \varepsilon_Z m \tag{5.17}$$

where E_{Ci} is the Coulomb energy of the state i, which is proportional to $\sqrt{B}$. $a_i B$ is the anisotropy energy that is proportional to the magnetic field B. The third term $\varepsilon_Z m$ is the Zeeman energy, which depends on the magnetization per particles m and is also proportional to B because ε_Z is proportional to B.

We consider two states $i = 0$ and $i = 1$. Their energies are given by:

$$\begin{aligned} \varepsilon_0 =& E_{C0} + a_0 B + \varepsilon_Z m_0 \\ \varepsilon_1 =& E_{C1} + a_1 B + \varepsilon_Z m_1 \end{aligned} \tag{5.18}$$

A spin transition happens between the two states 0 and 1 when the Coulomb energy difference $\Delta\varepsilon_{01} = E_{C1} - E_{C0}$ equals to the contribution from anisotropies and Zeeman energy. It happens at a critical magnetic field B_{crit} such that:

$$\Delta\varepsilon_{01}(B_{crit}) = (a_0 - a_1 + z)B_{crit} \tag{5.19}$$

The Zeeman factor z depends on the magnetization of the two competing states. In graphene, z takes different values at different places of the anisotropy phase diagram.

In the previous sections, we studied the competition between numerous fractional quantum Hall states having the same filling factor but with different flavor partitions. In this section, we studied the spin transition between them. We restrict our examination to the case where the magnetic field is perpendicular to the graphene plane and ignore the effect of spin canting.

5.5.1 . Fraction $\tilde{\nu} = 2/3$

At filling factor $\tilde{\nu} = 2/3$, the polarized state is nonsenstive to short-range valley-dependent anisotropies (encoded in the Hamiltonian $\mathcal{H}_V$) while the singlet state has the phase diagram of 4 phases: F, AF, CDW, and KD. The KD and CDW phases are spin singlet and insensitive to the Zeeman effect. Hence, there is no spin transition between the singlet state in KD and CDW phase to the one-component polarized state. Therefore, we expect a spin transition towards the fully polarized state (F). When the magnetic field gets stronger, the AF phase turns into the CAF phase and becomes finally the fully polarized F phase beyond some field value. This fully polarized F state lowers in energy at the same rate as the one-component $\tilde{\nu} = 2/3$ state, and consequently there is no crossing. In conclusion, there is no spin transition for the $\tilde{\nu} = 2/3$ state.

5.5.2 . Fraction $\tilde{\nu} = 4/3$

For fraction $\tilde{\nu} = 4/3$, there are two competing states $(1, 1/3)$ and $(2/3, 2/3)$. The phase diagrams of these two states have the same shape: they have the same number of phases and the phases lie on the same domains. However, they have different total magnetizations. The phase F in both cases have the same total spin value, so there is no crossing and no transition between the two states as we increase the magnetic field: both stay in their ferromagnetic state and the occupation of electrons in the components remains unchanged. For the phases KD and CDW, the state $(2/3, 2/3)$ has no net magnetization, while the state $(1, 1/3)$ has a net magnetization due to unequal occupation between the two components. For this reason, we expect a spin transition between the two states $(2/3, 2/3)$ and $(1, 1/3)$ when they are in those two phases.

5.5.3 . Fraction $\tilde{\nu} = 5/3$

For fraction $\tilde{\nu} = 5/3$, there are two competing states $(1, 2/3)$ and $(1, 1/3, 1/3)$. Their phase diagrams have different shapes and do not overlap in the $(V_\perp, V_z)$ plane, leading to a more complicated situation. We use the phase diagram of the $(1, 2/3)$ state as reference to examine the spin transition. In the region $-\pi/4 < \theta < +\pi/2$, the higher energy $(1, 2/3)$ state stays in the ferromagnetic phase and is fully spin polarized $M = M_{sat}$. In this region, the lower energy $(1, 1/3, 1/3)$ state stays in phase A or phase B, and is partially spin polarized $M = M_{sat}/\tilde{\nu} = 3M_{sat}/5$. Consequently, we expect a spin transition between the two states. In the region $+\pi/2 < \theta < +3\pi/4$, the $(1, 2/3)$ state stays in the AF phase with magnetization $M = M_{sat}/3$ while the $(1, 1/3, 1/3)$ state stays in the phase A with magnetization $M = M_{sat}/\tilde{\nu}$. We also expect a spin transition between the AF phase with flavor occupation fractions $(1, 2/3)$ and the A phase with flavor occupation fractions $(1, 1/3, 1/3)$. In the region $+3\pi/4 < \theta < +7\pi/4$, the $(1, 2/3)$ state stays in the KD and CDW phases and has magnetization $M = M_{sat}/5$. In this region, the $(1, 1/3, 1/3)$ state stays in phase C with $M = 0$ and phases E_1, E_2 with magnetization $M = M_{sat}/5$. It shows that there is no spin transition in the domains of the phases E_1 and E_2, whereas there is spin transition in the other regions of the phase diagram. The critical magnetic field B_{crit} is phase-dependent because there are the contributions a_i from anisotropies to the value of the critical field, and they are still unknown.

We summarize the general picture of spin transitions. Under small Zeeman energy, the states with maximal spread-out of electrons in various spin-valley components such as $(2/3, 2/3)$ and $(1, 1/3, 1/3)$ are preferred. At high Zeeman energy, spin transitions occur, leading to the transition to fewer-component states like $(1, 1/3)$ and $(1, 2/3)$.

5.6 . Conclusion

In this chapter, we have studied the effect of short-range valley-dependent anisotropies on graphene in the fractional quantum Hall regime. In the case of the two-component states (1/3,1/3), (2/3,2/3) and (1,2/3), the phase diagram is similar to that of the charge neutrality case $\nu = 0$. The phase diagram consists of four phases: F, AF, KD, and CDW. This phase diagram is given by exact diagonalizations in agreement with a variational approach involving Coulomb eigenstates. The quantum numbers of the phases are the same as in the case of charge neutrality for states (1/3,1/3) and (2/3,2/3) because they have equal occupation numbers in both components.

For state (1,2/3), due to the unequal occupation numbers between the two components, the phases AF, KD and CDW are partially spin polarized. In this case, the first-order phase transition between the AF and the CDW phases involves level crossing, because those phases do not have the same quantum numbers. This aspect is different to the cases where the two occupied components have the same filling factor. We also recognize an emergent SU(2) valley symmetry for the phase F, even though the Hamiltonian does not have this symmetry. This is because the (1,2/3) state is the particle-hole symmetric of the one-component Laughlin state, which does not feel point-contact short-range valley interaction, and consequently the later cannot lift its energy levels.

In the case of the (1,1/3) state, there are also four phases and the shape of the phase

diagram is similar to that of the previous cases. However, the quantum numbers are not those predicted by the variational method. The fully spin-polarized F phase also escapes the effect of the short-range valley-dependent anisotropies and exhibits the emergent SU(2) valley symmetry, similar to the case of the (1,2/3) state. The quantum numbers of the KD-like and the CDW-like phases are correctly predicted. However, the AF phase is spin singlet and has no net valley polarization.

The most interesting case is the state (1,1/3,1/3). There are five phases, two of them are predicted variationally. They lie in the region where $V_\perp + V_z > 0$. There are also two phases which differ in the Ising and XY-valley polarization, but according to the variational approach, they are degenerate. Notably, the last phase is spin singlet and has no net valley polarization while the variational approach predicts that it has Ising-like valley. This phase occurs in the region of negative Ising-like anisotropies. Actually, there is no wavefunction which were able to describe its behavior. The nature of this phase remains an open question. Experimentally realizing this phase requires low Zeeman energy to prevent phase transition to the more polarized (1,2/3) state.

Present experiments are likely to observe the two-component states (1,1/3) and (1,2/3). In samples with hBN substrate, the sublattice-splitting energy is of the order of meV to tens of meV, and is comparable to the Coulomb energy scale, so the valley degree of freedom is likely to be polarized, preferring two-component states. At charge neutrality $\nu = 0$, the effect of the sublattice-splitting energy is to shift the phase diagram so that the region of stability of the valley-polarized CDW phase smears out over the other phases for weak $V_\perp$ and V_z. The critical value of the magnetic field of the transition between singlet state and polarized state should be small and we are still uncertain about this critical value.

Actual experiments mainly focus on identifying the phase at charge neutrality $\nu = 0$. Though, isospin transition was observed for fractional quantum Hall states for various filling factors [97], suggesting a plethora of phase transitions whose nature needs to be investigated. By the way, recent scanning tunelling microscopy experiments have given evidence of a more complicated picture at charge neutrality $\nu = 0$, beyond the scope of the standard theory [31, 71]. Finally, experimentally controlling the parameters $V_\perp$ and V_z is still an open question.

Chapter6 - Quantum Hall effect in Bernal-stacked Bilayer graphene

6.1 . Introduction to the chapter

We move on to the second project of my thesis: *Competition between Laughlin state and Wigner crystal in Bernal-stacked bilayer graphene*. The results of this project are published in Ref. [105]. The content of this project spans over three chapters: In this chapter we review bilayer graphene and the quantum Hall effect in this material. Chapter 7 is a short review about the Wigner crystal phase - the solid of electrons - which is a competing phase to the quantum Hall liquid. And finally chapter 8 will present the result of our work: the competition between the quantum Hall liquid and the Wigner crystal in Bernal-stacked bilayer graphene at filling factor $\nu = 1/3$.

Bernal-stacked bilayer graphene (BLG) contains two monolayer graphene layers, stacked together so that one atom of the upper layer is above one atom of the lower layer, while the other two atoms do not have counterpart in the opposite layer. The two Landau levels $N = 0$ and $N = 1$ of BLG are nearly degenerate. They allow us to define the orbital degree of freedom, acting like a pseudospin with two values $N = 0$ (pseudospin-up) and $N = 1$ (pseudospin-down). This degree of freedom offers an easy way to control the many-body physics in BLG, due to its tunability. The eight single-electron states inside the central Landau level are characterized by three quantum numbers: spin, valley and orbital. One can control the energy splitting between any two of those eight single-electron levels by either changing the Zeeman and the pseudo-Zeeman energies. Hence, there are a plenty of single-electron level crossings inside the central Landau level. It promises to discover special properties of the quantum Hall physics in the vicinity of those level crossings.

In this chapter, we will begin by reviewing the experimental situation of the quantum Hall effect in BLG. And then, we will show the BLG crystalline and electronic structures. We will discuss the effective four-band model and derive a simpler low-energy two-band model. After that, we derive the Landau level spectrum using the two-band model. We will focus on the central Landau level and define the two parameters γ and Δ_{10} controlling the physics of this eightfold nearly degenerate Landau level. We will finish the chapter by discussing the Coulomb interaction and screening. The chapter prepares the necessary knowledge to discuss the competition between quantum Hall liquid and Wigner crystal in chapter 8.

6.2 . Experiments on the quantum Hall effect in Bernal-stacked Bilayer graphene

The quantum Hall effect was discovered in BLG in 2006 [22]. At that time, physicists knew two types of quantum Hall effects. The first one is the quantum Hall effect in conventional semiconductors (see Fig. 6.1a). It corresponds to the integral quantization of the Hall conductivity $\sigma_{xy} = Nge^2/h (N \in \mathbb{N})$ where g is the degeneracy due to the presence of the spin and valley degrees of freedom. The Landau levels in this quantum Hall

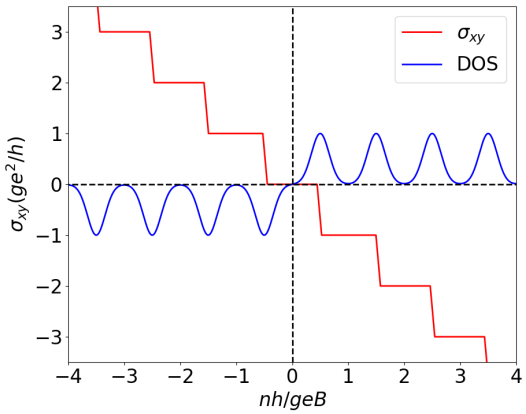

(a)

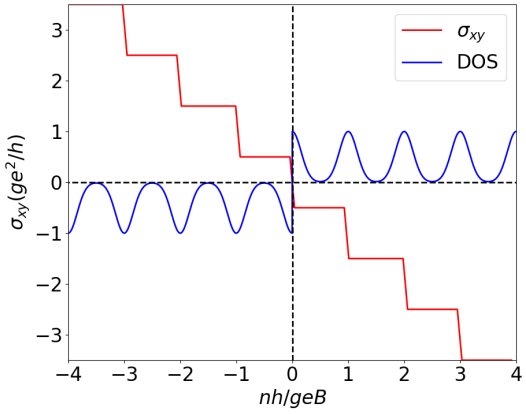

(b)

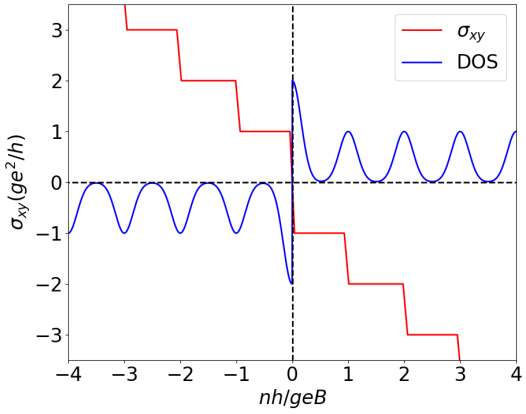

(c)

Figure 6.1: 3 types of quantum Hall effects: (a) The quantum Hall effect in conventional semiconductors. The Hall conductivity is quantized at integer values of ge^2/h. (b) The quantum Hall effect in monolayer graphene. The values of the Hall conductivity is shifted by 1/2 step compared to the Hall conductivity in conventional semiconductors. (c) The quantum Hall effect in BLG. The step of the Hall plateau at density $n = 0$ has twice the height as the other steps. In both cases (b) and (c) the central Landau level is half-filled at charge neutrality $n = 0$, represented by two maxima in density of states for electrons and holes at both sides of the vertical axis.

effect have spectrum $E_N = \hbar\omega_c(N + 1/2)(N \in \mathbb{N})$. The second kind of quantum Hall effect is the relativistic quantum Hall effect in monolayer graphene, which is associated to the half-integer quantization of the Hall conductivity $\sigma_{xy} = (N + 1/2)ge^2/h(N \in \mathbb{N})$ (Fig. 6.1b). Here $g = 4$ due to the presence of the spin and valley degrees of freedom. The Landau levels in this quantum Hall effect have spectrum $E_N = \pm\hbar\omega_c\sqrt{N}(N \in \mathbb{N})$. Its central Landau level has zero energy and is half-filled at charge neutrality. We discussed these kinds of quantum Hall effects in Chapters 2 and 3, respectively.

The quantum Hall effect in BLG is the third type of quantum Hall effect (Fig. 6.1c). It shows an integer quantization of the Hall conductivity $\sigma_{xy} = Nge^2/h(N \in \mathbb{N}, N \geq 1)$. The degeneracy is $g = 4$ because low-energy electrons in BLG have the spin and valley degrees of freedom. However, experiments do not observe the plateau $\sigma_{xy} = 0$ (Fig. 6.2). Nevertheless, the step at which σ_{xy} passes through the value 0 has twice the height as all the other steps. This transition happens when the electron density is $n = 0$, at which the longitudinal resistance ρ_{xx} has a high and broad peak. It suggests that the transition from the lowest hole level to the lowest electron level requires twice the number of carriers needed for the transitions between the other Landau levels. This implies that the central Landau level in BLG has a double degeneracy compared to all the other Landau levels. This experimental result is consistent with the theory, according to which the two Landau levels $N = 0$ and $N = 1$ are approximately energetically degenerate [106]. The approximate degeneracy of these two Landau levels allows for defining the orbital degree of freedom. Here the orbital $N = 0$ plays the role of the pseudospin-up while the orbital $N = 1$ plays the role of the pseudospin-down. These two nearly degenerate orbitals, with the spin and valley degrees of freedom form an eightfold nearly degenerate central Landau level. This central Landau level octet provides a richer example of the quantum Hall ferromagnetism [107].

The quantum Hall effects with all integer filling factor $-4 \leq \nu \leq 4$ were observed in BLG [109, 110]. They show evidence for the splitting of the central Landau level octet. Similarly to monolayer graphene, this phenomenon is explained by the breaking of the SU(4) symmetry of the Coulomb energy. Unlike monolayer graphene, it was difficult to observe the fractional quantum Hall effect in BLG. In 2010, Bao et al. observed a plateau-like feature near the filling factor $\nu = 1/3$, but this plateau is not fully developed to be considered as an incompressible state [23]. The first accepted evidence of the fractional quantum Hall effect in BLG was published in 2014. Kou et al. performed local compressibility measurement on high-quality BLG on hBN substrate and observed the sequences $\nu = 2p + 2/3$ and $\nu = 2p + 3/5$ with $p = -2, -1, 0, +1$ [25]. The even-denominator incompressible states were observed the same year by Ki et al. [24] and then in later experiments [108, 111]. These results pave the way to study non-abelian quantum Hall effects in the BLG platform and promise potential applications of topological quantum computing.

The approximate degeneracy of the two orbitals $N = 0$ and $N = 1$ can be lifted by applying an external electric field perpendicular to the BLG plane. Indeed, BLG is a zero-gap material, but one can open a band gap when the sample is subjected to a perpendicular electric field, such as in a gated system [112]. Moreover, this band gap is tunable, promising the creation of graphene-based field-effect devices. This property still occurs under a strong magnetic field. Here the two orbitals are separated by the splitting energy, which is tunable by controlling the applied electric field [113].

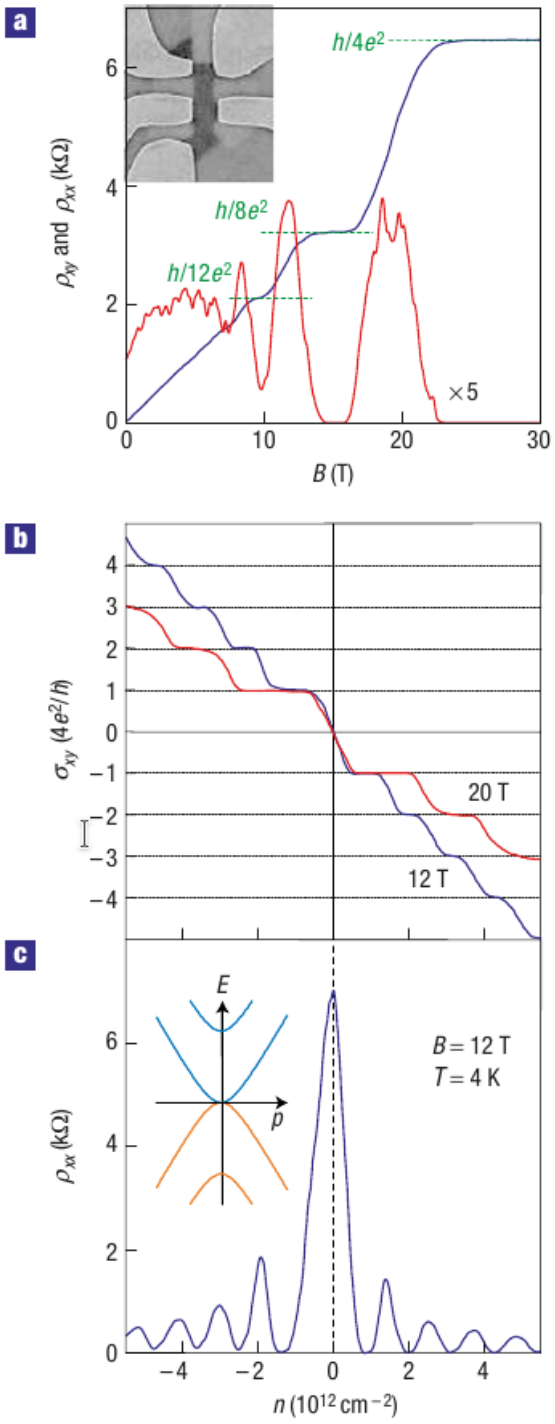

Figure 6.2: (a) Hall resistivity ρ_{xy} and longitudinal resistivity ρ_{xx} of BLG as a function of the magnetic field at fixed electron density $n = 2.5 \times 10^{12}$ cm^{-2}. Here we observe three plateaus corresponding to the filling factors $\nu = 4, 8, 12$. (b) The Hall conductivity σ_{xy} and longitudinal resistivity ρ_{xx} of BLG under magnetic field. Hall plateaus were observed for $\sigma_{xy} = N4e^2/h(|N| \geq 1)$. There is no Hall plateau corresponding to $\sigma_{xy} = 0$ and $n = 0$. (c) The longitudinal resistance ρ_{xx} has a high and broad peak at $n = 0$. This suggests that the central Landau level in BLG has twice the degeneracy than the other Landau levels. The figure is taken from Ref. [22]. *Reuse with permission from Springer Nature.*

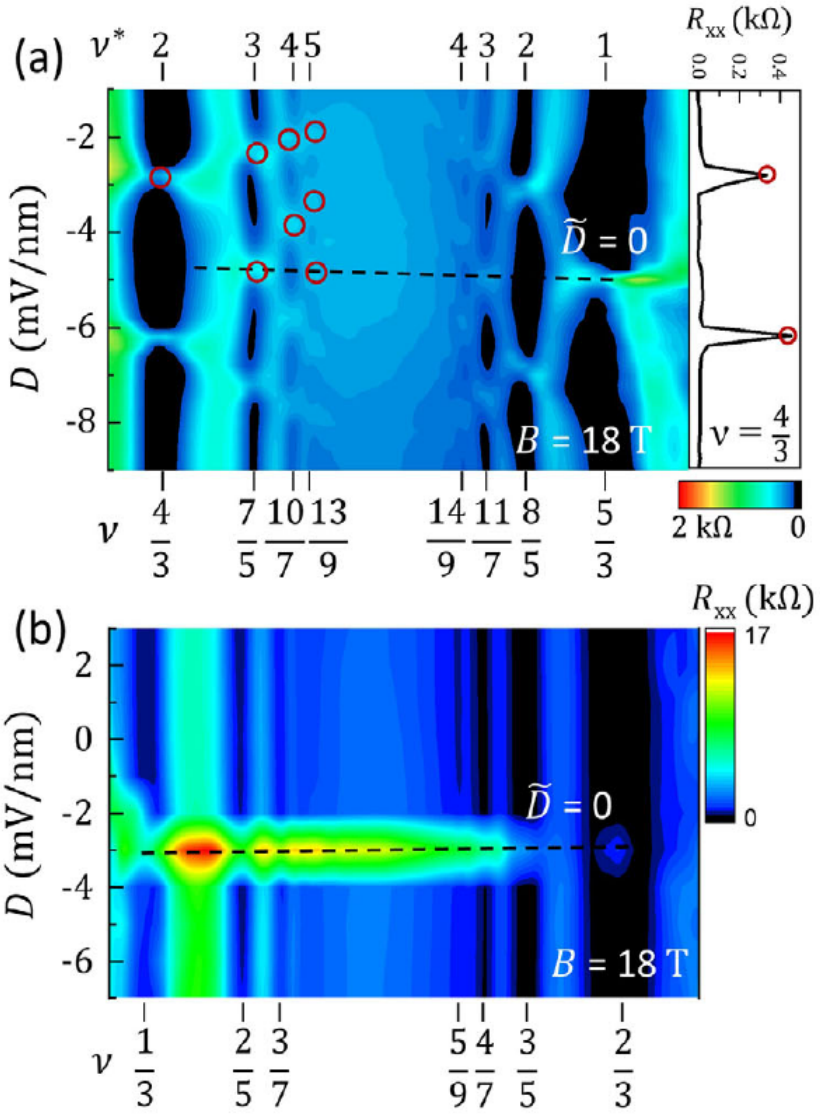

Figure 6.3: The false color map R_{xx} of BLG as a function of the filling factor ν and the electric displacement D between the two BLG layers for filling factors (a) $4/3 < \nu < 5/3$ and (b) $1/3 < \nu < 2/3$. The red circles indicate the valley isospin transition at filling factors $\nu = 4/3, 7/5, 10/7, 13/9$. There is no isospin transtion for filling factor $1/3 < \nu < 2/3$, showing that the ^{2}CFs in this range of filling factor are valley polarized. In this figure $\tilde{D} = D + 12.5\,\mathrm{mV\,nm^{-1}}$. The figure is taken from Ke Huang, Hailong Fu, Danielle Reifsnyder Hickey, Nasim Alem, Xi Lin, Kenji Watanabe, Takashi Taniguchi, and Jun Zhu, Phys. Rev. X 12, 031019 (2022) [108].

The appearance of intermediate integer filling factors in the central Landau level shows that the SU(4) symmetry of the spin and valley degrees of freedom is broken, giving rise to symmetry-breaking orders. We studied this phenomenon in monolayer graphene in Chapters 3 and 4. Various experimental works observed various symmetry-breaking phases and signature of phase transitions in integer [114–118] and fractional [108, 117, 119] quantum Hall regimes. Experiments on dual-gated BLG by Kim et al. shows a phase transition between a spin-polarized phase to a valley polarized-phase at charge-neutrality [120]. In 2014, Maher et al. observed the phase transition from the canted antiferromagnetic phase to a ferromagnetic phase [121]. Recently, Huang et al. observed the valley isospin transitions for Jain sequences $\nu = 4/3, 7/5, 10/7, 13/9$ while the states in the range of filling factor $1/3 < \nu < 2/3$ are valley polarized (Fig. 6.3) [108]. Several theoretical works also studied this phenomenon [122–124].

In those experiments, the interlayer potential bias, which induces the perpendicular electric field, plays a crucial role in controlling the phase transition. Especially in the orbital $N = 0$, single-electron wavefunctions with a defined valley quantum number are localized in one of the two layers, so that the valley and the layer degrees of freedom coincide. In this case, a large external electric field is able to create a layer polarized state, or in other words, a valley polarized state. By contrast, controlling the valley polarization in monolayer graphene is more difficult, and one should visualize the electron distribution using Scanning Tunneling Spectroscopy to make a conclusion on the valley polarization of the state.

Because the central Landau level octet can be split due to symmetry breaking, a key question is: in what order the eight components with different valley, spin and orbitals are filled as the electrons are added to the system? In 2017, Hunt et al. developed a layer polarization technique to determine the valley and orbital quantum numbers of the incompressible states [125]. They also established a theoretical model of spin, valley and orbital in the central Landau level. This model permits to determine the order the sub-Landau levels are filled knowing the values of the external magnetic and electric fields. According to this model, the phase transitions occur at the crossing points between the single-particle levels having different spin, valley, and orbital quantum numbers.

6.3 . Crystal structure of Bernal-stacked Bilayer graphene

The crystal structure of Bernal-stacked bilayer graphene (BLG) is shown in Fig. 6.4. The structure consists of two parallel graphene sheets, each has lattice parameter a =2.46 Å and two sublattices A and B. They are separated by a distance c =1.42 Å. By denoting the top layer by the index 1 and the bottom layer by the index 2, we denote the corresponding lattice sites (sublattices) by A1, B1, A2, and B2. Those four atoms are located at the positions: A1$\left(\frac{a}{2}, -\frac{a}{2\sqrt{3}}, c\right)$, B1$(0, 0, c)$, A2$(0, 0, 0)$, and B2$\left(\frac{a}{2}, \frac{a}{2\sqrt{3}}, 0\right)$. The bond joining the two sites A2 and B1 is perpendicular to the graphene plane, so these two sites are called the *dimer sites*. They are directly coupled by a relatively strong interlayer coupling. The two remaining sites A1 and B2 are called *non-dimer sites*. Therefore, a primitive cell of BLG contains four atoms. The primitive

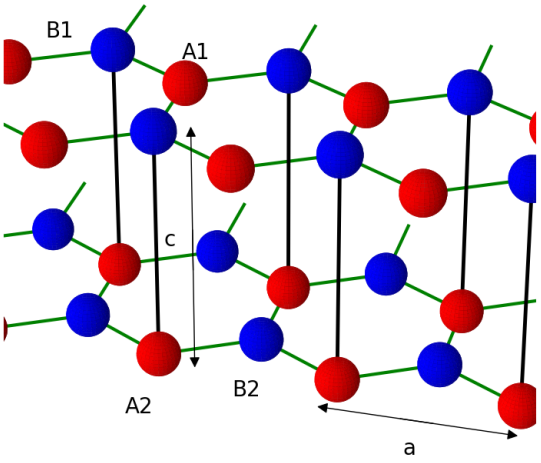

Figure 6.4: Crystal structure of Bernal-stacked Bilayer graphene. The structure consists of two layers (top layer-1 and bottom layer-2). Each layer is a graphene sheet having two sites A and B. Therefore, there are in total four sites: A1, B1, A2 and B2. The lattice parameter of each graphene layer is $a = 2.46$Å. The distance separating the two layers is $c = 1.42$Å. The bond joining the sites A2 and B1 is perpendicular to the graphene plane. Those sites are called the *dimer sites*. Here the atoms A are red and the atoms B are blue.

lattice vectors are the same as those of monolayer graphene:

$$\begin{aligned} \mathbf{a}_1 =& (a, 0) \\ \mathbf{a}_2 =& \left(\frac{a}{2}, \frac{\sqrt{3}}{2}a\right) \end{aligned} \tag{6.1}$$

This implies that the first Brillouin zone is a hexagonal and the primitive vectors of the reciprocal lattice are:

$$\begin{aligned} \mathbf{b}_1 =& \left(\frac{2\pi}{a}, \frac{2\pi}{\sqrt{3}a}\right) \\ \mathbf{b}_2 =& \left(\frac{2\pi}{a}, -\frac{2\pi}{\sqrt{3}a}\right) \end{aligned} \tag{6.2}$$

The two K-points are also located at $K\left(\frac{4\pi}{3a}, 0\right)$ and $K'\left(-\frac{4\pi}{3a}, 0\right)$ as in monolayer graphene.

6.4 . Electronic structure of Bernal-stacked Bilayer graphene

6.4.1 . Band structure: tight-binding model

In this section, we calculate the band structure of BLG by using the tight-binding method. Early tight-binding models of BLG were based on the model developed by

Slonczewski-Weiss-McClure (SWM) for graphite [126, 127]. One can find a detailed proof of the tight-binding model in the review by McCann and Koshino [128]. An accurate tight-binding model taking into account up to 17 nearest-neighbors was proposed by Jung and MacDonald [129]. Here we employ the tight-binding approximation to the nearest-neighbors.

As previously mentioned, a unit cell of BLG contains 4 atoms: A1, B1, A2, and B2. Each atom in the unit cell contributes one electron from its p_z orbital. In the tight-binding model, we denote each atom as well as its p_z orbital by the index $m = 1, \ldots, 4$. Let N be the total number of unit cells in the sample, we denote the unit cells by the index $i = 1, 2, \ldots, N$. The position $\mathbf{R}_i$ of the unit cell is coincident with the position of the B1 atom. The position of the atom m (m =A1, B1, A2, B2) in the unit cell i is determined by the vector $\mathbf{R}_{mi} = \mathbf{R}_i + \boldsymbol{\tau}_m$ where: $\boldsymbol{\tau}_1 = \mathbf{0}$ for A2, $\boldsymbol{\tau}_2 = \left(\frac{a}{2}, \frac{a}{2\sqrt{3}}, 0\right)$ for B2, $\boldsymbol{\tau}_3 = (0, 0, c)$ for B1, and $\boldsymbol{\tau}_4 = \left(\frac{a}{2}, -\frac{a}{2\sqrt{3}}, c\right)$ for A1.

We denote $\phi_m(\mathbf{r})$ the atomic wavefunction of the p_z orbital of atom m ($1 \leq m \leq 4$). Here we express the atomic wavefunction under the form of Maximally Localized Wannier Functions (MLWF) as in Ref. [129]. The expression for the Bloch wavefunction of momentum $\mathbf{k}$ for the orbital m is:

$$\Phi_{\mathbf{k},m}(\mathbf{r}) = \frac{1}{\sqrt{N}} \sum_{i=1}^{N} e^{i\mathbf{k}\cdot\mathbf{R}_{mi}} \phi_m(\mathbf{r} - \mathbf{R}_{mi}) \tag{6.3}$$

or in bra-ket form:

$$|\Phi_{\mathbf{k}m}\rangle = \frac{1}{\sqrt{N}} \sum_{i=1}^{N} e^{i\mathbf{k}\cdot\mathbf{R}_{mi}} |\phi_m(\mathbf{R}_{mi})\rangle \tag{6.4}$$

The Hamiltonian of the tight-binding model up to nearest-neighbor is given by:

$$H = \begin{bmatrix} \varepsilon_{A1} & -\gamma_0 f(\mathbf{k}) & \gamma_4 f(\mathbf{k}) & \gamma_3 f(\mathbf{k})^* \\ -\gamma_0 f(\mathbf{k})^* & \varepsilon_{B1} & \gamma_1 & \gamma_4 f(\mathbf{k}) \\ \gamma_4 f(\mathbf{k})^* & \gamma_1 & \varepsilon_{A2} & -\gamma_0 f(\mathbf{k}) \\ \gamma_3 f(\mathbf{k}) & \gamma_4 f(\mathbf{k})^* & -\gamma_0 f(\mathbf{k})^* & \varepsilon_{B2} \end{bmatrix} \tag{6.5}$$

The matrix is written in the basis $(\phi_{A1}, \phi_{B1}, \phi_{A2}, \phi_{B2})$. The structure factor has the same expression as in the case of monolayer graphene:

$$f(\mathbf{k}) = e^{ik_y \frac{a}{\sqrt{3}}} + 2e^{-ik_y \frac{a}{2\sqrt{3}}} \cos\frac{k_x a}{2} \tag{6.6}$$

The hopping parameters are defined as follows:

- γ_0 is the *intralayer hopping parameter* and has the formula:

$$\gamma_0 = -\langle \phi_{A1}(\mathbf{R}_i) | H | \phi_{B1}(\mathbf{R}_j) \rangle \tag{6.7}$$

  where the two atoms A1 and B1 are nearest-neighbors locating on the top layer. γ_0 is also the hopping parameter between the two sites A2 and B2.

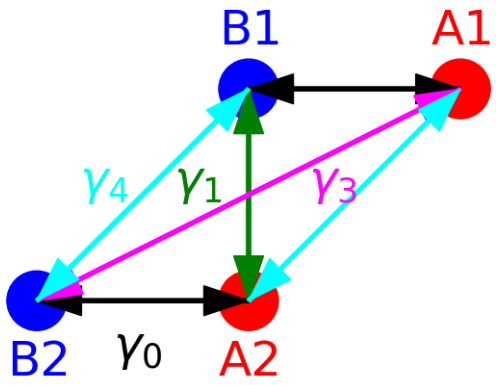

Figure 6.5: Definition of the hopping parameters between different atomic sites of the BLG lattice.

- γ_1 is the *hopping parameter between dimer sites*:

$$\gamma_1 = \langle \phi_{B1}(\mathbf{R}_i)|H|\phi_{A2}(\mathbf{R}_i)\rangle \tag{6.8}$$

- γ_3 is the *hopping parameter between non-dimer sites*:

$$\gamma_3 = \langle \phi_{A1}(\mathbf{R}_i)|H|\phi_{B2}(\mathbf{R}_j)\rangle \tag{6.9}$$

- γ_4 is the *interlayer hopping parameter between dimer site and non-dimer site*:

$$\gamma_4 = \langle \phi_{A1}(\mathbf{R}_i)|H|\phi_{A2}(\mathbf{R}_j)\rangle \tag{6.10}$$

We visualize the hopping parameters between nearest neighbors in Fig.6.5. The matrix elements ε_{A1}, ε_{B1}, ε_{A2} and ε_{B2} are the on-site energies of the orbitals. We impose the energy reference to be the average of the energy of the two non-dimer sites A1 and B2: $0 = \frac{\varepsilon_{A1} + \varepsilon_{B2}}{2}$. We define the following parameters:

- The *interlayer asymmetry* or the *interlayer bias*:

$$u = \frac{1}{2}[(\varepsilon_{A1} + \varepsilon_{B1}) - (\varepsilon_{A2} + \varepsilon_{B2})] \tag{6.11}$$

  The interlayer bias is due to a voltage difference between the two layers 1 and 2. It is associated to an external electric field $\mathbf{E}$ perpendicular to the BLG plane. The interlayer bias and the electric field strength are related by $|u| = eEc$.

- The *energy difference between dimer and non-dimer sites*:

$$\Delta' = \frac{1}{2}[(\varepsilon_{B1} + \varepsilon_{A2}) - (\varepsilon_{A1} + \varepsilon_{B2})] \tag{6.12}$$

- The *energy difference between A's sites and B's sites*:

$$\delta_{AB} = \frac{1}{2}[(\varepsilon_{A1} + \varepsilon_{A2}) - (\varepsilon_{B1} + \varepsilon_{B2})] \tag{6.13}$$

  This energy difference is dependent on the substrate, which induces strain between sublattices, giving rise to substrate-induced sublattice splitting energy similar to the case of monolayer graphene.

We can express the on-site energies as follows:

$$\begin{aligned}
\varepsilon_{A1} =& \frac{1}{2}(u + \delta_{AB}) \\
\varepsilon_{B1} =& \frac{1}{2}(u + 2\Delta' - \delta_{AB}) \\
\varepsilon_{A2} =& \frac{1}{2}(-u + 2\Delta' + \delta_{AB}) \\
\varepsilon_{B2} =& \frac{1}{2}(-u - \delta_{AB})
\end{aligned} \tag{6.14}$$

Numerical calculations of Ref. [129] give the values of the hopping parameters: $\gamma_0 = 3.010\text{eV}$, $\gamma_1 = 0.3310\text{eV}$, $\gamma_3 = 0.13912\text{eV}$ and $\gamma_4 = 0.09244\text{eV}$. Infrared spectroscopy experiments give: $\gamma_0 = 3.16\text{eV}$, $\gamma_1 = 0.381\text{eV}$, $\gamma_3 = 0.38\text{eV}$, $\gamma_4 = 0.14\text{eV}$, $\Delta' = 0.022\text{eV}$, $\delta_{AB} = 0$ [130]. The interlayer bias u can be controlled by tuning an electric field $\mathbf{E}$ perpendicular to the BLG plane.

If we neglect the hopping parameters γ_3 and γ_4, the Hamiltonian (6.5) gives four bands with energy:

$$E_{\pm}(\mathbf{k}) = \pm\sqrt{\gamma_0^2|f(\mathbf{k})|^2 + \frac{\gamma_1^2}{2} \pm \gamma_1\sqrt{\gamma_0^2|f(\mathbf{k})|^2 + \frac{\gamma_1^2}{4}}} \tag{6.15}$$

Fig. 6.6a gives the band structure of BLG, plotted in the 2-dimensional reciprocal space. The Hamiltonian (6.5) gives four bands: two conduction bands and two valence bands. The two bands in each pair of conduction bands or valence bands are split by an energy of the order γ_1 in most of the Brillouin zone. In the vicinity of the K-points, one valence band (the second lowest band) and one conduction band (the third lowest band) touch each other, while the other valence band and the other conduction band are split away. The two touching bands arise from the coupling between the orbitals of the non-dimer sites A1 and B2. They are also called *low-energy bands*. Whereas, the two split bands arise from the coupling between the atomic orbitals of the atoms B1 and A2 at the dimer sites, resulting in their strong energy splitting. In undoped BLG, the Fermi level also lies at the touching point of the two low-energy bands. Therefore, as in monolayer graphene, the momenta in the vicinity of the two K-points are of interest for the studies of the low-energy physics. Unlike monolayer graphene, the low-energy bands in BLG have parabolic dispersion instead of a linear relativistic-like dispersion (Fig. 6.6b).

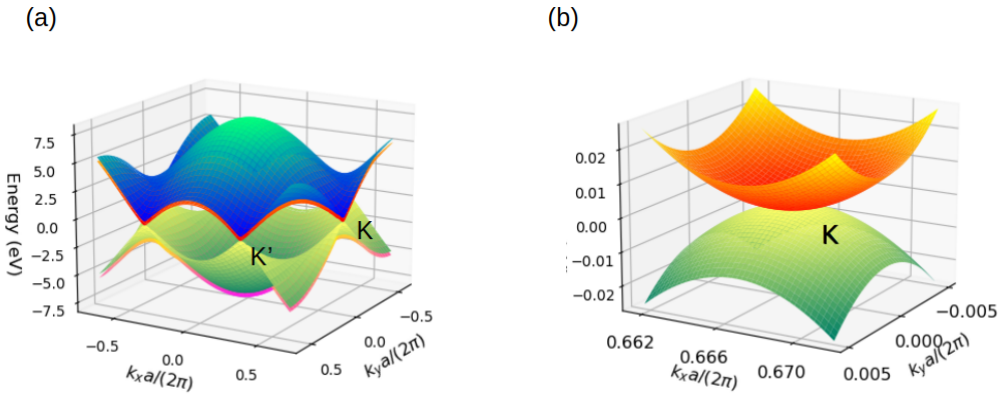

Figure 6.6: (a) Band structure of BLG in the first Brillouin zone. The plot was calculated from the approximate solution (6.15). There are 4 bands: the second lowest band and the third lowest band touch each other at the K-points. (b) In the vicinity of the point K, the dispersion is parabolic.

6.4.2 . Effective four-band model

The two inequivalent points K and K' define the valley degree of freedom. As in monolayer graphene, the valley degree of freedom is twofold degenerate and plays the role of a pseudospin. For this reason, low-energy electrons in BLG are fourfold degenerate because they have two degrees of freedom: spin and valley. Similar to the case of monolayer graphene, we denote the two K-points by the index ξ: $\xi = +1$ for K and $\xi = -1$ for K'. We introduce the momentum $\mathbf{p} = \hbar\mathbf{k} - \mathbf{K}_\xi$ in the vicinity of the K-point $\mathbf{K}_\xi(\xi = \pm 1)$. Therefore $\mathbf{k} = \mathbf{K}_\xi + \mathbf{q}$ with $\mathbf{q} = \mathbf{p}/\hbar$. Then we define the operators:

$$\begin{aligned} \pi &= \xi p_x + i p_y \\ \pi^\dagger &= \xi p_x - i p_y \end{aligned} \tag{6.16}$$

In the vicinity of the K-points ($|q|a \ll 1$), the structure factor is approximated by the following expression:

$$\begin{aligned} f(\mathbf{k}) &= -\frac{\sqrt{3}a}{2\hbar}\pi^\dagger + \frac{a^2}{8\hbar^2}\pi^2 + o(p^2) \\ f(\mathbf{k})^* &= -\frac{\sqrt{3}a}{2\hbar}\pi + \frac{a^2}{8\hbar^2}(\pi^\dagger)^2 + o(p^2) \end{aligned} \tag{6.17}$$

The formula of the Hamiltonian to first degree in $|p|$ is:

$$H = \begin{bmatrix} \varepsilon_{A1} & v\pi^\dagger & -v_4\pi^\dagger & -v_3\pi \\ v\pi & \varepsilon_{B1} & \gamma_1 & -v_4\pi^\dagger \\ -v_4\pi & \gamma_1 & \varepsilon_{A2} & v\pi^\dagger \\ -v_3\pi^\dagger & -v_4\pi & v\pi & \varepsilon_{B2} \end{bmatrix} \tag{6.18}$$

where $v = \frac{\sqrt{3}a}{2\hbar}\gamma_0$ is the band velocity, and $v_3 = \frac{\sqrt{3}a}{2\hbar}\gamma_3$, $v_4 = \frac{\sqrt{3}a}{2\hbar}\gamma_4$ are the effective velocity. The values of the velocities corresponding to the values of the hopping parameters γ_0, γ_1, γ_3, γ_4 in Ref. [129] are: $v = 9.74 \times 10^5 \mathrm{m\,s^{-1}}$, $v_1 = 1.07 \times 10^5 \mathrm{m\,s^{-1}}$, $v_3 = 4.50 \times 10^4 \mathrm{m\,s^{-1}}$, $v_4 = 2.99 \times 10^4 \mathrm{m\,s^{-1}}$. This is the ***effective four-band model*** near the K-points.

6.4.3 . Low-energy two-band model

We rewrite the Hamiltonian (6.18) in the basis $(\phi_{A1}, \phi_{B2}, \phi_{A2}, \phi_{B1})$:

$$H = \begin{bmatrix} \varepsilon_{A1} & -v_3\pi & -v_4\pi^\dagger & v\pi^\dagger \\ -v_3\pi^\dagger & \varepsilon_{B2} & v\pi & -v_4\pi \\ -v_4\pi & v\pi^\dagger & \varepsilon_{A2} & \gamma_1 \\ v\pi & -v_4\pi^\dagger & \gamma_1 & \varepsilon_{B1} \end{bmatrix} \tag{6.19}$$

We define the low-energy spinor θ and the dimer spinor χ:

$$\theta = \begin{bmatrix} \phi_{A1} \\ \phi_{B2} \end{bmatrix}, \chi = \begin{bmatrix} \phi_{A2} \\ \phi_{B1} \end{bmatrix} \tag{6.20}$$

and decompose the Hamiltonian into the blocks:

$$\begin{aligned} h_\theta &= \begin{bmatrix} \varepsilon_{A_1} & -v_3\pi \\ -v_3\pi^\dagger & \varepsilon_{B_2} \end{bmatrix}, h_\chi = \begin{bmatrix} \varepsilon_{A_2} & \gamma_1 \\ \gamma_1 & \varepsilon_{B_1} \end{bmatrix} \\ u &= \begin{bmatrix} -v_4\pi^\dagger & v\pi^\dagger \\ v\pi & -v_4\pi \end{bmatrix}, u^\dagger = \begin{bmatrix} -v_4\pi & v\pi^\dagger \\ v\pi & -v_4\pi^\dagger \end{bmatrix} \end{aligned} \tag{6.21}$$

The Schrödinger's equation is written as follows:

$$\begin{bmatrix} h_\theta & u \\ u^\dagger & h_\chi \end{bmatrix} \begin{bmatrix} \theta \\ \chi \end{bmatrix} = E \begin{bmatrix} \theta \\ \chi \end{bmatrix} \tag{6.22}$$

We expand this block Hamiltonian as follows:

$$\begin{aligned} h_\theta\theta + u\chi &= E\theta \\ u^\dagger\theta + h_\chi\chi &= E\chi \end{aligned} \tag{6.23}$$

The second equation of (6.23) allows us to write the relation between the dimer spinor χ and the low-energy spinor θ:

$$\chi = (E - h_\chi)^{-1} u^\dagger \theta \tag{6.24}$$

By substituting this relation into the first equation of (6.23), we obtain the eigenvalue equation of the low-energy spinor θ:

$$[h_\theta + u(E - h_\chi)^{-1} u^\dagger]\theta = E\theta \tag{6.25}$$

In the low energy limit, the inverse matrix $(E - h_\chi)^{-1}$ can be approximated to first order in E as:

$$(E - h_\chi)^{-1} = [h_\chi(Eh_\chi^{-1} - \mathbb{I})]^{-1} = -(\mathbb{I} - Eh_\chi^{-1})^{-1} h_\chi^{-1} = -(h_\chi^{-1} + Eh_\chi^{-2}) + o(E) \tag{6.26}$$

Therefore, we approximate the eigenvalue equation in the low-energy limit as follows:

$$(h_\theta - uh_\chi^{-1}u^\dagger)\theta = E(\mathbb{I} + uh_\chi^{-2}u^\dagger)\theta \tag{6.27}$$

We introduce the matrix $\mathcal{S} = \mathbb{I} + uh_\chi^{-2}u^\dagger$. The hermicity of h_χ implies that $\mathcal{S}$ is hermitian. We introduce the spinor $\Phi = \mathcal{S}^{1/2}\theta$ and get the eigenvalue equation:

$$\boxed{\mathcal{S}^{-1/2}(h_\theta - uh_\chi^{-1}u^\dagger)\mathcal{S}^{-1/2}\Phi = E\Phi} \tag{6.28}$$

This is the low-energy two-band eigenvalue equation with the effective two-band Hamiltonian:

$$H_2 = \mathcal{S}^{1/2}(h_\theta - uh_\chi^{-1}u^\dagger)\mathcal{S}^{-1/2} \tag{6.29}$$

In the low-energy limit $\chi = (E - h_\chi)^{-1}u^\dagger\theta \approx -h_\chi^{-1}u^\dagger\theta$. This confirms that the normalization of the spinor Φ is consistent with the normalization of the original state $(\theta^T, \chi^T)^T$.

From now, we expand the effective two-band Hamiltonian in the regime where the intralayer coupling γ_0 and the interlayer coupling at the dimer site γ_1 are larger than the other energies $\gamma_0, \gamma_1 \gg |E|, vp, |\gamma_3|, |\gamma_4|, |u|, |\Delta'|, |\delta_{AB}|$. The inverse of the matrix h_χ is:

$$h_\chi^{-1} = \frac{1}{\varepsilon_{A_2}\varepsilon_{B_1} - \gamma_1^2}\begin{bmatrix} \varepsilon_{B_1} & -\gamma_1 \\ -\gamma_1 & \varepsilon_{A_2} \end{bmatrix} \tag{6.30}$$

By doing some lengthy calculations, we obtain $uh_\chi^{-1}u^\dagger$ under the form:

$$uh_\chi^{-1}u^\dagger = \begin{bmatrix} A_{11}\pi^\dagger\pi & A_{12}(\pi^\dagger)^2 \\ A_{21}\pi^2 & A_{22}\pi\pi^\dagger \end{bmatrix} \tag{6.31}$$

with

$$\begin{aligned} A_{11} =& \frac{\varepsilon_{A_2}v^2 + 2\gamma_1 vv_4 + \varepsilon_{B_1}v_4^2}{\varepsilon_{A_2}\varepsilon_{B_1} - \gamma_1^2} \\ A_{12} =& A_{21} = -\frac{(\varepsilon_{A_2} + \varepsilon_{B_1})vv_4 + \gamma_1(v^2 + v_4^2)}{\varepsilon_{A_2}\varepsilon_{B_1} - \gamma_1^2} = -\frac{2\Delta' vv_4 + \gamma_1(v^2 + v_4^2)}{\varepsilon_{A_2}\varepsilon_{B_1} - \gamma_1^2} \\ A_{22} =& \frac{\varepsilon_{B_1}v^2 + 2\gamma_1 vv_4 + \varepsilon_{A_2}v_4^2}{\varepsilon_{A_2}\varepsilon_{B_1} - \gamma_1^2} \end{aligned} \tag{6.32}$$

Because $\gamma_1 \gg |u|, |\delta_{AB}|$, we approximate:

$$\frac{1}{\varepsilon_{A2}\varepsilon_{B1} - \gamma_1^2} \approx -\frac{1}{\gamma_1^2} \tag{6.33}$$

This approximation allows to write the coefficients A_{11}, A_{12}, A_{21} and A_{22} as follows:

$$\begin{aligned} A_{11} \approx& \frac{1}{2\gamma_1^2}(u - \delta_{AB})(v^2 - v_4^2) - \frac{\Delta'}{\gamma_1^2}(v^2 + v_4^2) - \frac{2vv_4}{\gamma_1} \\ A_{12} =& A_{21} \approx \frac{2\Delta' vv_4}{\gamma_1^2} + \frac{v^2 + v_4^2}{\gamma_1} \\ A_{22} \approx& -\frac{1}{2\gamma_1^2}(u - \delta_{AB})(v^2 - v_4^2) - \frac{\Delta'}{\gamma_1^2}(v^2 + v_4^2) - \frac{2vv_4}{\gamma_1} \end{aligned} \tag{6.34}$$

We simplify the notation by writting:

$$\begin{aligned} L =& \frac{1}{2\gamma_1^2}(u-\delta_{AB})(v^2-v_4^2) \\ M =& \frac{2\Delta' v v_4}{\gamma_1^2}+\frac{v^2+v_4^2}{\gamma_1} \\ N =& \frac{\Delta'}{\gamma_1^2}(v^2+v_4^2)+\frac{2vv_4}{\gamma_1} \end{aligned} \tag{6.35}$$

so that the expression of $uh_\chi^{-1}u^\dagger$ becomes:

$$uh_\chi^{-1}u^\dagger = L\begin{bmatrix}\pi^\dagger\pi & 0\\ 0 & -\pi\pi^\dagger\end{bmatrix} + M\begin{bmatrix}0 & (\pi^\dagger)^2\\ \pi^2 & 0\end{bmatrix} - N\begin{bmatrix}\pi^\dagger\pi & 0\\ 0 & \pi\pi^\dagger\end{bmatrix} \tag{6.36}$$

The matrix h_θ is expressed as follows:

$$h_\theta = \frac{1}{2}(u+\delta_{AB})\begin{bmatrix}1 & 0\\ 0 & 1\end{bmatrix} - v_3\begin{bmatrix}0 & \pi\\ \pi^\dagger & 0\end{bmatrix} \tag{6.37}$$

In the approximation where $\gamma_0, \gamma_1 \gg |E|, vp, |\gamma_3|, |\gamma_4|, |u|, |\Delta'|, |\delta_{AB}|$, we approximate the two-band Hamiltonian as:

$$H_2 = -\frac{1}{2m}\begin{bmatrix}0 & (\pi^\dagger)^2\\ \pi^2 & 0\end{bmatrix} \tag{6.38}$$

where $m = \gamma_1/(2v^2)$ is the **electron effective mass**. In the next section, we will quantize this two-band Hamiltonian in the presence of the magnetic field to obtain the Landau level spectrum of BLG.

6.5 . Landau level quantization

We start by considering the two-band model Hamiltonian:

$$H_2 = -\frac{1}{2m}\begin{bmatrix}0 & (\pi^\dagger)^2\\ \pi^2 & 0\end{bmatrix} \tag{6.39}$$

with the momentum operator $\mathbf{p} = (p_x, p_y) = (-i\hbar\partial_x, -i\hbar\partial_y)$ and the momentum ladder operators π and $\pi^\dagger$ are defined in the valley $\xi(\xi = \pm 1)$ as:

$$\begin{aligned} \pi =& \xi p_x + i p_y \\ \pi^\dagger =& \xi p_x - i p_y \end{aligned} \tag{6.40}$$

We discuss the scheme of the experimental setup (Fig. 6.7). The applied magnetic field $\mathbf{B}$ is perpendicular to the BLG plane and points from the top layer (1) to the bottom layer (2). That means $\mathbf{B}$ is given by the formula: $\mathbf{B} = -B\hat{z}$. In tilted field experiments, $\mathbf{B}$ can have components parallel to the BLG plane, but its z-component B_z keeps its direction from layer 1 to layer 2. Such magnetic field can be induced by a gauge $\mathbf{A}$ such that $\mathbf{B} = \nabla \times \mathbf{A}$. We apply a voltage u between layer 1 and layer 2. This corresponds to the interlayer bias u and results in an electric field $\mathbf{E}$ perpendicular to the BLG plane,

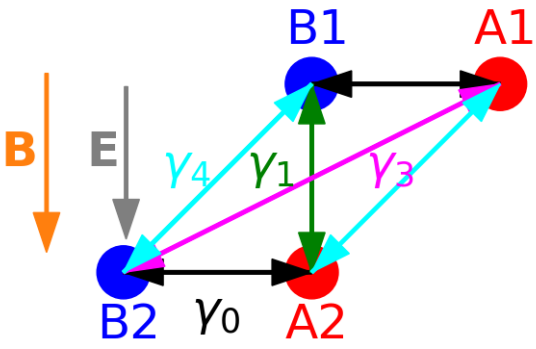

Figure 6.7: BLG under a perpendicular magnetic field $\mathbf{B}$ and a perpendicular electric field $\mathbf{E}$. We adopt the convention that the magnetic field $\mathbf{B}$ points from the top layer (1) to the bottom layer (2). The electric field $\mathbf{E}$ corresponds to an interlayer bias u between the two layers, such that $|u| = eEc$.

such that $|u| = eEc$. When $u > 0$, $\mathbf{E}$ points from layer 1 to layer 2 and is parallel to $\mathbf{B}$. Inversely, when $u < 0$, $\mathbf{E}$ points from layer 2 to layer 1 and is antiparallel to $\mathbf{B}$.

The momentum operators in the presence of the magnetic field are written as follows, according to the Peierls' substitution $\mathbf{p} \to \mathbf{p} + \frac{e}{c}\mathbf{A}$:

$$\begin{aligned} \Pi &= \xi \left(p_x + \frac{e}{c}A_x\right) + i\left(p_y + \frac{e}{c}A_y\right) \\ \Pi^\dagger &= \xi \left(p_x + \frac{e}{c}A_x\right) - i\left(p_y + \frac{e}{c}A_y\right) \end{aligned} \tag{6.41}$$

The commutator of the operators Π and $\Pi^\dagger$ is:

$$[\Pi, \Pi^\dagger] = -2\xi\hbar\frac{eB_z}{c} = 2\xi\hbar\frac{eB}{c} \tag{6.42}$$

The two-band Hamiltonian in the presence of the magnetic field reads:

$$H_2 = -\frac{1}{2m}\begin{bmatrix} 0 & (\Pi^\dagger)^2 \\ \Pi^2 & 0 \end{bmatrix} \tag{6.43}$$

We define the ladder operators:

$$\begin{aligned} a &= \frac{il}{\sqrt{2}\hbar}\Pi \\ a^\dagger &= -\frac{il}{\sqrt{2}\hbar}\Pi^\dagger \end{aligned} \tag{6.44}$$

We check that $(a^\dagger)^\dagger = a$. The eigenstates of those ladder operators are the eigenstates $\phi_N(\mathbf{r})$ of the harmonic oscillator ($N \in \mathbb{N}$). The two-band Hamiltonian is written as follows:

$$H_2 = \hbar\omega_c \begin{bmatrix} 0 & (a^\dagger)^2 \\ a^2 & 0 \end{bmatrix} \tag{6.45}$$

where $\omega_c = eB/(mc)$ is the *cyclotron frequency*. The commutator of the ladder operators equals:

$$[a, a^\dagger] = \xi \tag{6.46}$$

This commutation relation means that the roles of a and $a^\dagger$ are interchanged when we change from valley K to valley K':

- In valley K ($\xi = +1$): a is the lowering operator and $a^\dagger$ is the raising operator:

$$\begin{aligned} a\phi_N &= \sqrt{N}\phi_{N-1} \\ a^\dagger\phi_N &= \sqrt{N+1}\phi_{N+1} \end{aligned} \tag{6.47}$$

  for all $N \in \mathbb{N}$ and $a\phi_0 = 0$. For all $N \in \mathbb{N}$, the function ϕ_N is also an eigenstate of the number operator $a^\dagger a$:

$$a^\dagger a\phi_N = N\phi_N \tag{6.48}$$

- In valley K' ($\xi = -1$): $a^\dagger$ is the lowering operator while a is the raising operator:

$$\begin{aligned} a^\dagger\phi_N &= \sqrt{N}\phi_{N-1} \\ a\phi_N &= \sqrt{N+1}\phi_{N+1} \end{aligned} \tag{6.49}$$

  for all $N \in \mathbb{N}$ and $a^\dagger\phi_0 = 0$. For all $N \in \mathbb{N}$, the operator $aa^\dagger$ is the number operator:

$$aa^\dagger\phi_N = N\phi_N \tag{6.50}$$

We denote the eigenstate of the two-band Hamiltonian H_2 by the spinor:

$$\Phi_N = \begin{bmatrix} u_N \\ v_N \end{bmatrix} \tag{6.51}$$

and the corresponding energy eigenvalue E_N. The Schrödinger equation reads:

$$\hbar\omega_c \begin{bmatrix} 0 & (a^\dagger)^2 \\ a^2 & 0 \end{bmatrix} \begin{bmatrix} u_N \\ v_N \end{bmatrix} = E_N \begin{bmatrix} u_N \\ v_N \end{bmatrix} \tag{6.52}$$

This equation is equivalent to:

$$\begin{aligned} (a^\dagger)^2 v_N &= \left(\frac{E_N}{\hbar\omega_c}\right) u_N \\ a^2 u_N &= \left(\frac{E_N}{\hbar\omega_c}\right) v_N \end{aligned} \tag{6.53}$$

We solve for the Schrödinger's equation in each of the two valleys.

In the valley K $(\xi = +1)$**:**

We apply the number operator $\hat{a}^\dagger\hat{a}$ on u_N:

$$\hat{a}^\dagger\hat{a}u_N = \hat{a}^\dagger[\hat{a}, \hat{a}^\dagger]\hat{a}u_N = \hat{a}^\dagger(\hat{a}\hat{a}^\dagger - \hat{a}^\dagger\hat{a})\hat{a}u_N = (\hat{a}^\dagger\hat{a})^2u_N - (\hat{a}^\dagger)^2\hat{a}^2u_N \tag{6.54}$$

This implies that:

$$((\hat{a}^\dagger\hat{a})^2 - \hat{a}^\dagger\hat{a})u_N = (\hat{a}^\dagger)^2\hat{a}^2u_N = (\hat{a}^\dagger)^2\left(\frac{E_N}{\hbar\omega_c}\right)v_N = \left(\frac{E_N}{\hbar\omega_c}\right)^2 u_N \tag{6.55}$$

One possible solution is to choose $u_N = \phi_N$, so $v_N = \phi_{N-2}$. The energy eigenvalue is $E_N = \pm\hbar\omega_c\sqrt{N(N-1)}(N \in \mathbb{N})$. We consider 3 cases:

1. If $N = 0$ then the energy eigenvalue is $E_0 = 0$. The corresponding eigenstate is:

$$\Phi_0^K = \begin{bmatrix}\phi_0 \\ 0\end{bmatrix} \tag{6.56}$$

2. If $N = 1$ then the energy eigenvalue is $E_1 = 0$. The corresponding eigenstate is:

$$\Phi_1^K = \begin{bmatrix}\phi_1 \\ 0\end{bmatrix} \tag{6.57}$$

3. If $N \geq 2$ then the energy eigenvalue is $E_{\lambda N} = \lambda\hbar\omega_c\sqrt{N(N-1)}$ ($\lambda = +1$ for conduction band and $\lambda = -1$ for valence band). The eigenstate is described by the spinor:

$$\Phi_N^K = \frac{1}{\sqrt{2}}\begin{bmatrix}\phi_N \\ \lambda\phi_{N-2}\end{bmatrix} \tag{6.58}$$

In the valley K' ($\xi = -1$**):**

We get the similar results, the energy eigenvalue is $E_N = \pm\hbar\omega_c\sqrt{N(N-1)}(N \in \mathbb{N})$. The eigenstates are the same eigenstates as in the case of the valley K, providing that we interchange the two sublattices:

1. If $N = 0$ then the energy eigenvalue is $E_0 = 0$. The corresponding eigenstate is:

$$\Phi_0^{K'} = \begin{bmatrix}0 \\ \phi_0\end{bmatrix} \tag{6.59}$$

2. If $N = 1$ then the energy eigenvalue is $E_1 = 0$. The corresponding eigenstate is:

$$\Phi_1^{K'} = \begin{bmatrix}0 \\ \phi_1\end{bmatrix} \tag{6.60}$$

3. If $N \geq 2$ then the energy eigenvalue is $E_N = \lambda\hbar\omega_c\sqrt{N(N-1)}$ ($\lambda = +1$ for conduction band and $\lambda = -1$ for valence band). The corresponding eigenstate is:

$$\Phi_N^{K'} = \frac{1}{\sqrt{2}}\begin{bmatrix}\lambda\phi_{n-2} \\ \phi_N\end{bmatrix} \tag{6.61}$$

Overall, according to the low-energy two-band model, the two Landau levels $N = 0$ and $N = 1$ are degenerate in both valleys K and K'. More accurate calculations from the effective four-band model show that they are approximately degenerate [131]. By considering the spin degree of freedom, we consider that they form a nearly eightfold degenerate Zero-energy Landau level (ZLL). This is a particular property of the quantum Hall effect in BLG, compared to the quantum Hall effects in monolayer graphene and in conventional semiconductors. The other Landau levels are fourfold degnerate, similar to those of monolayer graphene. For the reason of convenience, we denote the Landau levels in the valence band ($\lambda = -1$) by the negative index, starting by Landau level $N = -2$, $N = -3$, down to minus infinity. The energy of the Landau level $-N(N \geq 2)$ is $E_{-N} = -\hbar\omega_c\sqrt{|N|(|N|-1)}$. To avoid double counting with the Landau level $N = 1$, we admit that there is no Landau level $N = -1$. In general, for all integer $N \neq -1$, the energy of the Landau level N is given by:

$$E_N \approx \text{sign}(N)\hbar\omega_c\sqrt{|N|(|N|-1)} \tag{6.62}$$

6.6 . Orbital degree of freedom

Definition of the orbital degree of freedom

In section 6.5, we have demonstrated that the two Landau levels $N = 0$ and $N = 1$ in BLG are nearly degenerate. This allows us to define a new twofold degree of freedom, which plays the role of a pseudospin. We call these two Landau levels *orbitals* and call the new degree of freedom the *orbital degree of freedom*. The orbital $N = 0$ is the *pseudospin-up*, and the orbital $N = 1$ is the *pseudospin-down*. Therefore, electrons occupying the ZLL octet in BLG have three degrees of freedom: spin, valley and orbital. We describe the single-particle state by the spinor $|\xi N\sigma\rangle$ where the quantum numbers are: valley $\xi = \pm$ (or K/K'), orbital $N = 0/1$ and spin $\sigma = \uparrow / \downarrow$.

The weight γ

The four-band tight-binding model gives the formula of the single-electron wavefunctions in the valleys K and K' for orbitals $N = 0$ and $N = 1$ as follows [36]:

$$\Psi_0^K = \begin{bmatrix} \phi_0 \\ 0 \\ 0 \\ 0 \end{bmatrix}, \Psi_1^K = \begin{bmatrix} \sqrt{1-\gamma}\phi_1 \\ 0 \\ \sqrt{\gamma}\phi_0 \\ 0 \end{bmatrix}, \Psi_0^{K'} = \begin{bmatrix} 0 \\ \phi_0 \\ 0 \\ 0 \end{bmatrix}, \Psi_1^{K'} = \begin{bmatrix} 0 \\ \sqrt{1-\gamma}\phi_1 \\ 0 \\ \sqrt{\gamma}\phi_0 \end{bmatrix} \tag{6.63}$$

Here the spinors are expressed in the basis (A1, B2, A2, B1). The parameter $\gamma(0 \leq \gamma \leq 1)$ is a function of the interlayer bias u and the magnetic field B. It is almost independent of u for $0 \leq u \leq 100\text{meV}$ and is an increasing function of B in the experimentally accessible region (Fig. 6.8). Here ϕ_0 and ϕ_1 are the eigenstates of the harmonic oscillator. The orbital $N = 0$ has the wavefunction ϕ_0 of the Lowest Gallilean Landau level and is localized at the non-dimer sites. The wavefunction in the orbital $N = 1$ is a linear combination of the wavefunctions ϕ_0 and ϕ_1, such that ϕ_1 resides at non-dimer sites and ϕ_0 resides at the dimer-sites (Fig. 6.9). The parameter γ is the weight of Ψ_1 at the dimer site. The valleys K and K' are interchanged if we replace A1 by B2, A2 by B1, and vice versa.

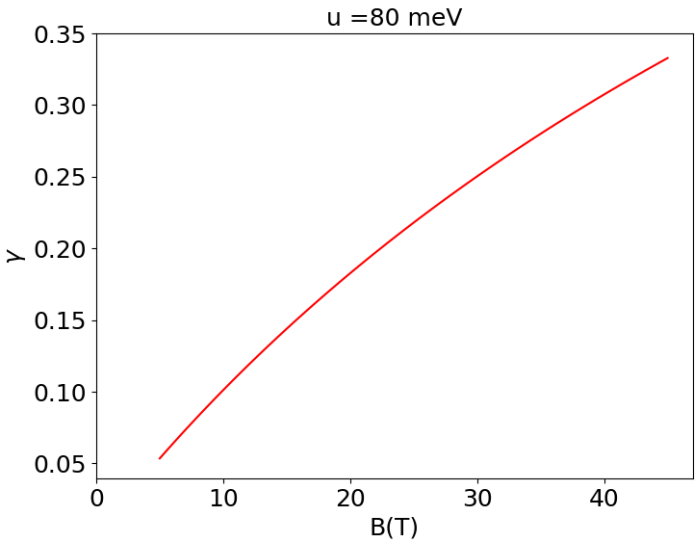

Figure 6.8: The parameter γ as a function of the magnetic field B for u =80 meV, calculated from the tight-binding model. The graph of $\gamma(u, B)$ is approximately the same as this graph for the other values of u such that $0\ \text{meV} \leq u \leq 100\,\text{meV}$.

Single-particle energy

Overall, the single-particle energy of an electron residing in the ZLL contains three contributions: (1) the energy due to the presence of the interlayer bias u, which is a linear function of u and depends on the valley and the orbital; (2) the intrinsic energy splitting $\Delta_{10}^{(0)}$ between the two orbitals; and (3) the Zeeman energy, which depends on the spin σ of the electron.

We summarize the single particle energy of an electron of valley $\xi(\xi = \pm 1)$, orbital $N(N = 0, 1)$ and spin $\sigma(\sigma = \uparrow / \downarrow)$ in the following formula:

$$\boxed{E_{\xi N\sigma}^{(1)} = -\xi\alpha_N \frac{u}{2} + N\Delta_{10}^{(0)} - E_Z\sigma} \tag{6.64}$$

At $B = 31\text{T}$, $\alpha_1 \approx 0.63$ while $\alpha_0 = 1$ [125]. The slopes α_0 and α_1 are different, leading to the crossings between the two orbitals when the spin and valley degrees of freedom are fixed. The value of $\Delta_{10}^{(0)} \approx \hbar\omega_c \left(\frac{\Delta'}{\gamma_1} + 2\frac{\gamma_4}{\gamma_0}\right)$ and has as value $\Delta_{10}^{(0)} \approx 9.7\,\text{meV}$ at B =31 T [125]. The Zeeman splitting energy $E_Z = g\mu_B B \approx 3.58\,\text{meV}$. The bare Landé g-factor for BLG is $g = 2$. Here $\sigma = +1/2$ for spin-up and $\sigma = -1/2$ for spin-down. We illustrate the single-electron energy Eq. (6.64) in Fig. 6.10.

Orbital splitting energy Δ_{10}

The diagram (Fig. 6.10) shows a variety of crossings between the two orbitals $N = 0$ and $N = 1$. We focus on the two levels $|K0\uparrow\rangle$ and $|K1\uparrow\rangle$. The splitting between these two orbitals can be modeled by a parameter:

$$\boxed{\Delta_{10}(u, B) = E_{K0\uparrow}^{(1)}(u) - E_{K1\uparrow}^{(1)}(u) = -\Delta_{10}^{(0)}(B) + (\alpha_1 - \alpha_0)\frac{u}{2}} \tag{6.65}$$

That means the energy difference of the two orbitals can be tuned by varying the interlayer bias u and the magnetic field B, similarly to the Zeeman field in the case of

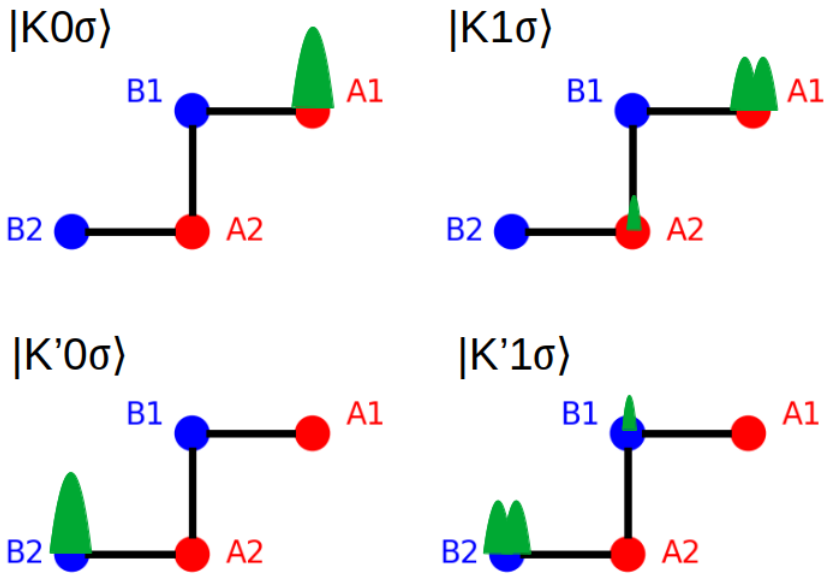

Figure 6.9: The wavefunctions of the four orbitals $|\xi N\sigma\rangle$ of the ZLL on the $(\phi_{A1}, \phi_{B2}, \phi_{A2}, \phi_{B1})$ sites.

the intrinsic spin. Here Δ_{10} plays the role of a pseudo-Zeeman energy for the orbital pseudospin. For a fixed value of the magnetic field B, Δ_{10} is a linear function of u and vanishes when $u = u^* = 2\Delta_{10}^{(0)}(B)/(\alpha_1 - \alpha_0)$. This is the situation where the two levels $|K0\uparrow\rangle$ and $|K1\uparrow\rangle$ cross each other.

6.7 . Coulomb interaction and screening

In this work, we focus on the case of spin and valley polarized quantum Hall states residing in the two orbitals $N = 0$ and $N = 1$. Therefore, we need to project the Coulomb interaction into these two orbitals, and assume that there is no mixing between these two Landau levels with higher Landau levels. This approximation allows to reduce the dimension of the Fock space and makes numerical exact diagonalizations accessible. Although such kind of approximation is accurate only in a small region of the parameter space, it permits to study the unique situation of orbital degeneracy in BLG.

The Coulomb interaction of the 2D electron systems in BLG is decomposed into the following three contributions:

$$H^{(2)} = H_C + H_{c_0} + H_V \tag{6.66}$$

The first contribution H_C is the long-range Coulomb interaction, which is SU(4)-symmetric in the Hilbert space of spin and valley. However, there is no SU(2) symmetry for the twofold nearly degerenate orbital degrees of freedom, because the effective interaction in the two orbitals has different form factors, resulting in different matrix elements. The Coulomb Hamiltonian H_C, projected to the ZLL, is given by [125]:

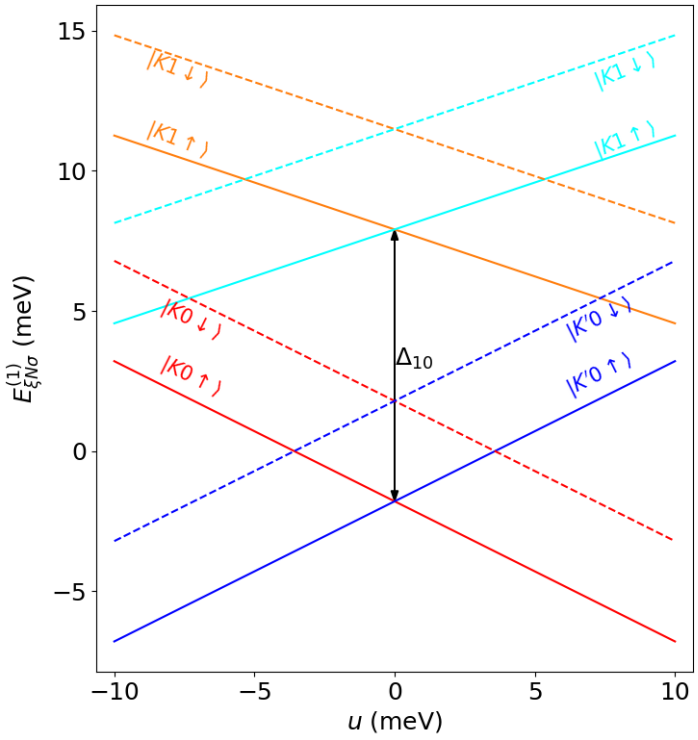

Figure 6.10: Diagram of the single-electron energy in the ZLL of BLG for $B = 31\,\mathrm{T}$. Here we plot the equation (6.64) with parameters $\Delta_{10}^{(0)} = 9.7\,\mathrm{meV}$, $E_Z = 3.58\,\mathrm{meV}$, $\alpha_0 = 1$, $\alpha_1 = 0.67$ (data taken from Ref. [125]).

$$H_C = \frac{1}{2}\int \frac{d^2\mathbf{q}}{(2\pi)^2}\rho_{ZLL}(\mathbf{q})\tilde{V}(q)\rho_{ZLL}(-\mathbf{q}) \tag{6.67}$$

In this formula $\rho_{ZLL}(\mathbf{q}) = \sum_{\xi N\sigma}\rho_{\xi N\sigma}(\mathbf{q})$ is the Fourier transform of the total density in the ZLL. The Fourier transform of the Coulomb potential is $\tilde{V}(q) = 2\pi e^2/(\varepsilon|q|)$. The bare Coulomb interaction is screened by three following effects: (1) the surrounding hBN dielectric, (2) the proximal metallic gates, and (3) the interaction between the electrons in the ZLL and the fully filled Landau levels below it.

In the presence of the surrounding hBN dielectric (for example the setup in Refs. [111, 125]), this dielectric environment modifies the dielectric constant in the Coulomb interaction. Here $\varepsilon = \varepsilon^{//}_{hBN}$ where $\varepsilon^{//}_{hBN} \approx 6.6\varepsilon_0$ is the in-plane dielectric constant of hexagonal boron nitride [132, 133]. The metallic gates are situated at distance D apart from the BLG plane. The typical value of this distance is $D \approx 20\,\mathrm{nm}$ [125]. The screening due to metallic gates results in modyfying the Coulomb interaction. In this work, we use the modification proposed in Ref. [134]:

$$V^{eff}(q) = \frac{\tilde{V}(q)}{1 + \frac{a}{ql}\tanh\left(\frac{q^2l^2}{2}\right)} \tag{6.68}$$

Here the parameter a is the screening strength and is treated as a parameter of the model. The interaction between the electrons in the ZLL and the electrons occupying the Landau levels below the ZLL is similar to the Lamb shift in hydrogen atom [131]. The Lamb shift per particle is given by the formula [125]:

$$\Delta_{Lamb} \approx -\frac{0.2e^2/(\varepsilon^{//}_{hBN} l)}{1+2.73a} = -\frac{8.58\text{meV}\sqrt{B[\text{T}]}}{1+2.73a} \tag{6.69}$$

The finite thickness $c = 1.42$ Å of the BLG lattice results in a capacitive charging energy. Its effect is to modify the Coulomb interaction $V(q) \to V(q)^{-qc} = V(q) - qcV(q) + o(cq)$ and gives rise to a small correction H_{c_0}. Because c is small to the magnetic length l so that $c/l \ll 1$, we neglect the small correction H_{c_0} in this work.

The contribution H_V is the short-range valley dependent interaction. We have considered the effect of this interaction in monolayer graphene in Chapters 3 and 4. This short-range interaction breaks the SU(4) symmetry of H_C and gives rise to a variety of symmetry-breaking orders such as the canted antiferromagnetic phase [124]. Because we are concentrating on the crossing between levels having the same valley, this point-contact interaction gives a vanishing energy, so we do not have to take it into account in this work.

6.8 . Summary

In this chapter, we have discussed the quantum Hall effect in BLG using the tight-binding model. We have used the low-energy two-band and the effective four-band models to demonstrate the Landau level spectrum of BLG. The main properties of BLG under the quantum Hall effect are as follows:

1. In BLG, the Landau levels $N = 0$ and $N = 1$ are nearly degenerate. They form a new degree of freedom, the so-called orbital degree of freedom, which acts like a pseudospin.

2. The zero-energy Landau level (ZLL) of BLG is approximately eightfold degenerate. The single-particle energy levels in this octet are characterized by three quantum numbers: spin, valley, and orbital.

3. The single-electron wavefunctions in orbital $N = 0$ are localized at the non-dimer sites of the BLG lattice. By contrast, the single-electron wavefunctions in orbital $N = 1$ are the superpositions of the Lowest Landau Level wavefunction localized at the dimer site of one layer and the Second Landau level wavefunction localized at the non-dimer site of the other layer. The weight of the dimer site wavefunction is given by a parameter $\gamma (0 < \gamma < 1)$.

4. The energy Δ_{10} separating the two orbitals $N = 0$ and $N = 1$ is controllable by tuning the interlayer potential bias u between the two layers. We have established the single-particle diagram of the states in the ZLL octet. Those single-particle levels cross each other at numerous crossing points. These level-crossing points promise interesting physics to explore.

In the next chapter, we will discuss the Wigner crystal. After that, we will show the results of this work: the competition between Laughlin state and Wigner crystal in BLG in Chapter 8.

Chapter7 - Wigner crystal

7.1 . Wigner crystal

The physics of an electron system is governed by the competition between its kinetic energy and the electron-electron Coulomb interaction energy. Kinetic energy prefers the ground state to be an electron gas or liquid, whereas electron-electron interaction favors the formation of the electron crystal phase. In the latter case, electrons form a periodic lattice, similar to the crystals formed by periodic lattices of atoms or ions we see every day. For a crystal to stabilize, the electrons must be localized to a size smaller than the lattice parameter. The uncertainty principle implies that this situation increases the uncertainty in electron momentum, resulting in a kinetic energy cost, which in turn destabilizes the electron crystal.

In 1934, Wigner predicted that when the kinetic energy vanishes, the ground state is a lattice of electrons, corresponding to the minimum of the interaction energy [48]. Let $r_0 = (3/(4\pi n))^{1/3}$ be the radius of the sphere containing one electron in three dimensions, here n is the electron density and $a_0 = 0.529$Å is the Bohr radius, we define the dimensionless interelectron distance $r_s = r_0/a_0$. In the high-density limit ($r_s \to 0$), the energy per particle of the electron system is given in the unit of Rydberg energy by [8, 48]:

$$\frac{E}{N_e} = \frac{2.21}{r_s^2} - \frac{0.916}{r_s} + \dots \tag{7.1}$$

In this formula, the first term is the kinetic energy, and the second term is the Coulomb electron-electron interaction energy. The formula implies that the kinetic energy dominates over the interaction energy in the high-density limit (r_s is small). The ground state is therefore an electron liquid. In the low-density limit (r_s is large), the energy per particle of the electron system equals [135]:

$$\frac{E}{N_e} = -\frac{1.792}{r_s} + \frac{2.66}{r_s^{3/2}} + \frac{b}{r_s^2} + \dots \tag{7.2}$$

The first term is the potential energy and the second term is the kinetic energy. In this situation, the interaction energy dominates over the kinetic energy. The ground state is an electron crystal. These results show a transition from the liquid phase at high-density to the solid phase at low-density. Because the electron solid phase was proposed by Wigner, this phase is later called ***Wigner crystal***. This state of matter should appear at low temperature where these calculations are valid.

It took a long time to realize the Wigner crystal in the laboratory experimentally. Cole and Cohen proved that the electrostatic image force in liquid helium leads the electrons to be bound to shallow surface states localized at the helium surface and form a 2-dimensional electron system [138]. Following this idea, Crandall and Williams proposed to search for a 2-dimensional Wigner crystal on the surface of liquid He [139]. Bonsall and Maradudin calculated the ground-state static energy and phonon dispersion of the five Bravais lattices of two-dimensional Wigner crystals [140]. They found that the hexagonal lattice is the most stable lattice. In 1979, Grimes and Adams observed

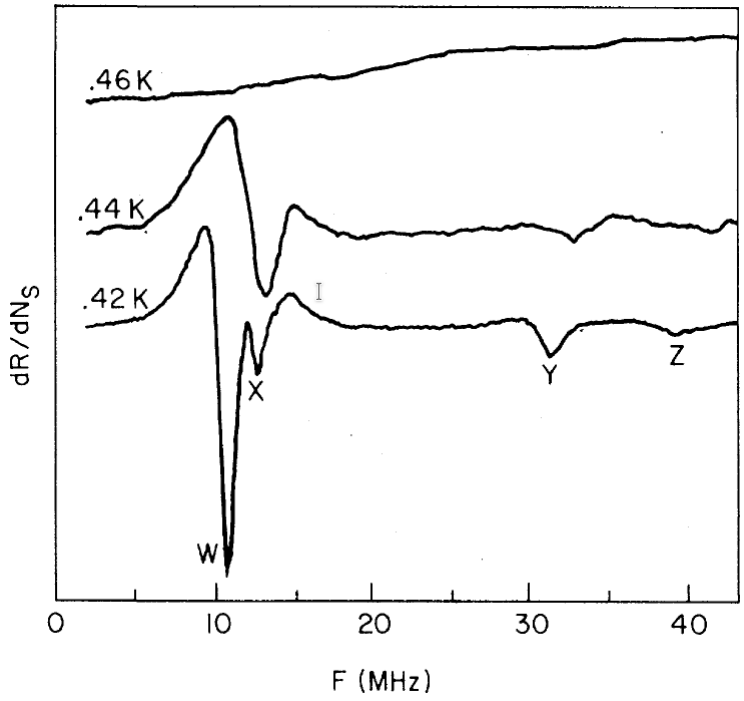

Figure 7.1: The experimental evidence of Wigner crystal in liquid He surface. The experiment was performed by Grimes and Adames [136]. They measured the coupled plasmon-ripplon mode and obtain 4 resonances: W, X, Y and Z. The resonances Y and Z agree with the $n = 3$ and $n = 4$ modes theoretical calculated by Fisher, Halperin and MacDonald [137]. The resonances W and X are attributed to the lowest mode $n = 1$. Reprinted figure with permission from C.C.Grimes and G.Adams, Phys. Rev. Lett. 42, 795 (1979) [136]. Copyright (2023) from American Physical Society.

the first evidence of the Wigner crystal in liquid He surface [136]. They measured the coupled resonance between the longitudinal phonon mode of the Wigner crystal and the excitations of standing capillary waves (ripplon) on the He surface. The resonance frequencies (Fig. 7.1) agree with the theoretical calculations of the phonon-ripplon mode of a triangular Wigner crystal [137]. The Wigner crystal forms at temperature lower than $0.457 \pm 0.005\mathrm{K}$. This confirmed that the Wigner crystal has hexagonal lattice, in agreement with the predictions by Crandall-Williams and Bonsall-Maradudin.

In general, the term *Wigner crystal* is not only used for electron crystals, but also for crystals of holes, and crystals of composite fermions.

7.2 . Competition between Wigner crystal and quantum Hall liquid

7.2.1 . Trial wavefunctions

The discovery of a 2-dimensional Wigner crystal in electron gas on the liquid helium surface opens new perspectives to realize the Wigner crystal in other 2-dimensional systems. One candidate is the 2-dimensional electron gas under a high magnetic field. In this system, the kinetic energy of electrons is quantized into flat Landau levels. The kinetic energy is quenched, and the interaction energy governs the physics. This possibility was shown theoretically in the work of Fukuyama, Platzmann, and Anderson [141]. After discovering the integer quantum Hall effect, this expectation motivated physicists to

observe the systems with lower density and under higher magnetic fields [1]. However, they observed the fractional quantum Hall effect [2]. Nevertheless, researchers believed the Wigner crystal would appear at lower filling fractions.

Apart from building the theory of the fractional quantum Hall effect, many authors proposed the trial wavefunctions for the Wigner crystal. Maki and Zotos proposed the uncorrelated Wigner crystal wavefunction, which is the Slater determinant of the Lowest Landau level single-electron wavefunctions localized at the lattice sites of a triangular lattice [142]. Let $\phi_{\mathbf{R}}(\mathbf{r})$ the Lowest Landau level wavefunction localized around the lattice site $\mathbf{R} = (X, Y)$:

$$\phi_{\mathbf{R}}(\mathbf{r}) = \frac{1}{(2\pi l^2)^{1/2}} \exp\left\{ -\frac{1}{4l^2}\left[(\mathbf{r}-\mathbf{R})^2 - 2i(xY - yX)\right] \right\} \tag{7.3}$$

The *Maki-Zotos wavefunction* for the Wigner crystal with triangular lattice $\mathbf{R}_j = \left(na_0 + \frac{m}{2}a_0, \frac{\sqrt{3}}{2}ma_0 \right)$ of lattice parameter a_0 ($m, n \in \mathbb{Z}$) for a system of N_e electrons of coordinates $\mathbf{r}_1, \mathbf{r}_2, \ldots, \mathbf{r}_{N_e}$ is given by:

$$\Psi_{MZ}(\{\mathbf{r}_i\}) = (N_e!)^{-1/2} \det\{\phi_{\mathbf{R}_j}(\mathbf{r}_i)\} \tag{7.4}$$

Lam and Girvin proposed a trial wavefunction for the correlated Wigner crystal with particle position $z_i = x_i + iy_i$ [143]:

$$\Psi_{LG}(\{z_i\}) = \exp\left(\frac{1}{4}\sum_{ij}(z_i - R_i)B_{ij}(z_j - R_j) \right) \det(\phi_{\mathbf{R}_i}(z_j)) \tag{7.5}$$

This wavefunction is the so-called *Lam-Girvin wavefunction*. The complex variational parameter $B_{ij} = B(\mathbf{R}_i - \mathbf{R}_j)$ determine the correlations.

Apart from the trial wavefunctions for the electron solid, several works introduced the Wigner crystal of composite fermions. Yi and Fertig proposed a trial wavefunction in which vortices are bound to the Maki-Zotos wavefunction of a triangular lattice [144]:

$$\Psi = \prod_{j<k}(z_j - z_k)^q \Psi_{MZ} \tag{7.6}$$

and showed that this wavefunction has lower energy than the Lam-Girvin wavefunction for filling factor $0.10 < \nu < 0.20$. Chang, Yeon and Jain continued developing the idea of binding vortices to electron crystals. They first project the Maki-Zotos wavefunction into a section of definite angular momentum L following the procedure of Yannouleas and Landman [145] to obtain the wavefunction Ψ_L^{EC}. Then, they bind $2p$ magnetic flux quanta to each electron in the crystal. The wavefunction for crystal of ^{2p}CF of angular L is given by the formula [146]:

$$\Psi_L^{2p-\mathrm{CFC}} = \prod_{j<k}(z_j - z_k)^{2p} \Psi_{L^*}^{EC} \tag{7.7}$$

where $L^* = L - pN_e(N_e - 1)$. The filling factor of the finite system containing N_e electrons is given by $\nu = N_e(N_e - 1)/(2L)$.

7.2.2 . Critical filling factor for the Wigner crystal

Knowing that the Wigner crystal would solidify at low electron density, a question arises: what is the critical filling factor for the transition between the Wigner crystal and the fractional quantum Hall liquid? At the beginning, physicists believed that there exists a critical filling factor ν_c separating the quantum Hall liquid and the Wigner crystal: for $\nu > \nu_c$, the ground state of the 2D electron system is the quantum Hall liquid, and for $\nu < \nu_c$, the ground state of the 2D electron system is the Wigner crystal. Levesque, Weis, and MacDonald compared the ground state energy of the Laughlin state and the uncorrelated Wigner crystal and concluded that the transition took place for filling factor $1/10 < \nu_c < 1/9$ [147]. However, the calculations of the Lam-Girvin wavefunction give a higher critical value of the filling factor $\nu_c \approx 1/6.5$ [143].

Numerical studies also obtained the same critical filling factor. Yang, Rezayi, and Haldane performed exact diagonalization studies for $N_e = 6$ electrons with filling factors $\nu = 1/6$, $\nu = 1/7$, and $\nu = 1/8$ on the torus [148]. The torus geometry is advantageous to study the Wigner crystal because its translational symmetry allows to define the many-body momentum, which serves as labeling the many-body state (for details about the torus geometry, see Appendix ! B). Another reason is that one can adjust the aspect ratio L_x/L_y to an appropriate value of the electron solid lattice. The critical value of the filling factor is $\nu = 1/7$, in agreement with analytical calculations on the correlated Lam-Girvin wavefunction. They also found that the phase transition between Wigner crystal and quantum Hall liquid is second-order or weakly first-order rather than a strong discontinuous phase transition.

7.2.3 . Re-entrant Wigner crystal

In parallel with theoretical works, a variety of experiments also made progress in detecting the Wigner crystal. The direct observation of Wigner crystal is difficult. Magnetotransport [149–154] and magneto-optical [155–157] measurements gave indirect observations of this phase of matter.

The first evidence of Wigner crystal was reported in 1988 by Andrei et al. [155]. In 1990, Goldman [150] and Jiang [149] observed the exponentially diverging longitudinal resistances R_{xx} in the filling factor regions $1/5 < \nu < 2/9$ and $\nu < 1/5$. These two regions surround an incompressible state at filling factor $\nu = 1/5$ (see Fig. 7.2). This behavior is called the *re-entrant Wigner crystal* and appears in later experiments. These discoveries suggest a sequence of three alternative phase transitions between the Wigner crystal and the quantum Hall liquid as a function of the decreasing filling factor rather than a single phase transition.

Soon after the discovery of the re-entrant Wigner crystal around filling factor $\nu = 1/5$, Santos et al. [153] observed the re-entrant Wigner crystal around filling factor $\nu = 1/3$ in a 2D hole system. They proposed an explanation for this behavior: holes have a larger effective mass than electrons, resulting in a higher Landau level mixing and favoring the Wigner crystallization at a higher filling factor. This observation enriches the physical picture behind the liquid-solid phase transition by pointing out the role of Landau level mixing in the formation of Wigner crystals.

The story does not end at this stage. One may believe that $\nu_c = 1/5$ would be the critical value of the filling factor (of a 2D electron system) below which the ground state was a Wigner crystal, not a quantum Hall liquid. However, experiments found

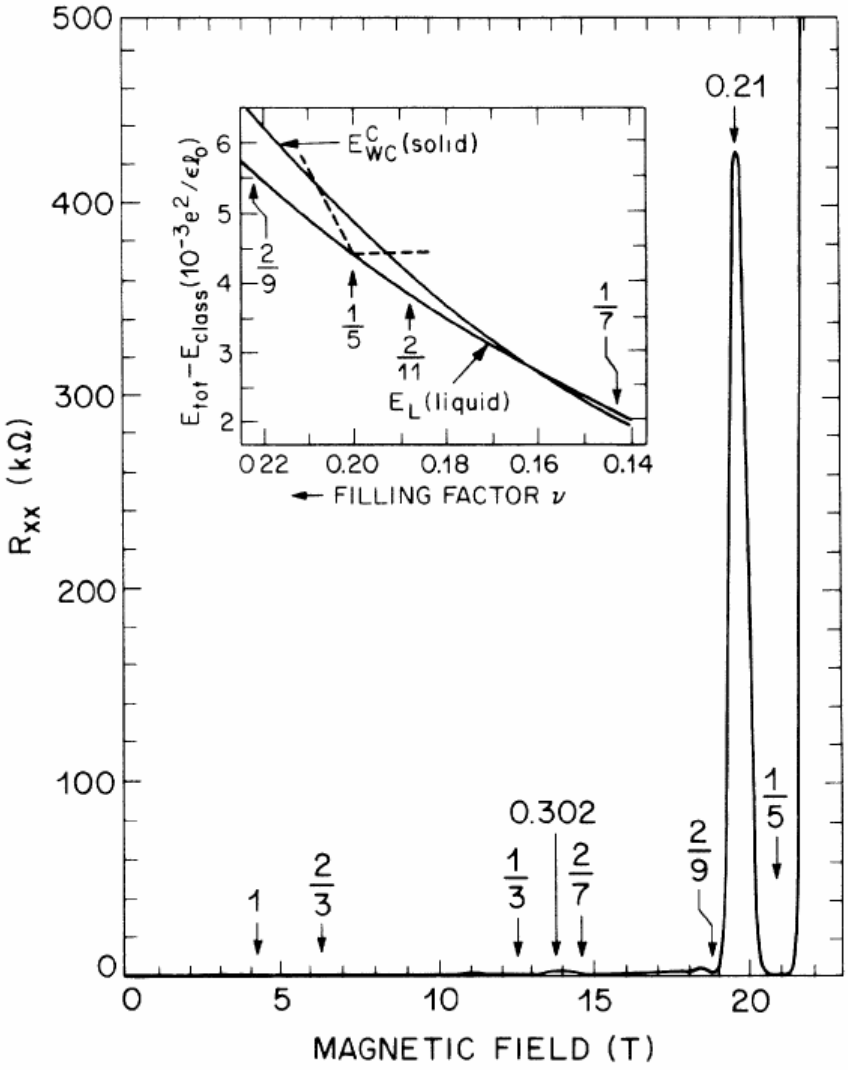

Figure 7.2: The re-entrant Wigner crystal behavior around the fractional quantum Hall liquid at filling factor $\nu = 1/5$. The transport measurement shows that the longitudinal resistance R_{xx} diverges for filling factors $2/9 > \nu > 1/5$ and on a small region $\nu < 1/5$. Those diverging behaviors are associated to the presence of the Wigner crystal phase. The inset shows the energy of the Wigner crystal and the quantum Hall liquid (substracting a classical energy $E_{class} = -0.782133\nu^{-1/2}$ for clarity). There is a cusp in the total energy, shown by the dashed lines that intersect the line representing the solid at $\nu = 0.19$ and $\nu = 0.21$. This behavior suggests that there are two phase transitions before and after the quantum Hall liquid at $\nu = 1/5$. Reprinted figure with permission from H.W.Jiang, R.L.Willett, H.L.Stormer, D.C.Tsui, L.N.Pfeiffer, and K.W.West Phys. Rev. Lett. 65, 633 (1988) [149]. Copyright (2023) by the American Physical Society.

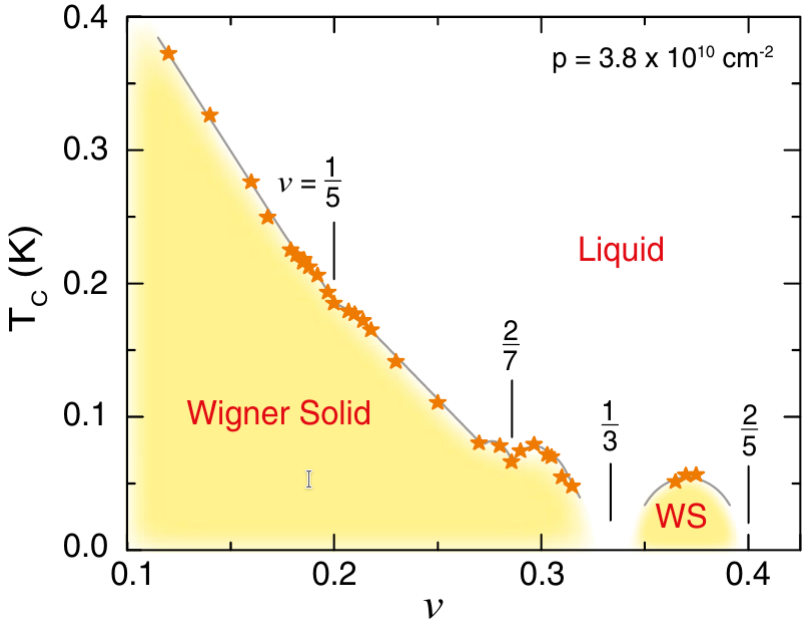

Figure 7.3: Thermal melting phase diagram of 2D hole system in low-disorder GaAs quantum well. The Wigner solid appears at low temperature in the yellow region. The re-entrant Wigner crystal is observed before and after the filling factor $\nu = 1/3$. The stars illustrate the experimental data points. Reprinted figure with permission from Meng K. Ma , K. A. Villegas Rosales, H. Deng, Y. J. Chung, L. N. Pfeiffer , K. W. West, K. W. Baldwin, R. Winkler, and M. Shayegan, Phys. Rev. Lett., 125, 036601 (2020) [159]. Copyright (2023) by the American Physical Society.

signature of quantum Hall effect at filling factor $\nu = 1/7$ [54], weak signal at $\nu = 2/11$ [158] and quantum Hall effect down to $\nu = 1/9$ [156]. In 2002, Pan et al. found a sequence of local minima in R_{xx} in GaAs/AlGaAs quantum well for filling factors $\nu = 2/11, 3/17, 3/19, 2/13, 1/7, 2/15, 2/17$ and $1/9$ [154]. That means there should be a sequence of alternating phase transitions between Wigner crystal and quantum Hall liquid at low filling factors. The sequence of minima disappears at a temperature below $T \leq 80\,\mathrm{mK}$. It confirms the role of another factor underlying the physics of Wigner crystal-quantum Hall liquid phase transition: temperature.

7.2.4 . Thermal melting of Wigner crystal

This subsection discusses the first factor governing the Wigner crystal-quantum Hall liquid transition: temperature. Usually, we know that a solid (of atoms or ions) melts into a liquid when the temperature increases. It is true for a Wigner crystal. Experiments show that the minima in R_{xx}, which are associated to the quantum Hall liquid, disappear when the temperature decreases down to $T = 0$K, and are replaced by the divergence in R_{xx}. In the experiments by Pan et al. [154], the sequence of minima in R_{xx} disappears, and R_{xx} diverges for $\nu < 2/11$ when T decreases below $T = 80\,\mathrm{meV}$. It corresponds to the freezing of the quantum Hall liquid into Wigner crystal when the temperature decreases. The thermal melting of Wigner crystal was also predicted theoretically by comparing the free energy of the two phases [160, 161].

Fig. 7.3 shows the thermal melting phase diagram of Wigner crystal in 2D hole system [159]. Due to the high Landau level mixing of holes, the re-entrant Wigner crystal appears around the filling factor $\nu = 1/3$ instead of around $\nu = 1/5$. The phase diagram

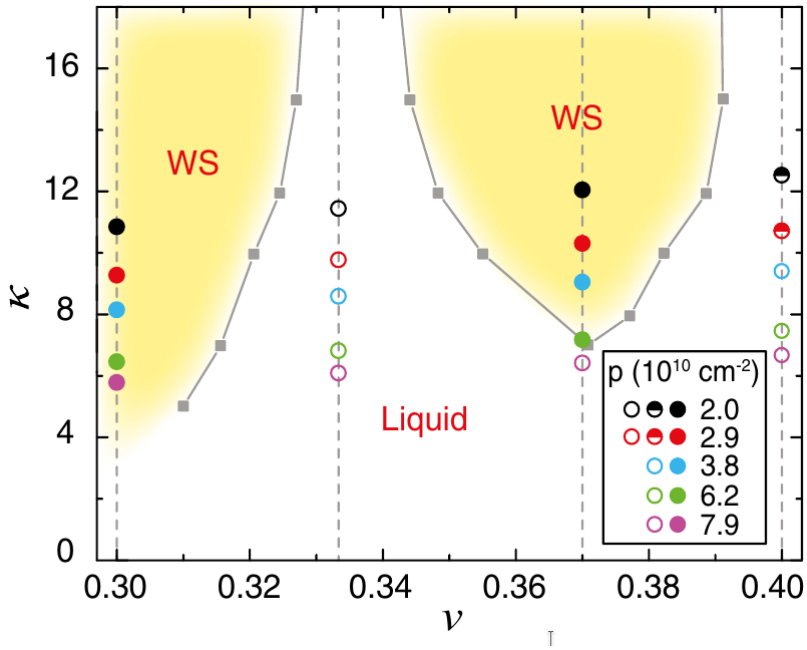

Figure 7.4: The quantum melting phase diagram of 2D hole system in low-disorder GaAs quantum well. The white and yellow regions are the region of stability of the quantum Hall liquid and the Wigner crystal, respectively. The filled and empty dots represent the experimental data for Wigner crystal and quantum Hall liquid, respectively. The half-filled dots show a competition between Wigner crystal and quantum Hall liquid. The grey boundary are theoretical results from Ref. [162]. Reprinted figure with permission from Meng K. Ma , K. A. Villegas Rosales, H. Deng, Y. J. Chung, L. N. Pfeiffer , K. W. West, K. W. Baldwin, R. Winkler, and M. Shayegan, Phys. Rev. Lett., 125, 036601 (2020) [159]. Copyright (2023) by the American Physical Society.

shows that the electron liquid crystallizes at low temperature, but the Wigner crystal is interrupted by the well-developed quantum Hall liquids at $\nu = 1/3$ and $\nu = 2/5$.

7.2.5 . Landau level mixing and quantum melting of Wigner crystal

In this subsection, we discuss the second factor governing the Wigner crystal-quantum Hall liquid phase transition: Landau level mixing. The re-entrant Wigner crystal around filling factor $\nu = 1/3$ in 2D hole system [153] is the first suggestion of the role of Landau level mixing in the formation of Wigner crystal. Wigner crystal appears at a low filling factor in a system having a stronger Landau level mixing.

Landau level mixing is characterized by the ratio between the Coulomb energy and the cyclotron energy:

$$\kappa = \frac{e^2/(\varepsilon l)}{\hbar\omega_c} \tag{7.8}$$

Because ω_c is inversely proportional to the charge carrier effective mass m, the Landau level mixing κ is proportional to m. Indeed, in GaAs the hole effective mass is 5 times larger than electron effective mass, leading to a stronger Landau level mixing than that of 2D electron systems. Landau level quantization is the quantization of the kinetic energy of a single particle of the system, so the cyclotron energy is the scale characterizing the kinetic energy. Therefore, even if the filling factor ν is high, if a system has a strong Landau level mixing, that means in this system the interaction energy dominates over the kinetic energy. This situation favors the formation of Wigner crystal rather than a

quantum Hall liquid. The stronger is the Landau level mixing, the higher the probability of forming a Wigner crystal, even though the charge carrier density is high. The melting of Wigner crystal due to the weakening of Landau level mixing is called the *quantum melting* of Wigner crystal.

The quantum melting phase diagram of 2D hole system is shown in Fig. 7.4. Experimental data clearly confirm that the Wigner crystal forms at high Landau level mixing κ, and the quantum Hall liquid forms at low Landau level mixing. We remark that theory does not predict the formation of Wigner solid at filling factor $\nu = 1/3$ for Landau level mixing up to $\kappa = 16$ [162]. The upper limit for κ at which the Wigner crystal forms at $\nu = 1/3$ is still an open question for future study. For $\nu = 2/5$, the experiments suggest that the Wigner crystal forms and competes with the quantum Hall liquid (see the half-filled dots in Fig. 7.4). This contradicts the prediction by the theory. The authors of Ref. [159] explain this discrepancy between experiments and theory by the presence of disorder, which favors the crystallization, but is neglected in theoretical calculations.

Chapter8 - Competition between Laughlin state and Wigner crystal in Bernal-bilayer graphene

8.1 . Introduction to the chapter

Chapters 6 and 7 reviewed the fundamental knowledge about the quantum Hall effect in Bernal-stacked bilayer graphene and the Wigner crystal. In this chapter, we discuss the results of this work: *the competition between the Laughlin state and the Wigner crystal in Bernal-stacked bilayer graphene*. The results of this work are published in Ref. [105]. The chapter begins with the Hamiltonian of the two-dimensional electron system in BLG. Here we focus on the regime in the vicinity of the crossing between the two levels $|K0\uparrow\rangle$ and $|K1\uparrow\rangle$. In this regime, the Hamiltonian has two parameters γ and Δ_{10} that we previously discussed in section 6.6. These two parameters determine the phase of the two-dimensional electron system under magnetic field. For the filling factor $\nu = 1/3$, by examining the polarization of the two orbitals, the quantum fidelity and ground state manifold, we show that the Wigner crystal appears when the two orbitals coincide. We also visualize the Wigner crystal state in real space, and the determine the phase boundary of the Wigner crystal phase. The chapter ends with the discussion on the fate of the state of filling factor $\nu = 2/3$.

8.2 . Hamiltonian of a two-dimensional electron system in Bernal-stacked Bilayer graphene at the crossing of two orbitals having the same spin and valley

We consider a system of N_e electrons under magnetic field $\mathbf{B} = -B\hat{\mathbf{z}}$ (Fig. 6.7). The number of magnetic flux quanta passing through the BLG plane is N_ϕ. This magnetic field corresponds to the vector potential $\mathbf{A} = (0, -Bx, 0)$. Let the system be a rectangle of size $L_x \times L_y$, we apply the periodic boundary conditions:

$$\begin{aligned} \psi(x + L_x, y) =& e^{-iL_x y/l^2}\psi(x, y) \\ \psi(x, y + L_y) =& \psi(x, y) \end{aligned} \tag{8.1}$$

and transform the finite-size system into a periodic lattice of rectangular unit cell of area $L_x L_y = 2\pi N_\phi l^2$. The system is like residing on the surface of a torus with the magnetic field perpendicular to the torus surface. We say that we study the system in the *Torus geometry* (see Appendix B for an introduction to the torus geometry). The electrons in the system not only interact with each other, but also interact with their images.

We choose to study the problem in the torus geometry because: (1) This geometry is a closed geometry so the degeneracy of each Landau level is finite, so the torus geometry is suitable to study finite systems. (2) By applying the periodic boundary conditions, the system naturally has the translational symmetry (rigorously, this is the symmetry via magnetic translations). This allows us to define the many-body momentum and represent the periodic lattice of the Wigner crystal without defects. The spherical geometry does not have the intrinsic translational symmetry and cannot avoid defects if the ground state is a crystal.

The basis wavefunctions for the single-electron Hilbert space in this lattice are given by:

$$\begin{aligned}\phi_{nj}(x,y) = \left(\frac{1}{L_y\sqrt{\pi}l}\right)^{1/2} \sum_{k=-\infty}^{+\infty} \frac{1}{\sqrt{2^n n!}} \exp\left[i\left(j\frac{2\pi}{L_y} + k\frac{L_x}{l^2}\right)y\right] \times \\ \times \exp\left[-\frac{1}{2}\left(\frac{x}{l} - j\frac{2\pi l}{L_y} - k\frac{L_x}{l}\right)^2\right] H_n\left(\frac{x}{l} - j\frac{2\pi l}{L_y} - k\frac{L_x}{l}\right)\end{aligned} \tag{8.2}$$

Here the index j runs from $1 \leq j \leq N_\phi$. In this work, we study the crossing between the two levels $|K0\uparrow\rangle$ and $|K1\uparrow\rangle$. We focus on the two Landau levels $N = 0$ and $N = 1$ of BLG, and neglect the interaction with higher Landau levels. The single-particle wavefunctions of these two levels are given by (according to (6.63)):

$$\begin{aligned}\psi^K_{0j}(\mathbf{r}) =& \phi_{0jA_1}(\mathbf{r}) \\ \psi^K_{1j}(\mathbf{r}) =& \sqrt{1-\gamma}\phi_{1jA_1}(\mathbf{r}) + \sqrt{\gamma}\phi_{0jA_2}(\mathbf{r})\end{aligned} \tag{8.3}$$

Here $\phi_{njA_1}(\mathbf{r})$ and $\phi_{njA_2}(\mathbf{r})$ are the basis wavefunctions localized at sublattices A1 and A2, respectively. The single-particle energy between the two levels is given by $\Delta_{10} = E_{K0\uparrow} - E_{K1\uparrow}$. The total Hamiltonian of the system is given by:

$$\mathcal{H} = \frac{1}{2} \sum_{\substack{N_1N_2N_3N_4 \\ j_1j_2j_3j_4}} \mathcal{A}^{N_1N_2N_3N_4}_{j_1j_2j_3j_4} c^\dagger_{N_1j_1} c^\dagger_{N_2j_2} c_{N_3j_3} c_{N_4j_4} + \Delta_{10}\hat{N}_0 \tag{8.4}$$

Here the indices N_1, N_2, N_3, N_4 indicate the orbital quantum number and can be either 0 or 1. The operator $\hat{N}_0$ counts the number of particles occupying the orbital $N = 0$. The matrix element $\mathcal{A}^{N_1N_2N_3N_4}_{j_1j_2j_3j_4}$ is evaluated as follows:

$$\mathcal{A}^{N_1N_2N_3N_4}_{j_1j_2j_3j_4} = \int d^2\mathbf{r}_1 d^2\mathbf{r}_2 \Psi^*_{N_1j_1}(\mathbf{r}_1)\Psi^*_{N_2j_2}(\mathbf{r}_2)V(\mathbf{r}_1 - \mathbf{r}_2)\Psi_{N_3j_3}(\mathbf{r}_2)\Psi_{N_4j_4}(\mathbf{r}_1) \tag{8.5}$$

We follow the same procedure as in Appendix B. We recall that the formula of the Fourier transform of the Coulomb interaction is:

$$V(\mathbf{r}) = \frac{1}{L_xL_y} \sum_{\substack{st \\ (s,t)\neq(0,0)}} \frac{2\pi e^2}{\varepsilon q} e^{i\mathbf{q}\cdot(\mathbf{r}_1 - \mathbf{r}_2)} \tag{8.6}$$

where $\mathbf{q} = \left(s\frac{2\pi}{L_x}, t\frac{2\pi}{L_y}\right)(s,t \in \mathbb{Z})$. The momentum $\mathbf{q} = \mathbf{0}(s = t = 0)$ is excluded because it corresponds to the direct interaction and is cancelled by the energy of the neutralizing background. The Coulomb matrix elements are given by the formula:

$$\begin{aligned}\mathcal{A}^{N_1N_2N_3N_4}_{j_1j_2j_3j_4} =& \frac{1}{L_xL_y} \sum_{\substack{st \\ (s,t)\neq(0,0)}} \frac{2\pi e^2}{\varepsilon q} \left(\int d^2\mathbf{r}_1 \psi^*_{N_1j_1}(\mathbf{r}_1)\psi_{N_4j_4}(\mathbf{r}) e^{i\mathbf{q}\cdot\mathbf{r}_1}\right) \times \\ & \times \left(\int d^2\mathbf{r}_2 \psi^*_{N_2j_2}(\mathbf{r}_2)\psi_{N_3j_3}(\mathbf{r}_2) e^{-i\mathbf{q}\cdot\mathbf{r}_2}\right)\end{aligned} \tag{8.7}$$

We evaluate the integral over $d^2\mathbf{r}_1$. It gives:

$$\int d^2\mathbf{r}_1 \psi^*_{N_1 j_1}(\mathbf{r}_1)\psi_{N_4 j_4}(\mathbf{r}_1)e^{i\mathbf{q}\cdot\mathbf{r}_1} = e^{-q^2l^2/4}e^{iq_x q_y l^2/2}e^{iq_x j_4 2\pi l^2/L_y}F_{N_1N_4}(q_x,q_y)\delta'_{t,j_1-j_4} \tag{8.8}$$

The symbol δ'_{t,j_1-j_4} means $t = j_1 - j_4(\mathrm{mod}N_\phi)$. The integral over $d^2\mathbf{r}_2$ is evaluated in the same way and gives:

$$\begin{aligned}\int d^2\mathbf{r}_2 \psi^*_{N_2 j_2}(\mathbf{r}_2)\psi_{N_3 j_2}(\mathbf{r}_2)e^{-i\mathbf{q}\cdot\mathbf{r}_2} \\ =e^{-q^2l^2/4}e^{-iq_x q_y l^2/2}e^{-iq_x j_3 2\pi l^2/L_y}F_{N_2N_3}(-q_x,-q_y)\delta'_{t,j_3-j_2}\end{aligned} \tag{8.9}$$

The form factors $F_{N_1N_4}(q_x,q_y)$ and $F_{N_2N_3}(q_x,q_y)$ are defined as follows:

$$\begin{aligned}F_{00}(q_x,q_y) =&1\\ F_{01}(q_x,q_y) =&\sqrt{1-\gamma}\frac{(iq_x+q_y)l}{\sqrt{2}}\\ F_{10}(q_x,q_y) =&\sqrt{1-\gamma}\frac{(iq_x-q_y)l}{\sqrt{2}}\\ F_{11}(q_x,q_y) =&\gamma L_0 + (1-\gamma)\left(1-\frac{q^2l^2}{2}\right)\end{aligned} \tag{8.10}$$

The form factors F_{00} and F_{11} are the form factors of the orbitals $N=0$ and $N=1$, respectively. F_{00} is exactly the form factor of the Lowest Landau Level, while F_{11} continuously interpolates between the form factors of the Lowest Landau Level ($\gamma=1$) and the second Landau level ($\gamma=0$). The form factors F_{01} and F_{10} lead to the mixing between the two orbitals. Overall, we evaluate the Coulomb matrix elements by using the formula:

$$\begin{aligned}\mathcal{A}^{N_1N_2N_3N_4}_{j_1j_2j_3j_4} =&\frac{1}{L_xL_y}\sum_{\substack{st\\(s,t)\neq(0,0)}}\delta_{q_x,s\frac{2\pi}{L_x}}\delta_{q_y,t\frac{2\pi}{L_y}}\frac{2\pi e^2}{\varepsilon q}e^{-q^2l^2/2}\times\\ &\times e^{i2\pi(j_1-j_3)s/N_\phi}F_{N_1N_4}(q_x,q_y)F_{N_2N_3}(-q_x,-q_y)\delta'_{t,j_1-j_4}\delta'_{j_1+j_2,j_3+j_4}\end{aligned} \tag{8.11}$$

When we take into account the screening effect due to the metallic gates, the Coulomb interaction is modified so the Coulomb matrix elements become:

$$\begin{aligned}\mathcal{A}^{N_1N_2N_3N_4}_{j_1j_2j_3j_4} =&\frac{1}{L_xL_y}\sum_{\substack{st\\(s,t)\neq(0,0)}}\delta_{q_x,s\frac{2\pi}{L_x}}\delta_{q_y,t\frac{2\pi}{L_y}}\frac{2\pi e^2/\varepsilon q}{1+\frac{a}{ql}\tanh\left(\frac{q^2l^2}{2}\right)}e^{-q^2l^2/2}\times\\ &\times e^{i2\pi(j_1-j_3)s/N_\phi}F_{N_1N_4}(q_x,q_y)F_{N_2N_3}(-q_x,-q_y)\delta'_{t,j_1-j_4}\delta'_{j_1+j_2,j_3+j_4}\end{aligned} \tag{8.12}$$

In the previous discussions, we presented the single-particle momentum k_y to label the single-electron wavefunction. However, we are examining a system of N_e electrons. Therefore, we need to define the quantum number of the many-body wavefunction. This kind of quantum number is defined using the *relative translation operator* (see Appendix B.5). The relative translation operators allow us to define the *many-body momentum* $\mathbf{K}$ as follows:

$$\mathbf{K} = \frac{2\pi}{L_x}(s-s_0)\hat{\mathbf{x}} + \frac{2\pi}{L_y}(t-t_0)\hat{\mathbf{y}}(s,t\in\mathbb{Z}) \tag{8.13}$$

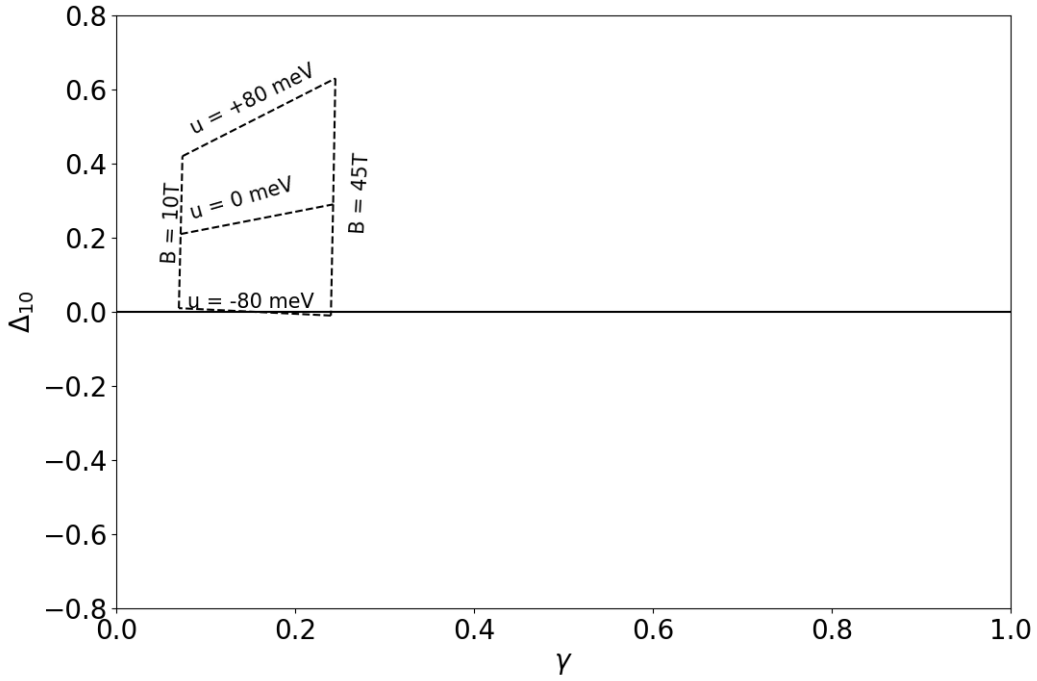

Figure 8.1: The (γ, Δ_{10}) plane. We show the typical values of γ and Δ_{10} accessible during the experiments between the curves corresponding to $-80\,\mathrm{meV} \leq u \leq 80\,\mathrm{meV}$ and $10\,\mathrm{T} \leq B \leq 45\,\mathrm{T}$.

Let N be the greatest common divisor of N_e and N_ϕ, we have $N_e = pN$ and $N_\phi = qN$. The **filling factor** equals:

$$\nu = \frac{N_e}{N_\phi} = \frac{p}{q} \tag{8.14}$$

The Brillouin zone of the many-body wavefunctions is a rectangular and contains N^2 many-body momenta $\mathbf{K}$. The area of the Brillouin zone is $A_{BZ} = (2\pi)^2 N^2/(L_x L_y)$. The center of the Brillouin zone $\mathbf{K} = \mathbf{0}$, however, does not correspond to $s = t = 0$, but corresponds to the quantum numbers s_0 and t_0 instead, and is determined as follows:

- If $pq(N_e - 1)$ is even, then $s_0 = t_0 = 0$
- If $pq(N_e - 1)$ is odd, then $s_0 = t_0 = N/2$

Overall, we study the ground state of the BLG system by varying two parameters: the weight γ which takes values $0 \leq \gamma \leq 1$, and the orbital splitting energy Δ_{10}. The third parameter is the screening a. We set $a = 0$. The systems with nonzero screening $a \neq 0$ have the same phase diagram as in the case where $a = 0$, only the phase boundaries are displaced.

8.3 . The Laughlin state $\nu = 1/3$

We study the fate of the quantum Hall state of filling factor $\nu = 1/3$ on the $\Delta_{10} - \gamma$ plane (Fig. 8.1). Along the $\gamma = 1$ line, the single-particle wavefunctions on both orbitals

$N = 0$ and $N = 1$ are the Lowest Gallilean Landau Level wavefunction, but localized on the two different sublattices A1 and A2, respectively. The two orbitals have the same form factor $F_{00} = F_{11} = 1$, and there is no mixing between them: $F_{01} = F_{10} = 0$. Hence, the physics is like in the one of a spinful quantum Hall system in the Lowest Landau level. The many-body wavefunction of the incompressible state is well approximated by the following wavefunction:

$$\Psi_{1/3}(\{z_i\}) = \prod_{i<j}(z_i - z_j)^3 |\text{symmetric spinor part}\rangle \tag{8.15}$$

in which the spatial part is the Laughlin wavefunction, and the spinor part is a symmetric ferromagnetic multiplet. Here we have an example of quantum Hall ferromagnetism. The Coulomb interaction has the SU(2) symmetry between the two components. The orbital splitting energy Δ_{10} plays the same role as the Zeeman energy in spinful systems and breaks the SU(2) symmetry of the Coulomb interaction. When $\Delta_{10} = 0$, the pseudo-Zeeman field vanishes, and the SU(2) symmetry of the total Hamiltonian is unbroken, so the spinor part of the groundstate is a multiplet with total pseudospin $P_{tot} = N_e/2$. A nonzero pseudo-Zeeman field Δ_{10} lifts this degeneracy. For $\Delta_{10} < 0$, the state with pseudospin $P^z = +N_e/2$ is favored, where the electrons tend to occupy the $N = 0$ orbital. By contrast, when $\Delta_{10} > 0$, the state with pseudospin $P^z = -N_e/2$ is the preferred one. In this case, the electrons favor to occupy the orbital $N = 1$. In other words, we can also say that for $\gamma = 1$ and large $|\Delta_{10}|$ the system is layer-polarized, because for $\gamma = 1$ the orbital degree of freedom coincides with the layer degree of freedom.

Now, we move on to the case where $|\Delta_{10}|$ is very large and discuss the ground state as a function of the parameter γ. For Δ_{10} large and negative, the system is fully polarized to the $N = 0$ orbital, so the ground state is one-component and independent of γ. The physics is that of the Laughlin state in the Lowest Landau Level. The many-body wavefunction can be approximately given by:

$$\Psi_{1/3}(\{z_i\}) = \prod_{i<j}(z_i - z_j)^3 |00\ldots0\rangle \tag{8.16}$$

For Δ_{10} large and positive, the system is fully polarized to the $N = 1$ orbital. The physics of the system is described by the form factor F_{11}, which is dependent on γ. For $\gamma = 1$, this is the physics of the layer-polarized Lowest Landau level wavefunction we previously discussed for the $\gamma = 1$ line. For $\gamma = 0$, the single-particle wavefunction becomes the second Landau level wavefunction. The form factor corresponds to the interaction in this Landau level. The ground state is therefore the Laughlin-like state of filling factor $\nu = 1/3$ in the second Landau level. In this Landau level, finite size effect is important and the Laughlin state needs to be stabilized by a finite width of the electron gas. For $\gamma = 1/2$, the form factor is the same like the form factor of the Landau level $N = 1$ of monolayer graphene.

For $\gamma = 0$, the single particle wavefunctions become localized to the same sublattice (sublattice A1 on the top layer). By varying the orbital splitting energy Δ_{10}, we continuously go from the physics of the Lowest Galilean Landau level $n = 0$ to the physics of the second Galilean Landau level $n = 1$. The two limiting cases for $|\Delta_{10}|$ very large have been discussed in the previous paragraphs. When $\Delta_{10} = 0$, we have the maximal mixing between the $n = 0$ and $n = 1$ Galilean Landau levels. In conventional

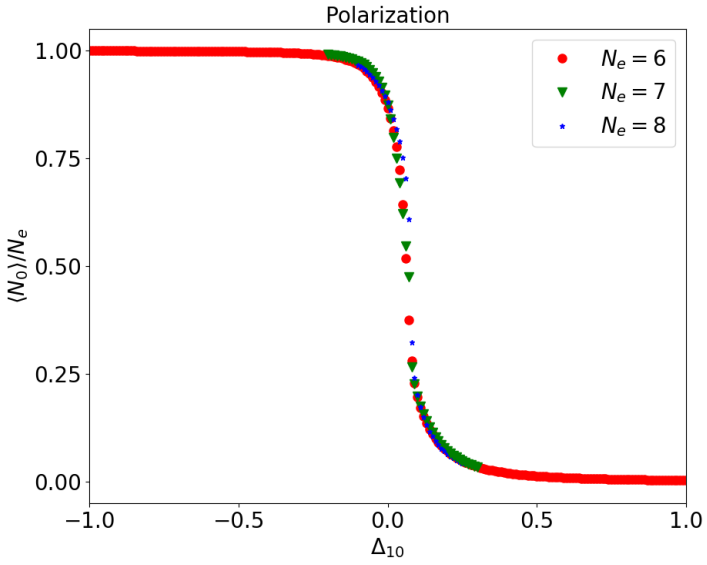

Figure 8.2: The polarization of the ground state of $\nu = 1/3$ at $\mathbf{K} = \mathbf{0}$ for $\gamma = 0$ as a function of Δ_{10}. The sizes of the system are $N_e = 6, 7, 8$ electrons. The corresponding aspect ratios of the torus are $L_x/L_y = 0.44, 0.35, 0.70$. The figure clearly shows a polarization transition at which electrons transfer from the orbital $N = 0$ to the orbital $N = 1$ as Δ_{10} increases from -1 to +1. The value of Δ_{10} at which the polarization transition happens is almost independent of the size of the system.

quantum Hall systems in semiconductors, if the cyclotron energy is small compared to the Coulomb energy, there are virtual transitions towards the empty higher Landau levels. Therefore, Landau level mixing modifies the interaction between electrons in the LLL, and destabilizes the quantum Hall liquid in favor of a Wigner crystal. In BLG, by neglecting the higher Landau levels, here the physics is reminiscent of an extreme mixing between the lowest and the second Landau levels. This situation is unique for bilayer graphene.

On the line $\Delta_{10} = 0$, we have the maximal mixing between the two orbitals $N = 0$ and $N = 1$. By varying γ, we continuously interpolate from the limit of extreme Landau level mixing - like ($\gamma = 0$) to the limit of an SU(2)-symmetric spinful system ($\gamma = 1$). In the next sections, we will study the physics for small γ and small Δ_{10} values. We expect than the polarization of the ground state varies as we vary the orbital splitting energy Δ_{10}. For this reason, we use the polarization of the ground state and the quantum fidelity as the indicators to locate the phase boundaries.

8.4 . Transition between the two orbitals

8.4.1 . Polarization transition

Let $|\Psi\rangle$ be a quantum state of the 2D electron system, we define the polarization of $|\Psi\rangle$ as the proportion of the number of electrons occupying the orbital $N = 0$ over the total number N_e of all the electrons:

$$\mathcal{P} = \langle\Psi|\hat{N}_0|\Psi\rangle/N_e = 1 - \langle\Psi|\hat{N}_1|\Psi\rangle/N_e \tag{8.17}$$

The value of $\mathcal{P}$ varies from $0 \leq \mathcal{P} \leq 1$. When $\mathcal{P} = 1$, all particles occupy the orbital $N = 0$. Inversely, when $\mathcal{P} = 0$, all particles occupy the orbital $N = 1$. The states whose

$\mathcal{P} = 0.5$ have a balanced occupation of electrons over the two orbitals. That means in those states, there are $N_e/2$ electrons occupying each orbital.

We consider the state of filling factor $\nu = 1/3$ and study the variation of the polarization on the line $\gamma = 0$ by varying Δ_{10} from $\Delta_{10} = -1$ to $\Delta_{10} = +1$. For large values of Δ_{10}, we know that the ground state is a quantum Hall liquid, so its many-body momentum is at $\mathbf{K} = \mathbf{0}$. The ground state manifold of the Wigner crystal, that is suspicious to compete with the quantum Hall liquid in the vicinity of $\Delta_{10} = 0$, also contains a state with many-body momentum $\mathbf{K} = \mathbf{0}$. Because we are interested in the polarization of the ground state, we fix the many-body momentum at $\mathbf{K} = \mathbf{0}$ and calculate the polarizaton $\mathcal{P}$ of the many-body ground state.

The polarization of the ground state of $N_e = 6, 7, 8$ is shown in Fig. 8.2. For $\Delta_{10} < 0$ and large, $\mathcal{P} \approx 1$, meaning that almost all particles occupy the orbital $N = 0$. As Δ_{10} increases, the polarization slowly decreases and remains $\mathcal{P} > 0.9$ until $\Delta_{10} \approx -0.02$. Since then, the polarization sharply goes down. The inflection point at which $\mathcal{P} = 0.5$ is not at $\Delta_{10} = 0$, but at $\Delta_{10} \approx 0.06$ instead. At this value of Δ_{10}, there is a balanced occupation of the electrons over the two orbitals. It shows that there is a transition at which electrons move from the orbital $N = 0$ to the orbital $N = 1$. The value of Δ_{10} at the transition is almost independent of the size of system. For $\Delta_{10} \geq 0.15$, $\mathcal{P} < 0.1$ and slowly decreases to $\mathcal{P} = 0$ with increasing Δ_{10}. For $\Delta_{10} > 0$ and large, almost all particles occupy the orbital $N = 1$.

Fig. 8.3 shows the polarization of the ground state at $\mathbf{K} = \mathbf{0}$ for $N_e = 6$ electrons as a function of the two parameters γ and Δ_{10}. For $\gamma < 1$, the transition from the orbital $N = 0$ to the orbital $N = 1$ happens at positive values of Δ_{10}. The reason is as follows: the exchange energy is stronger in the Lowest Landau Level than in the Second Landau Level. Therefore, even when $\Delta_{10} = 0$, electrons favorably occupy the orbital $N = 0$ instead of the orbital $N = 1$. Indeed, the former has a whole weight on the Lowest Landau level, while the latter has a finite weight on the Second Landau level. To balance the exchange energy, one needs a finite cost by adding a positive offset energy Δ_{10}. As γ increases, this finite offset decreases down to $\Delta_{10} = 0$, forming a boundary separating the red region (where electrons prefer to occupy the orbital $N = 0$) from the blue region (where electrons favor to occupy the orbital $N = 1$). When $\gamma = 1$, the two orbitals have the same form factor of the Lowest Landau level, the exchange interaction is as strong in orbital $N = 0$ as in orbital $N = 1$. The offset energy for a transition from orbital $N = 0$ to orbital $N = 1$ is $\Delta_{10} = 0$. In this case, we recover the physics of a fully SU(2)-symmetric system.

8.4.2 . Quantum fidelity

To confirm the existence of a phase transition, we use another indicator: the quantum fidelity. The idea is as follows: we fix the parameter γ and slightly change the parameter Δ_{10} by an infinitesimal increment ϵ. And then we calculate the overlap between the new ground state $|\Psi(\Delta_{10} + \epsilon)\rangle$ and the old ground state $|\Psi(\Delta_{10})\rangle$. The quantum fidelity is given by the formula:

$$\mathcal{F}(\Delta_{10}) = |\langle\Psi(\Delta_{10} + \epsilon)|\Psi(\Delta_{10})\rangle|^2 \tag{8.18}$$

If we are in the same phase, the quantum fidelity is close to unity. A phase transition happens when there is a strong dip in $\mathcal{F}$ away from the unity. Fig. 8.4 shows the quantum fidelity $\mathcal{F}(\Delta_{10})$ of the ground state at $\mathbf{K} = \mathbf{0}$ with filling factor $\nu = 1/3$ at $\gamma = 0$. The

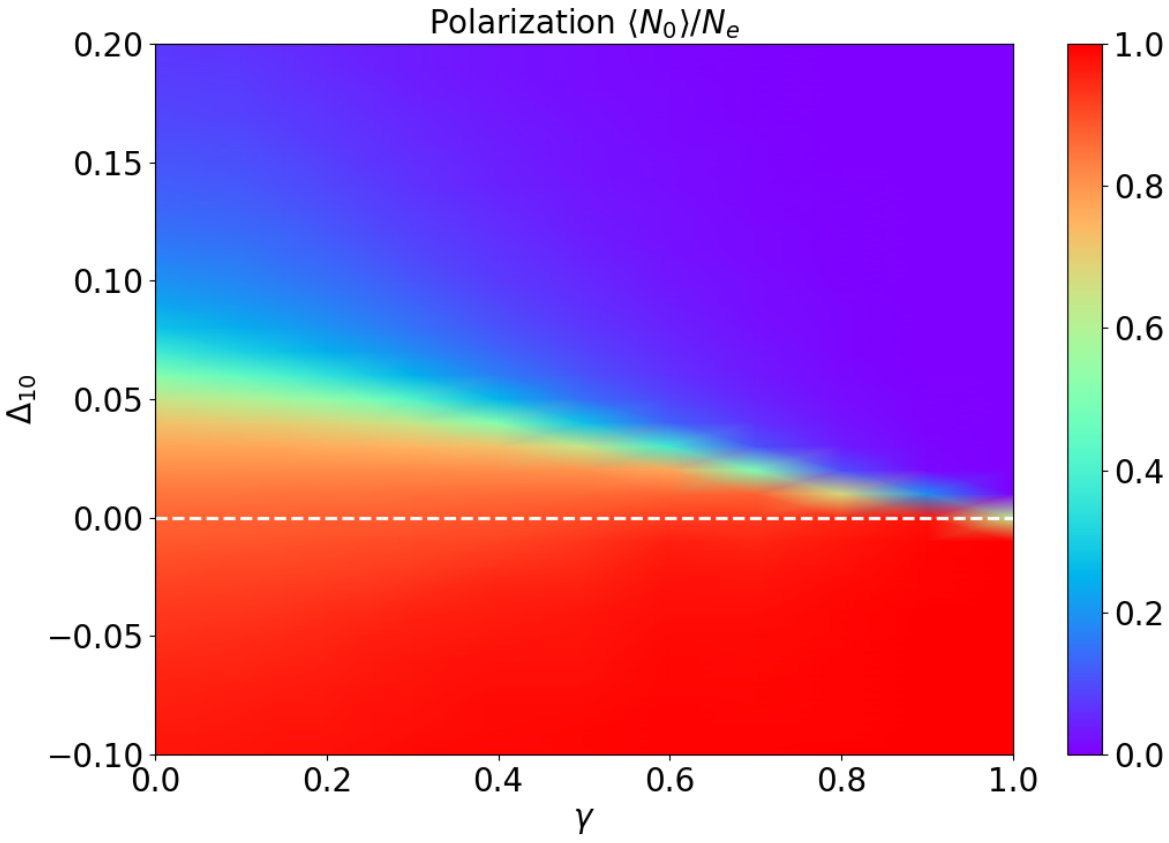

Figure 8.3: The polarization of the ground state at $\mathbf{K} = \mathbf{0}$ for $N_e = 6$, electrons, $N_\phi = 18$ magnetic flux quanta on a torus with aspect ration $L_x/L_y = 0.44$. The color bar illustrates the polarization $\mathcal{P} = \langle N_0 \rangle / N_e$. The lower half of the $\gamma - \Delta_{10}$ has red color ($\mathcal{P} > 0.5$), showing that electrons of the corresponding states tend to occupy the orbital $N = 0$. By contrast, the upper half of the $\gamma - \Delta_{10}$ plane has blue color ($\mathcal{P} < 0.5$), and electrons of the corresponding quantum states favor to occupy the $N = 1$ orbital. The two regions are separated by a green transition line ($\mathcal{P} \approx 0.5$) where electrons transfer between the two orbitals. The critical value Δ_{10} of the transition is positive because the exchange energy is stronger in orbital $N = 0$ than in orbital $N = 1$, so it requires a nonzero offset energy to balance the total energies of the two orbitals.

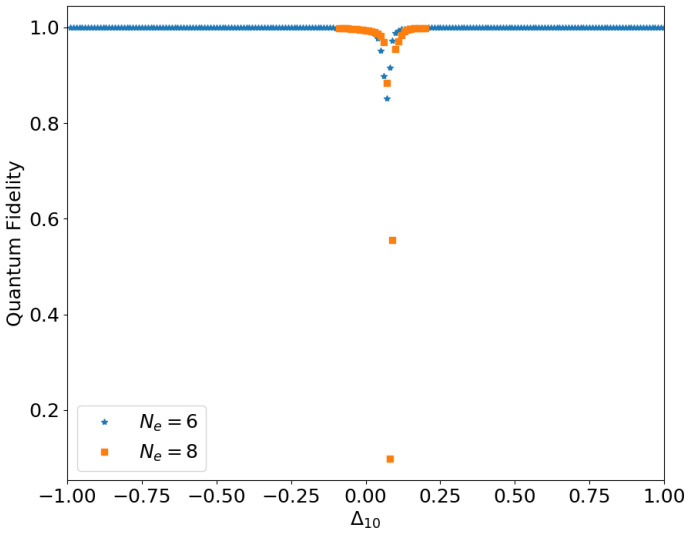

Figure 8.4: The quantum fidelity of the ground state $|\Psi(\Delta_{10})\rangle$ with filling factor $\nu = 1/3$ at $\mathbf{K} = \mathbf{0}$ for $\gamma = 0$. The increment step is $\delta = 0.01$. Here we show the quantum fidelity for $N_e = 6$ and $N_e = 8$. There is a strong dip in $\mathcal{F}$ at $\Delta_{10} = 0.06$, showing that a phase transition happens. It is consistent to the polarization transition we discussed in subsection 8.4.1.

step increment is $\delta = 0.01$. There is a strong dip at $\Delta_{10} \approx 0.06$, indicating a phase transition, consistent with the polarization transition we previously showed in subsection 8.4.1. The dip in the quantum fidelity grows with the size of the system. We conclude that the polarization and the quantum fidelity indicate the boundary at which there is a polarization transition. We find two phases: (i) the first phase with an electron occupation polarized to the $N = 0$ orbital ($\mathcal{P} > 0.5$) appears at low values of Δ_{10}, and (ii) the second phase with an electron occupation polarized to the $N = 1$ orbital ($\mathcal{P} < 0.5$) appears at high values of Δ_{10}.

8.5 . The Wigner crystal

We start by studying the state with $N_e = 6$, $N_\phi = 18$ at $\gamma = 0$ and $\Delta_{10} = 0$. We perform exact diagonalizations on the torus by varying the aspect ratio $0.2 \leq L_x/L_y \leq 1.0$ while keeping the area unchanged $L_x L_y = 2\pi N_\phi l^2$. We observe a clear ground state quasidegeneracy for aspect ratio around AR$= 0.44$ (Fig. 8.5). The quasidegenerate ground states have an energy splitting of the order $10^{-4}e^2/(\varepsilon l)$ and are well separated from the excited states by a gap of order $10^{-2}e^2/(\varepsilon l)$. We call the set of quasidegenerate ground states the *ground state manifold*. The system is no longer isotropic in space and manifests a broken translational symmetry. This phenomenon was observed at low filling factors or in higher Landau levels and is associated to the formation of charge density waves, stripe and bubble phases, Wigner crystals [148, 163–165]. In BLG, a broken translational symmetry phase called the helical phase was also predicted for filling factor $\nu = 1$ [35].

Fig. 8.6a shows the energy spectrum of $N_e = 6$ electrons, $N_\phi = 18$ magnetic flux quanta on the torus with aspect ratio $L_x/L_y = 0.44$. Here we set $\gamma = 0$ and $\Delta_{10} = 0$.

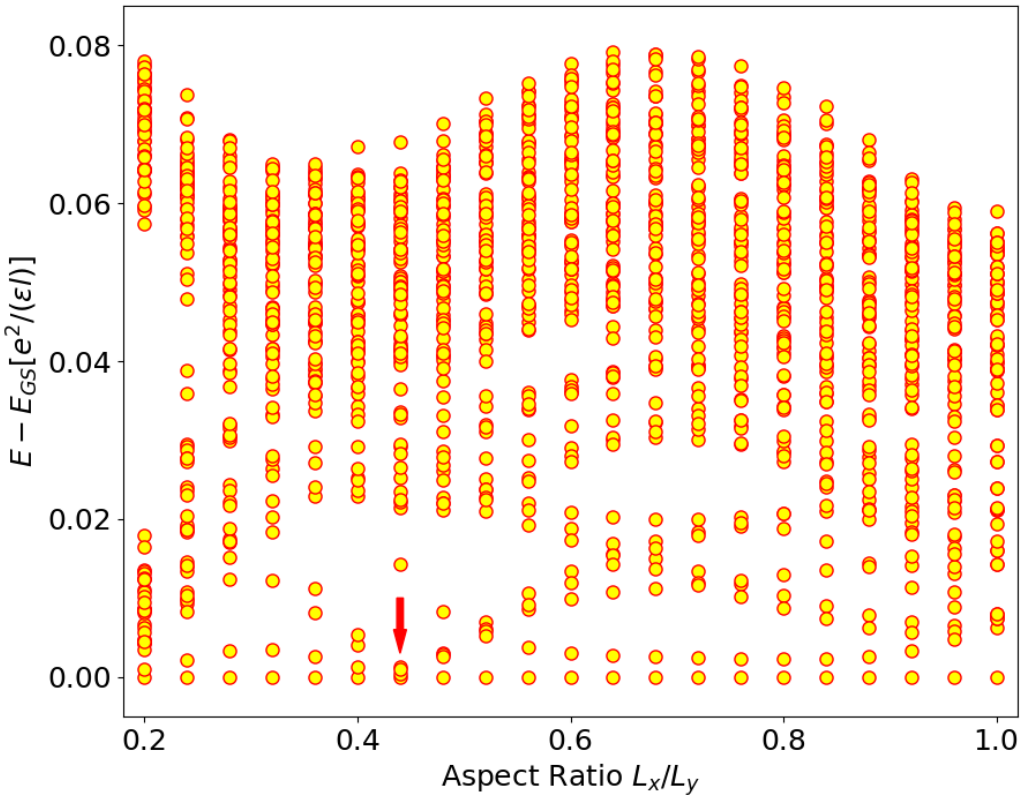

Figure 8.5: The spectrum of $N_e = 6$ electrons, $N_\phi = 18$ magnetic flux quanta (filling factor $\nu = 1/3$). The greatest common divisor of N_e and N_ϕ is $N = 6$. The parameters are $\gamma = 0$, $\Delta_{10} = 0$. Here we perform exact diagonalizations on the torus and vary the aspect ratio L_x/L_y such that $0.2 \leq L_x/L_y \leq 1.0$ so as to keep the area of the torus constant $L_x L_y = 2\pi N_\phi l^2$. The Brillouin zone of a torus with defined aspect ratio contains $N^2 = 36$ momenta $\mathbf{K}$. At each momentum $\mathbf{K}$, we calculate the 5 lowest energy eigenvalues. Each vertical line at fixed L_x/L_y contains the quantum states of the corresponding torus with all momenta $\mathbf{K}$. At aspect ratio $L_x/L_y = 0.44$, there is a crossing between levels (see the red arrow), meaning that the ground states are quasidegenerate. The spectrum of the case $L_x/L_y = 0.44$ is shown in Fig. 8.6a.

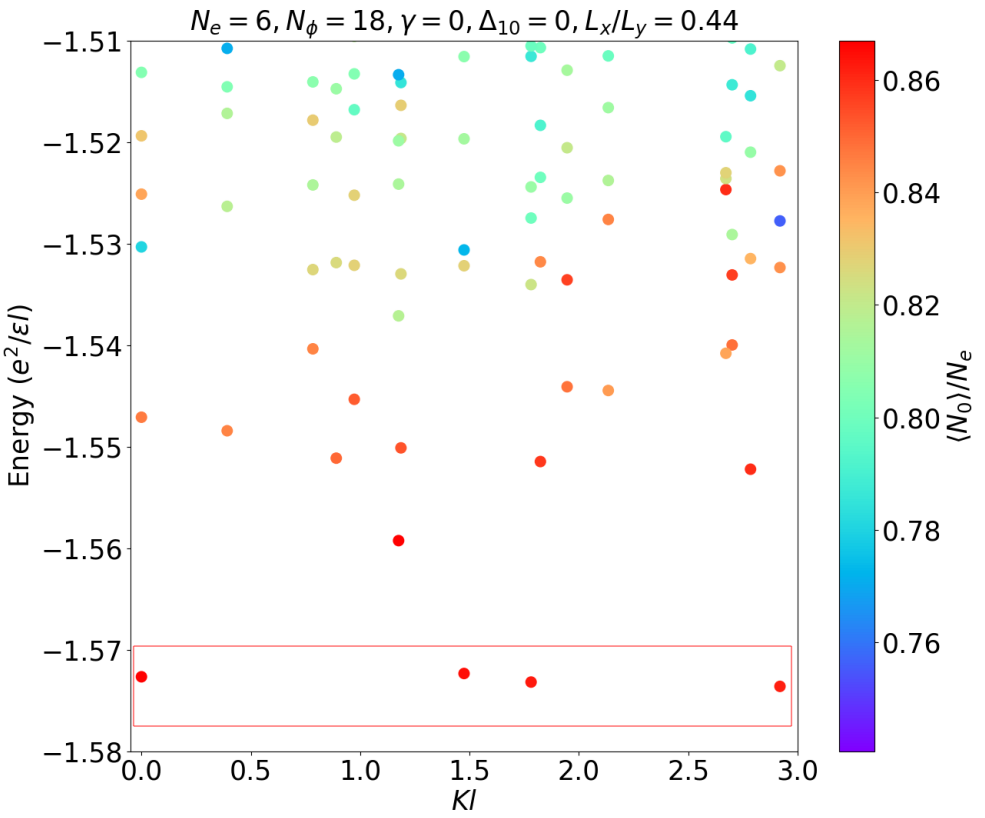

(a)

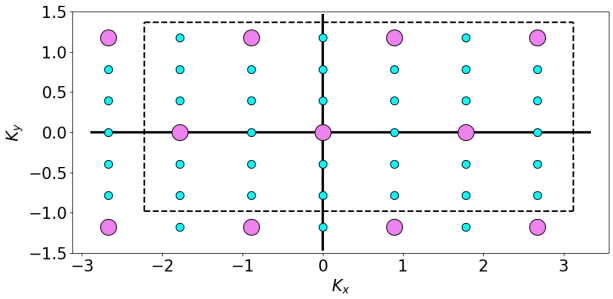

(b)

Figure 8.6: (a) The energy spectrum of $N_e = 6$ electrons, $N_\phi = 18$ magnetic flux quanta on the torus with aspect ratio $L_x/L_y = 0.44$. The parameters are $\gamma = 0$ and $\Delta_{10} = 0$. The colorbar shows the polarization $\mathcal{P}$ of the states. The states inside the red rectangle form the ground state manifold. (b) The many-body Brillouin zone of the corresponding torus. The dots (small cyan dots and big magenta dots) represent the allowed many-body momenta. The quasidegenerate ground states are represented by big magenta dots. The dashed rectangle contains $N^2 = 36$ non-equivalent momenta. The momenta outside the rectangle can be brought into equivalent counterparts inside the rectangle via translations along the edges of the Brillouin zone.

The spectrum clearly shows the quasidegenerate ground states, separated by a gap of size $0.01e^2/(\varepsilon l)$ from the excited states. The polarization is about $\mathcal{P} \approx 0.85$ for the ground states, showing that in the ground state the electrons tend to occupy the orbital $N = 0$. Although, in the ground states there is a finite but small number of electrons occupying the orbital $N = 1$. Excited states have lower polarizations $\mathcal{P}$, meaning that they have more electrons occupying the orbital $N = 1$ than in ground states.

In Fig. 8.6b, we plot the ground state manifold inside the Brillouin zone. The area of the many-body Brillouin zone is $(2\pi)^2 N^2/(L_x L_y)$. Let N be the greatest common divisor of N_e and N_ϕ, we have $N = 6$ [1]. Due to the breaking of the translational symmetry, the number of degenerate ground states is $N_D = 6$. This implies that the Brillouin zone of the symmetry-breaking phase is reduced by N_D times, and has an area of $(2\pi)^2 N^2/(L_x L_y N_D)$. In the real space, electrons form bubbles, which are periodically arranged in real space. Let N_b be the number of bubbles in a cell, each bubble becomes a unit cell with area $L_x L_y/N_b$. The area of the Brillouin zone of the symmetry-breaking phase is $(2\pi)^2/(L_x L_y/N_b)$. The equality $(2\pi)^2 N^2/(L_x L_y N_D) = (2\pi)^2/(L_x L_y/N_b)$ implies that $N_D N_b = N^2$. Therefore, the number of bubbles is $N_b = N^2/N_D = 6$ [165]. The number of electrons per bubble is $N_e/N_b = 1$, showing that the ground state is a ***Wigner crystal***.

One needs to fine tune the aspect ratio of the unit cell to observe the degeneracy because the Wigner crystal is sensitive to the aspect ratio. The optimal value of the aspect ratio at which the Wigner crystal appears is $L_x/L_y = 0.44$ for $N_e = 6$, $L_x/L_y = 0.37$ for $N_e = 7$, $L_x/L_y = 0.7$ for $N_e = 8$, and $L_x/L_y = 0.3$ for $N_e = 9$. To prove the periodic distribution of the electron in real space, we calculate the pair correlation function. The pair correlation function is the measure of the probability of finding two electrons separated by a distance $\mathbf{R}$. It is given by the formula:

$$g_{\alpha\beta}(\mathbf{R}) = \frac{1}{\rho N_e} \sum_{i<j} \delta(\mathbf{r}_i - \mathbf{r}_j - \mathbf{R})(|\alpha\rangle\langle\alpha|)_i(|\beta\rangle\langle\beta|)_j \tag{8.19}$$

In this formula, $\alpha, \beta = 0, 1$ are the orbital indices. The electrons are labeled by the indices i, j, and their positions are described by the vectors $\mathbf{r}_i$ and $\mathbf{r}_j$. The quantity $\rho = N_e/(L_x L_y)$ is the electron density. In second quantization language, we write the pair-correlation function between two electrons occupying orbitals α, β and separated further apart by a distance $\mathbf{R}$ as follows:

$$g_{\alpha\beta}(\mathbf{R}) = \frac{L_x L_y}{N_e^2} \int d^2\mathbf{r} d^2\mathbf{r}' \langle\Psi|\hat{\psi}_\alpha^\dagger(\mathbf{r})\hat{\psi}_\beta^\dagger(\mathbf{r}')\delta^{(2)}(\mathbf{r} - \mathbf{r}' - \mathbf{R})\hat{\psi}_\beta(\mathbf{r}')\hat{\psi}_\alpha(\mathbf{r})|\Psi\rangle \tag{8.20}$$

Because we apply the periodic boundary conditions on the finite-size system, the pair correlation function is periodic: $g_{\alpha\beta}(x + L_x, y) = g_{\alpha\beta}(x, y + L_y) = g_{\alpha\beta}(x + L_x, y + L_y) = g_{\alpha\beta}(x, y)$. It allows us to recover the value of the pair correlation function on the whole plane by replicating the calculated values on one single cell. Because the Wigner crystal is polarized to the orbital $N = 0$, we examine the spatial distribution of electrons by calculating the pair correlation function g_{00}. We show the pair correlation function g_{00} for $N_e = 6, 7, 8$ in Fig. 8.7. Due to periodicity, we only show g_{00} in a rectangular cell

[1] Here we use the symbol N for the greatest common divisor of N_e and N_ϕ because this notation is familiar in the literature. We recommend the reader to distinguish this notation from the symbol N of the orbital, depending on the context.

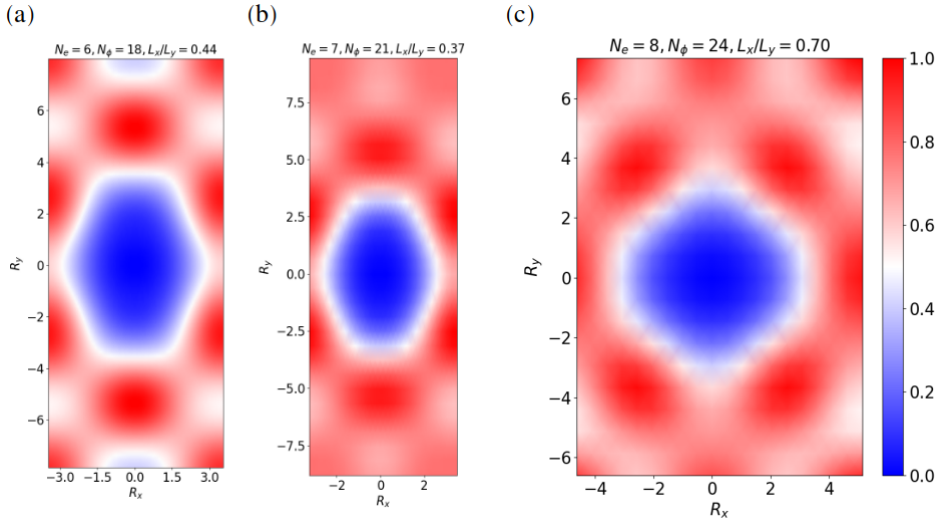

Figure 8.7: The pair correlation function $g_{00}(R_x, R_y)$ for $N_e = 6, 7, 8$ electrons at filling factor $\nu = 1/3$ for $\gamma = 0$ and $\Delta_{10} = 0$. We calculated the pair correlation function on a rectangular cell of size $L_x \times L_y$. The aspect ratio favoring the Wigner crystal is size-dependent. The pair correlation function is zero at the center $g_{00}(0, 0) = 0$ due to the Pauli exclusion principle.

of size $L_x \times L_y$. In all cases, at the center $R_x = R_y = 0$ the pair correlation function vanishes $g_{00}(0, 0) = 0$ because the fermionic nature of electrons forbids two electrons having the same quantum numbers to coincide in space (Pauli exclusion principle). Apart from the center, there exist overdensity regions, which are represented by the red bubbles. Here we observe the periodic modulation of the electron density in space. This is the characteristic of a Wigner crystal. The pair correlation function of a quantum Hall liquid, however, exhibits a crater-like feature around the position of the reference particle and a smooth background outside the first ring of overdensity (Fig. 8.9). *The pair correlation function visualizes the real space distribution of the electron density and confirms that electrons form a crystalline lattice in real space.* For $N_e = 6$ and $N_e = 7$, the electrons form triangular lattice, while for $N_e = 8$ the electrons form square lattice. We cannot conclude on the precise nature of the crystal,there is a competition between the triangular and the square lattices.

We explain the formation of this Wigner crystal as follows. In the vicinity of the crossing between the levels $|K0 \uparrow\rangle$ and $|K1 \uparrow\rangle$, the spin and valley degrees of freedom are frozen. The situation is like in the case where there are two Landau levels $N = 0$ and $N = 1$ (supposing that we neglect all mixing with higher Landau levels). Here the energy Δ_{10} plays the role of the cyclotron energy. By tuning the interlayer bias u, the value of Δ_{10} varies. When $\Delta_{10} = 0$, the two orbitals coincide and we arrive to a situation reminiscent to an extreme Landau level mixing. As we already know from chapter 7, strong Landau level mixing prefers the ground state to be a Wigner crystal rather than a quantum Hall liquid. That explains the formation of this electrically-induced Wigner crystal.

By examining the ground state manifold in the Brillouin zone, we see that the quasi-degenerate ground states characterizing the Wigner crystal disappear at the polarization transition from the orbital $N = 0$ to the orbital $N = 1$. This is consistent because we previously found that the Wigner crystal is almost polarized to the $N = 0$ orbital. This

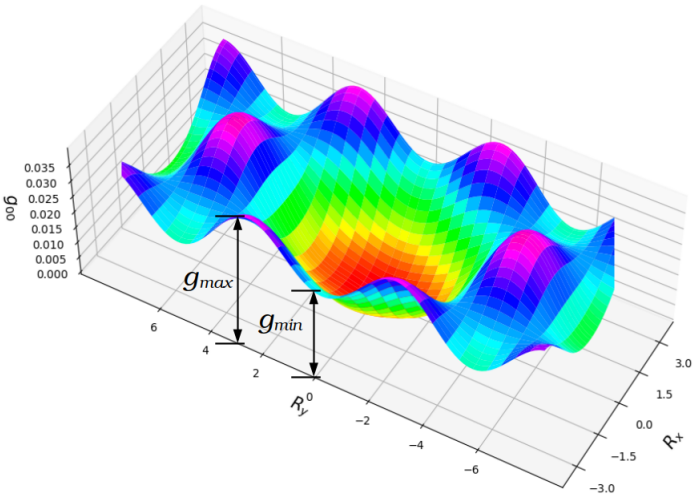

Figure 8.8: The method of determining the crytal strength. Here we show the pair correlation function of the ground state at $\mathbf{K} = \mathbf{0}$ for $N_e = 6$, $N_\phi = 18$, $\gamma = 0$, $\Delta_{10} = 0$, $L_x/L_y = 0.44$. The first ring of overdensity contains the six nearest maxima surrounding the central minimum ($R_x = R_y = 0$). g_{max} is the value of the pair correlation function at the maxima, while g_{min} is the minimum value of the pair correlation function in the middle of two consecutive maxima. The crystal strength is defined as the ratio $(g_{max} - g_{min})/g_{min}$.

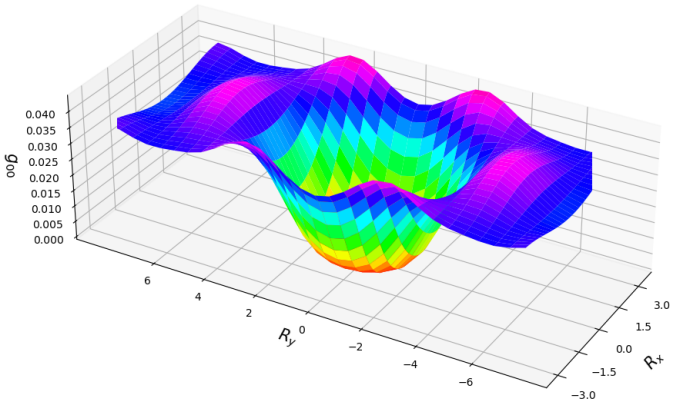

Figure 8.9: The crater-like feature of the pair correlation function g_{00} of the Laughlin state. Here we show the pair correlation function of $N_e = 6$, $N_\phi = 18$, $\gamma = 0$, $\Delta_{10} = -0.8$. The graph of the pair correlation function g_{00} on a unit cell has a minimum at the center $R_x = R_y = 0$, corresponding to the position of the reference particle. The ring of overdensity exists around the reference particle. Those overdensities indicate the "seed" positions at which the crystal forms when Δ_{10} approaches 0. In this case, the contrast $(g_{max} - g_{min})/g_{min}$ is too weak to form a Wigner crystal.

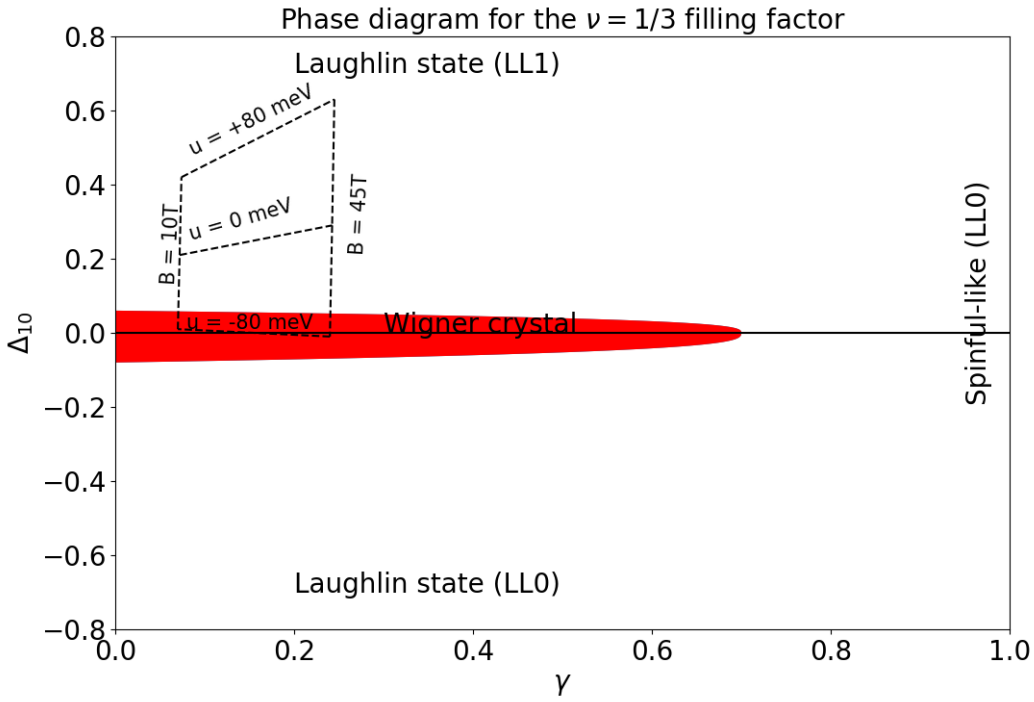

Figure 8.10: The phase diagram of the filling factor $\nu = 1/3$ in the $\gamma - \Delta_{10}$ plane. The Wigner crystal phase is shown inside the red region.

allows to define the upper boundary of the Wigner crystal phase on the phase diagram. To define the lower boundary of the Wigner crystal phase, we look at the crystal strength. We define the contrast of the first ring of overdensity in the pair correlation function to be $(g_{max} - g_{min})/g_{min}$. For a sake of simplicity, we illustrate the way of determining g_{max} and g_{min} for a system of size $N_e = 6$, $N_\phi = 18$ in Fig. 8.8. In the crystal phase the contrast is 0.44 for $\gamma = 0$, $\Delta_{10} = 0$, $N_e = 9$, $L_x/L_y = 0.3$. The Coulomb ground state of filling factor $\nu = 1/3$ in a single polarized Landau level has a contrast of about 0.04. Arbitrarily, we decide the ground state to be a liquid if the contrast is less than 0.1, and is a liquid otherwise. It allows to define the lower boundary of the crystal phase.

Finally, we show the phase diagram of the filling factor $\nu = 1/3$ in Fig. 8.10. The Wigner crystal phase occurs in the red region in the vicinity of $\Delta_{10} = 0$. As γ increase, the Wigner crystal state appears for γ up to 0.7. The dashed lines indicate that the Wigner crystal is experimentally accessible when we tune the interlayer bias to around $u = -80\,\mathrm{meV}$ and the magnetic field strength B is between $10\,\mathrm{T}$ and $45\,\mathrm{T}$. The prediction of this electrically-induced Wigner crystal is the main result of our work [105].

8.6 . The fraction $\nu = 2/3$

Last but not least, we discuss the fate of the state with filling factor $\nu = 2/3$. This state can be considered as composite fermion having 2 magnetic flux quanta under negative magnetic field. We begin with the case $\gamma = 1$. Here the Coulomb Hamiltonian is fully SU(2) symmetric, and this symmetry is broken by a nonzero pseudo-Zeeman field

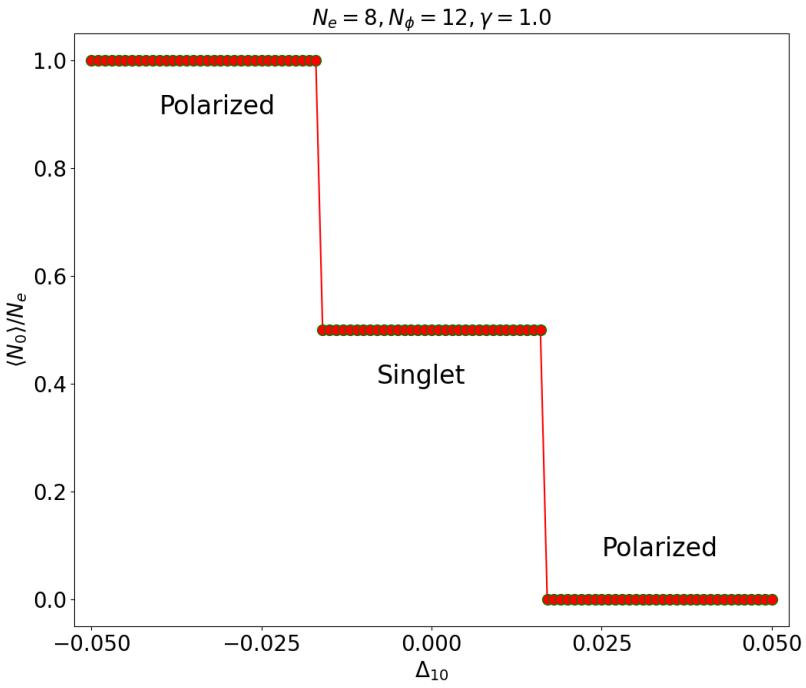

Figure 8.11: The polarization of the state $\nu = 2/3$ for $\gamma = 1$. The aspect ratio is $L_x/L_y = 0.85$. There are two abrupt changes in the polarization at $\Delta_{10} = \pm 0.016$, corresponding to two phase transitions between the pseudospin singlet state and the fully polarized states.

Δ_{10}. The two layers play the role of the pseudospin. There is the competition between the fully polarized state and the singlet state. For strong Δ_{10}, the ground state is fully polarized to one of the two layers. When Δ_{10} approaches 0, the ground state is the pseudospin-singlet state.

We show the polarization $\mathcal{P} = \langle N_0 \rangle / N_e$ in Fig. 8.11 to confirm the above arguments. The aspect ratio is $L_x/L_y = 0.85$. The graph of the polarization is a staircase with three steps. For $-0.016 < \Delta_{10} < +0.016$, the polarization is $\mathcal{P} = 0.5$. That means the two orbitals are equally occupied, and the singlet state is the ground state. For $\Delta_{10} < -0.016$, $\mathcal{P} = 1$ means that the ground state is fully polarized to the $N = 0$ orbital. For $\Delta_{10} > +0.016$, $\mathcal{P} = 0$ is consitent to a ground state that is fully polarized to the $N = 1$ orbital. There are two phase transitions at $\Delta_{10} = \pm 0.016$ between the singlet state and the two fully polarized states. Now we consider the case where $\gamma < 1$, the Coulomb interaction has no longer the pseudospin-SU(2) symmetry. The steps are rounded and there is no transition in the interior of the phase diagram. In conclusion, there is no Wigner crystal state at $\nu = 2/3$.

8.7 . Conclusion

In this chapter, we study the states $\nu = 1/3$ and $\nu = 2/3$ in Bernal bilayer graphene by using the exact diagonalization method on the torus geometry. Our interest focuses on the case of level crossing between the orbitals $N = 0$ and $N = 1$ when the spin and valley degrees of freedom are frozen. The energy Δ_{10} splitting the two orbitals is tuned

by varying the magnetic field B and the interlayer bias u across the two graphene layers. When the two orbitals almost coincide $\Delta_{10} \approx 0$, the Laughlin state is destabilized and replaced by the Wigner crystal state. In the reciprocal space of the many-body state, we recognize the Wigner crystal by the set of quasidegenerate ground states, showing that the translational symmetry is broken. The presence of the Wigner crystal is visualized in the real space by the map of pair correlation function, which shows that the overdensity bubbles form a periodic pattern.

We explain the formation of Wigner crystal as resulting from the coincidence between the two Landau levels $N = 0$ and $N = 1$, a situation reminiscent to an extreme Landau level mixing, which destablizes the Laughlin state and prefers the crystalline phase instead. This extreme Landau level mixing allows the crystallization of the electron system, even at a high filling factor. The phenomenon of re-entrant Wigner crystal at high filling factor was experimentally observed in 2D hole system [153]. This work shows that there is a re-entrant Wigner crystal around the filling factor $\nu = 1/3$, similarly to the re-entrant Wigner crystal behavior around the filling factor $\nu = 1/5$ and lower filling factors. The formation of Wigner crystal at high filling factors is due to the high effective mass of holes, which enhances the Landau level mixing.

Here we fix the filling factor at $\nu = 1/3$ and predict the formation of a Wigner crystal induced by the external electric field. One can experimentally detect this Wigner crystal by observing the variation of the longitudinal resistance R_{xx} as a function of the interlayer bias u at fixed filling factor. The formation of the electrically-induced Wigner crystal is recognized by a sharp peak in R_{xx} when the two levels are coincident. The Wigner crystal phase is observable for actually accessible magnetic field $B \leq 45\,\mathrm{T}$ and $|u| \approx 80\,\mathrm{meV}$, while the interlayer bias should be large enough so that the two orbitals coincide. The phase transition between Laughlin state and Wigner crystal is second order or weakly first-order. Our exact diagonalization studies find no signal of the Wigner crystal for the state of filling factor $\nu = 2/3$.

Chapter9 - Conclusion, perspectives and future directions

In this thesis, I studied the multicomponent quantum Hall effects in monolayer graphene and bilayer graphene. The thesis contains the results of two works in Refs. [67] and [105].

In the first project, I worked on the spin and valley ordering of monolayer graphene for the quantum Hall effects of filling factors $n/3(n = 1, 2, 4, 5)$. These symmetry-breaking orders arise from breaking the SU(4) symmetry of the Coulomb interaction due to short-range valley-dependent interaction. We first formulated a variational method and used this variational method to establish the phase diagram of the quantum Hall states in monolayer graphene. Then we performed numerical calculations by using the exact diagonalization method to identify the symmetry-broken phases. Our exact diagonalization studies found that for the state (1,1/3,1/3) there is a spin-singlet and valley-unpolarized phase that is not predicted by the variational calculations, which we call it phase C. For filling factors $\tilde{\nu} = 4/3$ and $\tilde{\nu} = 5/3$, present experiments are likely to observe the two-component (1,1/3) and (1,2/3) states. In tilted field experiments, one can change the direction of the total magnetic field to realize spin transition to the states (2/3,2/3) and (1,1/3,1/3). For $\tilde{\nu} = 4/3$, we expect that spin transitions between (2/3,2/3) and (1,1/3) happen for the KD and CDW phases. For filling factor $\tilde{\nu} = 5/3$, spin transitions are expected to occur between flavor compositions (1,2/3) and (1,1/3,1/3) for all values of the anisotropy angle θ.

There remain open questions for the problem of valley-dependent interaction in monolayer graphene. The first open question concerns finding a wavefunction which captures the phase C that we discovered for the state (1,1/3,1/3). Here I propose one direction to solve this problem in the future works. The wavefunction (4.46) is a general wavefunction of a three-component state formed by gluing an arbitrary two-component state to a fully-filled shell. One needs to find the relations between the coefficients $F_{\{m_i,n_j\}}$ such that this two-component state is a singlet eigenstate of the Coulomb interaction Hamiltonian. It may be a complicated problem to solve analytically due to the large number of $F_{\{m_i,n_j\}}$. This kind of wavefunction leads to new terms in the formula of the anisotropy energy E_V and allows to capture the singlet behavior of the phase C. The same reasoning can also apply to restrict the wavefunction (4.15) to a form that captures the antiferromagnetic phase of the state (1,1/3).

The variational phase diagram of the case $(1, 1/3, 1/3)$ was easily established, knowing that the pair correlation function between the two partially occupied components is negligible. This property is no longer valid for the four-component states and states where the partially filled components have unequal filling factors. We need to consider the terms in E_V containing the pair correlation functions between any two partially filled components to establish the variational phase diagram of such states. By the way, numerically establishing the phase diagram of such states is challenging due to the large size of the Hilbert spaces.

Previous research studied the edge states at filling factor $\nu = 0$ and found phases that are not present in the bulk [166]. The edge states under the fractional quantum

Hall regime could have an even more complicated spin and valley ordering than their counterpart in the integer quantum Hall regime. Understanding those edge states is crucial to design devices with potential applications in valleytronics, such as the quantum Hall valley splitter and the Mach-Zehnder interferometer [167]. Apart from that, there is another question about determining the properties of the excited states of the symmetry-breaking phases in both the integer and fractional quantum Hall regime. Both theoretical and numerical methods can examine this problem.

The authors of Ref. [104] studied the three-component and four-component singlet states of filling factor $\nu = 2/3$. Their numerical work shows that neither the composite fermion picture nor the multicomponent Halperin state wavefunction can explain the SU(3) and SU(4) singlet states. The nature of these singlet states at low filling factor remains an open question.

Most researches have focused on the symmetry-breaking phases in the zero Landau level. Some authors have recently expanded their interest in the Landau level $N = 1$ of graphene by studying the quantum Hall states at integer fillings [168]. In this Landau level, the valley and lattice degrees of freedom are decoupled, and the valley-dependent two-body interaction has another formula than (3.50). The nature of the symmetry-breaking phases for the fractional quantum Hall effect in this Landau level needs to be explored.

Simultaneously with our work, there is progress in both experiments and theory on the symmetry-breaking phases in charge-neutral graphene. The most striking discovery is the observation of a K-CDW phase, which coexists with the KD phase [77]. This K-CDW has a lattice parameter $\sqrt{3}$ times greater than the graphene lattice parameter and is a different phase than the CDW in the phase diagram of Kharitonov, which has the same lattice parameter as graphene. Explaining this new phase beyond the four known phases F, AF, KD, and CDW requires further theoretical investigations. The authors of Refs. [169] and [170] proposed relaxing the short-range valley-dependent interaction to a non-short-range interaction. With this assumption, they found three cases of phase coexistence at $\nu = 0$. However, we need further theoretical investigations to confirm if this argument is able to explain the K-CDW phase. The nature of the phase K-CDW is still an open question. By the way, determining and controlling the coupling parameters $g_\perp$ and g_z is still challenging in experiments.

In the second project, I worked on the states of filling factors $\nu = 1/3$ and $\nu = 2/3$ at the crossing between the two levels $|K0\uparrow\rangle$ and $|K1\uparrow\rangle$ in Bernal-stacked Bilayer graphene. In this material, the energy splitting these two orbitals can be easily controlled by tuning the interlayer bias across its layers. This property allows us to realize a situation reminiscent of an extreme Landau level mixing, provided that we neglect interaction with higher Landau levels. For the filling factor $\nu = 1/3$, there is competition between the Laughlin state and the Wigner crystal. When the pseudo-Zeeman field vanishes, the situation reminiscent of Landau level mixing leads to the formation of the Wigner crystal. Under strong pseudo-Zeeman field, electrons are polarized to either the $N = 0$ orbital or the $N = 1$ orbital, stabilizing the quantum Hall liquid. The phase transition between the electron solid and the quantum Hall liquid is continuous or weakly first-order. For the filling factor $\nu = 2/3$, there is no Wigner crystal.

Our prediction of this electrically-induced Wigner crystal shows that Bernal-stacked bilayer graphene is potentially a platform to study this phase of matter. This Wigner

crystal can be detected by observing the diverging peak in the longitudinal resistance of the sample during transport measurements. For $N_e = 6, 7, 9$ electrons, the lattice is closed to the triangular lattice, while for $N_e = 8$, the crystal lattice is approximately a square lattice. Due to the finite size of the accessible systems in exact diagonalization studies, we do not have a conclusive answer about the shape of the Wigner crystal lattice in the thermodynamic limit. We let it as an open question for future research. One way to definitely observe the Wigner crystal lattice structure is to use scanning tunneling microscopy as in Ref. [171]. However, the voltage bias between the tip and the sample may perturb the system and destabilize the electron crystal phase, possibly preventing this technique to visualize this state of matter.

The eight single-electron levels in the zero-energy Landau level of Bernal-bilayer graphene cross each other at a variety of level-crossing points. The rich phase diagram in the vicinity of the crossing between $|K0\uparrow\rangle$ and $|K1\uparrow\rangle$ was explored for the filling factors $\nu = 1, 1/2, 1/3$ in Refs. [35, 36] and in our work [105]. The other crossing points promise interesting physics to explore for both theory and experiments.

AppendixA - Spherical geometry

The spherical geometry was first introduced by Haldane in 1983 [57]. In 1986, Fano, Ortolani, and Colombo applied this geometry to calculate the ground state energy and the energy of the quasielectron and quasihole of the Laughlin states $\nu = 1/3$ and $\nu = 1/5$ [62]. Since then, the spherical geometry is used to calculate the energy spectrum, transport gap, magnetoroton dispersion, and correlation functions. This geometry plays a major role in studying the physics of the quantum Hall effect because of its advantages: First, it does not have edges and is suitable for studying the properties of the bulk. Second, because the area of the sphere is finite, the Landau levels have finite degeneracy. In the spherical geometry, the system is rotationally invariant and the angular momenta L and L_z of the electrons are the quantum number. One can find pedagogical introductions to the spherical geometry in either the paper of Fano, Ortolani, Colombo [62], in the books of Jain [8] or in the book of Chakraborty and Pietiläinen [172].

A.1 . Angular momentum of electrons on a sphere under radial magnetic field

In the spherical geometry, the two-dimensional plane containing the electrons is wrapped into a sphere (Fig. A.1). The magnetic field $\mathbf{B}$ is perpendicular to the surface of this sphere, and points along the radial direction. A magnetic monopole of charge $2Q = \pm N_\phi$ is placed at the center of the sphere so that the total magnetic flux passing through the surface equals $2Q\phi_0 = 4\pi R^2 B$. In the thermodynamic limit, the ratio $N_e/|2Q|$ tends to the filling factor ν:

$$\nu = \lim_{N_e \to \infty} \frac{N_e}{2|Q|} \tag{A.1}$$

Consequently, the radius R of the sphere is related to the magnetic monopole according to the formula:

$$R = \sqrt{|Q|}l \tag{A.2}$$

In this section, we use the spherical coordinate (r, θ, ϕ) with $0 \leq \theta \leq \pi$ and $0 \leq \phi < 2\pi$ with the following unit vectors:

$$\begin{aligned} \hat{\mathbf{r}} &= \sin\theta\cos\phi\hat{\mathbf{x}} + \sin\theta\sin\phi\hat{\mathbf{y}} + \cos\theta\hat{\mathbf{z}} \\ \hat{\theta} &= \cos\theta\cos\phi\hat{\mathbf{x}} + \cos\theta\sin\phi\hat{\mathbf{y}} - \sin\theta\hat{\mathbf{z}} \\ \hat{\phi} &= -\sin\phi\hat{\mathbf{x}} + \cos\phi\hat{\mathbf{y}} \end{aligned} \tag{A.3}$$

The position of the electron on the surface of the sphere is determined by the vector:

$$\mathbf{\Omega} = \frac{\mathbf{R}}{R} = \hat{\mathbf{r}} = \sin\theta\cos\phi\hat{\mathbf{x}} + \sin\theta\sin\phi\hat{\mathbf{y}} + \cos\theta\hat{\mathbf{z}} \tag{A.4}$$

The magnetic field pointing along the radial direction equals:

$$\mathbf{B} = \frac{2Q\phi_0}{4\pi R^2}\hat{\mathbf{r}} \tag{A.5}$$

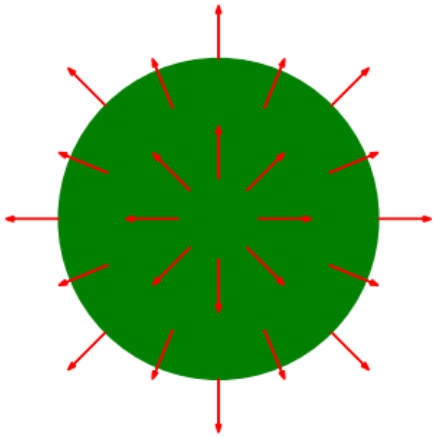

Figure A.1: Spherical geometry. The plane containing the two-dimensional system is wrapped into the green sphere. The magnetic field is represented by the red arrows. They point along the radial direction.

We can deduce this magnetic field from the gauge:

$$\mathbf{A} = -\frac{\hbar c Q}{eR}\cot\theta\hat{\phi} \tag{A.6}$$

The one-particle Hamiltonian of an electron on the sphere is:

$$H = \frac{\hbar^2}{2mR^2}\mathbf{\Lambda}^2 \tag{A.7}$$

where

$$\mathbf{\Lambda} = \mathbf{R}\times\left(-i\nabla + \frac{e}{\hbar c}\mathbf{A}(\mathbf{\Omega})\right) \tag{A.8}$$

We express the one-particle Hamiltonian in the spherical coordinate as follows:

$$H = \frac{\hbar^2}{2mR^2}\left[-\frac{1}{\sin\theta}\frac{\partial}{\partial\theta}\sin\theta\frac{\partial}{\partial\theta} + \left(Q\cot\theta + \frac{i}{\sin\theta}\frac{\partial}{\partial\phi}\right)^2\right] \tag{A.9}$$

We evaluate the commutator between the components of $\mathbf{\Lambda}$:

$$\begin{aligned}
[\Lambda_i,\Lambda_j] =& \left[\varepsilon_{ikl}R_k\left(-i\partial_l + \frac{e}{\hbar c}A_l\right), \varepsilon_{jmn}R_m\left(-i\partial_n + \frac{e}{\hbar c}A_n\right)\right] \\
=& -\varepsilon_{ikl}\varepsilon_{jmn}[R_k\partial_l, R_m\partial_n] - \frac{ie}{\hbar c}\varepsilon_{ikl}\varepsilon_{jmn}([R_k\partial_l, R_mA_n] \\
&+ [R_kA_l, R_m\partial_n]) \\
=& R_i\partial_j - R_j\partial_i - \frac{ie}{\hbar c}(R_jA_i - R_iA_j + \varepsilon_{jki}R_pR_kB_p) \\
=& R_i\partial_j - R_j\partial_i + \frac{ie}{\hbar c}(R_iA_j - R_jA_i) - \frac{ie}{\hbar c}\varepsilon_{ijk}R_k(\mathbf{R}\cdot\mathbf{B}) \\
=& i\varepsilon_{ijk}(\Lambda_k - Q\Omega_k)
\end{aligned} \tag{A.10}$$

Similarly, we obtain the commutator between the components of $\mathbf{\Lambda}$ and $\mathbf{\Omega}$:

$$[\Lambda_i,\Omega_j] = i\varepsilon_{ijk}\Omega_k \tag{A.11}$$

We define the operator $\mathbf{L} = \mathbf{\Lambda} + Q\mathbf{\Omega}$. The components of $\mathbf{L}$ satisfy the algebra:

$$[L_i, L_j] = i\varepsilon_{ijk}L_k \tag{A.12}$$

The corresponding raising and lowering operators $L_\pm = L_x \pm iL_y$ satisfy the relation:

$$[L_z, L_\pm] = \pm L_z \tag{A.13}$$

Therefore, the operator $\mathbf{L}$ has the properties of an angular momentum operator. The formulae of the operators L_z,$L_\pm$ in the spherical coordinate are:

$$\begin{aligned} L_z =& -i\frac{\partial}{\partial\phi} \\ L_\pm =& e^{\pm i\phi}\left(\pm\frac{\partial}{\partial\theta} + i\cot\theta\frac{\partial}{\partial\phi} + \frac{Q}{\sin\theta}\right) \end{aligned} \tag{A.14}$$

Because the vector $\mathbf{\Lambda}$ has no component perpendicular to the surface of the sphere, $\mathbf{\Lambda}\cdot\mathbf{\Omega} = \mathbf{\Omega}\cdot\mathbf{\Lambda} = 0$. Consequently, we have:

$$\mathbf{\Lambda}^2 = L^2 - Q^2 \tag{A.15}$$

A.2 . Monopole harmonics

The angular momentum operator $\mathbf{L}$ allows us to label the eigenstates of the Hamiltonian (A.7) by the corresponding quantum numbers l and m, as well as with the magnetic monopole Q. The corresponding eigenfunctions are the monopole harmonics Y_{Qlm}, which are the generalizations of the familiar spherical harmonics. One can find the systematic proof of the properties of the monopole harmonics in the papers of Wu and Yang [173, 174]. They satisfy the eigenvalue equations:

$$\begin{aligned} L^2Y_{Qlm} =& l(l+1)\hbar^2Y_{Qlm} \\ L_zY_{Qlm} =& m\hbar Y_{Qlm} \end{aligned} \tag{A.16}$$

The energy of the spherical harmonics Y_{Qlm} is equal to:

$$E = \frac{l(l+1) - Q^2}{2|Q|}\hbar\omega_c \tag{A.17}$$

The different angular momentum shells, which contain wavefunctions having the same energy eigenvalue, are the different Landau levels. The wavefunctions in the n$^{\text{th}}$ Landau level have the angular momentum $l = |Q| + n$ and energy:

$$E_n = \left(n + \frac{1}{2}\right)\hbar\omega_c + \frac{n(n+1)}{2|Q|}\hbar\omega_c \tag{A.18}$$

In the thermodynamic limit, $|Q|$ becomes very large and the energies of the Landau levels approach the familiar values:

$$E_n \approx \left(n + \frac{1}{2}\right)\hbar\omega_c \tag{A.19}$$

Because $2Q$ is an integer, the value of Q can be either integer or half integer. Consequently, the allowed values of l are $l = 0, \frac{1}{2}, 1, \frac{3}{2}, \ldots$. For each value of l, the corresponding values of m are $m = -l, -l+1, \ldots, l-1, l$. The second equation in (A.16) implies that the eigenfunctions Y_{Qlm} have the form:

$$Y_{Qlm}(\theta, \phi) = e^{im\phi} P_{Qlm}(\theta) \tag{A.20}$$

Explicit calculations give the formula of the spherical harmonics:

$$\begin{aligned} Y_{Qlm} =& N_{Qlm}(-1)^{l-m} u^{Q+m} v^{Q-m} \times \\ & \times \sum_{s=0}^{l-m} (-1)^s \binom{l-Q}{s} \binom{l+Q}{l-m-s} (v^* v)^{l-Q-s} (u^* u)^s \end{aligned} \tag{A.21}$$

The value of the normalization factor N_{Qlm} is:

$$N_{Qlm} = \left[\frac{2l+1}{4\pi} \frac{(l-m)!(l+m)!}{(l-Q)!(l+Q)!} \right]^{1/2} \tag{A.22}$$

The above analysis implies that different Landau levels have different degeneracies. The lowest Landau level has degeneracy $2|Q|+1$, the second Landau level has degeneracy $2|Q|+3$,... In general, the degeneracy of the n$^{\text{th}}$ Landau level equals to $2l+1 = 2(|Q|+n)+1$. If the system has n completely filled Landau levels, we have:

$$|Q| = \frac{N_e - n^2}{2n} \tag{A.23}$$

A.3 . Coulomb matrix elements

We write the Coulomb electron-electron interaction in the second quantization form as follows:

$$\begin{aligned} \sum_{i<j} V(|\mathbf{r}_i - \mathbf{r}_j|) = \frac{1}{2} \sum_{\substack{l_1 l_2 l_3 l_4 \\ m_1 m_2 m_3 m_4}} & \langle Q l_1 m_1, Q l_2 m_2 | V(\mathbf{r}_1 - \mathbf{r}_2) | Q l_3 m_3, Q l_4 m_4 \rangle \times \\ & \times a^\dagger_{Q l_1 m_1} a^\dagger_{Q l_2 m_2} a_{Q l_3 m_3} a_{Q l_4 m_4} \end{aligned} \tag{A.24}$$

where $V(\mathbf{r}_1 - \mathbf{r}_2) = e^2/(|\mathbf{r}_1 - \mathbf{r}_2|)$ is the Coulomb potential.

The matrix element equals to:

$$\begin{aligned} & \langle Q l_1 m_1, Q l_2 m_2 | V(\mathbf{r}_1 - \mathbf{r}_2) | Q l_3 m_3, Q l_4 m_4 \rangle \\ =& \int d\mathbf{\Omega}_1 d\mathbf{\Omega}_2 Y^*_{Q l_1 m_1}(\mathbf{r}_1) Y^*_{Q l_2 m_2}(\mathbf{r}_2) \frac{e^2}{|\mathbf{r}_1 - \mathbf{r}_2|} Y_{Q l_3 m_3}(\mathbf{r}_2) Y_{Q l_4 m_4}(\mathbf{r}_1) \\ =& \sum_{J=0}^{2S} \sum_{M=-J}^{+J} \langle Q l_1 m_1, Q l_2 m_2 | JM \rangle \langle JM | Q l_3 m_3, Q l_4 m_4 \rangle V_J^{(Q)} \frac{1}{R} \end{aligned} \tag{A.25}$$

The pseudopotential $V_J^{(Q)}$ expresses the interaction energy between two electrons with relative angular momentum J. Its formula is:

$$V_J^{(Q)} = 2 \frac{\binom{4Q-2J}{2Q-J} \binom{4Q+2J+2}{2Q+J+1}}{\binom{4Q+2}{2Q+1}^2} \tag{A.26}$$

The factors $\langle Q_1 l_1 m_1, Q l_2 m_2 | JM \rangle$ are the Clebsch-Gordan coefficients.

AppendixB - Torus geometry

Despite the advantages of the spherical geometry, it has some inconveniences. First, due to the nonzero curvature of the sphere, the filling factor ν is not equal to N_e/N_ϕ, but one must correct the formula by considering the Wen-Zee shift [175]. Consequently, one cannot compare the energies of two states having different shifts. Second, the spherical geometry lacks translational invariance. This results in defects when studying the crystal state. The torus geometry, however, has zero Wen-Zee shift and employs the periodic boundary condition. It naturally has the translational symmetry and is suitable to study the electron crystal phase.

In 1983, Yoshika et al. applied the periodic boundary condition to study the quantum Hall state with filling fraction $\nu = 1/3$ and found that the ground state is threefold degenerate [176]. In 1985, Haldane formulated the modern formalism of the torus geometry on the rectangular cell [177]. He showed that the ground state degeneracy is the center-of-mass degeneracy and has no physical significance. The periodic boundary condition was generated to the case of oblique cell or twisted torus by Haldane and Rezayi by using the elliptic theta function [178] and, recently, by using the "modified Weierstrass sigma functions" [179, 180]. The torus geometry is useful for studying fractional Chern insulators [181, 182].

We can find pedagogical introductions to the torus geometry in the book by Chakraborty and Pietiläinen [172] and in the paper by Bernevig and Regnault [183]. This section derives the formalism of the torus geometry on the rectangular cell.

B.1 . One-particle wavefunction

The Hamiltonian of one electron under magnetic field $\mathbf{B} = B\hat{\mathbf{z}}$ is given by:

$$H = \frac{1}{2m}\Pi^2 = \frac{1}{2m}\left(-i\hbar\nabla + \frac{e}{c}\mathbf{A}(\mathbf{r})\right)^2 \tag{B.1}$$

In the present section, we consider the problem in the Landau gauge $\mathbf{A} = (0, Bx, 0)$. According to subsection 2.2.2, the one-particle wavefunction is given by:

$$\phi_{n,k_y}(x,y) = e^{-ik_y y} e^{-\frac{(x-k_y l^2)^2}{2l^2}} H_n\left(\frac{x - k_y l^2}{l}\right) \tag{B.2}$$

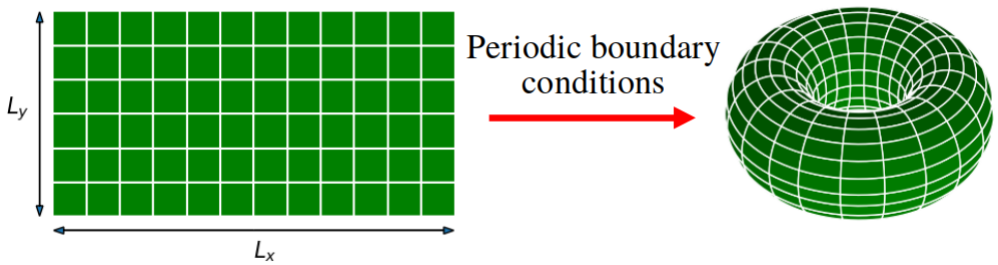

Figure B.1: The periodic boundary condition brings the rectangular cell into a torus.

Here, H_n is the n$^{\text{th}}$ Hermite polynomial. The condition $0 \leq X \leq L_x$ implies that the degeneracy of each Landau level equals the number N_ϕ of magnetic flux quanta passing through the sample. If the sample has N_e electrons, the filling factor is equal to $\nu = N_e/N_\phi$.

B.2 . Magnetic translation

Usually, we define the translation along the vector $\mathbf{L} = L_x\hat{\mathbf{x}} + L_y\hat{\mathbf{y}}$ by the operator:

$$T(\mathbf{L}) = \exp\left(\frac{i}{\hbar}\mathbf{L}\cdot\mathbf{p}\right) \tag{B.3}$$

whose action on a wavefunction $\Psi(x, y)$ gives [1]:

$$T(\mathbf{L})\Psi(x, y) = \Psi(x + L_x, y + L_y) \tag{B.4}$$

In the next section, we will apply the periodic boundary to our system. The periodic boundary condition makes the system translationnally invariant under the set of lattice vectors. In general, the gauge $\mathbf{A}$ is not periodic, so the translation operator $T(\mathbf{L})$ does not commute with the single-electron Hamiltonian. That means we cannot use $T(\mathbf{L})$ to classify the single-electron states under magnetic field. Therefore, we need to define a new operator that combines the translation and the gauge transformation. This operator is called the **magnetic translation operator**.

The generator for the magnetic translation is defined as:

$$\hat{\mathbf{K}} = \Pi - \frac{\hbar}{l^2}\hat{\mathbf{z}}\times\mathbf{r} \tag{B.5}$$

Explicitely, its x and y components are:

$$\begin{aligned}\hat{K}_x &= -i\hbar\frac{\partial}{\partial x} + \frac{e}{c}A_x + \frac{\hbar}{l^2}y \\ \hat{K}_y &= -i\hbar\frac{\partial}{\partial y} + \frac{e}{c}A_y - \frac{\hbar}{l^2}x\end{aligned} \tag{B.6}$$

Therefore, the expression for the magnetic translation operator along the vector $\mathbf{L}$ is:

$$\mathcal{T}(\mathbf{L}) = \exp\left(\frac{i}{\hbar}\mathbf{L}\cdot\hat{\mathbf{K}}\right) \tag{B.7}$$

Unlike ordinary translation operators, magnetic translation operators do not commute in general. For any two arbitrary vectors $\mathbf{a}$ and $\mathbf{b}$, we have:

$$\mathcal{T}(\mathbf{b})\mathcal{T}(\mathbf{a}) = \mathcal{T}(\mathbf{a})\mathcal{T}(\mathbf{b})\exp\left(\frac{i}{l^2}(\mathbf{a}\times\mathbf{b})\cdot\hat{\mathbf{z}}\right) \tag{B.8}$$

In the Landau gauge, the relation between the magnetic translation and the ordinary translation along the same vector $\mathbf{L}$ is:

$$\mathcal{T}(\mathbf{L}) = \exp\left(\frac{i}{2l^2}L_xL_y\right)\exp\left(\frac{i}{l^2}L_xy\right)T(\mathbf{L}) \tag{B.9}$$

[1] Standard textbooks often define the translation operator $T(\mathbf{L}) = \exp\left(-\frac{i}{\hbar}\mathbf{L}\cdot\mathbf{p}\right)$ whose effect is to transform the wavefunction as $T(\mathbf{L})\Psi(x, y) = \Psi(x - L_x, y - L_y)$.

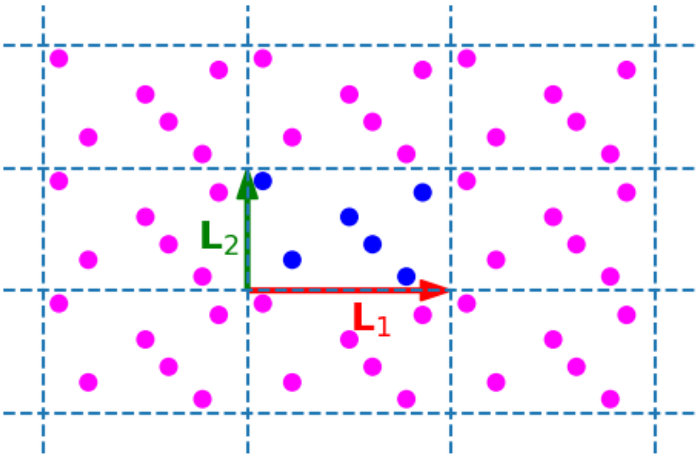

Figure B.2: The periodic boundary conditions transform a system of N_e electrons into an infinite lattice. Each cell in the lattice is a replica of the original system. Here the number of electrons $N_e = 6$. The original electrons are represented by the blue dots. The images of the electrons are represented by the magenta dots. The vectors $\mathbf{L}_1 = L_1\hat{\mathbf{x}}$ and $\mathbf{L}_2 = \hat{\mathbf{y}}$ are the primitive vectors of the lattice.

B.3 . Periodic boundary condition

We apply the periodic boundary condition on a rectangular cell of size $L_x \times L_y$:

$$\begin{aligned}\psi(x + L_x, y) =& e^{-iL_x y/l^2}\psi(x, y)\\ \psi(x, y + L_y) =& \psi(x, y)\end{aligned} \tag{B.10}$$

The periodic boundary condition implies that:

$$\psi(0, 0) = \psi(L_x, 0) = \psi(0, L_y) = \psi(L_x, L_y) \tag{B.11}$$

These values of the wavefunction $\psi(x, y)$ are related by the following relations:

$$\begin{aligned}\psi(L_x, 0) =& \mathcal{T}(L_x\hat{\mathbf{x}})\psi(0, 0)\\ \psi(0, L_y) =& \mathcal{T}(L_y\hat{\mathbf{y}})\psi(0, 0)\\ \psi(L_x, L_y) =& \mathcal{T}(L_x\hat{\mathbf{x}})\psi(0, L_y) = \mathcal{T}(L_y\hat{\mathbf{y}})\psi(L_x, 0)\end{aligned} \tag{B.12}$$

This implies that:

$$\mathcal{T}(L_x\hat{\mathbf{x}})\mathcal{T}(L_y\hat{\mathbf{y}}) = \mathcal{T}(L_y\hat{\mathbf{y}})\mathcal{T}(L_x\hat{\mathbf{x}}) \tag{B.13}$$

According to (B.8), the condition is satisfied if:

$$\exp\left(\frac{i}{l^2}(L_x\hat{\mathbf{x}} \times L_y\hat{\mathbf{y}}) \cdot \hat{\mathbf{z}}\right) = 1 \tag{B.14}$$

This is satisfied if the total magnetic field passing through the cell is quantized and equals an integer multiple N_ϕ of the magnetic flux quantum $\Phi_0 = hc/e$. This is consistent with the degeneracy of the Landau levels shown in subsection 2.2.2. The area of the rectangular cell is related to N_ϕ as:

$$L_x L_y = N_\phi 2\pi l^2 \tag{B.15}$$

The periodic boundary condition on the y-direction implies that the allowed values of k_y are:

$$k_y = \frac{2\pi}{L_y} n_y (n_y \in \mathbb{Z}) \tag{B.16}$$

Each Landau level has a degeneracy N_ϕ, so the set of allowed values of k_y is restricted to N_ϕ classes of equivalent momenta, defined modulo $N_\phi 2\pi/L_y$. We label each class with the integer $j (1 \leq j \leq N_\phi)$:

$$k_y = n_y \frac{2\pi}{L_y} = (j + kN_\phi)\frac{2\pi}{L_y} = j\frac{2\pi}{L_y} + k\frac{L_x}{l^2} (k \in \mathbb{Z}) \tag{B.17}$$

The basis for the Hilbert space of single-particle wavefunctions consists of N_ϕ wavefunctions. Each of them is a linear combination of all the wavefunctions whose momenta k_y belong to the same equivalent class. We denote each basis wavefunction as $\phi_{nj}(\mathbf{r})$ with $n (n \in \mathbb{N})$ as the Landau level, and j $(j \in \mathbb{N}, 1 \leq j \leq N_\phi)$ as the index for the momentum k_y. The expression for the basis wavefunction is:

$$\begin{aligned}
\phi_{nj}(\mathbf{r}) &= \left(\frac{1}{L_y\sqrt{\pi}l}\right)^{1/2} \sum_{k=-\infty}^{+\infty} \frac{1}{\sqrt{2^n n!}} \exp\left[-ik_y y - \frac{1}{2}\left(\frac{x - k_y l^2}{l}\right)^2\right] \times \\
&\quad \times H_n\left(\frac{x - k_y l^2}{l}\right) \\
&= \left(\frac{1}{L_y\sqrt{\pi}l}\right)^{1/2} \sum_{k=-\infty}^{+\infty} \frac{1}{\sqrt{2^n n!}} \exp\left[-i\left(j\frac{2\pi}{L_y} + k\frac{L_x}{l^2}\right) y\right] \times \\
&\quad \times \exp\left[-\frac{1}{2}\left(\frac{x}{l} - j\frac{2\pi l}{L_y} - k\frac{L_x}{l}\right)^2\right] H_n\left(\frac{x}{l} - j\frac{2\pi l}{L_y} - k\frac{L_x}{l}\right)
\end{aligned} \tag{B.18}$$

Although these wavefunctions are not invariant under the ordinary translation, they are invariant under magnetic translation along the vectors $\mathbf{L}_1 = L_x\hat{\mathbf{x}}$ and $\mathbf{L}_2 = L_y\hat{\mathbf{y}}$:

$$\begin{aligned}
\mathcal{T}(\mathbf{L}_1)\phi_{nj}(\mathbf{r}) &= \phi_{nj}(\mathbf{r}) \\
\mathcal{T}(\mathbf{L}_2)\phi_{nj}(\mathbf{r}) &= \phi_{nj}(\mathbf{r})
\end{aligned} \tag{B.19}$$

When we apply the periodic boundary condition, the system of N_e electrons under N_ϕ magnetic flux quanta becomes a primitive cell in an infinite lattice whose primitive lattice vectors are $\mathbf{L}_1$ and $\mathbf{L}_2$ (see Fig.B.2). Each cell in the lattice is a replica of the original system. The electrons in the system not only interact with each other but also interact with their images. Therefore, we should replace the iniital electron-electron Coulomb interaction by a periodic Coulomb interaction:

$$V(\mathbf{r}) = \frac{1}{L_x L_y} \sum_{\mathbf{q}\neq 0} \frac{2\pi e^2}{\varepsilon q} \exp(i\mathbf{q}\cdot\mathbf{r}) \tag{B.20}$$

where $\mathbf{q} = \left(\frac{2\pi}{L_x}s, \frac{2\pi}{L_y}t\right)$ $(s,t \in \mathbb{Z})$. The momentum $\mathbf{q} = \mathbf{0}$ $(s = t = 0)$ is excluded because it corresponds to the direct interaction and is cancelled by the energy of the neutralizing background.

B.4 . Coulomb matrix elements

In the second quantization language, the Coulomb interaction $\sum_{i<j} V(\mathbf{r}_i - \mathbf{r}_j)$ with $V(\mathbf{r})$ defined in (B.20) is expressed in the basis of wavefunctions $\phi_{nj}(\mathbf{r})$ defined in (B.18) as:

$$\sum_{i<j} V(\mathbf{r}_i - \mathbf{r}_j) = \frac{1}{2} \sum_{\substack{n_1 n_2 n_3 n_4 \\ j_1 j_2 j_3 j_4}} \mathcal{A}^{n_1 n_2 n_3 n_4}_{j_1 j_2 j_3 j_4} c^\dagger_{n_1 j_1} c^\dagger_{n_2 j_2} c_{n_3 j_3} c_{n_4 j_4} \tag{B.21}$$

where the Coulomb matrix elements $\mathcal{A}^{n_1 n_2 n_3 n_4}_{j_1 j_2 j_3 j_4}$ are evaluated using the formula:

$$\mathcal{A}^{n_1 n_2 n_3 n_4}_{j_1 j_2 j_3 j_4} = \int d^2\mathbf{r}_1 d^2\mathbf{r}_2 \phi^*_{n_1 j_1}(\mathbf{r}_1) \phi^*_{n_2 j_2}(\mathbf{r}_2) V(\mathbf{r}_1 - \mathbf{r}_2) \phi_{n_3 j_3}(\mathbf{r}_2) \phi_{n_4 j_4}(\mathbf{r}_1) \tag{B.22}$$

The expression of $V(\mathbf{r})$ in Eq.(B.20) allows us to separate the integral into the product of two integrals over $d^2\mathbf{r}_1$ and $d^2\mathbf{r}_2$ as follows:

$$\begin{aligned} \mathcal{A}^{n_1 n_2 n_3 n_4}_{j_1 j_2 j_3 j_4} =& \frac{1}{L_x L_y} \sum_{\substack{st \\ (s,t)\neq(0,0)}} \frac{2\pi e^2}{\varepsilon q} \int d^2\mathbf{r}_1 \phi^*_{n_1 j_1}(\mathbf{r}_1) \phi_{n_4 j_4}(\mathbf{r}_1) e^{i\mathbf{q}\cdot\mathbf{r}_1} \\ & \times \int d^2\mathbf{r}_2 \phi^*_{n_2 j_2}(\mathbf{r}_2) \phi_{n_3 j_3}(\mathbf{r}_2) e^{-i\mathbf{q}\cdot\mathbf{r}_2} \end{aligned} \tag{B.23}$$

The integral over $d^2\mathbf{r}_1$ is equal to:

$$\begin{aligned} & \int d^2\mathbf{r}_1 \phi^*_{n_1 j_1}(\mathbf{r}_1) \phi_{n_4 j_4}(\mathbf{r}_1) e^{i\mathbf{q}\cdot\mathbf{r}} \\ & \quad = e^{-q^2 l^2/4} e^{iq_x q_y l^2/2} e^{iq_x j_1 2\pi l^2/L_y} F_{n_1 n_4}(q_x, q_y) \delta'_{t, j_4 - j_1} \end{aligned} \tag{B.24}$$

In this expression, the symbol $\delta'_{m,n}$ means $m = n (\mathrm{mod}\ N_\phi)$. $F_{mn}(q_x, q_y)$ is the ***form factor*** with Landau level indices m, n:

$$\begin{aligned} & F_{mn}(q_x, q_y) \\ & \quad = \sqrt{\frac{(\mathsf{min}\{m,n\})!}{(\mathsf{max}\{m,n\})!}} \left(\frac{[iq_x + \mathsf{sgn}(m-n) q_y] l}{\sqrt{2}}\right)^{|m-n|} L^{|m-n|}_{\mathsf{min}\{m,n\}} \left(\frac{q^2 l^2}{2}\right) \end{aligned} \tag{B.25}$$

The polynomials $L^n_m(x)$ are the *Laguerre polynomials*:

$$L^n_m(x) = \frac{1}{m!} e^{-x} x^{-n} \frac{d^m}{dx^m}(e^{-x} x^{m+n}) = \sum_{k=0}^{m} (-1)^k \binom{m+n}{m-k} \frac{x^k}{k!} \tag{B.26}$$

We evaluate the integral over $d^2\mathbf{r}_2$ in a similar manner. Overall, the Coulomb matrix element equals to:

$$\begin{aligned} \mathcal{A}^{n_1 n_2 n_3 n_4}_{j_1 j_2 j_3 j_4} =& \frac{1}{L_x L_y} \sum_{\substack{st \\ (s,t)\neq(0,0)}} \delta_{q_x, s2\pi/L_x} \delta_{q_y, t2\pi/L_y} \frac{2\pi e^2}{\varepsilon q} e^{-q^2 l^2/2} e^{i2\pi(j_1 - j_3)s/N_\phi} \times \\ & \times F_{n_1 n_4}(q_x, q_y) F_{n_2 n_3}(-q_x, -q_y) \delta'_{t, j_4 - j_1} \delta'_{j_1 + j_2, j_3 + j_4} \end{aligned} \tag{B.27}$$

B.5 . Many-body wavefunction quantum number

After deriving the formula of the Hamiltonian matrix elements, we need to find the quantum numbers of the many-body wavefunctions. Let N be the greatest common divisor of N_e and N_ϕ, so that $N_e = pN$ and $N_\phi = qN$. The filling factor equals $\nu = p/q$. We define the center of mass translation operator $\tilde{T}(\mathbf{a})$ as the operator which magnetically moves all the particles by the vector $\mathbf{a}$:

$$\bar{T}(\mathbf{a}) = \prod_{i=1}^{N_e} \mathcal{T}_i(\mathbf{a}) \tag{B.28}$$

The translation of the particle i is decomposed into two parts: the center of mass translation and the relative translation, which is given by the *the relative translation operator*:

$$\tilde{T}_i(\mathbf{a}) = \prod_{j=1}^{N_e} \mathcal{T}_i\left(\frac{\mathbf{a}}{N_e}\right) \mathcal{T}_j\left(-\frac{\mathbf{a}}{N_e}\right) \tag{B.29}$$

The motion of particle i is compensated by the motion of the other particles in the opposite direction so that the position of the center-of-mass remains unchanged. The application of the relative translation operator on all the particles leaves the system invariant:

$$\prod_{i=1}^{N_e} \tilde{T}_i(\mathbf{a}) = 1 \tag{B.30}$$

Overall, we write the magnetic translation operator acting on the particle i as:

$$\mathcal{T}_i(\mathbf{a}) = \bar{T}\left(\frac{\mathbf{a}}{N_e}\right) \tilde{T}_i(\mathbf{a}) \tag{B.31}$$

The relative translation operator provides the quantum numbers to classify the many-body wavefunctions. The suitable relative translation operators should commute with the many-body Hamiltonian and commute with each other, that means $[\tilde{T}_i(\mathbf{a}), \tilde{T}_j(\mathbf{b})] = 0$ for all $1 \leq i, j \leq N_e$. The set of vectors $\mathbf{a}$, $\mathbf{b}$ satisfying these conditions is $\mathcal{M} = \{p\mathbf{L}_{mn} | m, n \in \mathbb{Z}\}$.

Let $\mathbf{Q} = (s2\pi/L_x, t2\pi/L_y)\,(s, t \in \mathbb{Z})$ be a reciprocal lattice vector, the following equality holds:

$$\tilde{T}_i(p\mathbf{L}_{mn}) \left(\sum_{k=1}^{N_e} e^{i\mathbf{Q}\cdot\mathbf{r}_k}\right) = e^{-i\mathbf{Q}\cdot p\mathbf{L}_{mn}/N_e} \left(\sum_{k=1}^{N_e} e^{i\mathbf{Q}\cdot\mathbf{r}_k}\right) \tilde{T}_i(p\mathbf{L}_{mn}) \tag{B.32}$$

Let $\Psi_{\mathbf{K}}(\mathbf{r}_1, \ldots, \mathbf{r}_{N_e})$ be an eigenfunction of the relative translation operator $\tilde{T}_i(p\mathbf{L}_{mn})$ with eigenvalue $e^{-i\mathbf{K}\cdot p\mathbf{L}_{mn}/N_e}$, we have:

$$\tilde{T}_i(p\mathbf{L}_{mn})\Psi_{\mathbf{K}} = e^{-i\mathbf{k}\cdot p\mathbf{L}_{mn}/N_e}\Psi_{\mathbf{K}} \tag{B.33}$$

The equality (B.32) implies that $\left(\sum_{k=1}^{N_e} e^{i\mathbf{Q}\cdot\mathbf{r}_K}\right)\Psi_{\mathbf{K}}$ is also an eigenfunction of $\tilde{T}_i(p\mathbf{L}_{mn})$ with quantum number $\mathbf{K} + \mathbf{Q}$. Therefore, we identify $\mathbf{K}$ as the *momentum*

of the *many-body wavefunction*, or the *many-body momentum*. The momentum $\mathbf{K}$ is quantized and takes the same values as the reciprocal lattice vectors $\mathbf{Q}$. It has the form:

$$\mathbf{K} = \frac{2\pi}{L_x} s\hat{\mathbf{x}} + \frac{2\pi}{L_y} t\hat{\mathbf{y}} (s, t \in \mathbb{Z}) \tag{B.34}$$

The eigenvalues of the relative translation operator $\tilde{T}_i(p\mathbf{L}_{mn})$ have the form $e^{i2\pi(sm+tn)/N}$. We can label the many-body wavefunction by the quantum numbers s and t. s and t can take N values $s, t = 0, 1, \ldots, N-1$. The set of allowed many-body momenta contains N^2 vectors, and form a rectangular Brillouin zone in the reciprocal space. The eigenvalue equation is written as:

$$\tilde{T}_i(p\mathbf{L}_{mn})\Psi_{st} = e^{-i2\pi(ms+nt)/N}\Psi_{st} \tag{B.35}$$

In general, the quantum numbers $s = t = 0$ do not correspond to $\mathbf{K} = \mathbf{0}$. In fact, the point $\mathbf{K} = \mathbf{0}$ has the highest symmetry and is invariant under all symmetry operations. Therefore:

$$\tilde{T}_i(p\mathbf{L}_1)\Psi_{\mathbf{K}=\mathbf{0}} = \tilde{T}_i(p\mathbf{L}_2)\Psi_{\mathbf{K}=\mathbf{0}} = \tilde{T}_i(-p\mathbf{L}_1)\Psi_{\mathbf{K}=\mathbf{0}} = \tilde{T}_i(p\mathbf{L}_2 - p\mathbf{L}_1)\Psi_{\mathbf{K}=\mathbf{0}} \tag{B.36}$$

We can show that

$$\tilde{T}_i(p\mathbf{L}_2 - p\mathbf{L}_1) = (-1)^{pq(N_e-1)}\tilde{T}_i(-p\mathbf{L}_1)\tilde{T}_i(p\mathbf{L}_2) \tag{B.37}$$

Hence, the many-body wavefunction $\Psi_{\mathbf{K}=\mathbf{0}}$ is the eigenfunction of all lattice vectors $\mathbf{L}_{mn}(m, n \in \mathbb{Z})$ with the same eigenvalue $(-1)^{pq(N_e-1)}$. The many-body momentum $\mathbf{K}$ is defined as:

$$\mathbf{K} = \frac{2\pi}{L_x}(s - s_0)\hat{\mathbf{x}} + \frac{2\pi}{L_y}(t - t_0)\hat{\mathbf{y}} (s, t \in \mathbb{Z}) \tag{B.38}$$

The values s_0 and t_0 are determined from the observations:

$$\tilde{T}_i(p\mathbf{L}_1)\Psi_{s_0t_0} = e^{-i2\pi s_0/N}\Psi_{s_0t_0} = (-1)^{pq(N_e-1)}\Psi_{s_0t_0} \tag{B.39}$$

and

$$\tilde{T}_i(p\mathbf{L}_2)\Psi_{s_0t_0} = e^{-i2\pi t_0/N}\Psi_{s_0t_0} = (-1)^{pq(N_e-1)}\Psi_{s_0t_0} \tag{B.40}$$

Consequently, we have:

$$\begin{aligned} e^{i2\pi s_0/N} &= (-1)^{pq(N_e-1)} \\ e^{i2\pi t_0/N} &= (-1)^{pq(N_e-1)} \end{aligned} \tag{B.41}$$

The quantum numbers of the momentum $\mathbf{K} = \mathbf{0}$ depends on the parity of p,q and N_e:

- If $pq(N_e - 1)$ is even, then $s_0 = t_0 = 0$
- If $pq(N_e - 1)$ is odd, then $s_0 = t_0 = N/2$

Let $\lambda = L_x/L_y$ be the aspect ratio, we can express the many-body momentum as follows:

$$\mathbf{K}l = \sqrt{\frac{2\pi}{N_\phi \lambda}}[(s - s_0)\hat{\mathbf{x}} + \lambda(t - t_0)\hat{\mathbf{y}}] \tag{B.42}$$

The Brillouin zone contains N^2 points. Its center $\mathbf{K} = \mathbf{0}$ corresponds to the quantum numbers (s_0, t_0).

We denote $|j_1, j_2, \ldots, j_{N_e}\rangle$ the state of N_e electrons constructed from the single-particle states (B.18) in which the particle $k(1 \leq k \leq N_e)$ has quantum number $j_k(1 \leq j_k \leq N_\phi)$. For a sake of simplicity, we omit the Landau level index and the spin of the particle. This product state is the eigenstate of a subset of relative translation operators along the y-direction:

$$\tilde{T}_i(npL_y\hat{\mathbf{y}})|j_1, j_2, \ldots, j_{N_e}\rangle = \exp\left(i2\pi\frac{n}{N}t\right)|j_1, j_2, \ldots, j_{N_e}\rangle \tag{B.43}$$

In this expression, t is the sum of the individual momenta of all particles: $t = \sum_{k=1}^{N_e} j_k$ (mod N). By contrast, the relative translation operator along the x-direction maps this state into another state:

$$\tilde{T}_i(mpL_x\hat{\mathbf{x}})|j_1, j_2, \ldots, j_{N_e}\rangle = |j_1 - qm, j_2 - qm, \ldots, j_{N_e} - qm\rangle \tag{B.44}$$

Let $\mathcal{L}$ be the minimum set of all states $|j_1, j_2, \ldots, j_{N_e}\rangle$ such that $\sum_{k=1}^{N_e} j_k = t(\mathrm{mod}N)$ and the elements of $\mathcal{L}$ are related by each other by the relation:

$$|j_1', j_2', \ldots, j_{N_e}'\rangle = |j_1 - qk, j_2 - qk, \ldots, j_{N_e} - qk\rangle \tag{B.45}$$

for some integer k. The number of elements of the set $\mathcal{L}$ is $|\mathcal{L}| \leq N$. The normalized state

$$|(s,t);\mathcal{L}\rangle = \frac{1}{\sqrt{|\mathcal{L}|}}\sum_{k=0}^{|\mathcal{L}|-1}\exp\left(i2\pi\frac{s}{N}k\right)|j_1 - qk, j_2 - qk, \ldots, j_{N_e} - qk\rangle \tag{B.46}$$

has the momentum defined in (B.42). We use those states as basis states for the many-body wavefunctions.

To summarize, let (s,t) be the quantum numbers representing the many-body momentum $\mathbf{K}$ defined in (B.42), we construct the corresponding basis for the Hilbert space of many-body wavefunctions having momentum $\mathbf{K}$ as follows:

1. Construct the set of all the states $|j_1, j_2, \ldots, j_{N_e}\rangle$ such that $\sum_{k=1}^{N_e} j_k = t(\mathrm{mod}N_\phi)$. (Here we remember that $0 \leq t < N$).

2. Partition this set into equivalent classes $\mathcal{L}$ such that each member of the class is related by another member by (B.45).

3. In each class $\mathcal{L}$, for each quantum number s $(0 \leq s < N)$, we have a state $|(s,t);\mathcal{L}\rangle$ given in (B.46) having the momentum defined in (B.42).

B.6 . Summary of the torus geometry

Overall, we summarize the key points of the torus geometry:

1. The torus geometry is equivalent to applying the periodic boundary condition on a system under a magnetic field. To perform simultaneously the translation and the gauge transformation, we use the magnetic translation operators $\mathcal{T}(\mathbf{L})$ instead of the ordinary translation operators $T(\mathbf{L})$.

2. The quantum numbers of the many-body wavefunction are defined using the relative translation operators (B.29). They allow us to define the many-body momentum $\mathbf{K}$ in (B.42).

3. The Brillouin zone of the many-body wavefunctions contains N^2 many-body momenta $\mathbf{K}$, where N is the greatest common divisor of N_e and N_ϕ.

4. The quantum numbers s_0 and t_0 corresponding to the center of the Brillouin zone (many-body momentum $\mathbf{K} = \mathbf{0}$) are defined from the parity of the product $pq(N_e - 1)$. If $pq(N_e - 1)$ is even then $s_0 = t_0 = 0$; otherwise, $s_0 = t_0 = N/2$.

Synthèse en français

L'effect Hall quantique a été découvert dans les années 1980 et est devenu l'un des sujets les plus étudiés de la physique. Il y a deux versions de l'effet Hall quantique: l'effet Hall quantique entier est lié à la quantification de la conductance de Hall, et l'effet Hall quantique fractionnaire est caractérisé par une conductance qui est une fraction de l'inverse de la constante de von Klitzing. Tandis que le premier est expliqué dans une description à un électron, le dernier doit être expliqué en considérant l'interaction électron-électron. Laughlin a expliqué avec succès les effets Hall quantique de facteur de remplissage $\nu = 1/m$ en proposant une fonction d'onde d'essai qui porte son nom. Jain a proposé la théorie des fermions composites, qui considère l'effet Hall quantique fractionnaire des électrons comme l'effet Hall quantique entier des fermions composites sous un champ magnétique effectif. Sous un champ magnétique fort, les spins des électrons dans l'état fondamental d'un système de Hall quantique sont polarisés. Mais si l'énergie de Zeeman est faible, les électrons préfèrent inverser leur spins et forment un état de Hall quantique singulet qui est plus stable. La compétition entre les effets Hall quantiques polarisé et singulet de facteur de remplissage $\nu = 2/3$ est un exemple de l'effet Hall quantique multicomposantes et a été observée dans les expériences.

En principe, on peut observer l'effet Hall quantique dans tous les systèmes d'électrons bidimensionnels sous un champ magnétique. Au début, ce phénomène a été observé dans les gaz d'électrons bidimensionnels sous champ magnétique dans les semiconducteurs. Après la découverte de graphène, les physiciens ont rapidement observé l'effet Hall quantique dans ce matériau. L'effet Hall quantique a été aussi découvert dans la bicouche de graphène. Les effets Hall quantiques dans ces matériaux constituent les trois différentes sortes de l'effet Hall quantique.

Dans cette thèse, nous étudions l'effet Hall quantique fractionnaire dans les monocouches de graphène et les bicouches de graphène. Dans ces matériaux, outre le spin, les électrons possèdent des autres degrés de liberté, qui jouent le rôle des pseudospins. Ces deux cas sont des exemples du ferromagnétisme de Hall quantique. La thèse se compose de deux parties. Dans la première partie, nous étudions les phases de symétrie brisée dans les monocouches de graphène pour les facteurs de remplissage $\nu = n/3(n = 1, 2, 4, 5)$. La symmétrie SU(4) de l'Hamiltonien Coulombien est brisée par des anisotropies. Cela entraîne la formation de différentes phases avec une variété d'ordre de spin et de vallée. Dans la seconde partie de la thèse, nous étudions la compétition entre l'état de Laughlin et le cristal de Wigner dans les bicouches de graphène dont le facteur de remplissage est $\nu = 1/3$. Dans les bicouches de graphène, les deux niveaux de Landau $N = 0$ et $N = 1$ sont approximativement dégénérés. On peut contrôler la différence entre leurs énergies en variant la tension électrique entre les deux couches. En négligeant le mélange avec les niveaux de Landau les plus hauts, on peut arriver à une situation qui ressemble à un mélange extrême des niveaux de Landau, qui favorise la formation du cristal de Wigner.

Nous commençons la première partie de la thèse en rappelant les propriétés de l'effet Hall quantique dans le graphène. La zone de Brillouin du graphène est un hexagone, dont les sommets sont classifiés en deux points non-équivalents. Ces points sont nommés points de Dirac. Les électrons à basse énergie dans le graphène ont une dispersion linéaire au voisinage des points de Dirac. Cela permet de définir la vallée, qui joue le rôle du

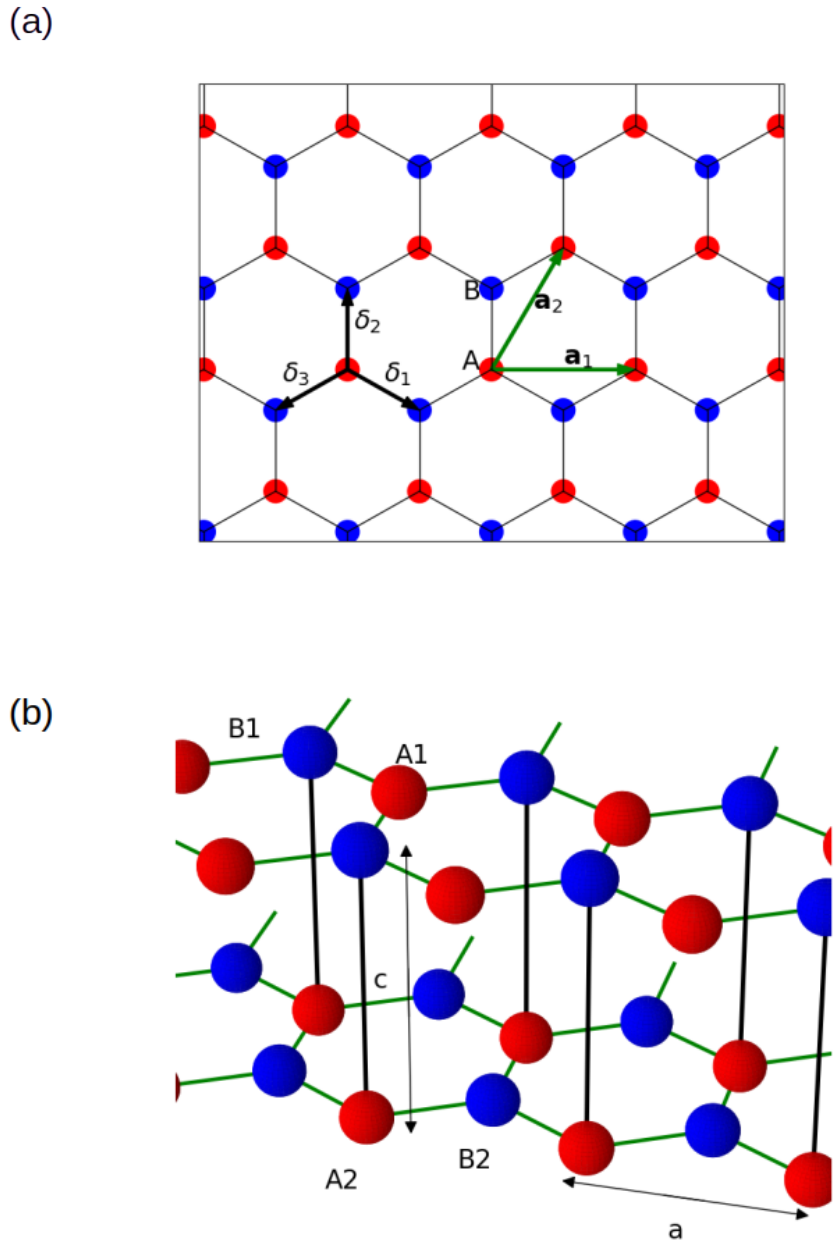

Figure B.3: Crystal structure of (a) monolayer graphene and (b) Bernal-stacked bilayer graphene.

pseudospin. Les niveaux de Landau du graphène sont donc quatre fois dégénérés, dû à la présence des deux degrés de liberté: le spin et la vallée. À la neutralité des charges $\nu = 0$, le niveau de Landau central, qui a une énergie zéro, est demi-occupé. Sous l'effet Hall quantique, la symétrie SU(4) de l'interaction Coulombienne est brisée par l'interaction à deux électrons dépendante de la vallée. Cela entraîne l'apparition de plusieurs phases avec une variété d'ordre de spin et de vallée. Le diagramme de phase du graphène à $\nu = 0$ contient quatre phases: la phase ferromagnétique, la phase antiferromagnétique, la phase de Kékulé, et la densité de charge. Les expériences ont confirmé l'existence de toutes ces quatre phases. Les expériences STM ont découvert des phases qui ne sont pas prédites par la théorie.

Dans ce projet, nous étudions les phases de symétrie brisée sous l'effet Hall quantique fractionnaire. Nous employons deux méthodes: la méthode variationnelle et la méthode numérique. Tout d'abord, nous proposons les fonctions d'onde variationnelles des états à deux et trois composantes. Ensuite, nous calculons les énergies d'anisotropies dépendantes de la vallée pour chaque fonction d'onde d'essai. Puis, nous minimisons l'énergie pour obtenir l'ordre de spin et de la vallée des états fondamentaux. Le diagramme de phase de l'état à deux composantes $(1, \nu)(0 < \nu < 1)$ ressemble à celui du cas de la neutralité des charges $\nu = 0$. Il y a des phases ferromagnétique, antiferromagnétique, phase de Kékulé, et densité de charge. Dans le cas de l'état à trois composantes $(1, \nu, \nu)(0 < 2\nu < 1)$, le diagramme de phase a une autre allure et contient quatre phases A, B, E et F.

Dans le cas de l'état $\tilde{\nu} = 1/3$, l'état fondamental est un état de Laughlin qui possède une dégénérescence de vallée. Dans le cas de l'état $\tilde{\nu} = 2/3$, il y a une compétition entre l'état polarisé et l'état singulet. Le diagramme de phase de l'état singulet de facteur de remplissage $\tilde{\nu} = 2/3$ ressemble à celui du cas de la neutralité des charges $\nu = 0$. Pour vérifier la validité de la méthode variationnelle pour les états $\tilde{\nu} = 4/3$ et $\tilde{\nu} = 5/3$, nous utilisons des calculs de diagonalisations exactes. Pour le facteur de remplissage $\tilde{\nu} = 4/3$, il y a la compétition entre l'état (1,1/3) et l'état (2/3,2/3). Dans la limite où l'effet Zeeman est nul, l'état (2/3,2/3) est le plus stable et possède un diagramme de phase similaire à celui du cas $\nu = 0$. L'état $(1, 1/3)$ possède le même diagramme de phase que l'état $(2/3, 2/3)$ avec les phases ferromagnétique, antiferromagnétique, phase de Kékulé et la densité de charge. Pourtant, la phase antiferromagnétique est une phase singulet de spin, même si les facteurs de remplissage des deux composantes sont différentes. Pour la phase ferromagnétique, il y a une dégénérescence de vallée tandis que l'Hamiltonien ne possède pas la symétrie $SU(2)_v$. Ces aspects ne sont pas prédits par la méthode variationnelle.

Pour le facteur de remplissage $\tilde{\nu} = 5/3$, il y a la compétition entre les états $(1, 2/3)$ et $(1, 1/3, 1/3)$. Sous un effet Zeeman négligeable, l'état à trois composantes $(1, 1/3, 1/3)$ est l'état fondamental. Le diagramme de phase de l'état $(1, 2/3)$ est similaire au cas de l'état $(1, 1/3)$. La phase ferromagnétique possède aussi une dégénérescence de vallée, mais la phase antiferromagnétique n'est pas une phase singulet de spin. Le diagramme de phase de l'état $(1, 1/3, 1/3)$ calculé numériquement est différent de celui prédit par la méthode variationnelle. Il y a 5 phases, dont les phases A et B sont capturées variationnellement. La phase E est remplacée par deux phases E1 et E2 qui ont des vallées d'Ising et XY, respectivement. La phase F est totalement remplacée par une phase C qui est une phase singulet de spin et vallée non-polarisée. La nature de la phase C reste une question ouverte.

Les conditions expérimentales actuelles favorisent les phases de spin polarisé $(1, 1/3)$ et $(1, 2/3)$. Les transitions de spin vers les états singulet $(2/3, 2/3)$ et $(1, 1/3, 1/3)$ pourraient être obtenues en réduisant la composante du champ magnétique $\mathbf{B}$ qui est parallèle au plan du graphène.

Dans la seconde partie de la thèse, nous étudions la compétition entre l'état de Laughlin et le cristal de Wigner chez le graphène à bicouche avec facteur de remplissage $\nu = 1/3$. Nous commençons en rappelant la structure cristalline du graphène à bicouche. Puis, nous présentons le modèle effectif à quatre bandes et le modèle à deux bandes. Ensuite, nous démontrons le spectre des niveaux de Landau dans le graphène à bicouche. Dans ce matériau, les deux niveaux de Landau $N = 0$ et $N = 1$ sont approximativement dégénérés, et forment un niveau de Landau central qui est approximativement huit fois dégénéré. C'est un aspect particulier du graphène à bicouche. Dans le niveau de Landau central, les huit niveaux d'énergie d'un seul électron se croisent. Nous nous concentrons au croisement entre les niveaux $|K0\uparrow\rangle$ et $|K1\uparrow\rangle$. Ce régime est gouverné par deux paramètres: le poids γ et la différence Δ_{10} entre les énergies des deux niveaux de Landau. L'énergie Coulombienne est réduite par l'écrantage du substrat hBN et des bornes métalliques. Il y a un décalage de Lamb qui est dû à l'interaction entre les électrons du niveau de Landau central avec les électrons occupant les niveaux de Landau les plus bas.

Après la discussion sur le graphène à bicouche, nous avons discuté le cristal de Wigner. C'est une phase qui est en compétition avec le liquide de Hall quantique. Le cristal de Wigner peut être observé lors des expériences de transport. Quand la résistance R_{xx} diverge exponentiellement, le liquide de Hall quantique est remplacé par le cristal de Wigner. Les scientifiques ont observé le cristal de Wigner autour de l'effet Hall quantique de facteur de remplissage $\nu = 1/5$ - le cristal de Wigner reentrant. Nous avons discuté deux facteurs qui influencent la transition entre le liquide de Hall quantique et le cristal de Wigner: la température et le mélange des niveaux de Landau. À basse température, le liquide de Hall quantique se solidifie et le cristal de Wigner apparaît. Dans un système à fort mélange entre les niveaux de Landau, le cristal de Wigner peut former aux grands facteurs de remplissage. Un exemple est l'observation du cristal de Wigner dans un gas de trous bidimensionnel dont $\nu = 1/3$. Dans ce cas, la masse effective des trous est plus large que celle des électrons, ce qui entraîne un plus fort mélange entre les niveaux de Landau, et favorise le cristal de Wigner sur le liquide de Hall quantique.

À la lumière des connaissances sur l'effet Hall quantique dans le graphène à bicouche et les cristaux de Wigner, nous étudions la physique au voisinage du croisement des niveaux $|K0\uparrow\rangle$ et $|K1\uparrow\rangle$. Nous examinons l'état dont le facteur de remplissage est $\nu = 1/3$. La physique de ce régime est contrôlée par deux paramètres: γ et Δ_{10}, qui dépendent du champ magnétique B et du biais intercouche u. Si $|\Delta_{10}|$ est grand, on arrive à la physique des états de Laughlin des niveaux de Landau galiléens $n = 0$ et $n = 1$. Au voisinage de $\Delta_{10} = 0$, on arrive à une situation similaire à un extrême mélange entre les niveaux de Landau, qui favorise la formation du cristal de Wigner. Cet argument est confirmé par les calculs de diagonalisations exactes, qui donnent la variété des états fondamentaux. Nous avons visualisé la structure cristalline par la fonction de corrélation de paire. Nous avons établi le diagramme de phase de l'état $\nu = 1/3$. La transition entre le liquide de Hall quantique et le cristal de Wigner est continue ou faiblement du premier ordre. Nous ne trouvons pas de cristal de Wigner pour le facteur de remplissage $\nu = 2/3$.

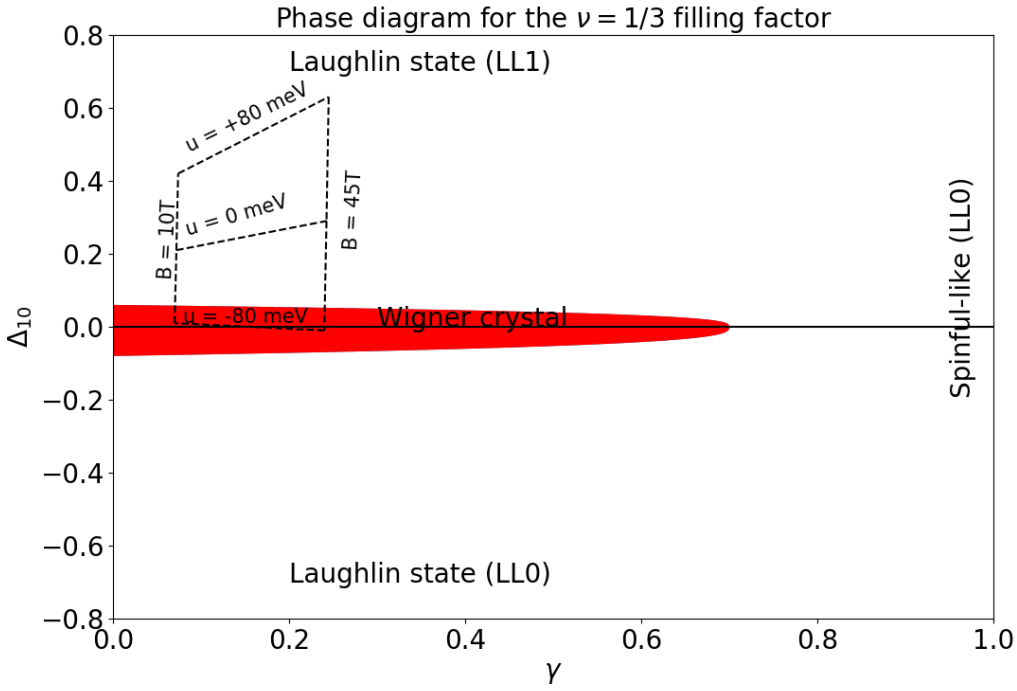

Figure B.4: Phase diagram of Bernal Bilayer graphene in the vicinity of the crossing between the levels $|K0\uparrow\rangle$ and $|K1\uparrow\rangle$.

Tout au long de cette thèse, nous avons étudié l'effet Hall quantique fractionnaire multicomposante dans le graphène et le graphène à bicouche. Dans le graphène, nous avons étudié l'ordre de spin et de vallée des fractions $n/3(n = 1, 2, 4, 5)$, qui sont les plus faciles à observer dans les expériences. Notre travail suggère des questions ouvertes comme proposer des fonctions d'onde d'essai pour expliquer les phases singulet de spin que nous avons trouvées par la méthode numérique. Dans le graphène à bicouche, nous prédisons la formation du cristal de Wigner au croisement des niveaux $|K0\uparrow\rangle$ et $|K1\uparrow\rangle$. Notre travail montre que le graphène à bicouche est une bonne plateforme pour étudier le cristal de Wigner.

Bibliography

[1] K. v. Klitzing, G. Dorda, and M. Pepper. "New Method for High-Accuracy Determination of the Fine-Structure Constant Based on Quantized Hall Resistance". In: *Phys. Rev. Lett.* 45 (6 Aug. 1980), pp. 494–497. DOI: 10.1103/PhysRevLett.45.494.

[2] D. C. Tsui, H. L. Stormer, and A. C. Gossard. "Two-Dimensional Magne totransport in the Extreme Quantum Limit". In: *Phys. Rev. Lett.* 48 (22 May 1982), pp. 1559–1562. DOI: 10.1103/PhysRevLett.48.1559.

[3] F. D. M. Haldane. "Model for a Quantum Hall Effect without Landau Levels: Condensed-Matter Realization of the "Parity Anomaly"". In: *Phys. Rev. Lett.* 61 (18 Oct. 1988), pp. 2015–2018. DOI: 10.1103/PhysRevLett.61.2015.

[4] C. L. Kane and E. J. Mele. "Z_2 Topological Order and the Quantum Spin Hall Effect". In: *Phys. Rev. Lett.* 95 (14 Sept. 2005), p. 146802. DOI: 10.1103/PhysRevLett.95.146802.

[5] B. Andrei Bernevig, Taylor L. Hughes, and Shou-Cheng Zhang. "Quantum Spin Hall Effect and Topological Phase Transition in HgTe Quantum Wells". In: *Science* 314.5806 (2006), pp. 1757–1761. DOI: 10.1126/science.1133734. eprint: https://www.science.org/doi/pdf/10.1126/science.1133734.

[6] Markus König et al. "Quantum Spin Hall Insulator State in HgTe Quantum Wells". In: *Science* 318.5851 (2007), pp. 766–770. DOI: 10.1126/science.1148047. eprint: https://www.science.org/doi/pdf/10.1126/science.1148047.

[7] J. K. Jain. "Composite-fermion approach for the fractional quantum Hall effect". In: *Phys. Rev. Lett.* 63 (2 July 1989), pp. 199–202. DOI: 10.1103/PhysRevLett.63.199.

[8] Jainendra K. Jain. *Composite Fermions*. Cambridge University Press, 2007. DOI: 10.1017/CBO9780511607561.

[9] X. G. Wen. "Vacuum degeneracy of chiral spin states in compactified space". In: *Phys. Rev. B* 40 (10 Oct. 1989), pp. 7387–7390. DOI: 10.1103/PhysRevB.40.7387.

[10] X. G. Wen. "Topological orders in rigid states". In: *International Journal of Modern Physics B* 04.02 (1990), pp. 239–271. DOI: 10.1142/S0217979290000139. eprint: https://doi.org/10.1142/S0217979290000139.

[11] R. B. Laughlin. "Anomalous Quantum Hall Effect: An Incompressible Quantum Fluid with Fractionally Charged Excitations". In: *Phys. Rev. Lett.* 50 (18 May 1983), pp. 1395–1398. DOI: 10.1103/PhysRevLett.50.1395.

[12] V. J. Goldman and B. Su. "Resonant Tunneling in the Quantum Hall Regime: Measurement of Fractional Charge". In: *Science* 267.5200 (1995), pp. 1010–1012. DOI: 10.1126/science.267.5200.1010. eprint: https://www.science.org/doi/pdf/10.1126/science.267.5200.1010.

[13] L. Saminadayar et al. "Observation of the $e/3$ Fractionally Charged Laughlin Quasiparticle". In: *Phys. Rev. Lett.* 79 (13 Sept. 1997), pp. 2526–2529. DOI: 10.1103/PhysRevLett.79.2526.

[14] J.M. Leinass and J Myrheim. "On the theory of identical particles". In: *Nuovo Cim B* 37 (1977), pp. 1–23. DOI: 10.1007/BF02727953.

[15] Frank Wilczek. "Magnetic Flux, Angular Momentum, and Statistics". In: *Phys. Rev. Lett.* 48 (17 Apr. 1982), pp. 1144–1146. DOI: 10.1103/PhysRevLett.48.1144.

[16] Frank Wilczek. "Quantum Mechanics of Fractional-Spin Particles". In: *Phys. Rev. Lett.* 49 (14 Oct. 1982), pp. 957–959. DOI: 10.1103/PhysRevLett.49.957.

[17] H. Bartolomei et al. "Fractional statistics in anyon collisions". In: *Science* 368.6487 (2020), pp. 173–177. DOI: 10.1126/science.aaz5601. eprint: https://www.science.org/doi/pdf/10.1126/science.aaz5601.

[18] K.S. Novoselov et al. "Two-dimensional gas of massless Dirac fermions in graphene". In: *Nature* 438 (7065 Nov. 2005), pp. 197–200. DOI: https://doi.org/10.1038/nature04233.

[19] Yuanbo Zhang et al. "Experimental observation of the quantum Hall effect and Berry's phase in graphene". In: *Nature* 438.7065 (Nov. 2005), pp. 201–204. ISSN: 1476-4687. DOI: 10.1038/nature04235. URL: https://doi.org/10.1038/nature04235.

[20] Xu Du et al. "Fractional quantum Hall effect and insulating phase of Dirac electrons in graphene". In: *Nature* 462.7270 (2009), pp. 192–195. ISSN: 1476-4687. DOI: 10.1038/nature08522. URL: https://doi.org/10.1038/nature08522.

[21] Kirill I. Bolotin et al. "Observation of the fractional quantum Hall effect in graphene". In: *Nature* 462.7270 (Nov. 2009), pp. 196–199. ISSN: 1476-4687. DOI: 10.1038/nature08582. URL: https://doi.org/10.1038/nature08582.

[22] K. S. Novoselov et al. "Unconventional quantum Hall effect and Berry's phase of 2π in bilayer graphene". In: *Nature Physics* 2.3 (Mar. 2006), pp. 177–180. ISSN: 1745-2481. DOI: 10.1038/nphys245. URL: https://doi.org/10.1038/nphys245.

[23] Wenzhong Bao et al. "Magnetoconductance Oscillations and Evidence for Fractional Quantum Hall States in Suspended Bilayer and Trilayer Graphene". In: *Phys. Rev. Lett.* 105 (24 Dec. 2010), p. 246601. DOI: 10.1103/PhysRevLett.105.246601.

[24] Dong-Keun Ki et al. "Observation of Even Denominator Fractional Quantum Hall Effect in Suspended Bilayer Graphene". In: *Nano Letters* 14.4 (Apr. 2014), pp. 2135–2139. ISSN: 1530-6984. DOI: 10.1021/nl5003922. URL: https://doi.org/10.1021/nl5003922.

[25] A. Kou et al. "Electron-hole asymmetric integer and fractional quantum Hall effect in bilayer graphene". In: *Science* 345.6192 (2014), pp. 55–57. DOI: 10.1126/science.1250270. eprint: https://www.science.org/doi/pdf/10.1126/science.1250270.

[26] Qianhui Shi et al. "Odd- and even-denominator fractional quantum Hall states in monolayer WSe2". In: *Nature Nanotechnology* 15.7 (July 2020), pp. 569–573. ISSN: 1748-3395. DOI: 10.1038/s41565-020-0685-6. URL: https://doi.org/10.1038/s41565-020-0685-6.

[27] A. K. Geim and K. S. Novoselov. "The rise of graphene". In: *Nature Materials* 6.3 (Mar. 2007), pp. 183–191. ISSN: 1476-4660. DOI: 10.1038/nmat1849. URL: https://doi.org/10.1038/nmat1849.

[28] A. H. Castro Neto et al. "The electronic properties of graphene". In: *Rev. Mod. Phys.* 81 (1 Jan. 2009), pp. 109–162. DOI: 10.1103/RevModPhys.81.109.

[29] K. S. Novoselov et al. "Two-dimensional atomic crystals". In: *Proceedings of the National Academy of Sciences* 102.30 (2005), pp. 10451–10453. DOI: 10.1073/pnas.0502848102. eprint: https://www.pnas.org/doi/pdf/10.1073/pnas.0502848102.

[30] M. O. Goerbig. "Electronic properties of graphene in a strong magnetic field". In: *Rev. Mod. Phys.* 83 (4 Nov. 2011), pp. 1193–1243. DOI: 10.1103/RevModPhys.83.1193.

[31] Maxim Kharitonov. "Phase diagram for the $\nu = 0$ quantum Hall state in monolayer graphene". In: *Phys. Rev. B* 85 (15 Apr. 2012), p. 155439. DOI: 10.1103/PhysRevB.85.155439.

[32] Fengcheng Wu et al. "SO(5) symmetry in the quantum Hall effect in graphene". In: *Phys. Rev. B* 90 (23 Dec. 2014), p. 235432. DOI: 10.1103/PhysRevB.90.235432.

[33] I. Sodemann and A. H. MacDonald. "Broken SU(4) Symmetry and the Fractional Quantum Hall Effect in Graphene". In: *Phys. Rev. Lett.* 112 (12 Mar. 2014), p. 126804. DOI: 10.1103/PhysRevLett.112.126804.

[34] J. I. A. Li et al. "Excitonic superfluid phase in double bilayer graphene". In: *Nature Physics* 13.8 (Aug. 2017), pp. 751–755. ISSN: 1745-2481. DOI: 10.1038/nphys4140. URL: https://doi.org/10.1038/nphys4140.

[35] Thierry Jolicoeur, Csaba Toke, and Inti Sodemann. "Quantum Hall ferroelectric helix in bilayer graphene". In: *Phys. Rev. B* 99 (11 Mar. 2019), p. 115139. DOI: 10.1103/PhysRevB.99.115139. URL: https://link.aps.org/doi/10.1103/PhysRevB.99.115139.

[36] Zheng Zhu, D. N. Sheng, and Inti Sodemann. "Widely Tunable Quantum Phase Transition from Moore-Read to Composite Fermi Liquid in Bilayer Graphene". In: *Phys. Rev. Lett.* 124 (9 Mar. 2020), p. 097604. DOI: 10.1103/PhysRevLett.124.097604. URL: https://link.aps.org/doi/10.1103/PhysRevLett.124.097604.

[37] E.H. Hall. "On a new action of the magnet on electric currents". In: *American Journal of Mathematics* 2 (Nov. 1879), pp. 287–292.

[38] David Tong. "The quantum Hall effect: TIFR Infosys Lectures".

[39] R S Popović. *Hall effect devices: magnetic sensors and characterization of semiconductors*. 1st ed. IOP Publishing, 1991. ISBN: 0-7503-0096-5.

[40] R. B. Laughlin. "Quantized Hall conductivity in two dimensions". In: *Phys. Rev. B* 23 (10 May 1981), pp. 5632–5633. DOI: 10.1103/PhysRevB.23.5632.

[41] Rolf Landauer. "Electrical resistance of disordered one-dimensional lattices". In: *The Philosophical Magazine: A Journal of Theoretical Experimental and Applied Physics* 21.172 (1970), pp. 863–867. DOI: 10.1080/14786437008238472. eprint: https://doi.org/10.1080/14786437008238472.

[42] M. Büttiker. "Absence of backscattering in the quantum Hall effect in multiprobe conductors". In: *Phys. Rev. B* 38 (14 Nov. 1988), pp. 9375–9389. DOI: 10.1103/PhysRevB.38.9375.

[43] J. K. Jain and S. A. Kivelson. "Landauer-type formulation of quantum-Hall transport: Critical currents and narrow channels". In: *Phys. Rev. B* 37 (8 Mar. 1988), pp. 4276–4279. DOI: 10.1103/PhysRevB.37.4276.

[44] J. K. Jain and S. A. Kivelson. "Quantum Hall effect in quasi one-dimensional systems: Resistance fluctuations and breakdown". In: *Phys. Rev. Lett.* 60 (15 Apr. 1988), pp. 1542–1545. DOI: 10.1103/PhysRevLett.60.1542.

[45] P. Streda, J. Kucera, and A. H. MacDonald. "Edge states, transmission matrices, and the Hall resistance". In: *Phys. Rev. Lett.* 59 (17 Oct. 1987), pp. 1973–1975. DOI: 10.1103/PhysRevLett.59.1973.

[46] D. J. Thouless et al. "Quantized Hall Conductance in a Two-Dimensional Periodic Potential". In: *Phys. Rev. Lett.* 49 (6 Aug. 1982), pp. 405–408. DOI: 10.1103/PhysRevLett.49.405.

[47] L. Landau. "Diamagnetismus der Metalle". In: *Zeitschrift für Physik* 64.9 (Sept. 1930), pp. 629–637. ISSN: 0044-3328. DOI: 10.1007/BF01397213.

[48] E. Wigner. "On the Interaction of Electrons in Metals". In: *Phys. Rev.* 46 (11 Dec. 1934), pp. 1002–1011. DOI: 10.1103/PhysRev.46.1002.

[49] H. L. Stormer et al. "Fractional Quantization of the Hall Effect". In: *Phys. Rev. Lett.* 50 (24 June 1983), pp. 1953–1956. DOI: 10.1103/PhysRevLett.50.1953.

[50] A. M. Chang et al. "Higher-Order States in the Multiple-Series, Fractional, Quantum Hall Effect". In: *Phys. Rev. Lett.* 53 (10 Sept. 1984), pp. 997–1000. DOI: 10.1103/PhysRevLett.53.997.

[51] E. E. Mendez et al. "Fractionally quantized Hall effect in two-dimensional systems of extreme electron concentration". In: *Phys. Rev. B* 30 (12 Dec. 1984), pp. 7310–7312. DOI: 10.1103/PhysRevB.30.7310.

[52] G. S. Boebinger et al. "Competition between neighboring minima in the fractional quantum Hall effect". In: *Phys. Rev. B* 32 (6 Sept. 1985), pp. 4268–4271. DOI: 10.1103/PhysRevB.32.4268.

[53] R.G. Clark et al. "Odd and even fractionally quantized states in GaAs-GaAlAs heterojunctions". In: *Surface Science* 170.1 (1986), pp. 141–147. ISSN: 0039-6028. DOI: https://doi.org/10.1016/0039-6028(86)90953-2.

[54] V. J. Goldman, M. Shayegan, and D. C. Tsui. "Evidence for the Fractional Quantum Hall State at $\nu = \frac{1}{7}$". In: *Phys. Rev. Lett.* 61 (7 Aug. 1988), pp. 881–884. DOI: 10.1103/PhysRevLett.61.881.

[55] T. Sajoto et al. "Fractional quantum Hall effect in very-low-density GaAs/$Al_xGa_{1-x}As$ heterostructures". In: *Phys. Rev. B* 41 (12 Apr. 1990), pp. 8449–8460. DOI: 10.1103/PhysRevB.41.8449.

[56] R. Willett et al. "Observation of an even-denominator quantum number in the fractional quantum Hall effect". In: *Phys. Rev. Lett.* 59 (15 Oct. 1987), pp. 1776–1779. DOI: 10.1103/PhysRevLett.59.1776.

[57] F. D.M. Haldane. "Fractional quantization of the hall effect: A hierarchy of incompressible quantum fluid states". In: *Physical Review Letters* 51.7 (1983), pp. 605–608. ISSN: 00319007. DOI: 10.1103/PhysRevLett.51.605.

[58] B. I. Halperin. "Statistics of Quasiparticles and the Hierarchy of Fractional Quantized Hall States". In: *Phys. Rev. Lett.* 52 (18 Apr. 1984), pp. 1583–1586. DOI: 10.1103/PhysRevLett.52.1583.

[59] Gregory Moore and Nicholas Read. "Nonabelions in the fractional quantum hall effect". In: *Nuclear Physics B* 360.2 (1991), pp. 362–396. ISSN: 0550-3213. DOI: https://doi.org/10.1016/0550-3213(91)90407-O.

[60] N. Read and E. Rezayi. "Beyond paired quantum Hall states: Parafermions and incompressible states in the first excited Landau level". In: *Phys. Rev. B* 59 (12 Mar. 1999), pp. 8084–8092. DOI: 10.1103/PhysRevB.59.8084.

[61] F. D. M. Haldane and E. H. Rezayi. "Finite-Size Studies of the Incompressible State of the Fractionally Quantized Hall Effect and its Excitations". In: *Phys. Rev. Lett.* 54 (3 Jan. 1985), pp. 237–240. DOI: 10.1103/PhysRevLett.54.237.

[62] G. Fano, F. Ortolani, and E. Colombo. "Configuration-interaction calculations on the fractional quantum Hall effect". In: *Physical Review B* 34.4 (1986), pp. 2670–2680. ISSN: 01631829. DOI: 10.1103/PhysRevB.34.2670.

[63] The Ioffe Institute. *GaAs - Gallium Arsenide*. URL: https://www.ioffe.ru/SVA/NSM/Semicond/GaAs/basic.html (visited on 04/18/2023).

[64] Ireneusz Strzalkowski, Sharad Joshi, and C. R. Crowell. "Dielectric constant and its temperature dependence for GaAs, CdTe, and ZnSe". In: *Applied Physics Letters* 28.6 (1976), pp. 350–352. DOI: 10.1063/1.88755. URL: https://doi.org/10.1063/1.88755.

[65] X. C. Xie, Yin Guo, and F. C. Zhang. "Fractional quantum Hall effect with spin reversal". In: *Phys. Rev. B* 40 (5 Aug. 1989), pp. 3487–3490. DOI: 10.1103/PhysRevB.40.3487.

[66] R. R. Du et al. "Fractional Quantum Hall Effect around $\nu = \frac{3}{2}$: Composite Fermions with a Spin". In: *Phys. Rev. Lett.* 75 (21 Nov. 1995), pp. 3926–3929. DOI: 10.1103/PhysRevLett.75.3926. URL: https://link.aps.org/doi/10.1103/PhysRevLett.75.3926.

[67] Ngoc Duc Le and Thierry Jolicoeur. "Spin and valley ordering of fractional quantum Hall states in monolayer graphene". In: *Phys. Rev. B* 105 (7 Feb. 2022), p. 075203. DOI: 10.1103/PhysRevB.105.075203.

[68] Y. Zhang et al. "Landau-Level Splitting in Graphene in High Magnetic Fields". In: *Phys. Rev. Lett.* 96 (13 Apr. 2006), p. 136806. DOI: 10.1103/PhysRevLett.96.136806.

[69] Z. Jiang et al. "Quantum Hall States near the Charge-Neutral Dirac Point in Graphene". In: *Phys. Rev. Lett.* 99 (10 Sept. 2007), p. 106802. DOI: 10.1103/PhysRevLett.99.106802.

[70] Kentaro Nomura and Allan H. MacDonald. "Quantum Hall Ferromagnetism in Graphene". In: *Phys. Rev. Lett.* 96 (25 June 2006), p. 256602. DOI: 10.1103/PhysRevLett.96.256602.

[71] Jason Alicea and Matthew P. A. Fisher. "Graphene integer quantum Hall effect in the ferromagnetic and paramagnetic regimes". In: *Phys. Rev. B* 74 (7 Aug. 2006), p. 075422. DOI: 10.1103/PhysRevB.74.075422.

[72] I. L. Aleiner, D. E. Kharzeev, and A. M. Tsvelik. "Spontaneous symmetry breaking in graphene subjected to an in-plane magnetic field". In: *Phys. Rev. B* 76 (19 Nov. 2007), p. 195415. DOI: 10.1103/PhysRevB.76.195415.

[73] A. F. Young et al. "Spin and valley quantum Hall ferromagnetism in graphene". In: *Nature Physics* 8.7 (May 2012), pp. 550–556. ISSN: 3745-2481. DOI: 10.1038/nphys2307. URL: https://doi.org/10.1038/nphys2307.

[74] A. F. Young et al. "Tunable symmetry breaking and helical edge transport in a graphene quantum spin Hall state". In: *Nature* 505.7484 (Jan. 2014), pp. 528–532. ISSN: 1476-4687. DOI: 10.1038/nature12800.

[75] Si-Yu Li et al. "Scanning tunneling microscope study of quantum Hall isospin ferromagnetic states in the zero Landau level in a graphene monolayer". In: *Phys. Rev. B* 100 (8 Aug. 2019), p. 085437. DOI: 10.1103/PhysRevB.100.085437. URL: https://link.aps.org/doi/10.1103/PhysRevB.100.085437.

[76] Xiaomeng Liu et al. "Visualizing broken symmetry and topological defects in a quantum Hall ferromagnet". In: *Science* 375.6578 (2022), pp. 321–326. DOI: 10.1126/science.abm3770. eprint: https://www.science.org/doi/pdf/10.1126/science.abm3770. URL: https://www.science.org/doi/abs/10.1126/science.abm3770.

[77] Alexis Coissard et al. "Imaging tunable quantum Hall broken-symmetry orders in graphene". In: *Nature* 605.7908 (2022), pp. 51–56. ISSN: 1476-4687. DOI: 10.1038/s41586-022-04513-7. URL: https://doi.org/10.1038/s41586-022-04513-7.

[78] Jeil Jung and Allan H. MacDonald. "Tight-binding model for graphene π-bands from maximally localized Wannier functions". In: *Phys. Rev. B* 87 (19 May 2013), p. 195450. DOI: 10.1103/PhysRevB.87.195450.

[79] Fusayoshi J. Ohkawa and Yasutada Uemura. "Theory of Valley Splitting in an N-Channel (100) Inversion Layer of Si I. Formulation by Extended Zone Effective Mass Theory". In: *Journal of the Physical Society of Japan* 43.3 (1977), pp. 907–916. DOI: 10.1143/JPSJ.43.907. eprint: https://doi.org/10.1143/JPSJ.43.907.

[80] L. J. Sham et al. "Valley-Valley Splitting in Inversion Layers on a High-Index Surface of Silicon". In: *Phys. Rev. Lett.* 40 (7 Feb. 1978), pp. 472–475. DOI: 10.1103/PhysRevLett.40.472.

[81] O. Gunawan et al. "Valley Susceptibility of an Interacting Two-Dimensional Electron System". In: *Phys. Rev. Lett.* 97 (18 Nov. 2006), p. 186404. DOI: 10.1103/PhysRevLett.97.186404.

[82] O. Gunawan et al. "Quantized conductance in an AlAs two-dimensional electron system quantum point contact". In: *Phys. Rev. B* 74 (15 Oct. 2006), p. 155436. DOI: 10.1103/PhysRevB.74.155436.

[83] Zengwei Zhu et al. "Field-induced polarization of Dirac valleys in bismuth". In: *Nature Physics* 8.1 (Jan. 2012), pp. 89–94. ISSN: 1745-2481. DOI: 10.1038/nphys2111.

[84] Fabio Bussolotti et al. "Roadmap on finding chiral valleys: screening 2D materials for valleytronics". In: *Nano Futures* 2.3 (June 2018), p. 032001. DOI: 10.1088/2399-1984/aac9d7. URL: https://dx.doi.org/10.1088/2399-1984/aac9d7.

[85] Zefei Wu et al. "Intrinsic valley Hall transport in atomically thin MoS2". In: *Nature Communications* 10.1 (Feb. 2019), p. 611. ISSN: 2041-1723. DOI: 10.1038/s41467-019-08629-9.

[86] John R. Schaibley et al. "Valleytronics in 2D materials". In: *Nature Reviews Materials* 1.11 (Aug. 2016), p. 16055. ISSN: 2058-8437. DOI: 10.1038/natrevmats.2016.55.

[87] K. S. Novoselov et al. "Electric Field Effect in Atomically Thin Carbon Films". In: *Science* 306.5696 (2004), pp. 666–669. DOI: 10.1126/science.1102896. eprint: https://www.science.org/doi/pdf/10.1126/science.1102896.

[88] V. P. Gusynin and S. G. Sharapov. "Unconventional Integer Quantum Hall Effect in Graphene". In: *Phys. Rev. Lett.* 95 (14 Sept. 2005), p. 146801. DOI: 10.1103/PhysRevLett.95.146801.

[89] N. M. R. Peres, F. Guinea, and A. H. Castro Neto. "Electronic properties of disordered two-dimensional carbon". In: *Phys. Rev. B* 73 (12 Mar. 2006), p. 125411. DOI: 10.1103/PhysRevB.73.125411.

[90] Kun Yang. "Spontaneous symmetry breaking and quantum Hall effect in graphene". In: *Solid State Communications* 143.1 (2007). Exploring graphene, pp. 27–32. ISSN: 0038-1098. DOI: https://doi.org/10.1016/j.ssc.2007.03.051.

[91] K. S. Novoselov et al. "Room-Temperature Quantum Hall Effect in Graphene". In: *Science* 315.5817 (2007), pp. 1379–1379. DOI: 10.1126/science.1137201. eprint: https://www.science.org/doi/pdf/10.1126/science.1137201.

[92] Fereshte Ghahari et al. "Measurement of the $\nu = 1/3$ Fractional Quantum Hall Energy Gap in Suspended Graphene". In: *Phys. Rev. Lett.* 106 (4 Jan. 2011), p. 046801. DOI: 10.1103/PhysRevLett.106.046801.

[93] Benjamin E. Feldman et al. "Unconventional Sequence of Fractional Quantum Hall States in Suspended Graphene". In: *Science* 337.6099 (2012), pp. 1196–1199. DOI: 10.1126/science.1224784. eprint: https://www.science.org/doi/pdf/10.1126/science.1224784.

[94] Benjamin E. Feldman et al. "Fractional Quantum Hall Phase Transitions and Four-Flux States in Graphene". In: *Phys. Rev. Lett.* 111 (7 Aug. 2013), p. 076802. DOI: 10.1103/PhysRevLett.111.076802.

[95] C. R. Dean et al. "Boron nitride substrates for high-quality graphene electronics". In: *Nature Nanotechnology* 5.10 (2010), pp. 722–726. ISSN: 1748-3395. DOI: 10.1038/nnano.2010.172. URL: https://doi.org/10.1038/nnano.2010.172.

[96] C. R. Dean et al. "Multicomponent fractional quantum Hall effect in graphene". In: *Nature Physics* 7.9 (Sept. 2011), pp. 693–696. ISSN: 1745-2481. DOI: 10.1038/nphys2007. URL: https://doi.org/10.1038/nphys2007.

[97] A. A. Zibrov et al. "Even-denominator fractional quantum Hall states at an isospin transition in monolayer graphene". In: *Nature Physics* 14.9 (Sept. 2018), pp. 930–935. ISSN: 1745-2481. DOI: 10.1038/s41567-018-0190-0. URL: https://doi.org/10.1038/s41567-018-0190-0.

[98] Youngwook Kim et al. "Even denominator fractional quantum Hall states in higher Landau levels of graphene". In: *Nature Physics* 15.2 (2019), pp. 154–158. ISSN: 1745-2481. DOI: 10.1038/s41567-018-0355-x. URL: https://doi.org/10.1038/s41567-018-0355-x.

[99] Suraj S. Hegde and Inti Sodemann Villadiego. "Theory of competing charge density wave, Kekulé, and antiferromagnetically ordered fractional quantum Hall states in graphene aligned with boron nitride". In: *Phys. Rev. B* 105 (19 May 2022), p. 195417. DOI: 10.1103/PhysRevB.105.195417.

[100] Jason Alicea and Matthew P.A. Fisher. "Interplay between lattice-scale physics and the quantum Hall effect in graphene". In: *Solid State Communications* 143.11 (2007), pp. 504–509. ISSN: 0038-1098. DOI: https://doi.org/10.1016/j.ssc.2007.06.035.

[101] Gabriele Giuliani and Giovanni Vignale. *Quantum Theory of the Electron Liquid*. Cambridge University Press, 2005. DOI: 10.1017/CBO9780511619915.

[102] F. Amet et al. "Composite fermions and broken symmetries in graphene". In: *Nature Communications* 6.1 (Jan. 2015), p. 5838. ISSN: 2041-1723. DOI: 10.1038/ncomms6838. URL: https://doi.org/10.1038/ncomms6838.

[103] Walter Pfeiffer. *The Lie algebras su(N): An introduction*. 1st ed. Birkhäuser Basel, 2003. ISBN: 978-3-7643-2418-6. DOI: https://doi.org/10.1007/978-3-0348-8097-8.

[104] Fengcheng Wu et al. "SU(3) and SU(4) Singlet Quantum Hall States at $\nu = 2/3$". In: *Phys. Rev. Lett.* 115 (16 Oct. 2015), p. 166805. DOI: 10.1103/PhysRevLett.115.166805. URL: https://link.aps.org/doi/10.1103/PhysRevLett.115.166805.

[105] Ngoc Duc Le and Thierry Jolicoeur. "Competing Laughlin state and Wigner crystal in Bernal bilayer graphene". In: *Phys. Rev. B* 107 (12 Mar. 2023), p. 125129. DOI: 10.1103/PhysRevB.107.125129. URL: https://link.aps.org/doi/10.1103/PhysRevB.107.125129.

[106] Edward McCann and Vladimir I. Fal'ko. "Landau-Level Degeneracy and Quantum Hall Effect in a Graphite Bilayer". In: *Phys. Rev. Lett.* 96 (8 Mar. 2006), p. 086805. DOI: 10.1103/PhysRevLett.96.086805. URL: https://link.aps.org/doi/10.1103/PhysRevLett.96.086805.

[107] Yafis Barlas et al. "Intra-Landau-Level Cyclotron Resonance in Bilayer Graphene". In: *Phys. Rev. Lett.* 101 (9 Aug. 2008), p. 097601. DOI: 10.1103/PhysRevLett.101.097601. URL: https://link.aps.org/doi/10.1103/PhysRevLett.101.097601.

[108] Ke Huang et al. "Valley Isospin Controlled Fractional Quantum Hall States in Bilayer Graphene". In: *Phys. Rev. X* 12 (3 July 2022), p. 031019. DOI: 10.1103/PhysRevX.12.031019. URL: https://link.aps.org/doi/10.1103/PhysRevX.12.031019.

[109] Benjamin E. Feldman, Jens Martin, and Amir Yacoby. "Broken-symmetry states and divergent resistance in suspended bilayer graphene". In: *Nature Physics* 5.12 (Dec. 2009), pp. 889–893. ISSN: 1745-2481. DOI: 10.1038/nphys1406. URL: https://doi.org/10.1038/nphys1406.

[110] Y. Zhao et al. "Symmetry Breaking in the Zero-Energy Landau Level in Bilayer Graphene". In: *Phys. Rev. Lett.* 104 (6 Feb. 2010), p. 066801. DOI: 10.1103/PhysRevLett.104.066801. URL: https://link.aps.org/doi/10.1103/PhysRevLett.104.066801.

[111] A. A. Zibrov et al. "Tunable interacting composite fermion phases in a half-filled bilayer-graphene Landau level". In: *Nature* 549.7672 (Sept. 2017), pp. 360–364. ISSN: 1476-4687. DOI: 10.1038/nature23893. URL: https://doi.org/10.1038/nature23893.

[112] Jeroen B. Oostinga et al. "Gate-induced insulating state in bilayer graphene devices". In: *Nature Materials* 7.2 (Feb. 2008), pp. 151–157. ISSN: 1476-4660. DOI: 10.1038/nmat2082. URL: https://doi.org/10.1038/nmat2082.

[113] Eduardo V. Castro et al. "Biased Bilayer Graphene: Semiconductor with a Gap Tunable by the Electric Field Effect". In: *Phys. Rev. Lett.* 99 (21 Nov. 2007), p. 216802. DOI: 10.1103/PhysRevLett.99.216802. URL: https://link.aps.org/doi/10.1103/PhysRevLett.99.216802.

[114] R. T. Weitz et al. "Broken-Symmetry States in Doubly Gated Suspended Bilayer Graphene". In: *Science* 330.6005 (2010), pp. 812–816. DOI: 10.1126/science.1194988. eprint: https://www.science.org/doi/pdf/10.1126/science.1194988. URL: https://www.science.org/doi/abs/10.1126/science.1194988.

[115] J. Velasco et al. "Transport spectroscopy of symmetry-broken insulating states in bilayer graphene". In: *Nature Nanotechnology* 7.3 (Mar. 2012), pp. 156–160. ISSN: 1748-3395. DOI: 10.1038/nnano.2011.251. URL: https://doi.org/10.1038/nnano.2011.251.

[116] J. Velasco Jr et al. "Competing ordered states with filling factor two in bilayer graphene". In: *Nature Communications* 5.1 (July 2014), p. 4550. ISSN: 2041-1723. DOI: 10.1038/ncomms5550. URL: https://doi.org/10.1038/ncomms5550.

[117] Yanmeng Shi et al. "Energy Gaps and Layer Polarization of Integer and Fractional Quantum Hall States in Bilayer Graphene". In: *Phys. Rev. Lett.* 116 (5 Feb. 2016), p. 056601. DOI: 10.1103/PhysRevLett.116.056601. URL: https://link.aps.org/doi/10.1103/PhysRevLett.116.056601.

[118] Hailong Fu et al. "Gapless Spin Wave Transport through a Quantum Canted Antiferromagnet". In: *Phys. Rev. X* 11 (2 Apr. 2021), p. 021012. DOI: 10.1103/PhysRevX.11.021012. URL: https://link.aps.org/doi/10.1103/PhysRevX.11.021012.

[119] Patrick Maher et al. "Tunable fractional quantum Hall phases in bilayer graphene". In: *Science* 345.6192 (2014), pp. 61–64. DOI: 10.1126/science.1252875. eprint: https://www.science.org/doi/pdf/10.1126/science.1252875. URL: https://www.science.org/doi/abs/10.1126/science.1252875.

[120] Seyoung Kim, Kayoung Lee, and E. Tutuc. "Spin-Polarized to Valley-Polarized Transition in Graphene Bilayers at $\nu = 0$ in High Magnetic Fields". In: *Phys. Rev. Lett.* 107 (1 June 2011), p. 016803. DOI: 10.1103/PhysRevLett.107.016803. URL: https://link.aps.org/doi/10.1103/PhysRevLett.107.016803.

[121] P. Maher et al. "Evidence for a spin phase transition at charge neutrality in bilayer graphene". In: *Nature Physics* 9.3 (Mar. 2013), pp. 154–158. ISSN: 1745-2481. DOI: 10.1038/nphys2528. URL: https://doi.org/10.1038/nphys2528.

[122] E. V. Gorbar, V. P. Gusynin, and V. A. Miransky. "Dynamics and phase diagram of the $\nu = 0$ quantum Hall state in bilayer graphene". In: *Phys. Rev. B* 81 (15 Apr. 2010), p. 155451. DOI: 10.1103/PhysRevB.81.155451. URL: https://link.aps.org/doi/10.1103/PhysRevB.81.155451.

[123] E. V. Gorbar et al. "Broken symmetry $\nu = 0$ quantum Hall states in bilayer graphene: Landau level mixing and dynamical screening". In: *Phys. Rev. B* 85 (23 June 2012), p. 235460. DOI: 10.1103/PhysRevB.85.235460. URL: https://link.aps.org/doi/10.1103/PhysRevB.85.235460.

[124] Maxim Kharitonov. "Canted Antiferromagnetic Phase of the ν=0 Quantum Hall State in Bilayer Graphene". In: *Phys. Rev. Lett.* 109 (4 July 2012), p. 046803. DOI: 10.1103/PhysRevLett.109.046803. URL: https://link.aps.org/doi/10.1103/PhysRevLett.109.046803.

[125] B. M. Hunt et al. "Direct measurement of discrete valley and orbital quantum numbers in bilayer graphene". In: *Nature Communications* 8.1 (Oct. 2017), p. 948. ISSN: 2041-1723. DOI: 10.1038/s41467-017-00824-w. URL: https://doi.org/10.1038/s41467-017-00824-w.

[126] J. C. Slonczewski and P. R. Weiss. "Band Structure of Graphite". In: *Phys. Rev.* 109 (2 Jan. 1958), pp. 272–279. DOI: 10.1103/PhysRev.109.272. URL: https://link.aps.org/doi/10.1103/PhysRev.109.272.

[127] J. W. McClure. "Theory of Diamagnetism of Graphite". In: *Phys. Rev.* 119 (2 1960), pp. 606–613. DOI: 10.1103/PhysRev.119.606. URL: https://link.aps.org/doi/10.1103/PhysRev.119.606.

[128] Edward McCann and Mikito Koshino. "The electronic properties of bilayer graphene". In: *Reports on Progress in Physics* 76.5 (2013), p. 056503. DOI: 10.1088/0034-4885/76/5/056503. URL: https://doi.org/10.1088/0034-4885/76/5/056503.

[129] Jeil Jung and Allan H. MacDonald. "Accurate tight-binding models for the π bands of bilayer graphene". In: *Phys. Rev. B* 89 (3 Jan. 2014), p. 035405. DOI: 10.1103/PhysRevB.89.035405.

[130] A. B. Kuzmenko et al. "Determination of the gate-tunable band gap and tight-binding parameters in bilayer graphene using infrared spectroscopy". In: *Phys. Rev. B* 80 (16 Oct. 2009), p. 165406. DOI: 10.1103/PhysRevB.80.165406. URL: https://link.aps.org/doi/10.1103/PhysRevB.80.165406.

[131] K. Shizuya. "Structure and the Lamb-shift-like quantum splitting of the pseudo-zero-mode Landau levels in bilayer graphene". In: *Phys. Rev. B* 86 (4 July 2012), p. 045431. DOI: 10.1103/PhysRevB.86.045431. URL: https://link.aps.org/doi/10.1103/PhysRevB.86.045431.

[132] R. Geick, C. H. Perry, and G. Rupprecht. "Normal Modes in Hexagonal Boron Nitride". In: *Phys. Rev.* 146 (2 June 1966), pp. 543–547. DOI: 10.1103/PhysRev.146.543. URL: https://link.aps.org/doi/10.1103/PhysRev.146.543.

[133] Nobuko Ohba et al. "First-principles study on structural, dielectric, and dynamical properties for three BN polytypes". In: *Phys. Rev. B* 63 (11 Mar. 2001), p. 115207. DOI: 10.1103/PhysRevB.63.115207. URL: https://link.aps.org/doi/10.1103/PhysRevB.63.115207.

[134] Z. Papić and D. A. Abanin. "Topological Phases in the Zeroth Landau Level of Bilayer Graphene". In: *Phys. Rev. Lett.* 112 (4 Jan. 2014), p. 046602. DOI: 10.1103/PhysRevLett.112.046602. URL: https://link.aps.org/doi/10.1103/PhysRevLett.112.046602.

[135] W. J. Carr. "Energy, Specific Heat, and Magnetic Properties of the Low-Density Electron Gas". In: *Phys. Rev.* 122 (5 June 1961), pp. 1437–1446. DOI: 10.1103/PhysRev.122.1437. URL: https://link.aps.org/doi/10.1103/PhysRev.122.1437.

[136] C. C. Grimes and G. Adams. "Evidence for a Liquid-to-Crystal Phase Transition in a Classical, Two-Dimensional Sheet of Electrons". In: *Phys. Rev. Lett.* 42 (12 Mar. 1979), pp. 795–798. DOI: 10.1103/PhysRevLett.42.795. URL: https://link.aps.org/doi/10.1103/PhysRevLett.42.795.

[137] Daniel S. Fisher, B. I. Halperin, and P. M. Platzman. "Phonon-Ripplon Coupling and the Two-Dimensional Electron Solid on a Liquid-Helium Surface". In: *Phys. Rev. Lett.* 42 (12 Mar. 1979), pp. 798–801. DOI: 10.1103/PhysRevLett.42.798. URL: https://link.aps.org/doi/10.1103/PhysRevLett.42.798.

[138] Milton W. Cole and Morrel H. Cohen. "Image-Potential-Induced Surface Bands in Insulators". In: *Phys. Rev. Lett.* 23 (21 Nov. 1969), pp. 1238–1241. DOI: 10.1103/PhysRevLett.23.1238. URL: https://link.aps.org/doi/10.1103/PhysRevLett.23.1238.

[139] R.S. Crandall and R. Williams. "Crystallization of electrons on the surface of liquid helium". In: *Physics Letters A* 34.7 (1971), pp. 404–405. ISSN: 0375-9601. DOI: https://doi.org/10.1016/0375-9601(71)90938-8. URL: https://www.sciencedirect.com/science/article/pii/0375960171909388.

[140] Lynn Bonsall and A. A. Maradudin. "Some static and dynamical properties of a two-dimensional Wigner crystal". In: *Phys. Rev. B* 15 (4 Feb. 1977), pp. 1959–1973. DOI: 10.1103/PhysRevB.15.1959. URL: https://link.aps.org/doi/10.1103/PhysRevB.15.1959.

[141] H. Fukuyama, P. M. Platzman, and P. W. Anderson. "Two-dimensional electron gas in a strong magnetic field". In: *Phys. Rev. B* 19 (10 May 1979), pp. 5211–5217. DOI: 10.1103/PhysRevB.19.5211. URL: https://link.aps.org/doi/10.1103/PhysRevB.19.5211.

[142] Kazumi Maki and Xenophon Zotos. "Static and dynamic properties of a two-dimensional Wigner crystal in a strong magnetic field". In: *Phys. Rev. B* 28 (8 Oct. 1983), pp. 4349–4356. DOI: 10.1103/PhysRevB.28.4349. URL: https://link.aps.org/doi/10.1103/PhysRevB.28.4349.

[143] Pui K. Lam and S. M. Girvin. "Liquid-solid transition and the fractional quantum-Hall effect". In: *Phys. Rev. B* 30 (1 July 1984), pp. 473–475. DOI: 10.1103/PhysRevB.30.473. URL: https://link.aps.org/doi/10.1103/PhysRevB.30.473.

[144] Hangmo Yi and H. A. Fertig. "Laughlin-Jastrow-correlated Wigner crystal in a strong magnetic field". In: *Phys. Rev. B* 58 (7 Aug. 1998), pp. 4019–4027. DOI: 10.1103/PhysRevB.58.4019. URL: https://link.aps.org/doi/10.1103/PhysRevB.58.4019.

[145] Constantine Yannouleas and Uzi Landman. "Two-dimensional quantum dots in high magnetic fields: Rotating-electron-molecule versus composite-fermion approach". In: *Phys. Rev. B* 68 (3 July 2003), p. 035326. DOI: 10.1103/PhysRevB.68.035326. URL: https://link.aps.org/doi/10.1103/PhysRevB.68.035326.

[146] Chia-Chen Chang, Gun Sang Jeon, and Jainendra K. Jain. "Microscopic Verification of Topological Electron-Vortex Binding in the Lowest Landau-Level Crystal State". In: *Phys. Rev. Lett.* 94 (1 Jan. 2005), p. 016809. DOI: 10.1103/PhysRevLett.94.016809. URL: https://link.aps.org/doi/10.1103/PhysRevLett.94.016809.

[147] D. Levesque, J. J. Weis, and A. H. MacDonald. "Crystallization of the incompressible quantum-fluid state of a two-dimensional electron gas in a strong magnetic field". In: *Phys. Rev. B* 30 (2 July 1984), pp. 1056–1058. DOI: 10.1103/PhysRevB.30.1056. URL: https://link.aps.org/doi/10.1103/PhysRevB.30.1056.

[148] Kun Yang, F. D. M. Haldane, and E. H. Rezayi. "Wigner crystals in the lowest Landau level at low-filling factors". In: *Phys. Rev. B* 64 (8 Aug. 2001), p. 081301. DOI: 10.1103/PhysRevB.64.081301. URL: https://link.aps.org/doi/10.1103/PhysRevB.64.081301.

[149] H. W. Jiang et al. "Quantum liquid versus electron solid around ν=1/5 Landau-level filling". In: *Phys. Rev. Lett.* 65 (5 July 1990), pp. 633–636. DOI: 10.1103/PhysRevLett.65.633. URL: https://link.aps.org/doi/10.1103/PhysRevLett.65.633.

[150] V. J. Goldman et al. "Evidence for two-dimentional quantum Wigner crystal". In: *Phys. Rev. Lett.* 65 (17 Oct. 1990), pp. 2189–2192. DOI: 10.1103/PhysRevLett.65.2189. URL: https://link.aps.org/doi/10.1103/PhysRevLett.65.2189.

[151] Yuan P. Li et al. "Low-frequency noise in the reentrant insulating phase around the 1/5 fractional quantum Hall liquid". In: *Phys. Rev. Lett.* 67 (12 Sept. 1991), pp. 1630–1633. DOI: 10.1103/PhysRevLett.67.1630. URL: https://link.aps.org/doi/10.1103/PhysRevLett.67.1630.

[152] H. W. Jiang et al. "Magnetotransport studies of the insulating phase around ν=1/5 Landau-level filling". In: *Phys. Rev. B* 44 (15 Oct. 1991), pp. 8107–8114. DOI: 10.1103/PhysRevB.44.8107. URL: https://link.aps.org/doi/10.1103/PhysRevB.44.8107.

[153] M. B. Santos et al. "Observation of a reentrant insulating phase near the 1/3 fractional quantum Hall liquid in a two-dimensional hole system". In: *Phys. Rev. Lett.* 68 (8 Feb. 1992), pp. 1188–1191. DOI: 10.1103/PhysRevLett.68.1188. URL: https://link.aps.org/doi/10.1103/PhysRevLett.68.1188.

[154] W. Pan et al. "Transition from an Electron Solid to the Sequence of Fractional Quantum Hall States at Very Low Landau Level Filling Factor". In: *Phys. Rev. Lett.* 88 (17 Apr. 2002), p. 176802. DOI: 10.1103/PhysRevLett.88.176802. URL: https://link.aps.org/doi/10.1103/PhysRevLett.88.176802.

[155] E. Y. Andrei et al. "Observation of a Magnetically Induced Wigner Solid". In: *Phys. Rev. Lett.* 60 (26 June 1988), pp. 2765–2768. DOI: 10.1103/PhysRevLett.60.2765. URL: https://link.aps.org/doi/10.1103/PhysRevLett.60.2765.

[156] H. Buhmann et al. "Magneto-optical evidence for fractional quantum Hall states down to filling factor 1/9". In: *Phys. Rev. Lett.* 65 (8 Aug. 1990), pp. 1056–1059. DOI: 10.1103/PhysRevLett.65.1056. URL: https://link.aps.org/doi/10.1103/PhysRevLett.65.1056.

[157] Yong Chen et al. "Microwave Resonance of the 2D Wigner Crystal around Integer Landau Fillings". In: *Phys. Rev. Lett.* 91 (1 July 2003), p. 016801. DOI: 10.1103/PhysRevLett.91.016801. URL: https://link.aps.org/doi/10.1103/PhysRevLett.91.016801.

[158] J. R. Mallett et al. "Experimental studies of the $\upsilon = \frac{1}{5}$ hierarchy in the fractional quantum Hall effect". In: *Phys. Rev. B* 38 (3 July 1988), pp. 2200–2203. DOI: 10.1103/PhysRevB.38.2200. URL: https://link.aps.org/doi/10.1103/PhysRevB.38.2200.

[159] Meng K. Ma et al. "Thermal and Quantum Melting Phase Diagrams for a Magnetic-Field-Induced Wigner Solid". In: *Phys. Rev. Lett.* 125 (3 July 2020), p. 036601. DOI: 10.1103/PhysRevLett.125.036601. URL: https://link.aps.org/doi/10.1103/PhysRevLett.125.036601.

[160] P. M. Platzman and Rodney Price. "Quantum freezing of the fractional quantum Hall liquid". In: *Phys. Rev. Lett.* 70 (22 May 1993), pp. 3487–3489. DOI: 10.1103/PhysRevLett.70.3487. URL: https://link.aps.org/doi/10.1103/PhysRevLett.70.3487.

[161] Rodney Price et al. "Freezing of the quantum Hall liquid at ν=1/7 and 1/9". In: *Phys. Rev. B* 48 (15 Oct. 1993), pp. 11473–11476. DOI: 10.1103/PhysRevB.48.11473. URL: https://link.aps.org/doi/10.1103/PhysRevB.48.11473.

[162] Jianyun Zhao, Yuhe Zhang, and J. K. Jain. "Crystallization in the Fractional Quantum Hall Regime Induced by Landau-Level Mixing". In: *Phys. Rev. Lett.* 121 (11 Sept. 2018), p. 116802. DOI: 10.1103/PhysRevLett.121.116802. URL: https://link.aps.org/doi/10.1103/PhysRevLett.121.116802.

[163] E. H. Rezayi, F. D. M. Haldane, and Kun Yang. "Charge-Density-Wave Ordering in Half-Filled High Landau Levels". In: *Phys. Rev. Lett.* 83 (6 Aug. 1999), pp. 1219–1222. DOI: 10.1103/PhysRevLett.83.1219. URL: https://link.aps.org/doi/10.1103/PhysRevLett.83.1219.

[164] E. H. Rezayi and F. D. M. Haldane. "Incompressible Paired Hall State, Stripe Order, and the Composite Fermion Liquid Phase in Half-Filled Landau Levels". In: *Phys. Rev. Lett.* 84 (20 May 2000), pp. 4685–4688. DOI: 10.1103/PhysRevLett.84.4685. URL: https://link.aps.org/doi/10.1103/PhysRevLett.84.4685.

[165] F. D. M. Haldane, E. H. Rezayi, and Kun Yang. "Spontaneous Breakdown of Translational Symmetry in Quantum Hall Systems: Crystalline Order in High Landau Levels". In: *Phys. Rev. Lett.* 85 (25 Dec. 2000), pp. 5396–5399. DOI: 10.1103/PhysRevLett.85.5396. URL: https://link.aps.org/doi/10.1103/PhysRevLett.85.5396.

[166] Angelika Knothe and Thierry Jolicoeur. "Edge structure of graphene monolayers in the $\nu = 0$ quantum Hall state". In: *Phys. Rev. B* 92 (16 Oct. 2015), p. 165110. DOI: 10.1103/PhysRevB.92.165110.

[167] M. Jo et al. "Quantum Hall Valley Splitters and a Tunable Mach-Zehnder Interferometer in Graphene". In: *Phys. Rev. Lett.* 126 (14 Apr. 2021), p. 146803. DOI: 10.1103/PhysRevLett.126.146803. URL: https://link.aps.org/doi/10.1103/PhysRevLett.126.146803.

[168] Nikolaos Stefanidis and Inti Sodemann Villadiego. "Competing spin-valley entangled and broken symmetry states in the $N = 1$ Landau level of graphene". In: *Phys. Rev. B* 107 (4 Jan. 2023), p. 045132. DOI: 10.1103/PhysRevB.107.045132.

[169] Ankur Das, Ribhu K. Kaul, and Ganpathy Murthy. "Coexistence of Canted Antiferromagnetism and Bond Order in $\nu = 0$ Graphene". In: *Phys. Rev. Lett.* 128 (10 Mar. 2022), p. 106803. DOI: 10.1103/PhysRevLett.128.106803.

[170] Suman Jyoti De et al. "Global phase diagram of charge-neutral graphene in the quantum Hall regime for generic interactions". In: *Phys. Rev. B* 107 (12 Mar. 2023), p. 125422. DOI: 10.1103/PhysRevB.107.125422. URL: https://link.aps.org/doi/10.1103/PhysRevB.107.125422.

[171] Hongyuan Li et al. "Imaging two-dimensional generalized Wigner crystals". In: *Nature* 597.7878 (Sept. 2021), pp. 650–654. ISSN: 1476-4687. DOI: 10.1038/s41586-021-03874-9. URL: https://doi.org/10.1038/s41586-021-03874-9.

[172] Tapash Chakraborty and Pekka Pietiläinen. *The Quantum Hall Effects*. 2nd ed. Springer-Verlag Berlin Heidelberg, 1995. ISBN: 978-3-540-58515-2. DOI: https://doi.org/10.1007/978-3-642-79319-6.

[173] Tai Tsun Wu and Chen Ning Yang. "Dirac monopole without strings: Monopole harmonics". In: *Nuclear Physics, Section B* 107.3 (1976), pp. 365–380. ISSN: 05503213. DOI: 10.1016/0550-3213(76)90143-7.

[174] Tai Tsun Wu and Chen Ning Yang. "Some properties of monopole harmonics". In: *Phys. Rev. D* 16 (4 Aug. 1977), pp. 1018–1021. DOI: 10.1103/PhysRevD.16.1018. URL: https://link.aps.org/doi/10.1103/PhysRevD.16.1018.

[175] X. G. Wen and A. Zee. "Shift and spin vector: New topological quantum numbers for the Hall fluids". In: *Phys. Rev. Lett.* 69 (6 Aug. 1992), pp. 953–956. DOI: 10.1103/PhysRevLett.69.953.

[176] D. Yoshioka, B. I. Halperin, and P. A. Lee. "Ground State of Two-Dimensional Electrons in Strong Magnetic Fields and $\frac{1}{3}$ Quantized Hall Effect". In: *Phys. Rev. Lett.* 50 (16 Apr. 1983), pp. 1219–1222. DOI: 10.1103/PhysRevLett.50.1219.

[177] F. D. M. Haldane. "Many-Particle Translational Symmetries of Two-Dimensional Electrons at Rational Landau-Level Filling". In: *Phys. Rev. Lett.* 55 (20 Nov. 1985), pp. 2095–2098. DOI: 10.1103/PhysRevLett.55.2095.

[178] F. D. M. Haldane and E. H. Rezayi. "Periodic Laughlin-Jastrow wave functions for the fractional quantized Hall effect". In: *Phys. Rev. B* 31 (4 Feb. 1985), pp. 2529–2531. DOI: 10.1103/PhysRevB.31.2529.

[179] F. D. M. Haldane. "A modular-invariant modified Weierstrass sigma-function as a building block for lowest-Landau-level wavefunctions on the torus". In: *Journal of Mathematical Physics* 59.7 (July 2018). 071901. ISSN: 0022-2488. DOI: 10.1063/1.5042618. URL: https://doi.org/10.1063/1.5042618.

[180] Jie Wang et al. "Lattice Monte Carlo for quantum Hall states on a torus". In: *Phys. Rev. B* 99 (12 Mar. 2019), p. 125123. DOI: 10.1103/PhysRevB.99.125123.

[181] Patrick J. Ledwith et al. "Fractional Chern insulator states in twisted bilayer graphene: An analytical approach". In: *Phys. Rev. Res.* 2 (2 May 2020), p. 023237. DOI: 10.1103/PhysRevResearch.2.023237.

[182] Jie Wang et al. "Chiral approximation to twisted bilayer graphene: Exact intravalley inversion symmetry, nodal structure, and implications for higher magic angles". In: *Phys. Rev. Res.* 3 (2 May 2021), p. 023155. DOI: 10.1103/PhysRevResearch.3.023155.

[183] B. Andrei Bernevig and N. Regnault. "Emergent many-body translational symmetries of Abelian and non-Abelian fractionally filled topological insulators". In: *Phys. Rev. B* 85 (7 Feb. 2012), p. 075128. DOI: 10.1103/PhysRevB.85.075128. URL: https://link.aps.org/doi/10.1103/PhysRevB.85.075128.